University of Kentucky
UKnowledge

Theses and Dissertations--Electrical and Computer Engineering

Electrical and Computer Engineering

2014

Virtualized Welding Based Learning of Human Welder Behaviors for Intelligent Robotic Welding

Yukang Liu
University of Kentucky, webberliu@gmail.com

Right click to open a feedback form in a new tab to let us know how this document benefits you.

Recommended Citation

Liu, Yukang, "Virtualized Welding Based Learning of Human Welder Behaviors for Intelligent Robotic Welding" (2014). *Theses and Dissertations--Electrical and Computer Engineering*. 51.
https://uknowledge.uky.edu/ece_etds/51

This Doctoral Dissertation is brought to you for free and open access by the Electrical and Computer Engineering at UKnowledge. It has been accepted for inclusion in Theses and Dissertations--Electrical and Computer Engineering by an authorized administrator of UKnowledge. For more information, please contact UKnowledge@lsv.uky.edu.

STUDENT AGREEMENT:

I represent that my thesis or dissertation and abstract are my original work. Proper attribution has been given to all outside sources. I understand that I am solely responsible for obtaining any needed copyright permissions. I have obtained needed written permission statement(s) from the owner(s) of each third-party copyrighted matter to be included in my work, allowing electronic distribution (if such use is not permitted by the fair use doctrine) which will be submitted to UKnowledge as Additional File.

I hereby grant to The University of Kentucky and its agents the irrevocable, non-exclusive, and royalty-free license to archive and make accessible my work in whole or in part in all forms of media, now or hereafter known. I agree that the document mentioned above may be made available immediately for worldwide access unless an embargo applies.

I retain all other ownership rights to the copyright of my work. I also retain the right to use in future works (such as articles or books) all or part of my work. I understand that I am free to register the copyright to my work.

REVIEW, APPROVAL AND ACCEPTANCE

The document mentioned above has been reviewed and accepted by the student's advisor, on behalf of the advisory committee, and by the Director of Graduate Studies (DGS), on behalf of the program; we verify that this is the final, approved version of the student's thesis including all changes required by the advisory committee. The undersigned agree to abide by the statements above.

Yukang Liu, Student

Dr. YuMing Zhang, Major Professor

Dr. Cai-Cheng Lu, Director of Graduate Studies

VIRTUALIZED WELDING BASED LEARNING OF HUMAN WELDER BEHAVIORS FOR INTELLIGENT ROBOTIC WELDING

DISSERTATION

A dissertation submitted in partial fulfillment of the requirements for the degree of Doctor of Philosophy in the College of Engineering at the University of Kentucky

By

Yukang Liu

Lexington, Kentucky

Director: Dr. YuMing Zhang, Professor of Electrical and Computer Engineering

Lexington, Kentucky

2014

Copyright © Yukang Liu 2014

ABSTRACT OF DISSERTATION

VIRTUALIZED WELDING BASED LEARNING OF HUMAN WELDER BEHAVIORS FOR INTELLIGENT ROBOTIC WELDING

Combining human welder (with intelligence and sensing versatility) and automated welding robots (with precision and consistency) can lead to next generation intelligent welding systems. In this dissertation intelligent welding robots are developed by process modeling / control method and learning the human welder behavior.

Weld penetration and 3D weld pool surface are first accurately controlled for an automated Gas Tungsten Arc Welding (GTAW) machine. Closed-form model predictive control (MPC) algorithm is derived for real-time welding applications. Skilled welder response to 3D weld pool surface by adjusting the welding current is then modeled using Adaptive Neuro-Fuzzy Inference System (ANFIS), and compared to the novice welder. Automated welding experiments confirm the effectiveness of the proposed human response model.

A virtualized welding system is then developed that enables transferring the human knowledge into a welding robot. The learning of human welder movement (i.e., welding speed) is first realized with Virtual Reality (VR) enhancement using iterative K-means based local ANFIS modeling. As a separate effort, the learning is performed without VR enhancement utilizing a fuzzy classifier to rank the data and only preserve the high ranking “correct” response. The trained supervised ANFIS model is transferred to the

welding robot and the performance of the controller is examined. A fuzzy weighting based data fusion approach to combine multiple machine and human intelligent models is proposed. The data fusion model can outperform individual machine-based control algorithm and welder intelligence-based models (with and without VR enhancement).

Finally a data-driven approach is proposed to model human welder adjustments in 3D (including welding speed, arc length, and torch orientations). Teleoperated training experiments are conducted in which a human welder tries to adjust the torch movements in 3D based on his observation on the real-time weld pool image feedback. The data is off-line rated by the welder and a welder rating system is synthesized. ANFIS model is then proposed to correlate the 3D weld pool characteristic parameters and welder's torch movements. A foundation is thus established to rapidly extract human intelligence and transfer such intelligence into welding robots.

KEY WORDS: Welder response modeling, welder rating system, virtualized welding, intelligent welding robot, GTAW

Yukang Liu

September 1, 2014

VIRTUALIZED WELDING BASED LEARNING OF HUMAN WELDER BEHAVIORS FOR INTELLIGENT ROBOTIC WELDING

By

Yukang Liu

Dr. YuMing Zhang

_____

Director of Dissertation

Dr. Cai-Cheng Lu

_____

Director of Graduate Studies

September 1, 2014

_____

Date

ACKNOWLEDGEMENTS

The research work in this dissertation is funded by the National Science Foundation (NSF) Project under grant IIS-1208420 entitled "Virtualized Welding: A New Paradigm for Intelligent Welding Robots in Unstructured Environment" and CMMI-0927707 entitled "Machine-Human Cooperative Control of Welding Process".

Firstly I would like to sincerely thank my advisor Dr. YuMing Zhang for his invaluable guidance, continuous encouragement and constructive suggestions. Dr. Zhang's expertise in system identification, control system design, and welding processes helped me throughout the research. He encouraged me to be a better individual researcher, better research collaborator, better teaching instructor, and better person.

I am also grateful to Drs. Alan T. Male, Larry Holloway, Yuan Liao, and Fuqian Yang for their helpful insight and supervision as my committee members and outside examiner. I want to thank my research collaborators Mr. Bo Fu and Prof. Ruigang Yang in Department of Computer Science, University of Kentucky, for their expertise in computer vision and augmented system design and implementation. I would like to give my thanks to all of my colleagues in the Welding Research Lab: WeiJie Zhang, Ning Huang, Xiaoji Ma, Yi Lu, Chuansong Wu (visiting scholar), Xuewu Wang (visiting scholar), Yusheng Liu (visiting scholar), Yu Shi (visiting scholar), Xiangrong Li, Yi Huang, Kun Qian, Zhenzhou Wang, Zeng Shao, Jinsong Chen, Yan Shao, Xiang Zhang, Zuming Liu, Jun Xiao and Zhijiang Wang for their helpful suggestions for my work.

In addition, I want to give my thanks to my parents for their endless love and support throughout all my life. Lastly I'd like to express my great appreciation to my wife, Leni Liu, for her encouragement and sharing with me so many wonderful things in my life.

Table of Contents

List of Tables

List of Figures

Chapter 1 Introduction

1.1 Background

Currently two most widely-used welding processes in manufacturing industries are gas tungsten arc welding (GTAW) and gas metal arc welding (GMAW) [1]. They both are arc welding process, in which heat is generated by an electric arc struck between an electrode and the work piece. In GTAW, also known as Tungsten Inert Gas (TIG) Arc Welding, a tungsten rod is used as a non-consumable electrode to ease the emission of electrons to maintain a stationary arc. The heat produced by the arc melts the weld joints' edges and joins them together. An optional filler rod may be used, if required. Furthermore the weld pool is shielded by an inert gas (argon, helium, etc.) protecting the molten metal from atmospheric contamination. This process is illustrated in Figure 1.1 (left). GMAW, also known as Metal Inert Gas (MIG) Arc Welding, is similar in

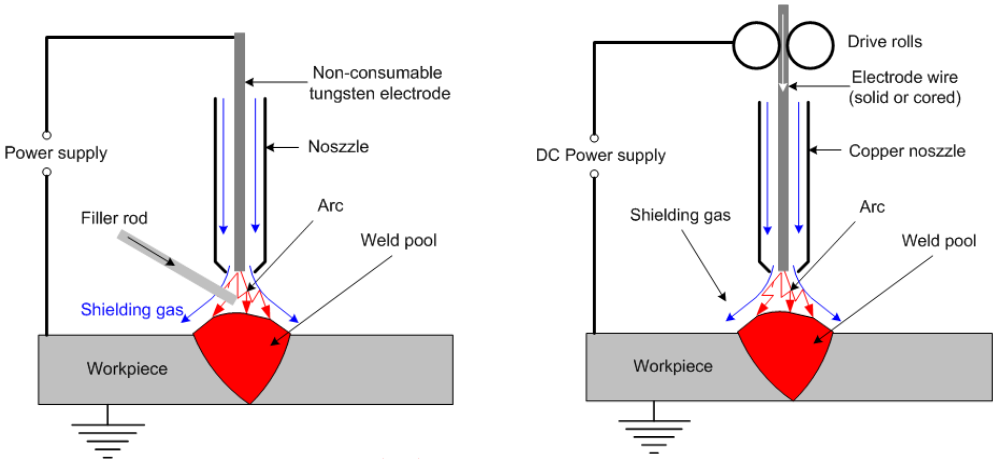

Figure 1.1 Two of the most widely-used welding processes. (left) GTAW (TIG) with optional filler rod in use; (right) GMAW (MIG).

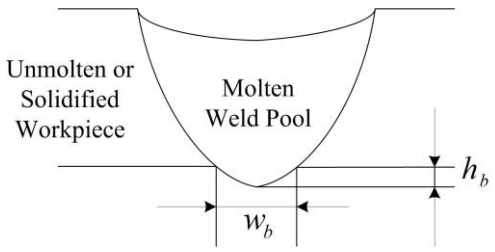

Figure 1.2 Weld pool and full penetration.

principle to GTAW. However, a consumable electrode wire, having chemical composition similar to that of the parent material or other required chemical composition, is continuously fed from a spool to the arc zone, as shown in Figure 1.1 (right).

Manual GTAW process is commonly used in industry especially for the applications where the weld quality is critical. In this process, a skilled welder can make adjustments based on their observations of the liquid weld pool surface. Those real-time adjustments often lead to desired weld bead geometry characterized by back-side bead width w_b and positive reinforcement h_b (Figure 1.2). However, skills needed for critical welding operations typically require a long time to develop. Shortage of skilled welder has become an urgent issue the manufacturing industry is currently facing [2].

Automated welding robots, on the other hand, outperform human welders whose performance may degrade because of their physical limitations (inconsistent concentration, fatigue, stress and long-term health issues, etc.). Unfortunately, current industrial welding robots are basically articulated arm with pre-programmed movement. Although some robots are equipped with seam tracking capabilities, they all lack the intelligence skilled human welders possess. They require precision prepared work pieces with little variation in geometry and material properties. Their applications are thus mostly limited to assembly lines for mass-produced products, such as automobiles, where the work-piece preparation is controllable at reasonable costs. However, as outlined in the national robotic report [3], the trend of manufacturing is to produce customized products in small batches, where ideal automated production lines are not cost effective. Intelligent welding robots that possess intelligence comparable to skilled welders but with less physical restrictions and can work in harsh environment will thus be one of the keys to maintaining a competitive manufacturing industry despite relatively high labor costs/wages.

The goal of the proposed research is to enable the development of the future generation of welding robots that can sense and adapt to different welding jobs with little or no

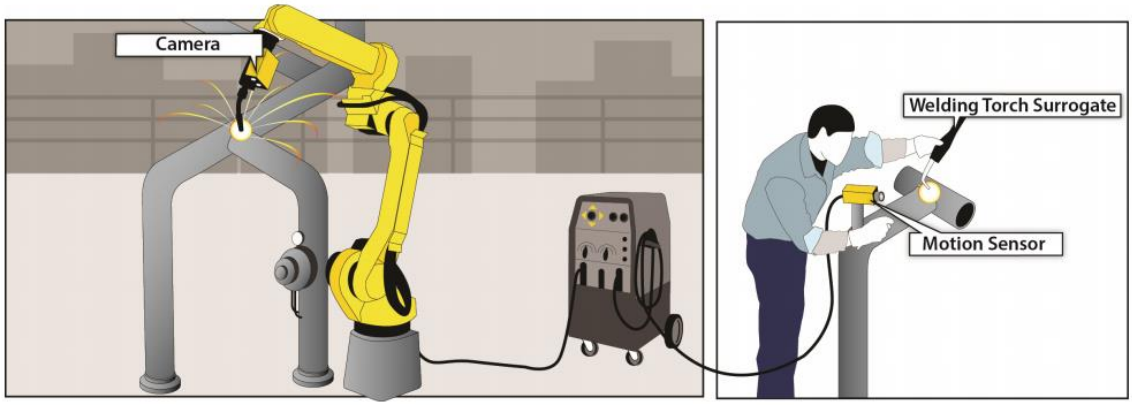

Figure 1.3 Illustration of our virtualized welding operation.

human intervention. Toward this goal of intelligent welding robots with autonomy, we propose an innovative robotic welding platform that is capable of monitoring the welding process using 3D imaging techniques and visualize the welding process remotely using virtual reality (VR) techniques, which we refer to as Virtualized Welding. As shown in Figure 1.3, a traditional welding robot is augmented with a number of sensors to acquire all the relevant information in a welding process, including welding torch position, weld pool surface geometry, work piece geometry, welding current, etc. These parameters are transferred to a visualization workstation to "re-enact" the welding process. The workstation uses a projector to project and simulate the welding environment. Note that the projection surface, constructed from template pieces, is a proxy for the actual welding pieces.

Our Virtualized Welding can be operated at two different levels: (a) remote-controlled welding (teleoperation): similar to the well-known da Vinci surgical robot, now a welder can remotely operate the welding torch by controlling the surrogate in the visualization station, with the benefit of looking at the welding process from different viewpoints, as if he/she is right in front of the work piece. This would enable welding in hazardous areas for human operators; and (b) autonomous welding: the weld robot is running in a fully automatic way under closed-loop control. The control decision is based on the sensor input, such as 3D geometry of the weld pool and the work piece. This type of adaptive control is fundamentally more advanced than the current welding robots.

1.2 Objectives and Approach

As can be seen from previous analysis, both automated GTAW process and manual GTAW process have their advantages and limitations. It would thus be beneficial to combine the adequate sensing, invaluable experience, and intelligence from human welders with accurate machine execution and physical capabilities from the welding robots. To this end, as a part of NSF project "Virtualized Welding: A New Paradigm for Intelligent Welding Robots in Unstructured Environment", the objectives of this dissertation are:

- to accurately control the welding process using 3D weld pool surface feedback;
- to understand skilled welder response to 3D weld pool surface (by adjusting welding current) and transfer the skilled welder intelligence to an automated welding machine;
- to establish the hardware/software foundation to allow a welding robot to combine its accurate motion control and physical strengths with the intelligence of a human welder through real-time human-robot cooperation;
- to formulate a framework that can distill human intelligence in welding to robotic control algorithms.

The technical challenges include visualization of the welding process, modeling of the complex relationship among welder actions, welding parameters, and the final weld bead quality. To address these, we propose the following approaches: (a) VR visualization schemes that use surrogates and geometric proxies to mitigate common problems in teleoperation; and (b) data driven system modeling that estimates statistical correlation between the status of welding and the adjustment a human welder has applied, based on which optimal control can be derived; the effectiveness of our modeling approach will be validated with off-line data and its success will establish the foundation for fully automatous welding in virtualized welding.

1.3 Dissertation Outline

In this dissertation accurate welding process control and intelligent welding robots are developed by process modeling / control method and learning the human welder adjustment on welding current, welding speed, arc length, and torch orientations. The dissertation is organized as follows.

Chapter 1: Introduction

The background and motivation of the proposed research is discussed as well as the objectives of the research.

Chapter 2: Literature Review

The sensing of the welding process is firstly surveyed, including pool oscillation, ultrasonic, infrared, arc sensing, and vision-based sensing method. Control of the welding process is then briefly reviewed. Human intelligence modeling is further discussed. Finally, virtual reality based welder training system is surveyed with current state-of-the-art welder training systems.

Chapter 3-5 is devoted to controlling automated pipe GTAW process using an automated welding machine where the pipe rotates and the welding torch / sensing system is stationary (i.e., 1G welding position).

Chapter 3: Weld Penetration Control for Automated GTAW Process

Weld penetration is accurately controlled in this chapter for an automated welding machine. Dynamic experiments are conducted to establish the model that relates the back-side bead width to the welding current and speed. Weld penetration is accurately estimated by the 3D weld pool surface characteristic parameters. Dynamic linear model is first constructed and the modeling result is analyzed. The linear model is then improved by incorporating a nonlinear operating point modeled by an Adaptive Neuro-Fuzzy Inference System (ANFIS). Model Predictive Control (MPC) algorithm is then derived.

Welding experiments confirm that the developed control system is effective in achieving the desired weld joint penetration under various disturbances and initial conditions.

Chapter 4: 3D Weld Pool Surface Control

In this chapter the dynamic response of 3D weld pool characteristic parameters to welding current and speed as control variables is modeled. A predictive control algorithm is developed to control these characteristic parameters. Welding experiments confirm that the developed control system is effective in achieving the desired 3D weld pool surface geometry despite various disturbances.

Chapter 5: Skilled Human Welder Response Modeling and Intelligent Control

Chapter 5 presents the learning of the skilled welder adjustment on the welding current in this automated welding machine. The skilled welder response is modeled using ANFIS, and compared to the novice welder. Control experiments confirm the effectiveness of the proposed human response model.

Chapter 6-10 presents the proposed virtualized welding platform where a welding robot (carrying welding torch / sensors) moves along the pipe to perform welding and the pipe is stationary (i.e., 5G welding position), and various methods for learning human welder movements.

Chapter 6: Virtualized Welding Platform and Teleoperation

Chapter 6 presents a virtualized welding system that enables learning from human welder intelligence for transferring into a welding robot. Teleoperation experiments are conducted under different welding currents and experimental results are analyzed. A correlation between the welding current and welding speed is proposed for GTAW pipe welding with specified welding conditions. Consistent penetration and satisfactory welds are generated in automated welding experiments.

Chapter 7: Learning Human Welder Movement with Virtual Reality Enhancement

Chapter 7 illustrates the learning of human welder movement with virtual reality enhancement. Machine-human cooperative control scheme is firstly introduced, and the virtual reality enhancement is provided. Learning experiments are conducted and the human welder response is modeled using an iterative K-means based ANFIS model.

Chapter 8: Learning Human Welder Movement without Virtual Reality Enhancement

Chapter 8 introduces the learning of human welder movement without virtual reality enhancement. To better distill the correct movement of the human welder, a fuzzy classifier is proposed to rank the data and only preserve the high ranking “correct”

response. The trained ANFIS model is then transferred to the welding robot and the performance of the controller is examined.

Chapter 9: Fuzzy Weighting Based Data Fusion: Combining Machine and Human Intelligence

A fuzzy weighting based data fusion approach to combine multiple machine and human intelligent models described in previous chapters is proposed for developing intelligent welding robot in pipe GTAW process. The data fusion model outperform individual machine algorithm (super welder) and welder intelligence models (both with and without VR enhancement).

Chapter 10: Full 3D Position and Orientation Learning and Control

This chapter presents a data-driven approach to model human welder intelligence in 3D. Teleoperated training experiments are conducted in which a human welder tries to adjust the torch movements in 3D (including welding speed, arc length, and torch orientations) based on his/her observation on the real-time weld pool image feedback. The data is off-line rated by the welder and a welder rating system is synthesized. ANFIS model is then proposed to correlate the 3D weld pool characteristic parameters and welder's torch movements.

Chapter 11: Conclusion and Future Work

The main findings and contributions are summarized and the future work to improve the proposed research is detailed.

Chapter 2 Literature Review

Welding is the final stage for manufacturing of many high value-added products, which has been widely applied in automotive assembly, aircraft production, and micro-electric components joining, etc. Achieving accurate sensing, intelligent control of welding process and developing the intelligent welding robots has becoming the trend for next generation welding machine. The difficulty is primarily due to the invisibility of the liquid metal bottom surface underneath the weld pool and the extreme brightness of the arc [4]. Various methods have thus been extensively studied to monitor the weld pool and weld penetration, including pool oscillation, ultrasound, infrared sensor, and vision-based sensing method, etc. Each sensing method is firstly reviewed in the first subsection. Then various welding process control methods utilizing different sensing methods are introduced. Human intelligence modeling is surveyed in Section 2.3, and virtual reality based welder training systems currently available in industry are finally briefly reviewed in Section 2.4.

2.1 Sensing of the Welding Process

The sensing of the welding process should provide information about the penetration depth and penetration type, i.e. full penetration and partial penetration, as well as other information about the welding process, including weld pool surface [4]. Extensive works have been done to develop sensing technology for the welding process. According to the measurement method, the sensing of the welding process can be categorized into the following types: pool oscillation [5-14], ultrasonic sensing [15-22], infrared sensing [23-25], arc sensing [26-31], and vision sensing method [32-54]. In the following a literature review regarding these sensing methods is presented.

2.1.1 Pool Oscillation Method

Sensing the weld penetration based on monitoring weld pool oscillation behavior is based on the fact that a weld pool can be brought into natural oscillation and the oscillation frequency of the weld pool is related to the weld pool geometry [4]. This phenomenon may be used to monitor the weld pool in a feedback control system.

The pioneering work in pool oscillation was conducted by Kotecki [5], and Richardson [6]. Hardt [7] and their co-workers proposed a method to determine the back-side bead width by measuring the natural frequency of pool motion when driven by a time varying arc plasma force. However, the results were obtained for stationary weld pools, and it was unclear if similar results occur when the welding torch was moving. G. den Ouden found an abrupt change in the oscillation frequency of the pool during the transition from partial to full penetration [8, 9]. Andersen [10] developed a synchronous weld pool

oscillation method for controlling the weld pool dimensions and state of penetration. Hartman [11] further evaluated this synchronous excitation method and developed a control system that regulated the total heat input to maintain constant fusion zone geometry by monitoring the arc light reflection from the oscillation of the molten metal surface. Ju [12] proposed a new vibration method: the Pulse Shielding Gas (PSG) oscillating method. A control system was constructed by controlling the welding current based on the natural vibration frequency measurements from an arc sensor. Yudodibroto [13] implemented the weld penetration control based on weld pool oscillation sensing method during GTAW process with cold filler wire addition.

2.1.2 Ultrasonic Method

Ultrasonic sensors [14-23] are used to determine the boundaries of the liquid and metal in the weld pool. In [14] the developed ultrasonic sensing system could locate and track the welding seam ensuring correct positioning of the welding head relatively to the joint preparation. Recently, to overcome the contact requirement of the ultrasonic sensing method, various non-contact ultrasonic sensing methods have been developed, such as laser ultrasonic sensing [18-20], electromagnetic acoustic transducer (EMAT) ultrasonic sensing [21], and laser-EMAT ultrasonic sensing [22], etc. However, these sensing systems are highly expensive and complicated, which are not preferable for welding application.

2.1.3 Infrared Based Method

Infrared sensing [23-25] is a type of non-contact thermal measurement technique which has been widely used in various applications. Infrared sensors can detect infrared radiation emitted by materials. In [24] infrared sensor is used to monitor weld process parameters including weld bead width, penetration depth, and torch position. However, the infrared camera is much more expensive than regular optical camera, and thus limits its applicability for the industrial welding applications.

2.1.4 Arc Sensing

Arc sensing [26-31] has many applications in welding process monitoring, some of which (such as automatic voltage control, AVC) has been dated back over forty years. The advantage of arc sensing is that by using the arc itself as sensor, there is no need for external sensors with their associated costs and concern for reliability in the harsh welding arc environment [4]. Arc sensing has been used in arc stability control [26, 27], seam tracking [28, 29], and weld penetration control [30, 31].

2.1.5 Vision Based Sensing

The weld pool surface provides important information for understanding welding processes and is the most direct source of information for human welders to obtain feedback. Observing the weld pool surface and measuring its parameters is thus vital to developing intelligent welding machines that can mimic a skilled human welder, who estimate the welding process by visually observing the weld pool and adjust welding parameters accordingly.

Pioneering work on weld pool observation was conducted at the Ohio State University by Rokhlin and Guu [32-34], using radiography. The radiation of the received X-ray increases with the depression depth. However, the principle behind this method is to measure the material thickness. For full penetration where backside pool surface deformation occurs, the pool surface shape will be difficult to extract.

Minch [35, 36] developed a stereovision system for in situ weld pool measurement using high frame rate. Two high-speed cameras were synchronized with robotic welder to capture images during the time when the arc is off. By using stereo image processing algorithms the weld pool shape was rendered in 3D. Zhao [37] used shape from shading (SFS) algorithm to reconstruct the surface from one single weld pool image. Kovacevic and Zhang [38, 39] proposed a novel mechanism for observing the GTA weld pool surface shape through two major advances. First, to eliminate the influence of the bright arc light, a short duration pulsed laser was projected onto the weld pool surface. The camera shutter was synchronized with the pulse duration. Second, a frosted glass was used to allow each laser ray as a new point light source which disperses light with a certain diffuse angle. The camera views the grid openings through their reflection from the weld pool surface and obtained image consists of bright strips deformed by the weld pool surface deformation.

The proposed method can obtain specular reflection from the weld pool under the presence of the bright arc. An iterative algorithm was used to calculate the surface of the weld pool. However, the synchronization of the laser and high-speed shutter requires specific, high-costly, and sophisticated equipment. Also, in order to suppress the arc light, the power of the laser during the pulse must be very high and the frame rate can thus not be very high because a high frame rate would increase the average power of the illumination laser.

While the laser-camera synchronization can be considered a “hard” way, a “soft” way may be to take advantage of the difference between the arc light and illumination laser. It is known that arc light intensity decreases rapidly with the distance but the laser does not significantly lose its intensity. This principle has proven to work in the back lighting method used to image droplets in GMAW [40] which projects a laser from one side of the

torch and intercepts the laser that has been partially blocked by the droplet at the opposite side. Saeed [41-45] studied the structured light method in sensing GTA weld pool surface. Song [46-51] extended this approach by projecting a low-power dot-matrix laser pattern onto the GTA weld pool surface and observing the intercepted reflected laser on an imaging plane.

This approach makes use of relatively simple idea to facilitate a practical solution to overcome the two challenges (bright arc and specular surface) aforementioned: by exploiting the propagation difference between laser and plasma, the laser rays mirrored form the weld pool surface can be clearly imaged in the presence to bright plasma, thus changing the specular surface from a difficulty to an advantage. More specifically, the reflected laser keeps straight travel without significant loss of intensity over distance while the radiation of the arc energy decays rapidly over distance. However, the quality of the reflected images is highly sensitive with the shape of the weld pool. Zhang [52-54] modified the image processing algorithm accordingly and the 3D weld pool surface can be reconstructed in real-time. The weld pool width, length, and convexity was further proven to be an acceptable set to effectively characterize the 3D weld pool surface geometry representing the weld penetration [55].

2.2 Control of the Welding Process

Robust and reliable control method of the welding process is needed for the purpose of achieving low cost and high productivity. When the uncertainties and variations in welding process are substantial, welding parameters must be adjusted on-line to assure the production of quality welds. Control of the weld pool is thus an essential capability for next generation intelligent robotic welding systems and should be further explored. Researchers have established various control systems to control the welding process over the past few decades. The following subsection is devoted to provide an overview of the control method in welding process.

Depending on the sensing method used, the control systems can be categorized into pool oscillation-based control [56, 57], radiography-based control [58], thermal-based control [59-62], and vision-based control [63-74].

Andersen [56] developed a synchronous weld pool oscillation method for sensing the state of penetration. Hartman [57] further evaluated this method and developed a control system that regulated the total heat input to maintain constant fusion zone geometry. Guu [58] utilized real-time radiography for controlling the penetration in solidified areas and depression of the weld pool. Song [59] developed a closed-loop system to control the weld pool depth using a thermally based depth estimator from point temperatures measured on the backside of the workpiece. In [60] a self-organizing fuzzy control method was proposed to obtain a uniform weld pool size in GMAW by regulating the

surface temperature at a desired level. Chen [61] and Banerjee [62] found the slope of the infrared intensity became zero when the liquid-solid interface of the weld pool is crossed, which might be utilized to control the welding process.

Compared to the above mentioned sensing and control methods, vision-based control method is more direct and prominent as an emulation of the estimation and decision making process of the human welder. Extensive researches have been conducted to explore the possibility to control the weld pool to some extent. Vorman [63] used a line scanner to detect the weld pool region and control the weld pool width. Ohshima [64] proposed a pool width control in pulsed GMAW by observing the weld pool using a CCD camera in low current intervals of the pulsed current. Pietrzak [65] developed a weld pool width control system which uses a miniature camera mounted in a modified coaxial viewing torch to view the weld pool. Song [66] controlled the depth and width of the weld pool using top-side and back-side sensors. Zhang [67-69] proposed adaptive predictive and neuro-fuzzy model based control algorithm to control the front-side weld pool width and back-side bead width. Chen [70] proposed a self-learning fuzzy neural network controller to simultaneously control the weld pool length and width. Zhao [71] developed a control system to control the back-side bead width and front-side reinforcement. Tsai [72] proposed an automatic pulsed GTAW pipe welding system with fuzzy control technique to control the width of the pool. Kong [73] and Chen [74] controlled the penetration of the Al alloy welding through passive vision of the weld seam and weld pool.

2.3 Human Intelligence Modeling

Despite the trend of growing automation degree in industrial processes and machines, the human operator/controller is still irreplaceable in various applications [75-77]. What makes the identification of human operators' behavior such as a challenging endeavor is that the human operator is a nonlinear, often time-varying controller whose coefficients might vary rapidly with factors such as motivation, workload, fatigue, and other physiological variations [78, 79]. Specifically in welding operations, a welder makes decisions primarily based on past learned experiences/skills which might not involve a fundamental understanding of the laws of welding physics. Also, a human welder assesses and controls a welding process using a humanistic approach where the feedback sensory information acquired by the welder might be imprecise and only reflects partial truths about the instant status of the weld process [54].

Modeling and identifying the dynamics of a human controller/operator originated from the theories of servomechanism and filtering in the 1940's [54]. A series of preliminary experiments were conducted on human tracking in one-dimensional compensatory task [80]. McRuer and Jex conducted a systematic measurement of the human operator with a variety of controlled system dynamics and random-appearing inputs of different

bandwidths [81, 82]. A crossover model of human operator was proposed that can describe the linear portion of the human operation in a single-loop compensatory task in a frequency range around crossover frequency.

Optimal control theory was then introduced in human operator behavior identification [83]. It was based on an assumption that the well-trained human operator behaves in a nearly optimal manner subject to the inherent physio-physical limitations. Based on the assumption, an optimal control model (OCM) was proposed in 1970 on the dynamic characteristics of a pilot [84]. The transfer function was considered as the cascaded of the inherent part of reaction time delays and lags attributed to the neuromuscular system and the equalization part adjustable to the task requirement, where the time delay comes from the various internal time delays associated with visual, center processing, and neuro-motor pathways.

The OCM was later extended by Tomizuka to cover preview tracking [85, 86]. In addition, a modified optimal control model (MOCM) was proposed by Davidson and Schmit in 1992 [87]. The MOCM replaced the time delay of the OCM with a Pade approximation that allowed one to obtain a soletransfer function representation of the operator. Many researchers have continuously studied the tracking ability and characteristics of the human operator as an adaptive controller [88], a tele-manipulator [89] or an optimal controller [90]. Unfortunately, these methods lead to typically high order for the obtained models. For instance, the order of these OCM-based models is equal to the sum of the orders of the controlled element, disturbance filter, neuro-motor lag and Pade delay. This feature makes insight into the operator control model difficult to determine. A fixed-order optimal control model based on MOCM was thus proposed to reduce the order while keeping the model optimality [91]. Nonlinear methods such as neural networks, neuro-fuzzy or adaptive models were employed as well to model the human actions [92-96].

The modeling of the human operator has been studied in the physiological perspective. Based on [97, 98], in the learning stage the cerebral cortex is playing the role of controller in the feedback path. In [99], the feedback error learning model was proposed. The model considered that the human hand/thumb motion skill comes from the feed-forward structure of the cerebellum representing the inverse model of the hand/thumb system. In addition, an iterative manual control model has been proposed based on human operator's physiological perspective [100]. A recalling factor has been introduced in the model representing the human operator's experiences/skills. The model indicates that human operators tune their control actions using error and error rate in each iteration.

A human operator intermittently scans the state of the controlled system and continuously operates. A skillful operation means that the information is scanned less frequently. A control action similar to the minimum attention [101] might be found in human operation.

In addition to such minimum attention, Ito's observation in that if the operation skill level exceeds to a certain extent, the operation becomes of feed-forward type, can be interpreted as that the interval of the attention becomes longer as the skill becomes better. Therefore, for a skilled operator, the control action would tend to be feed-forward type, while an unskilled operator controls the system in a feedback close loop. Also, the observation of the system state might be achieved by the trigger of the special occasion of the event [102].

2.4 Virtual Reality Based Welder Training System

Welder training systems have been investigated in manufacturing industry to accelerate the learning process and compensate for the shortage of welding instructor (e.g., EWI AdvanceTrainerTM [103] and RealWeld Trainer [104]). Recently, virtual reality (VR) has been recognized for its value in welder training [105]. Some sophisticated systems for training with Head Mounted Display (HMD) have been proposed recently, such as ARC+ [106], the Fronius Virtual Welding system [107], VRTEX 360 [108]. However, these systems do not employ see-through method, instead, they apply fully simulated environment on the display. Among these VR methods, VRTEX 360 is considered as one of the most sophisticated welder training system. A mock-up welding torch is equipped with sensors so that it can be fully tracked. A welder's helmet is fitted with HMD to provide simulated images. As a training tool, the images shown to the trainee are entirely simulated. While this may be adequate for the purpose of training, it is unlikely to be able to simulate the complexity and possible variations in a real welding environment. Another drawback is that the focus distance is fixed in most display types, resulting poor eye accommodation. In this dissertation we choose to use Augmented Reality (AR) techniques [109, 110] for the visualization aspect of virtualized welding. AR allows a user to see the real world, with virtual objects superimposed upon or composited with the real world. Although AR has been used in many application areas including education, health care, the military, and entertainment, its application in welding and welder intelligence learning has not yet been reported. In Chapter 6, proposed virtualized welding system is briefly introduced.

Chapter 3 Weld Penetration Control for Automated GTAW Process

Skilled welders can estimate and control the weld joint penetration, which is primarily measured by the back-side bead width, based on weld pool observation. This suggests that an advanced control system could be developed to control the weld joint penetration by emulating the estimation and decision making process of the human welder [111]. In this chapter an innovative 3D vision sensing system [4] is used to measure the characteristic parameters of the weld pool in real-time for GTAW. The measured characteristic parameters are used to estimate the back-side bead width, using an ANFIS as an emulation of skilled welder. Dynamic experiments are conducted to establish the model that relates the back-side bead width to the welding current and speed. Dynamic linear model is first constructed and the modeling result is analyzed. The linear model is then improved by incorporating a nonlinear operating point modeled by an ANFIS. Because the weld pool needs to gradually change, as controlled by a skilled welder, a model predictive control is used to follow a trajectory to reach the desired back-side bead width and the control increment is penalized. Because the weld pool is not supposed to change in an extremely large range, the resultant controller is actually liner and an analytical solution has been derived. Welding experiments confirm that the developed control system is effective in achieving the desired weld joint penetration under various disturbances and initial conditions.

3.1 Experimental Platform

In this subsection an innovative vision-based sensing system for GTAW process

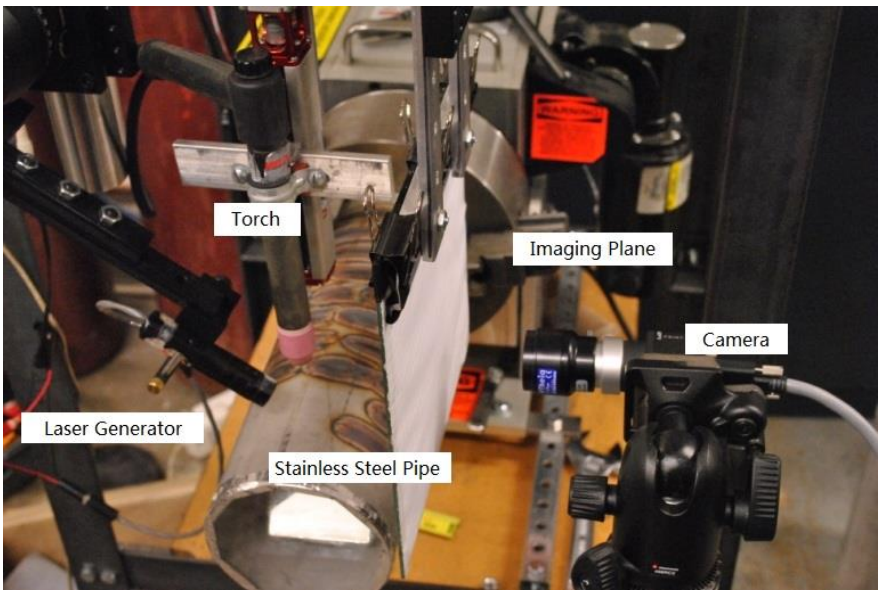

Figure 3.1 Experimental setup with the proposed sensing system [111].

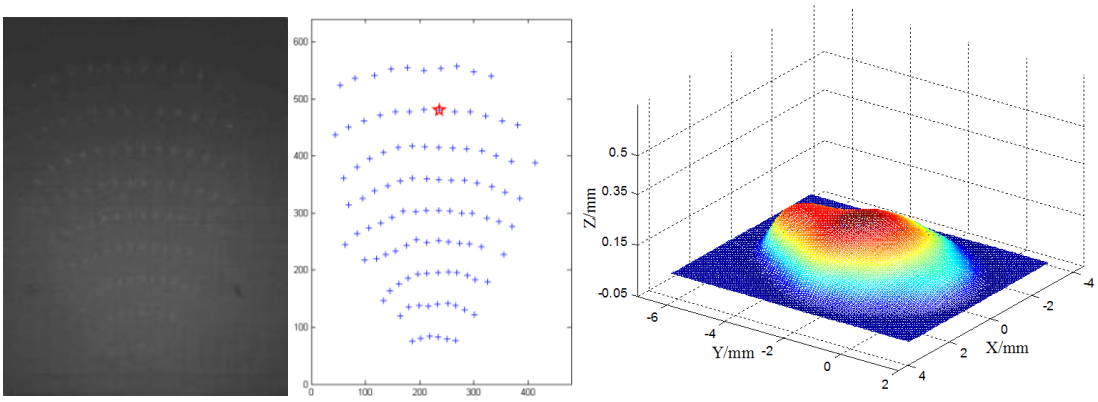

(a) (b) (c)

Figure 3.2 Image processing and three-dimensional reconstruction results.(a) Captured image using the sensing system; (b) Resultant dots in the captured image using image processing. The asterisk in the figure is the reference dot matching the dot at the 10throw and 10thcolumn in the projected laser dot matrix; (c) Interpolated 3D weld pool surface [111].

developed in the Welding Lab at the University of Kentucky [4] is briefly reviewed. This system is illustrated in Figure 3.1 together with the experimental setup. In this system a 20mw illumination laser generator at a wavelength of 685nm with variable focus is used to project a 19-by-19 dot matrix structured light pattern on the weld pool region. Part of the dot matrix projected inside the weld pool is reflected by the specular (mirror-like) weld pool surface, which is depressed and distorted because of the plasma impact from the arc and thus distorts the reflected dot matrix. The distorted dot matrix thus contains the 3D geometrical information about the weld pool surface.

An imaging plane is installed with a distance about 100 mm from the torch. A camera is located behind the imaging plane directly aiming at it. By using the specific image processing and 3D reconstruction scheme, the 3D weld pool surface can be reconstructed in real-time [4]. Examples of image processing result and reconstructed 3D weld pool surface are shown in Figure 3.2.

The welds are made using Direct-Current Electrode-Negative (DCEN) GTAW process. The material of the pipe is stainless steel 304. The wall thickness of the pipe is 2.03 mm. The pipe rotates during welding while the positions of the torch (except for its height from the pipe surface), the imaging plane, the laser structure light generator and the camera are stationary. The rotation speed and torch height are controlled by a computer to achieve required welding speed and arc length. The welding current is controlled by the computer through its analog output to the power supply. The workpiece is grounded before welding experiments. A clean workpiece provides a better surface conductivity (i.e., reduced arc voltage) and improves arc stability.

3.2 Estimation of Weld Penetration under Varying GTA Pools

The measured 3D weld pool surface was characterized by its width, length, and convexity [55]. These characteristic parameters were found capable of predicting the weld joint penetration as measured by the back-side bead width. However, to control the weld joint penetration, the welding current should be adjusted [112]. It is unclear if these characteristic parameters may still be used to predict the weld joint penetration in an acceptable accuracy when the weld pool varies substantially. To answer this question and estimate the penetration under varying weld pools, various dynamic experiments under different welding conditions were conducted using varying welding currents to acquire (front-side weld pool surface) characteristic parameters and corresponding back-side bead width as data pairs [112]. Data analysis revealed a nonlinear correlation of the backside bead width with the characteristic parameters. Further, the backside bead width at a particular location requires characteristic parameters from its neighboring weld pools to estimate if the pool varies. Hence, a dynamic ANFIS model was developed [112] to correlate the backside bead width nonlinearly to characteristic parameters in neighboring weld pools and used to on-line predict the backside bead width in real-time. It was found that the weld joint penetration as measured by the backside bead width was able to be predicted in real-time from the characteristic parameters in neighboring weld pools with an acceptable accuracy despite variations in weld pools by the nonlinear ANFIS model developed.

3.2.1 Data and Data Preprocessing

Before the experiments are conducted to produce the data pairs for analysis and modeling, a welding experiment is used to demonstrate the data and data preparation involved. As shown by this illustrative experiment, the data of interest from experiments include inputted welding current, inputted welding speed and measured front-side weld pool surface characteristic parameters as given in Figure 3.3. The back-side weld bead width in Figure 3.3 is measured from the back-side weld bead as shown in Figure 3.4 off-line after welding.

The characteristic parameters are measured at 30Hz by the vision system. They are noisy and their measurements in the data presented as shown in Figure 3.3 have been filtered using a low-pass filter:

$$y_f(k) = \alpha y_f(k-1) + (1-\alpha) y(k) \tag{3.1}$$

where $y(k)$ is the measured parameters (vector) at instant k, $y_f(k)$ is the filtered parameters (vector), and α is the coefficient of the filter. A greater α gives a stronger filtering producing smoother data but the response speed is reduced. There should be a trade-off between smoothness and response speed. It is found that when α=0.8 the

TABLE 3.1 EXPERIMENTAL AND IMAGING PARAMETERS

Welding Parameters			
Current / A	Welding speed / (mm/s)	Arc length / mm	Argon flow rate / (L/min)
50-76	1-2	4	11.8
Illumination and Imaging Parameters			
Laser projection angle / degree	Laser to weld pool distance / mm	Imaging plane to weld pool distance / mm	
35.5	24.7	101	
Camera Parameters			
Shutter speed/ms	Frame rate/fps	Camera to imaging plane distance/mm	
4	30	57.8	

measurement noise is sufficiently suppressed while the dynamic response is adequately

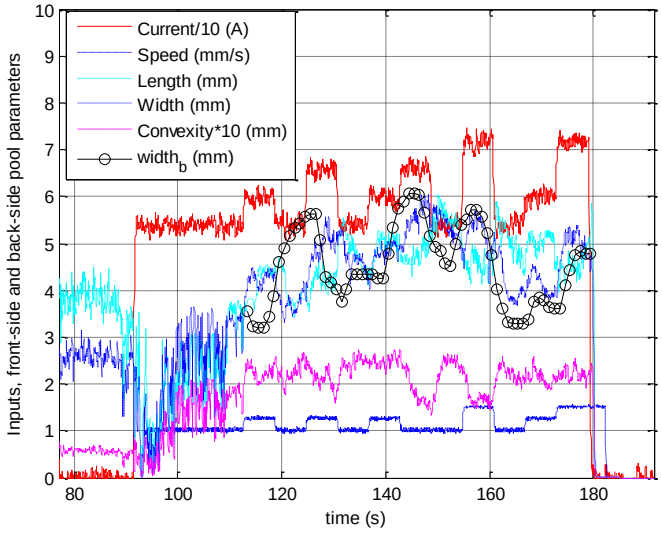

Figure 3.3 Input signal (welding current and speed), measured front-side weld pool characteristic parameters (the weld pool width, length, and convexity) and back-side bead width in a demonstrative welding experiment.

Figure 3.4 Image of back-side weld bead in the demonstrative welding experiment. The back-side bead width can be measured off-line and the results are shown in Figure 3.3.

preserved. The presented measurements of the characteristic parameters in Figure 3.3 and all of the following experiments are filtered using this filter with α=0.8.

3.2.2 Experimental Efforts

Various welding experiments are performed as bead-on-plate to produce data pairs for establishing the correlation between the front-side weld pool characteristic parameters and back-side bead width. These data of measurements are prepared as aforementioned. Ranges of welding parameters used to conduct welding experiments are shown in Table 3.1. Monitoring and camera parameters are also listed. It is noted that the welding current and speed were systematically varied to achieve varying degrees of full penetration. The sampling time in this study is chosen to be 0.5 second, or 2 Hz.

Seven experiments have been conducted to produce the data pairs for analysis and modeling. Their input parameters are plotted in Figure 3.5 (a), which have produced fully penetrated weld pools. The measured parameters of the weld pools in these experiments are plotted in Figure 3.5 (b).

3.2.3 Neuro-Fuzzy Modeling

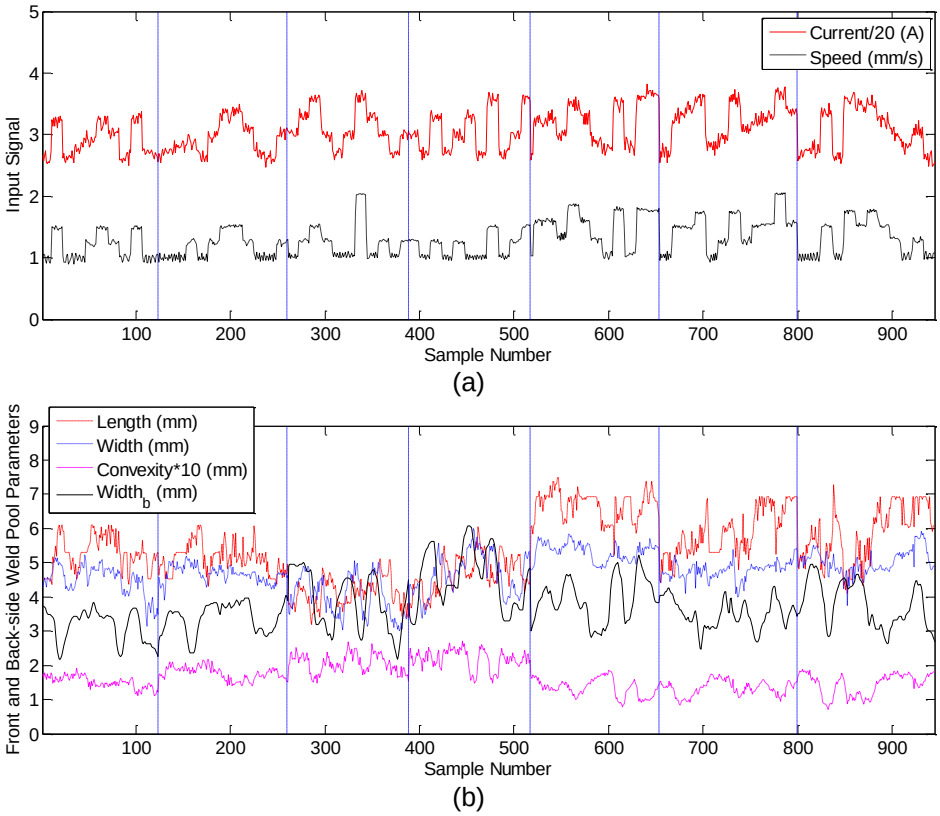

Figure 3.5 Measured data in seven welding experiments (a) Inputted welding parameters (welding current and speed) (b) Measured front-side weld pool characteristic parameters and back-side bead width.

As will be demonstrated, the back-side bead width correlates with the characteristic parameters nonlinearly and dynamically when the weld pool varies. The neuro-fuzzy models are suitable for modeling this type of correlations. This is because fuzzy systems can be used to model human intelligence that is typically nonlinear. However, the extraction of human intelligence, e.g. extracting how the human welders to estimate the weld joint penetration from their observation of weld pools, is difficult and tedious. Neuro-fuzzy approach (i.e. the fusion of the neural networks and fuzzy logic) provides an effective method to determine the parameters in fuzzy models (extracting the fuzzy rules that represent the human intelligence) using automated learning techniques developed in neural networks and has found success in various areas [113-116]. In particular, the ANFIS developed by Jang [117, 118] using a hybrid learning procedure possesses the advantages of adaptive rule changing capability, fast convergence rate, and does not require extensive experiences about the process to construct the fuzzy rules. Recently, ANFIS has been employed to model nonlinear functions, identify nonlinear components in control systems, and predict chaotic time series [119-121]. Hence, ANFIS will be used to model the back-side bead width to the characteristic parameters. As preparation, neuro-fuzzy modeling and ANFIS modeling are briefly reviewed first below.

A typical fuzzy rule in a Sugeno-type model [117] has the form:

$$\text{IF } x \text{ is } A \text{ and } y \text{ is } B, \text{ THEN } z=f(x, y) \tag{3.2}$$

where A and B are fuzzy sets, and $z=f(x, y)$ is a linear function.

ANFIS can construct an input–output mapping in the form of Sugeno type if-then rules by using a hybrid learning procedure [117]. A fuzzy logic control/decision network is constructed automatically by learning from the training data.

The membership function adopted in this study is generalized bell MF (membership function), which is specified by three parameters [118]:

$$A_{ji}(p_j; a_{ji}, b_{ji}, c_{ji}) = \frac{1}{1+\left|\frac{p_j - c_{ji}}{a_{ji}}\right|^{2b_{ji}}} \tag{3.3}$$

where $p_j\,(j=1,...,M)$ is the fuzzy variables with M being the number of fuzzy variables, and a_{ji}, b_{ji}, c_{ji} are the input fuzzy membership function parameters. In this study, the fuzzy variables will be the characteristic parameters that are the input variables of the model.

For a given set of input variables (for example p_1, p_2, and p_3), the following rule is implemented [118]:

Rule (i_1, i_2,i_3): IF $p_1$is A_{1i_1} , p_2 is A_{2i_2} , and p_3 is A_{3i_3}

THEN $y(i_1, i_2, i_3)=d_1(i_1, i_2, i_3)p_1+d_2(i_1, i_2, i_3)p_2+d_3(i_1, i_2, i_3)p_3+d_0(i_1, i_2, i_3)$ (3.4)

where d_j's are the so-called consequent parameters.

The final output of the fuzzy model is [118]:

$$y=\sum_{i_1=1}^{2}\sum_{i_2=1}^{2}\sum_{i_3=1}^{2} w(i_1,i_2,i_3)y(i_1,i_2,i_3) \tag{3.5}$$

where $w(i_1,i_2,i_3)$ is the weight representing the truth degree for the premise: p_1 is A_{1i_1} , p_2 is A_{2i_2} , and p_3 is A_{3i_3} , and is expressed by the following equation [118]:

$$w(i_1,i_2,i_3)=\prod_{j=1}^{3} A_{ji_k}(p_j) \tag{3.6}$$

The output equation (3.5) together with the weighting equation (3.6), membership function (3.3), and the fuzzy rule (3.4) form an ANFIS model. Its model parameters a_{ji}, b_{ji}, c_{ji} and d_j's can be identified using the Matlab ANFIS toolbox from experimental data pairs.

Once a model is identified, its quality/performance can be evaluated using the model average error and maximum error defined by:

$$E_{ave}=\frac{1}{N}\sum_{k=1}^{N}\left|\hat{y}(k)-y(k)\right| \tag{3.7}$$

$$E_{\max}=\max\left|\hat{y}(k)-y(k)\right|,(k=1,...,N) \tag{3.8}$$

where N is the number of samples, $y(k)$ is the measured back-side bead width, and $\hat{y}(k)$ is the model estimated back-side bead width at instant k. The root mean square error (RMSE) of the model can also be used:

$$RMSE=\sqrt{\sum_{k=1}^{N}(\hat{y}(k)-y(k))^2\Big/N} \tag{3.9}$$

3.2.4 Estimation of the Weld joint penetration

Denote the measured data as:

$$\left\{w_b(k),p_1(k),p_2(k),p_3(k)\right\}(k=1,2,...,N) \tag{3.10}$$

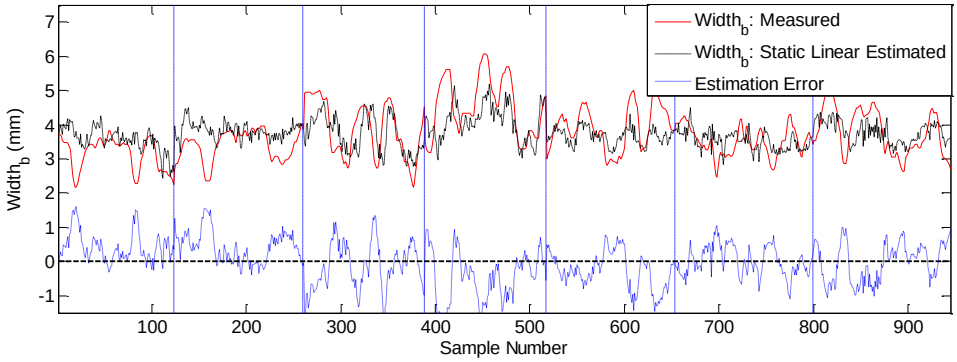

(a)

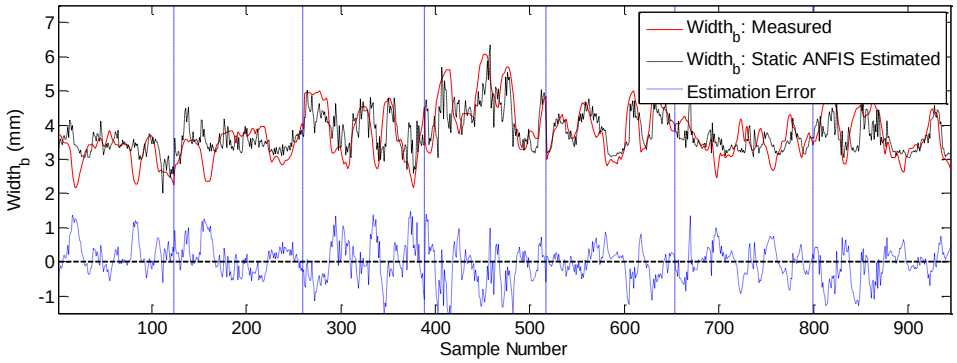

(b)

Figure 3.6 Static model based estimation results (a) linear modeling of the joint penetration (b) nonlinear ANFIS modeling of the joint penetration.

where $w_b(k)$, $p_1(k)$, $p_2(k)$, $p_3(k)$ are the back-side bead width, weld pool width, length, and convexity at the k^{th} sample instant, respectively.

In general, the static model can be written as:

$$w_b(k)=f(p_1(k), p_2(k), p_3(k)) \tag{3.11}$$

The simplest form of (3.11) can be expressed by the following linear model:

$$w_b(k)=\alpha_0+\alpha_1 p_1(k)+\alpha_2 p_2(k)+\alpha_3 p_3(k) \tag{3.12}$$

Using the standard least squares method the linear model can be fitted from the raw data. The identified model is:

$$w_b(k)=1.70+0.90W(k)-0.45L(k)+1.27C(k) \tag{3.12A}$$

The estimation results are shown in Figure 3.6 (a). It can be observed that the measured back-side bead width can be estimated by the characteristic parameters of the weld pool. The average model error is 0.50 mm, the maximum model error is 1.93 mm, and the RMSE is 0.64 mm. Although this implies that the characteristic parameters contain

information about the weld joint penetration, substantial fitting errors are observed frequently.

In order to further improve the modeling accuracy, static model (3.11) is realized using an ANFIS nonlinear model introduced in Section 3.2.3. The estimation result is plotted in Figure 6 (b). The fuzzy input variables are partitioned by 2, as can be seen in Table 3.2. The ANFIS adopted in this study thus has 3 inputs, with 2 membership functions assigned to each input. Each generalized bell shaped membership function contains 3 parameters (see Eq. (3)). Hence, the total number of the premise parameters is 18. Further, there are 8 fuzzy rules (see Eq. (3.4)), resulting in 32 consequent parameters. The total number of fitting parameters is thus 50 and all of them are automated determined through the neural network learning algorithm/process the data pairs from Figure 3.5(b). The total number of the data pairs from Figure 3.5(b) is N=945that is enough for an ANFIS model with 50 parameters.

It can be seen from Figure 3.6 (b) that the modeling accuracy is improved using the proposed ANFIS model. In Figure 3.6 (a) severe model errors are primarily observed in data ranging from 270 to 290, 390 to 500, and 580 to 650. These errors have been substantially reduced in Figure 3.6 (b). Thus, the nonlinearity does improve the capability of the model in approximating the correlation between the front-side weld pool characteristic parameters and the back-side bead width. The obtained nonlinear model has an average model error 0.40 mm, the maximum model error 1.87 mm, and RMSE 0.52 mm, all of which are smaller than the static linear model.

To statistically justify the usage of nonlinear ANFIS model, F test is adopted to compare linear model (model 1) and nonlinear ANFIS model (model 2).The definition of F test is given by:

$$F = \left(\frac{RSS_1 - RSS_2}{p_2 - p_1} \right) \Big/ \left(\frac{RSS_2}{N - p_2} \right) \tag{3.13}$$

where RSS_i is the residual sum of squares of model i. p_i is the number of parameters in each models.

The critical value of F distribution is 1.3318 for P=5%. This means if the calculated F is greater than this critical value, the hypothesis that model 2 (nonlinear ANFIS model) does not provide a significant better fit than model 1 (linear model) is rejected. The calculated F-test value is 8.3544, which indicates that the nonlinear ANFIS model does provide a better estimation statistically.

Figure 3.7 depicts the nonlinear static ANFIS model surface for two different weld pool convexity partitions (Figure 3.7 (a) for small convexity, i.e. convexity = 0.07 mm and Figure 3.7 (b) for large convexity, i.e. convexity = 0.27mm). As can be seen nonlinearity

TABLE 3.2 PARTITION OF FUZZY INPUT VARIABLES

Fuzzy Variables	Number of Fuzzy Sets	Partition
Width	2	wide, narrow
Length	2	long, short
Convexity	2	large, small

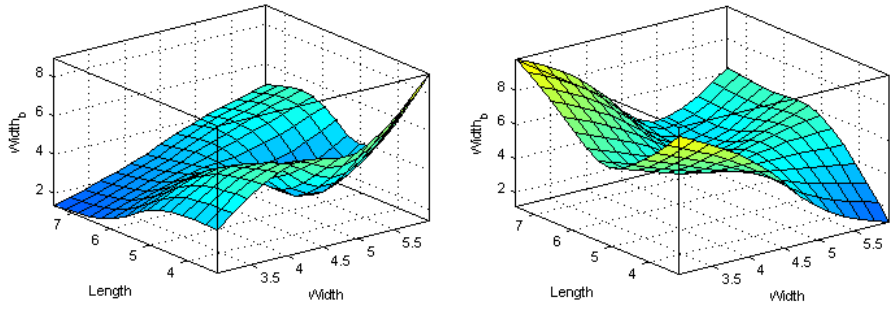

(a) (b)

Figure 3.7 Nonlinear static ANFIS model surface for different weld pool convexity (a) convexity = 0.07mm (b) convexity = 0.27mm. Nonlinearity is substantial for both small and large convexity. Here $width_b$ is the model calculated back-side bead width using the given convexity with the front-side weld pool surface length and width as parameters.

is substantial for both small and large convexity. Based on the linear model the average correlation between the (front-side) width and w_b (back-side bead width) is 0.9, indicating a positive correlation. However, Figure 3.7 indicates when the convexity is small and the length is short, the increase of the width does not cause an increase in w_b. When the convexity is large, the effect of width on w_b is nonlinear for long length and negative for short length. As can be observed, the nonlinearity is substantial for the effect of width on the back-side bead width. The average effect of length on w_b is -0.45. Figure 3.7 indicates for both small and large convexity, the effect of length on w_b is highly nonlinear. For small convexity and narrow width, w_b tends to increase as the length increases from 4mm to 5.5mm, yet decreases as the length continues to grow. When the width is large, however, w_b tends to decrease for short length but increase as the length grows. Similar nonlinearity effect of length on w_b can be observed for large convexity case. It is clear that the proposed nonlinear ANFIS model can derive a more detailed correlation between the weld pool geometry and penetration states than the static linear model.

In the following subsections, the developed estimation of the weld penetration will be utilized to accurately control the welding penetration.

3.3 Modeling Experiments

Twelve dynamic experiments have been conducted, with the welding parameters and imaging parameters specified in Table 3.1. Figure 3.8(a) plots the inputs in all the experiments where the inputs have produced fully penetrated welds. The measured weld

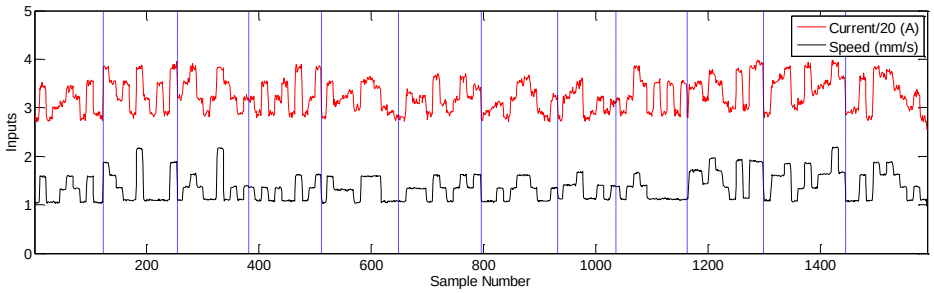

(a)

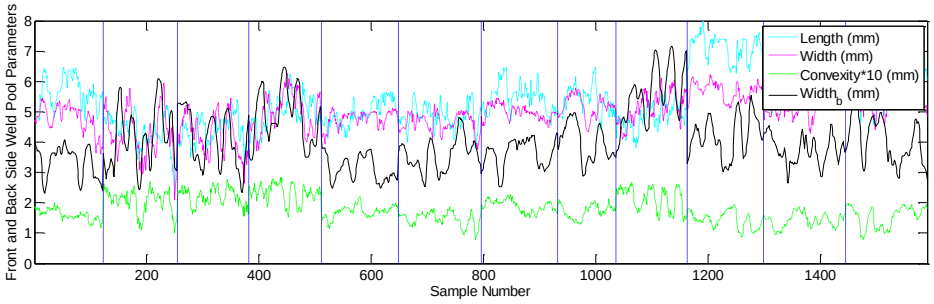

(b)

Figure 3.8 Measured data in twelve dynamic experiments (a) Inputted welding parameters (welding current and speed) (b) Measured front-side weld pool characteristic parameters and back-side bead width.

pool characteristic parameters and the offline measured back-side bead width in these dynamic experiments are given in Figure 3.8(b). The welding current and speed are varied randomly but constrained in a range such that the full penetration state is ensured. The sampling period in this study is 0.5 s because the penetration control must be realized through changing the entire weld pool and is thus a relatively slow process.

Figure 3.9 shows the distribution of the control variables in these dynamic experiments. It

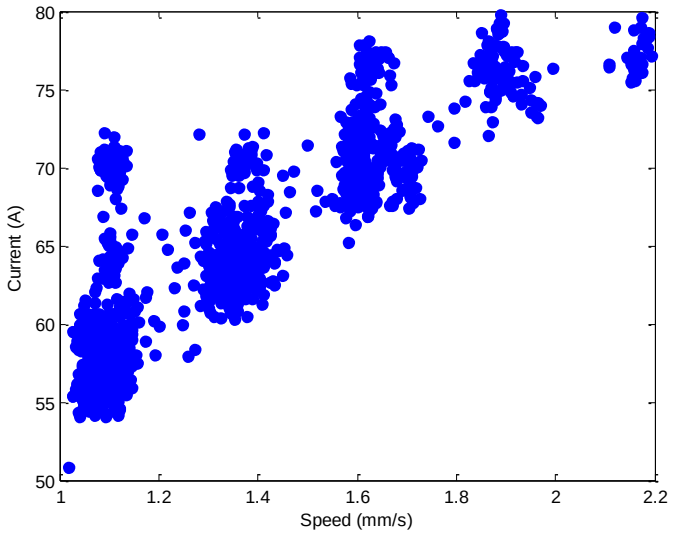

Figure 3.9 Distribution of inputs in twelve dynamic experiments.

TABLE 3.3 LINEAR MA MODEL PARAMETERS

$a(j)$, j=1,...,3	$b(j)$, j=1,...,5	c
[11.57, 0.35, 0.93]	[-2.26, -0.058, -0.33,0.043, -0.52]	-0.094

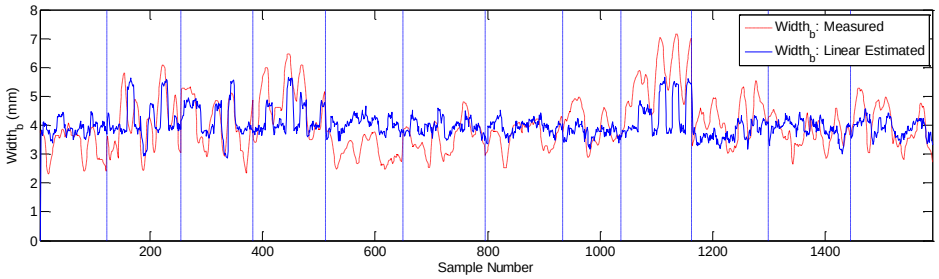

Figure 3.10 Linear modeling results.

can be seen that the welding parameters have filled a certain range of control variables in which fully penetrated welds can be produced. This distribution implies that the resultant model can be used during closed-loop control if the control variables are in the range specified by this distribution.

3.4 System Modeling

In this section the system modeling is performed using the acquired inputs and output data.

3.4.1 Linear Modeling

The linear model can be expressed as the following Moving Average (MA) model:

$$\hat{w}_b(k)=\sum_{j=1}^{N_1} a(j)u_1(k-j)+\sum_{j=1}^{N_2} b(j)u_2(k-j)+c \tag{3.14}$$

where u_1 and u_2 are the inputs (welding current and speed), $a(j)$, $b(j)$, c are the model parameters, and N_1, N_2 are the MA model orders associated with u_1 and u_2, respectively.

The dynamic linear model is obtained by using the standard least squares method, and the linear model orders N_1, N_2 are selected based on F-test. It is shown that the best N_1 and N_2 statistically are 3 and 5, respectively.

The linear modeling results are plotted in Figure 3.10. The identified dynamic linear model parameters are listed in Table 3.3. The static gain for the current is 12.85 mm/(100A), and the static gain for the speed is -3.12 mm/(mm/s).The average model error, maximum model error, and RMSE are 0.66 mm, 2.71 mm, and 0.82 mm, respectively. It is found that the back-side bead width can be estimated by the inputs with acceptable accuracy. However, substantial static fitting errors are observed frequently.

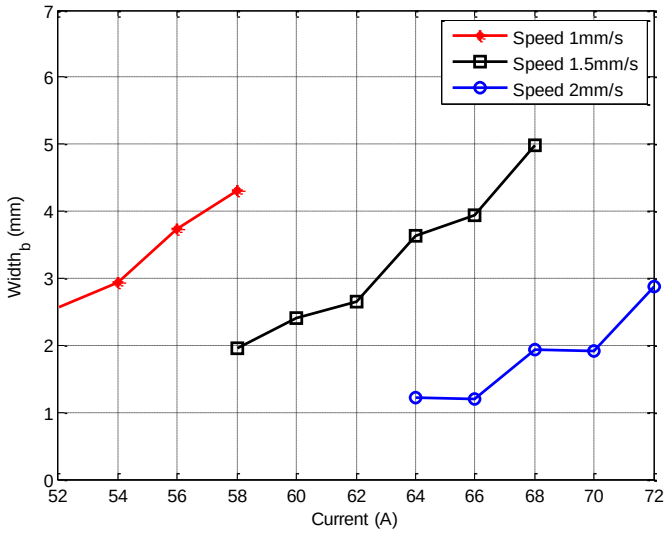

Figure 3.11 Static correlations between the welding current and back-side bead width.

3.4.2 Nonlinear ANFIS Modeling

The linear model described in the first subsection accounts for the average effect of the inputs on the back-side bead width in the large input range. In order to further improve the model accuracy, nonlinear ANFIS modeling method described previously is utilized in this section.

Static correlations between the back-side bead width and the welding current are plotted in Figure 3.11 for different welding speed. It is observed that although the correlations are nonlinear, the nonlinearity is slight. Different model trails are also performed by incorporating nonlinear terms I^2, v^2, and cross-coupling terms $I \cdot v$. The modeling results are not significantly improved. This implies that the inputs themselves may not provide enough information about the back-side bead width. On the other hand, the weld pool states can provide additional information about the back-side bead width and can thus be used to better model the nonlinear relationship between the welding parameters and the back-side bead width.

Thus, the nonlinear model can be expressed as the following equation:

$$\hat{w}_b(k)=\sum_{j=1}^{N_1} a(j)u_1(k-j)+\sum_{j=1}^{N_2} b(j)u_2(k-j)+C(\Omega) \tag{3.15}$$

where $C(\Omega)$ is a nonlinear operating point, which is correlated to the weld pool state at current instant.

The fitting result using the proposed nonlinear model can be seen in Figure 3.12. It is observed that the modeling accuracy is improved. Figure 3.10 illustrates relatively large

model errors in the ranges from 520 to 620, 950 to 1180, and 1250 to 1300. These errors have been substantially reduced in Figure 3.12. The resultant average model error, maximum model error, and RMSE are 0.52 mm, 2.31 mm, and 0.66 mm, respectively. In all of the three criteria, the nonlinear modeling results are superior to those from the

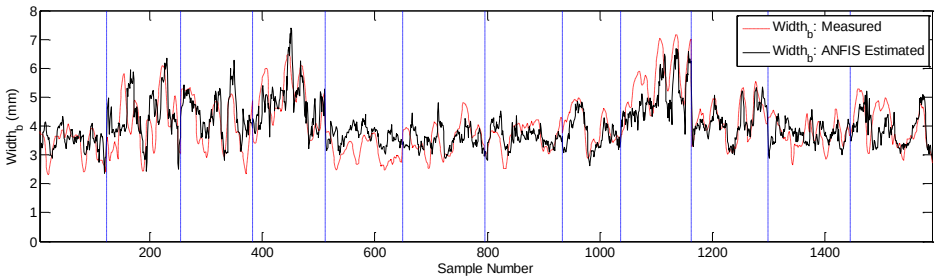

Figure 3.12 Nonlinear ANFIS modeling results.

TABLE 3.4 MODEL COMPARISON BETWEEN NONLINEAR MODEL AND LINEAR MODEL

	RMSE /mm	Average Model Error /mm	Maximum Model Error /mm
Linear Model	0.82	0.66	2.71
Nonlinear Model	0.66	0.52	2.31

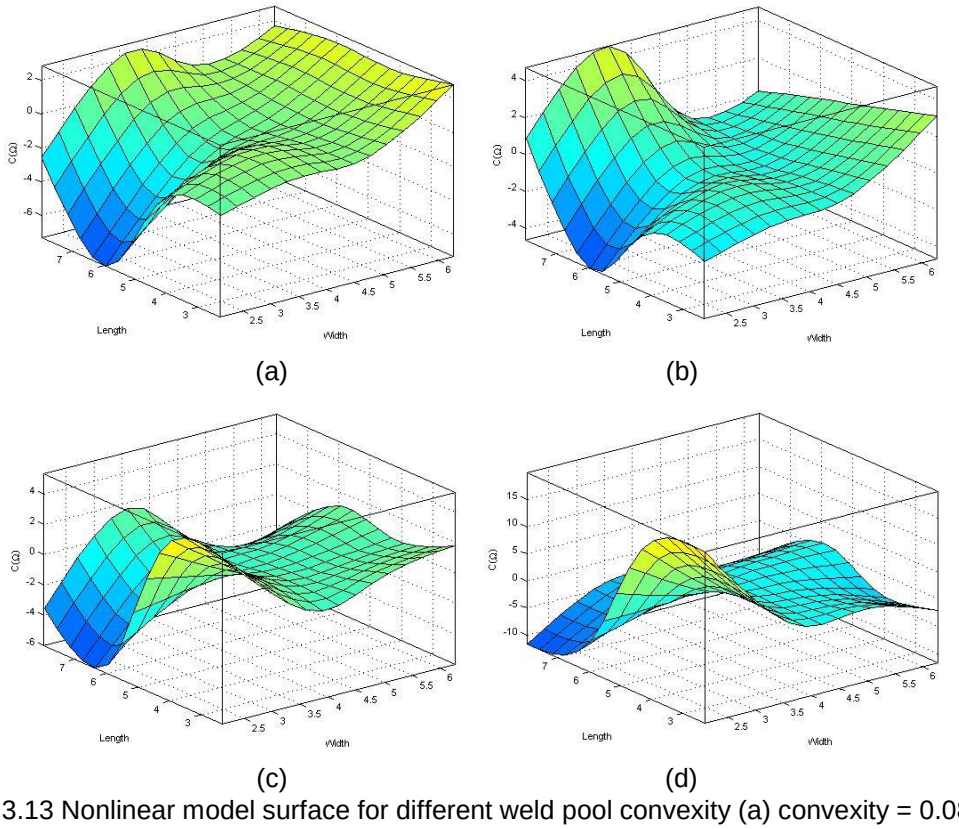

Figure 3.13 Nonlinear model surface for different weld pool convexity (a) convexity = 0.08 (b) = 0.18 (c) 0.22 (d) 0.28.

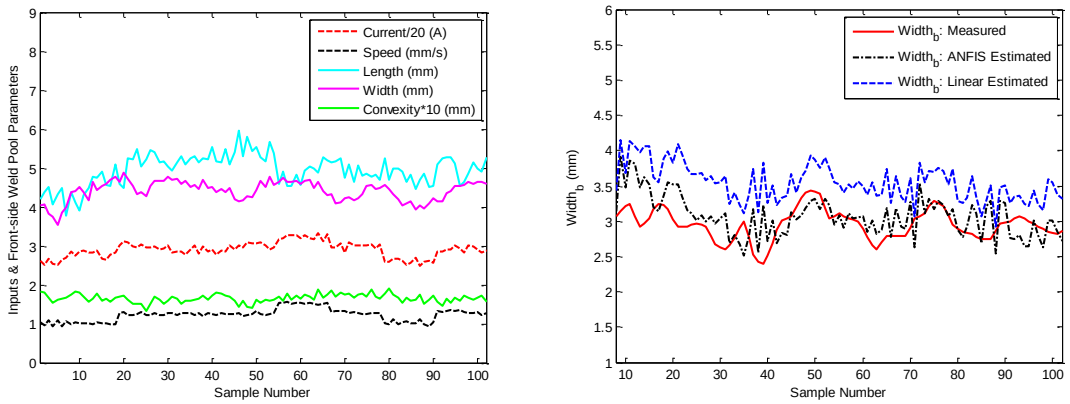

(a) (b)

Figure 3.14 Model validation experiment. (a) inputs and measured front-side weld pool parameters (b) estimated back-side bead width and offline measurements.

linear model. It is noted that although the proposed ANFIS model can better correlate the welding inputs and weld penetration, large errors cannot be fully eliminated. This is primarily due to the un-modeled factors which can also affect the weld penetration.

Figure 3.13 depicts the nonlinear model surface for different weld pool convexity. The nonlinearity is substantial in all cases and the nonlinear surface is different for different weld pool convexity.

In order to validate the proposed nonlinear model, validation experiment is carried out. The inputs and measured front-side weld pool characteristic parameters are plotted in Figure 3.14 (a). The current and the speed are randomly varied but constrained such that the full penetration state is ensured. The offline measured back-side bead width and the estimated back-side bead width using both linear and nonlinear ANFIS model are plotted in Figure 3.14 (b). As can be observed the nonlinear model can better estimate the back-side bead width than the linear model.

3.5 Model Predictive Control Algorithm

In this section the model predictive control algorithm for GTAW penetration control is derived.

At instant *k*, the controller needs to determine the control action $u_1(k)$ and $u_2(k)$ based on the feedback $\hat{w}_b(k)$ to drive the welding process to the desired penetration state. In a predictive control, prediction equations should be first developed to predict the output based on the inputs.

According to (3.15), the system model can be expressed as:

$$\hat{w}_b(k) = \sum_{j=1}^{N_1} a(j)u_1(k-j) + \sum_{j=1}^{N_2} b(j)u_2(k-j) + C(\Omega) \tag{3.16}$$

Suppose the future control action is constant, i.e. $\Delta u_{1,2}(k+j) = 0,\ j = 1,...,N$, where N is the prediction range, 1-step-ahead prediction yields:

$$\begin{aligned} \hat{w}_b(k+1) &= \sum_{j=1}^{N_1} a(j)u_1(k+1-j) + \sum_{j=1}^{N_2} b(j)u_2(k+1-j) + C(\Omega) \\ &= \hat{w}_b(k) + a(1)\Delta u_1(k) + b(1)\Delta u_2(k) \end{aligned} \tag{3.17}$$

Similarly, the *i*-step-ahead prediction is:

$$\begin{aligned} \hat{w}_b(k+i) &= \hat{w}_b(k) + \sum_{j=2}^{i} a(j)\left(u_1(k-1) - u_1(k-j)\right) + \sum_{j=1}^{i} a(j)\Delta u_1(k) \\ &+ \sum_{j=2}^{i} b(j)(u_2(k-1) - u_2(k-j)) + \sum_{j=1}^{i} b(j)\Delta u_2(k) \end{aligned} \tag{3.18}$$

The prediction equations can be further expressed in matrix form:

$$\mathbf{W_b} = \mathbf{W_{b,k}} + \mathbf{FU} + \mathbf{S}\Delta\mathbf{u} \tag{3.19}$$

where

$$\mathbf{W_b} = \begin{bmatrix} \hat{w}_b(k+1) \\ \vdots \\ \hat{w}_b(k+N) \end{bmatrix}_{N\times 1}, \quad \mathbf{W_{b,k}} = \begin{bmatrix} \hat{w}_b(k) \\ \vdots \\ \hat{w}_b(k) \end{bmatrix}_{N\times 1}, \quad \Delta\mathbf{u} = \begin{bmatrix} \Delta u_1(k) \\ \Delta u_2(k) \end{bmatrix}$$

$$\mathbf{U} = \begin{bmatrix} u_1(k-1) - u_1(k-1) \\ \vdots \\ u_1(k-1) - u_1(k-N) \\ u_2(k-1) - u_2(k-1) \\ \vdots \\ u_2(k-1) - u_2(k-N) \end{bmatrix}_{2N\times 1}, \quad \mathbf{S} = \begin{bmatrix} \sum_{j=1}^{1} a(j) & \sum_{j=1}^{1} b(j) \\ \vdots & \vdots \\ \sum_{j=1}^{N} a(j) & \sum_{j=1}^{N} b(j) \end{bmatrix}_{N\times 2}$$

$$\mathbf{F} = \begin{bmatrix} \sum_{j=2}^{1} a(j) & & 0 & \sum_{j=2}^{1} b(j) & & 0 \\ & \ddots & & & \ddots & \\ 0 & & \sum_{j=2}^{N} a(j) & 0 & & \sum_{j=2}^{N} b(j) \end{bmatrix}_{N\times 2N}$$

In order to achieve a desirable control, it is required the following cost function is minimized:

$$J(k,\Delta\mathbf{u})=\sum_{j=1}^{N}\left(\hat{w}_b(k+j)-w_b^*(k+j)\right)^2 \tag{3.20}$$

In a long-range predictive control, the prediction range N should be large enough to achieve a desirable control. However, the regulation speed decreases as N increases. It is found that N=5 can achieve a satisfactory regulation speed and robustness for the application being addressed. The desired trajectory $w_b^*(k+j)$ is defined as:

$$\begin{cases} w_b^*(k+j)=\alpha w_b^*(k+j-1)+(1-\alpha)w_b^0,\ j=1,...,N \\ w_b^*(k)=\hat{w}_b(k) \end{cases} \tag{3.21}$$

where $\alpha\in(0,1)$ is the smoothing coefficient. As α becomes larger, the system will track the set point with slower speed but better robustness and smoothness. In this study α=0.9 achieves an appropriate tradeoff between response speed and robustness.

The fluctuations in the welding parameters will generate non-smooth weld bead, which is not desirable in our application. Thus, energetic control actions must be avoided. The following cost function is used to penalize changes in control:

$$\begin{aligned} J(k,\Delta\mathbf{u}) &= \sum_{j=1}^{N}\left(\hat{w}_b(k+j)-w_b^*(k+j)\right)^2+\Delta\mathbf{u}^T\mathbf{\Lambda}\Delta\mathbf{u} \\ &= \left[\mathbf{W_b}-\mathbf{W_b^*}\right]^T\left[\mathbf{W_b}-\mathbf{W_b^*}\right]+\Delta\mathbf{u}^T\mathbf{\Lambda}\Delta\mathbf{u} \end{aligned} \tag{3.22}$$

where $\mathbf{\Lambda}=diag(\lambda_1,\lambda_2)$ is the diagonal control weighting matrix, and $\mathbf{W_b^*}=\left[w_b^*(k+1)\ \ \cdots\ \ w_b^*(k+N)\right]_{N\times1}^T$.

The values of the weights λ_1 and λ_2 can be determined based on the scales of their static gains to the output. In this study $\lambda_1=10^2$ (mm/100A)^2 and $\lambda_2=20^2$ (mm/1mm/s)^2 are chosen. This implies that an error of 1mm in the prediction has the same contribution to the cost function as current change of 0.1*100A = 10A, and speed change of 0.05mm/s.

However, it is found in welding experiments that such constant coefficients will produce over adjustments resulting in fluctuation of the back-side bead width, which is not acceptable for our application. Careful analysis reveals that this phenomenon is understandable because the significant thermal inertia of the welding process causes a time delay from the heat input increases to the front-side weld pool, and to the back-side weld pool. The developed controller should behave differently for different weld pool

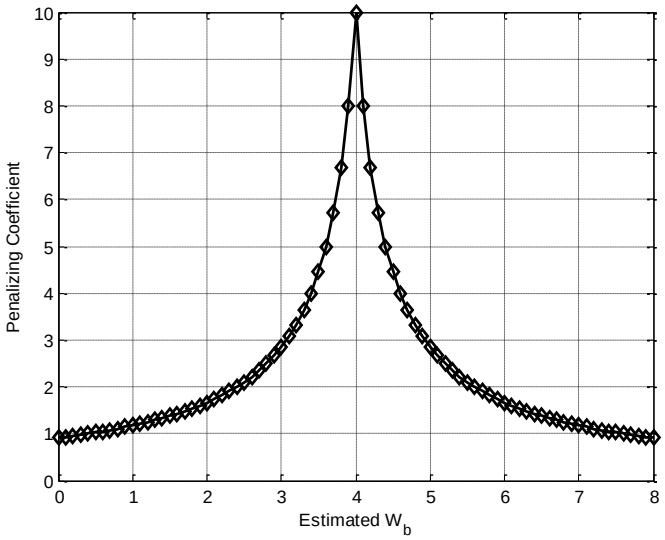

Figure 3.15 Nonlinear penalizing coefficient over estimated back-side bead width.

states. Specifically, the controller should maintain its fast response time if the penetration states are far away from the set-point, yet become slower as approaching the set-point. In this sense, the diagonal control weighting matrix $\mathbf{\Lambda}=diag(\lambda_1,\lambda_2)$ is changed to $\mathbf{\Psi}=\eta\mathbf{\Lambda}$, and the following nonlinear penalizing coefficient is defined:

$$\eta = 1/\left(0.1+\left|\hat{w}_b - w_b\right| / w_b\right) \tag{3.23}$$

This nonlinear penalizing coefficient is visualized in Figure 3.15. As can be observed, the penalizing coefficient remains small (<3) when the estimated the back-side bead width is smaller than 3mm. As the estimated back-side bead width becomes nearer to the set-point (4mm in this case), the penalizing coefficient becomes larger. Its maximum of 10 is achieved when the estimated w_b is 4mm.

The control law is calculated such that:

$$\frac{\partial J(k,\Delta\mathbf{u})}{\partial\Delta\mathbf{u}}=0 \tag{3.24}$$

It can be further calculated as:

$$\frac{\partial J(k,\Delta\mathbf{u})}{\partial\Delta\mathbf{u}} = \frac{\partial\left(\left[\mathbf{W_b}-\mathbf{W_b^*}\right]^T\left[\mathbf{W_b}-\mathbf{W_b^*}\right]+\Delta\mathbf{u}^T\boldsymbol{\Psi}\Delta\mathbf{u}\right)}{\partial\Delta\mathbf{u}}$$
$$= \frac{\partial\left(\left[\mathbf{W_{b,k}}-\mathbf{W_b^*}+\mathbf{FU}+\mathbf{S}\Delta\mathbf{u}\right]^T\left[\mathbf{W_{b,k}}-\mathbf{W_b^*}+\mathbf{FU}+\mathbf{S}\Delta\mathbf{u}\right]\right)}{\partial\Delta\mathbf{u}} \tag{3.25}$$
$$+\frac{\partial\left(\Delta\mathbf{u}^T\boldsymbol{\Psi}\Delta\mathbf{u}\right)}{\partial\Delta\mathbf{u}} = 2\mathbf{S}^T\left(\mathbf{W_{b,k}}-\mathbf{W_b^*}+\mathbf{FU}\right)+2\left(\boldsymbol{\Psi}+\mathbf{S}^T\mathbf{S}\right)\Delta\mathbf{u}=0$$

The control signal is finally expressed as:

$$\Delta\mathbf{u}=-\left(\boldsymbol{\Psi}+\mathbf{S}^T\mathbf{S}\right)^{-1}\mathbf{S}^T\left(\mathbf{W_{b,k}}-\mathbf{W_b^*}+\mathbf{FU}\right) \tag{3.26}$$

It is apparent that (3.26) provides a closed form solution and no online optimization is required. Thus, the obtained control algorithm can be easily incorporated into the real-time monitoring and control of the weld penetration/ back-side bead width in GTAW process. It is noticed that linear model is used by assuming that the weld pool is not supposed to change in an extremely large range. Nonlinear ANFIS model can better correlate the welding process inputs and back-side bead width and help understand the nonlinear relationship between them. However, nonlinear ANFIS model based predictive control involves nonlinear optimizations which are not preferred for online industrial applications.

3.6 Welding Experiments

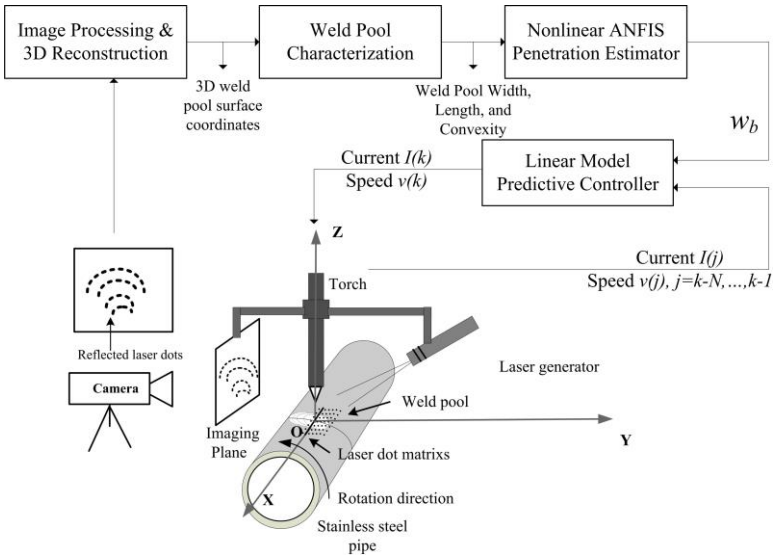

Figure 3.16 Proposed control system schematic.

The developed closed-loop control system can be illustrated using the diagram in Figure 3.16. In this diagram, the sensing system is identical to Figure 3.1. Nonlinear ANFIS penetration estimator is applied to estimate the back-side bead width. This estimated back-side bead width is applied to the proposed linear model predictive controller as the feedback, and the calculated welding current / welding speed are applied to the welding process to maintain the back-side bead width at the desired level.

In order to demonstrate the robustness of the developed control system, various dynamic welding experiments have been designed and conducted in this section under different welding conditions and disturbances. In subsection 3.6.1, different initial currents are applied. In subsection 3.6.2 and 3.6.3 the welding current and welding speed disturbances are applied respectively, and the robustness of the controller with input disturbances is tested. The arc length is changed from 5mm to 3mm in subsection 3.6.4, and the

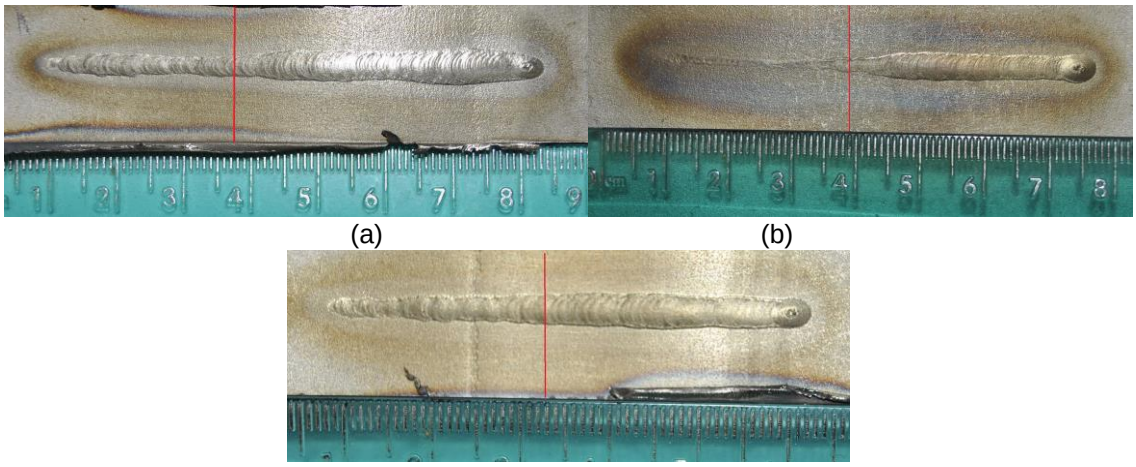

Figure 3.17 Back-side weld bead appearances under different initial current (a) Initial current = 52A (b) Initial current = 54A (c) Initial current = 56A. Vertical solid line indicates the start time of the closed-loop control.

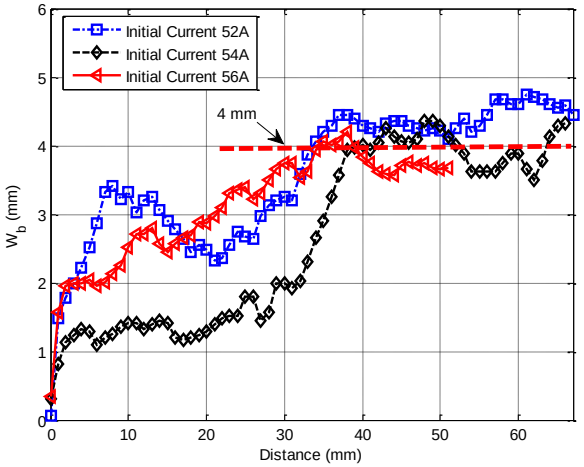

Figure 3.18 Measured back-side bead width under different initial current.

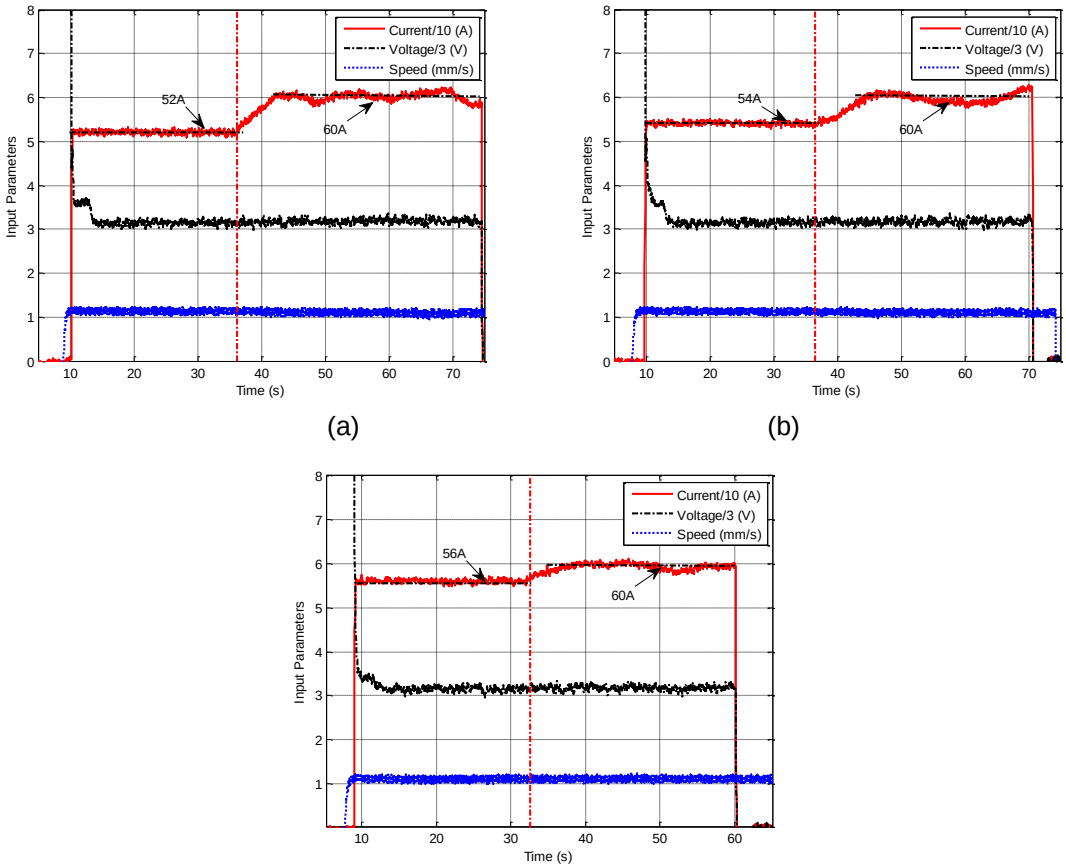

Figure 3.19 Welding process input parameters under different initial current (a) Initial current = 52A, (b) Initial current = 54A, (c) Initial current = 56A.

controller's robustness under varying arc length is verified.

3.6.1 Experiment 1: Different Initial Current

Experiments with different initial welding currents are conducted in this subsection to test the robustness of the controller with different initial conditions. Three experiments are conducted, with initial current set to 52A, 54A and 56A. The arc length is set to 5mm. The initial welding speed is 1.1 mm/s and the set point for the back-side bead width is 4mm in all three experiments. An open-loop period of about 25 seconds for all three experiments is applied to drive the welding process to the full penetration mode before the closed-loop control starts. The back-side weld beads obtained are shown in Figure 3.17, and the measured back-side bead widths are plotted in Figure 3.18. As can be observed from these two figures, despite the difference in the initial current, the proposed control algorithm can drive the system to the desired back-side bead width of 4 mm.

The control inputs in these three experiments are depicted in Figure 3.19. When the initial current is 52A (Figure 3.19(a)), the open-loop period brings the back-side bead width to

about 3 mm, which is not sufficient for our application. As the closed-loop control starts at 37s, the current increases to about 60A and the speed decreases to about 1mm/s in order to increase the heat input into the process to make a greater penetration with the back-side bead width at about 4mm. For the initial current equals 54 A and 56 A, the open-loop period brings the back-side bead width to different levels (about 1.5 mm and 3 mm respectively). In both cases the controller is able to increase the current to about 60A and bring the penetration specified by its back-side width to about 4 mm.

It is noticed that although larger initial current generally indicates larger penetration at the end of the open-loop period, it is not always the case. Actually when the initial current is 54 A, the penetration specified by the back-side bead width is about 1.5 mm at the end of the open-loop period, which is much smaller than that of the 52 A initial current. The reason is that the values of the welding parameters as well as the welding conditions are both nominal. Variations (including eccentric pipe, arc length, and purging

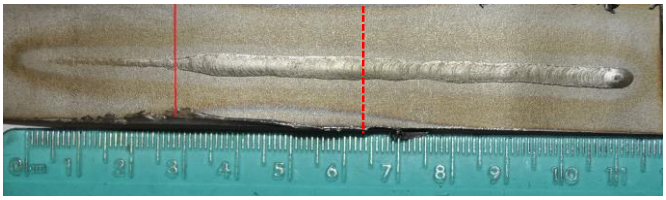

(a)

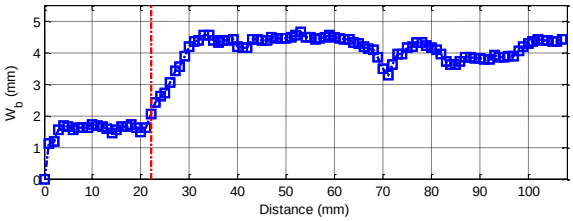

(b)

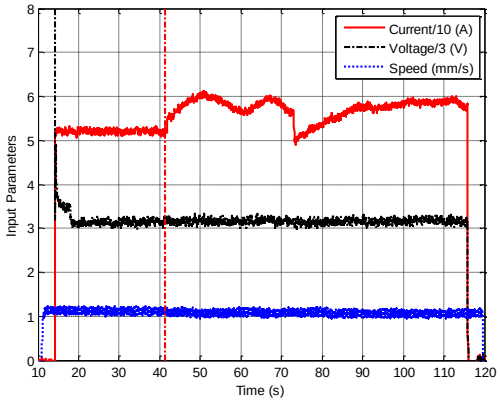

(c)

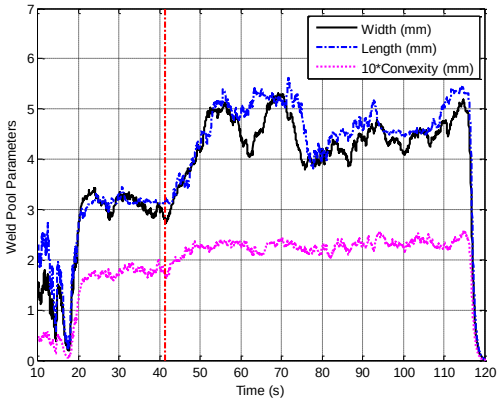

(d)

Figure 3.20 Welding experiment results under current disturbance (a) Back-side weld bead appearances, with the vertical solid line indicates the start of the closed-loop control, and the vertical dash line indicates when current disturbance occurs (b) Measured back-side bead width (c) Control input (d) Front-side weld pool parameters.

gas flow rate, etc.) may cause deviations of the actual welding parameters and conditions from their nominal values/specifications affecting the output produced during the open-loop control period. However, in all three cases despite the initial current the controller is able to bring the process to a desired full penetration states (4 mm in this case) within a short time (about 5 s), indicating the controller's robustness against different initial current.

3.6.2 Experiment 2: Current Disturbance

In this experiment the robustness of the control algorithm against current disturbances is evaluated. The arc length is set at 5mm. An artificial error between the calculated and applied values of the welding current is applied. The process begins with an open-loop period of about 27s (with initial current 52A and initial welding speed 1.1mm/s), which brings the back-side bead width to about 1.8mm. In the first 30 s after the open-loop period, no error exists between the calculated current and applied current. The controller is able to bring the back-side bead width states to about 4.2mm by increasing the welding current to about 60A and decreasing the welding speed to about 1.0mm/s (see Figure 3.20(b)(c)). In t=74 s, the current is set at 50A, which is about 5A smaller than the calculated value. As the result, both the weld pool width and the weld pool length decrease to about 4mm (see Figure 16(d)), indicating a decrease in the weld penetration thus in the back-side bead width. However, the controller is able to adjust the welding current and welding speed to compensate this artificial error (see Figure 3.20 (c)), and the back-side bead width can be maintained around the desired value (i.e., 4mm) again (see Figure 3.20 (b)) with a relatively quick response time. It is noticed, however, that the obtained back-side bead width is not exactly 4mm in the welding experiments. This is primarily due to the difficulties in estimating the back-side bead width with absolute accuracy. In our application, 0.5mm error margin can be considered acceptable in precise penetration control of GTAW process.

3.6.3 Experiment 3: Speed Disturbance

In experiment 3, an artificial error between the actual and calculated values of the welding speed is applied to evaluate the robustness of the proposed control algorithm against welding speed disturbances. During the first 30 s after the open-loop period, no error exists between the actual welding speed applied to the process and the welding speed calculated by the control algorithm. However, at t=73s, the welding speed is set to 1.2 mm/s, which is about 0.2mm/s larger than the calculated welding speed required for the desired penetration state. As can be seen from Figure 3.21 (a)(b) the back-side bead width is decreased to 2mm, indicating the strong effect of the welding speed over the weld penetration. Accordingly, the weld pool width is decreased from 4.5mm to 3.5mm, and the weld pool length is also decreased to about 3.8mm (see Figure 3.21 (d)). If no closed-loop controller is applied, the increase in the welding speed will decrease the weld

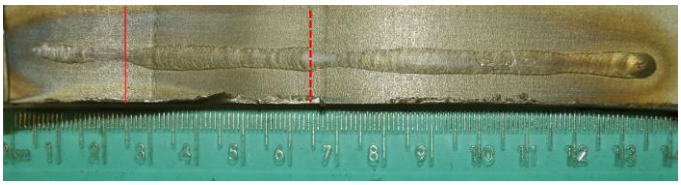

(a)

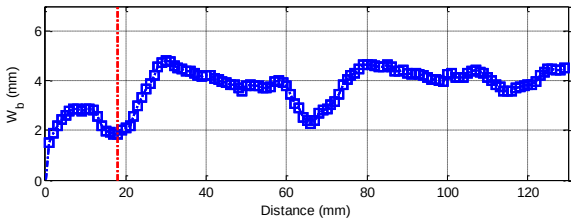

(b)

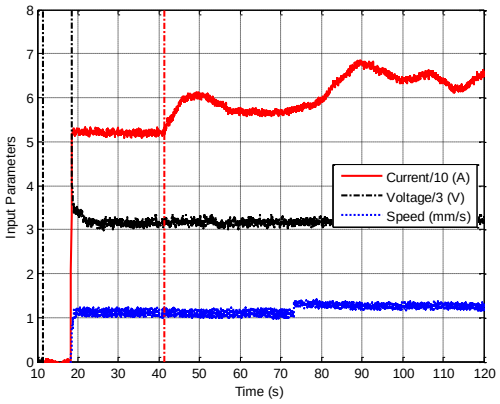

(c)

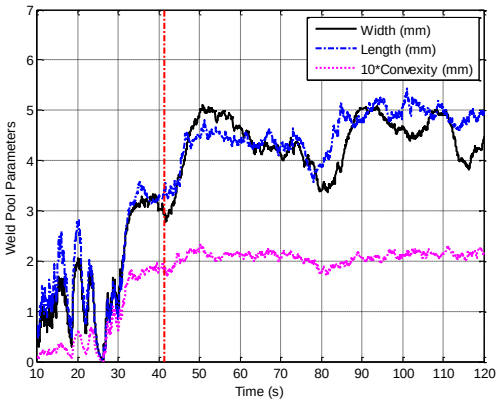

(d)

Figure 3.21 Welding experiment results under speed disturbance (a) Back-side weld bead appearances (b) Measured back-side bead width (c) Control input (d) Front-side weld pool parameters.

penetration. However, by applying the controller the desired back-side bead width is maintained. From Figure 3.21(c) it can be observed that the controller is able to overcome the disturbance by increasing the welding current, and decreasing the welding speed, respectively. This experiment shows that the developed close-loop control system is robust to the variation in the welding speed.

3.6.4 Experiment 4: Arc Length Disturbance

Arc length is another welding condition which has impact on the weld penetration. In this subsection the robustness of the proposed controller with arc length disturbance is examined. In the experiment, the initial arc length is 5mm. At t= 60 s, the arc length changes to 3.5mm. As a result, the weld pool width immediately decreases, and the weld pool convexity also decreases (see Figure 3.22(d)). If the current is unchanged (i.e., 58A in Figure 3.22(c)), the back-side bead width will be decreased. As can be observed in Figure 3.22(c), by increasing the current, the closed-loop control system successfully

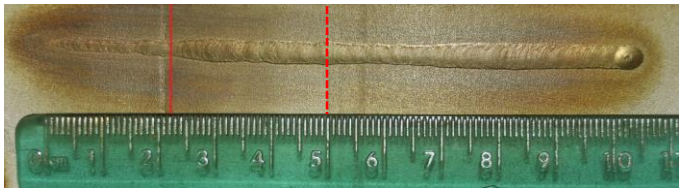

(a)

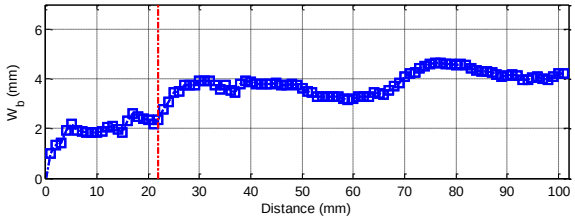

(b)

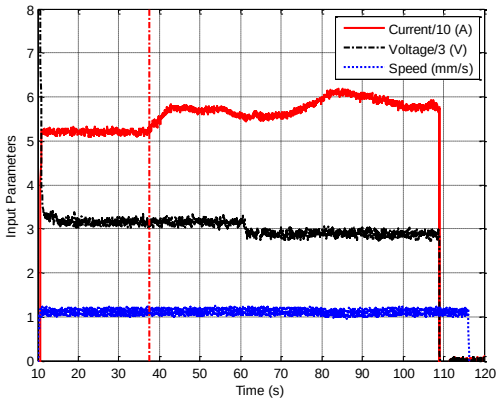

(c)

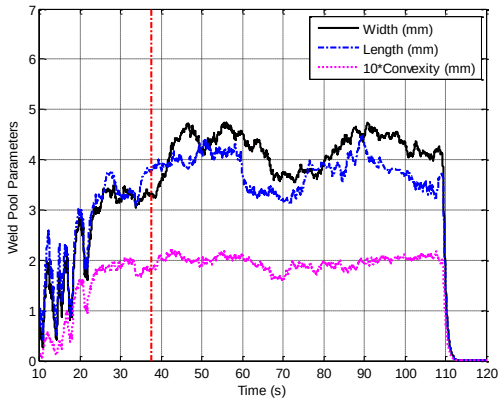

(d)

Figure 3.22 Welding experiment results under arc voltage disturbance (a) Back-side weld bead appearances (b) Measured back-side bead width. (c) Control input (d) Front-side weld pool parameters.

overcome the influence of the arc length variation and the resultant back-side bead width is about 4mm with 0.5mm variation.

3.7 Summary

In this chapter a linear model based predictive controller is developed to control the weld penetration specified by the back-side bead width in GTAW process. Dynamic experiments are conducted to establish the correlation between the back-side bead width and the welding current and speed. This correlation is first modeled using a dynamic linear MA model and then a nonlinear ANFIS model is utilized to improve the modeling accuracy. A linear MPC is constructed and an analytical solution is obtained. The control experiments demonstrated the controller's robustness against variations in initial current, welding inputs, and arc length.

Chapter 4 3D Weld Pool Surface Control

In the previous chapter, weld penetration specified by the backside bead width is accurately controlled [111]. However, accurately estimating the back-side penetration is still challenging due to the highly dynamic and significant inertia of the process. Alternatively, 3D weld pool may be directly controlled [122]. Control of the weld pool is considered as an essential capability for next generation intelligent robotic welding systems and should be further explored. In this chapter the dynamic response of the weld pool characteristic parameters to welding current and speed as control variables is modeled. Based on the identified dynamic model, a predictive control algorithm is developed to control these characteristic parameters. The proposed algorithm is given in a closed form and no online optimization is required. Welding experiments confirm that the developed control system is effective in achieving the desired 3D weld pool surface geometry despite various disturbances.

In GTAW the major adjustable welding parameters are the welding current, arc length, and welding speed. Other possible welding parameters include heat transfer condition, material, thickness and chemical composition of the workpiece, shielding gas, and angle of the electrode tip, etc. In a particular welding process control system, however, only a few selected welding parameters should be adjusted to compensate for possible variations of the process. Among all the welding parameters, an increase in the welding current and a decrease in the welding speed will significantly increase the heat input into the welding process thus influencing the weld pool surface geometry considerably. The controlled GTAW process can therefore be defined as a two-input-three-output system, with the welding current and speed as its inputs, and the weld pool characteristic parameters including the pool width, length, and convexity as its outputs [122].

4.1 Experimentation

Five dynamic experiments have been conducted as bead-on-plate welding [122], with the welding parameters and imaging parameters specified in Table 4.1. Figure 4.1(a) plots the inputs in all the experiments. The measured weld pool characteristic parameters are given in Figure 4.1(b). Figure 4.2 shows the distribution of the control variables in these dynamic experiments. It can be seen that the welding parameters have filled a certain range of control variables. This distribution implies that the resultant model can be used during control if the control variables are in the range specified by this distribution.

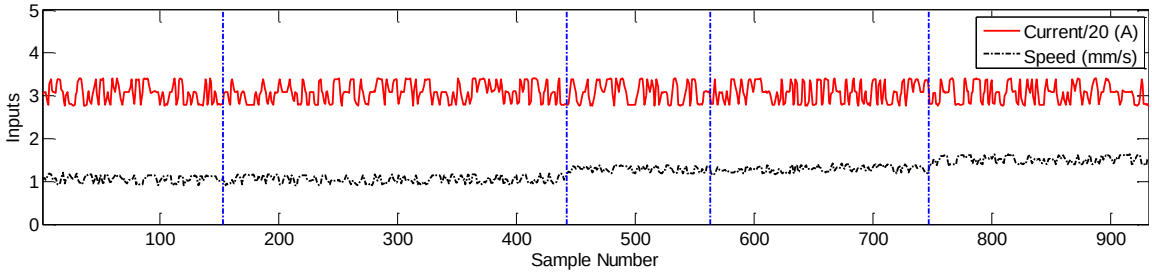

(a)

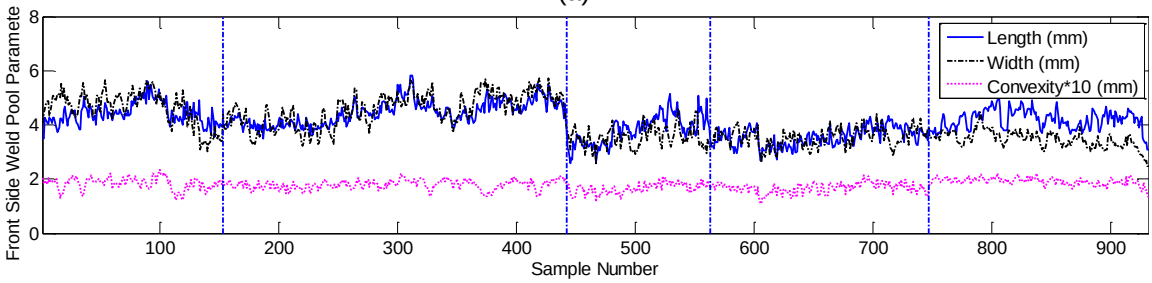

(b)

Figure 4.1 Measured data in five dynamic experiments (a) Inputted welding parameters (welding current and speed) (b) Measured front-side weld pool characteristic parameters.

TABLE 4.1 EXPERIMENTAL AND IMAGING PARAMETERS

Welding Parameters			
Current / A	Welding speed / (mm/s)	Arc length / mm	Argon flow rate / (L/min)
56-68	0.9-1.6	5	11.8
Monitoring Parameters			
Laser projection angle / degree	Laser to weld pool distance / mm	Imaging plane to weld pool distance / mm	
35.5	24.7	101	
Camera Parameters			
Shutter speed/ms	Frame rate/fps	Camera to imaging plane distance/mm	
4	30	57.8	

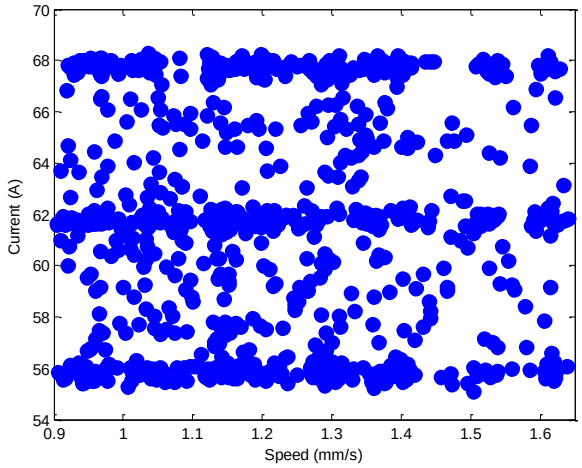

Figure 4.2 Distribution of inputs in five dynamic experiments.

4.2 System Modeling

4.2.1 Nonlinearity

The welding process is generally considered to be dynamic and nonlinear. In order to examine the nonlinear correlation between the system outputs (weld pool width, length, and convexity) and inputs (welding current and speed), various static experiments are carried out and the empirical static correlations are shown in Figure 4.3.

Figure 4.3(a) and (d) depict the weld pool width in response to the welding current and speed, respectively. It is observed that the width is roughly linearly correlated to the welding process inputs. Slight nonlinearity occurs when the current is large (68A in Figure 4.3(d)). Actually when the welding speed is slow (i.e., 0.9mm/s), large current may cause over penetration and possible burn-through. In this case the weld pool width is small. As the welding speed increases, the width also increases because more metal is melted. However, as the speed becomes larger than 1.1mm/s, total heat input becomes smaller, causing the weld pool width to decrease. Consider the weld pool length (shown in Figure 6(b) and (e)), the increase of the current generally indicates the increase of the length for the welding speed ranging from 1.0mm/s to 1.5mm/s (Figure 4.3(b)). The correlation between the length and the welding speed, however, is nonlinear (Figure 4.3(e)). When the speed is relatively slow (i.e., <1.3mm/s), the length decreases as the welding speed increases. This makes sense because the increase of the welding speed will decrease the total heat input into the welding process. The weld pool area is decreased and the length will also be decreased, accordingly. However, when the welding speed is

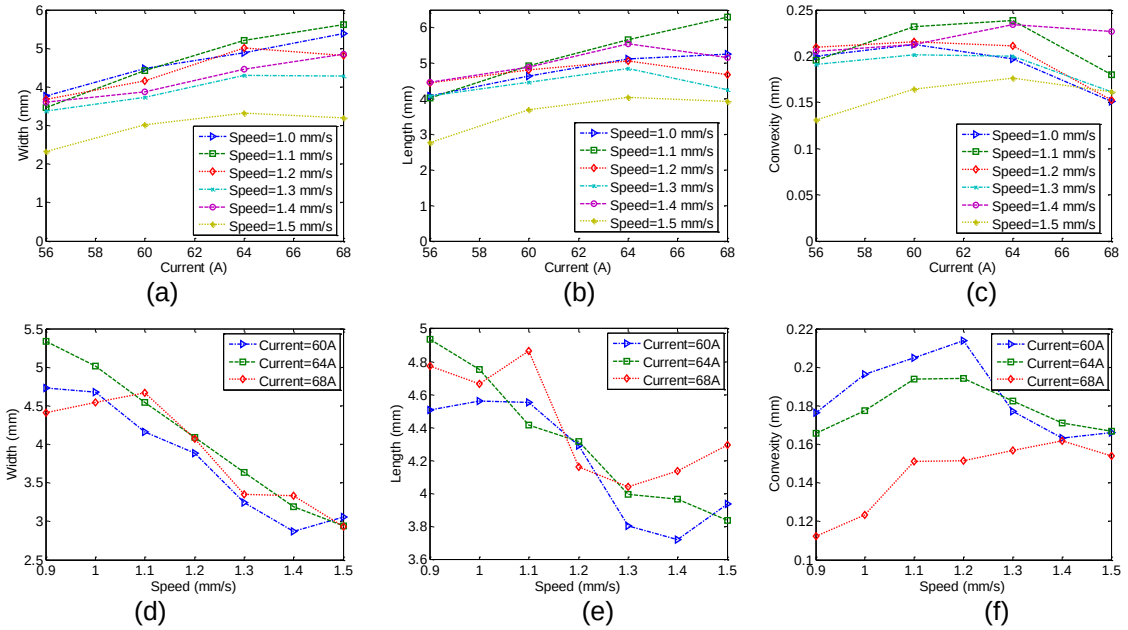

Figure 4.3 Empirical static response for welding process inputs (a)-(c) Weld pool width, length, convexity respect to welding current for different welding speed, (d)-(f) Weld pool width, length, convexity respect to welding speed for different welding current.

relatively high (i.e., >1.3mm/s), the weld pool length increases because the penetration is not sufficient and the heat transfer in the transverse direction is faster than that along the longitudinal direction. Similarly, the correlation between the weld pool convexity and welding process input is nonlinear. From Figure 4.3(c) it is observed that as the current increases, the convexity first increases then decreases as the current continues to increase. This is understandable because when the current is relatively small, the penetration is not sufficient. Thus, the increase in the welding current causes increase in heat input and the amount of melted metal, i.e., the increase of the convexity. However, as the current continues to increase, the penetration becomes excessive, and the melted metal flows under the workpiece rather than piles above the workpiece. On the other hand, the large current indicating large arc pressure, which makes the weld pool more concave, i.e., the convexity, is small. Figure 4.3(f) depicts the relationship between the convexity and the welding speed. As the speed increases, the convexity also increases because in excessive penetration states large speed indicates small heat input. The penetration capability becomes weaker as the speed becomes larger, i.e., the larger convexity. However, when the speed is relatively large, the heat input is not sufficient to produce full penetration. As the speed becomes larger, the melted metal becomes less, so that the convexity becomes smaller.

Although the above analysis indicates the strong nonlinearity between the weld pool characteristic parameters and welding process inputs, in this study the operating point is constrained to a relatively small range (with welding speed being about 1mm/s and the welding current ranges from 50A to 60A). In this range the system can be considered as a linear system and the linear model may be a good approximation for our specific control purpose. More sophisticated nonlinear model based control are needed for large input range. Other applications may also require different set of characteristic parameters of the 3D weld pool surface geometry, and the correlation between other characteristic parameters and welding inputs may also be nonlinear. However, these topics are beyond the scope of this present study. In the following subsection, linear model is constructed and analyzed.

4.2.2 Linear Modeling

The linear model can be expressed as the following state space model:

$$x_{k+1} = Ax_k + Bu_k \tag{4.1}$$

where $x_k = \left[W_k, L_k, C_k\right]^T$ is the weld pool state (W_k, L_k, C_k are the weld pool width, length, and convexity at time *k*, respectively), $u_k = \left[I_k, S_k\right]^T$ is the control input (I_k, S_k are the welding current and welding speed at time *k*, respectively). Matrices *A* and *B* are the system parameters.

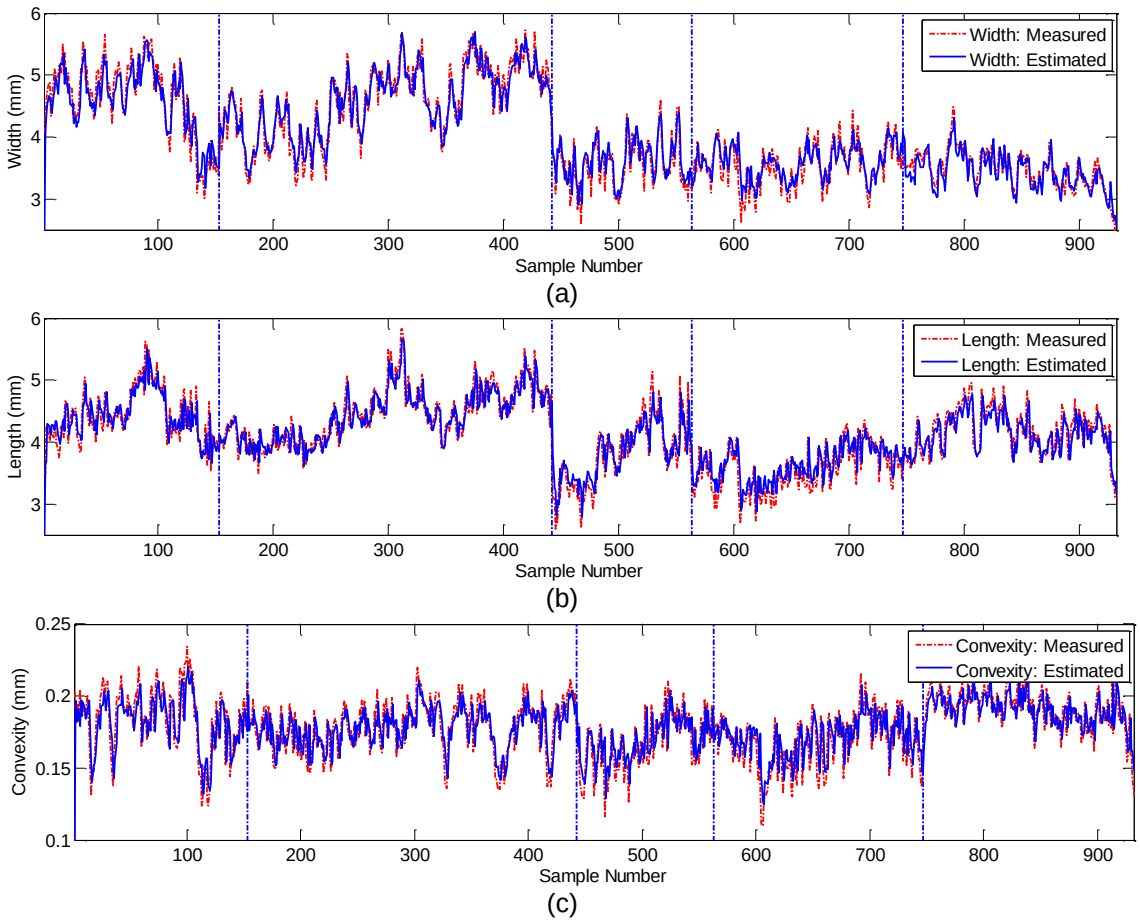

Figure 4.4 Linear modeling results (a) weld pool width (b) length (c) convexity.

The dynamic linear model parameters are obtained by using the standard least squares method. It is found that the width, length, and convexity can be estimated by the inputs with acceptable accuracy. The identified linear model parameters are listed in Table 4.2.

The linear modeling performance can be observed in Figure 4.4. The calculated average model error and RMSE for the width are 0.1713mm, and 0.2168mm, respectively. The calculated average model error and RMSE for the length are 0.1925mm, and 0.2470mm, respectively. The calculated average model error and RMSE for the convexity are 0.0106mm, and 0.0133mm, respectively. It is observed that the proposed model is able to correlate the dynamic relationship between the weld pool state and welding process inputs with acceptable accuracy.

The width, length, and convexity are coupled with the other two characteristic parameters. Specifically, the width is positively correlated to the previous width with coefficient 0.7728, positively correlated to the previous length with coefficient 0.098, and negatively correlated to the previous convexity with -1.8404 as its coefficient. This makes sense because large length and small convexity generally indicates large penetration, i.e., large back-side bead width. Similarly, the length and convexity are positively correlated to

themselves at previous sampling time. It is noticed that the convexity is not largely dependent on the width and length. This is understandable since the varying pools produced by the dynamic experiments result in severe fluctuations in the pool, especially the weld pool convexity, which can also be observed in Figure 4.3(b). Further, the strong nonlinearity of the convexity over the input range also makes the convexity not noticeably correlated to the weld pool width and length.

Consider the weld pool characteristic parameters in relation to the system inputs, the width is positively correlated to the current and the coefficient is 2.4093. The welding speed, on the other hand, has a negative effect on the weld pool width, with the coefficient being -0.5293. The 10A increase in the current will have 0.24mm increase in the weld pool width, and the 1mm/s increase in the welding speed will have 0.53mm decrease in the width. The length is positively correlated to the current and speed, with 0.55 and 0.05 being the coefficients, respectively. Because the nonlinearity of the length in response to the current and the speed is substantial, the positive linear coefficients are the average effect over the entire input range. For the convexity, the coefficients for the current and speed are 0.011 and 0.014, respectively. Similarly for the length, the linear model for the convexity is an average effect over the entire input range.

4.2.3 Model Verification

In order to validate the proposed dynamic linear model, validation experiment is carried out. The inputs and measured front-side weld pool characteristic parameters are plotted in

TABLE 4.2 LINEAR MODEL PARAMETERS

A	B
$\begin{bmatrix} 0.7728 & 0.0980 & -1.8404 \\ 0.1088 & 0.7869 & 0.2126 \\ 0.0001 & 0.0068 & 0.6871 \end{bmatrix}$	$\begin{bmatrix} 2.4093 & -0.5293 \\ 0.5504 & 0.0540 \\ 0.0108 & 0.0140 \end{bmatrix}$

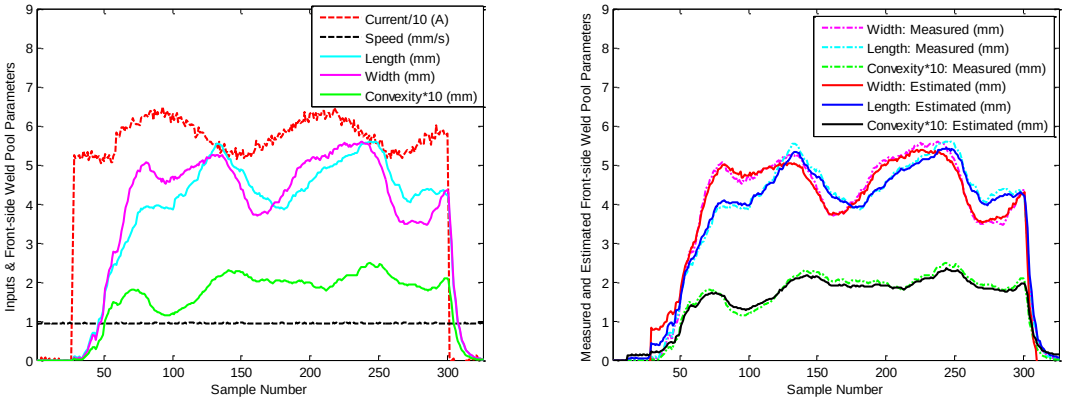

(a) (b)

Figure 4.5 Model verification experiment results. The current and the speed are varied in a sinusoid waveform and the welding speed is 1mm/s.

Figure 4.5 (a). The current and the speed are varied in a sinusoid waveform from 52A to 64A and the welding speed is 1mm/s throughout the experiment. Other experimental parameters are the same as those listed in Table 4.2.

It is observed that the weld pool width and length are increased with the increase of the welding current, and the convexity is decreased, indicating a more depressed weld pool. Figure 4.5(b) plots the measured weld pool characteristic parameters and estimated values by the dynamic linear model. It is observed that the weld pool parameters can be estimated with sufficient accuracy using the obtained linear model. In the next section, a predictive control algorithm is developed to control of the weld pool characteristic parameters in real-time.

4.3 Predictive Control Algorithm

In this section predictive control algorithm for GTAW weld pool control is derived. At instant k, the controller needs to determine the control action ($u_{1,k}$, $u_{2,k}$) based on the feedback x_k to drive the welding process to reach the desired weld pool state x_0.

According to (4.1), the weld pool states at instant k and k+1 can be expressed as:

$$\begin{cases} x_k = Ax_{k-1} + Bu_{k-1} \\ x_{k+1} = Ax_k + Bu_k \end{cases} \tag{4.2}$$

Subtracting the two equations yields:

$$x_{k+1} - x_k = A\left(x_k - x_{k-1}\right) + B\Delta u_k \tag{4.3}$$

Or

$$x_{k+1} = x_k + A\left(x_k - x_{k-1}\right) + B\Delta u_k \tag{4.4}$$

which is the 1-step prediction equation.

Suppose the future control action is constant, i.e. $\Delta u_{k+j} = 0,\ j = 1,...,N$, where N is the prediction range, 2-step prediction yields:

$$x_{k+2} = x_{k+1} + A^2\left(x_k - x_{k-1}\right) = x_k + \left(A^2 + A\right)\left(x_k - x_{k-1}\right) + B\Delta u_k \tag{4.5}$$

Similarly, the i-step prediction is:

$$x_{k+i} = x_k + \left(\sum_{j=0}^{i-1} A^{i-j}\right)\left(x_k - x_{k-1}\right) + B\Delta u_k \tag{4.6}$$

The prediction equation can be further expressed in matrix form:

$$\mathbf{X} = \mathbf{X}_k + \mathbf{F}\left(x_k - x_{k-1}\right) + \mathbf{G}\Delta u_k \tag{4.7}$$

where

$$\mathbf{X}=\begin{bmatrix} x_{k+1} \\ \vdots \\ x_{k+N} \end{bmatrix}_{3N\times 1} \quad \mathbf{X}_k=\begin{bmatrix} x_k \\ \vdots \\ x_k \end{bmatrix}_{3N\times 1} \quad \mathbf{F}=\begin{bmatrix} A \\ A^2+A \\ \vdots \\ A^N+\ldots+A \end{bmatrix}_{3N\times 3} \quad \mathbf{G}=\begin{bmatrix} B \\ B \\ \vdots \\ B \end{bmatrix}_{3N\times 2}$$

In an predictive control, the prediction range N should be large enough to achieve a robust control. However, the regulation speed decreases as N increases. It is found that N=5 can achieve the satisfactory regulation speed and good robustness. The desired trajectory x^*_{k+j} is defined as:

$$\begin{cases} x^*_{k+j} = \alpha x^*_{k+j-1} + (1-\alpha)x^0_{k+j},\ j = 1,\ldots,N \\ x^*_k = x_k \end{cases} \tag{4.8}$$

where $\alpha \in (0,1)$ is the smoothing coefficient. As α becomes larger, the system will track the set point with slower speed but better robustness and smoothness. In this study α=0.9 to achieve a good tradeoff between response speed and robustness.

The fluctuations in the welding parameters will generate non-smooth weld appearance, which is not acceptable in our application. Thus, energetic control actions must be avoided. The following cost function is used:

$$\begin{aligned} J_k(\Delta u_k) &= \sum_{j=1}^{N}\left[\left(x_{k+j} - x^*_{k+j}\right)^T P_1\left(x_{k+j} - x^*_{k+j}\right)\right] + \Delta u_k{}^T \mathbf{\Lambda}\Delta u_k \\ &= \left[\mathbf{X} - \mathbf{X}^*\right]^T \mathbf{P}\left[\mathbf{X} - \mathbf{X}^*\right] + \Delta u_k{}^T \mathbf{\Lambda}\Delta u_k \end{aligned} \tag{4.9}$$

where $\mathbf{P}_{3N\times 3N} = diag(P_1,\ldots,P_1)$ is the state penalty weighting matrix, $\mathbf{\Lambda}$=$diag(\lambda_1,\lambda_2)$ is the diagonal control weighting matrix, and $\mathbf{X}^*=\begin{bmatrix} x^*_{k+1} & \cdots & x^*_{k+N} \end{bmatrix}^T_{3N\times 1}$.

The cost function defined in equation (4.9) combines three characteristic parameters and forms a single control objective. By optimizing this cost function, a trade-off between three characteristic parameters will be achieved. This makes sense because the weld pool characteristic parameters are correlated to each other (see A matrix in Table 4.2) and the control algorithm should obtain a 3D weld pool geometry which is a trade-off between

three characteristic parameters, rather than trying to optimize three control objectives separately.

P_1 is a 3 by 3 diagonal matrix with each of the element quantifying the penalty of the weld pool state. The values of P_1 is determined by the physical meaning of the correlation between the weld pool states. In our application, 1mm in weld pool width is approximately equals to 1mm in the length and 0.1mm in the convexity. Thus the diagonal values of P_1 are selected to be 1, 1, and 100 corresponding to the weld pool width, length, and convexity, respectively.

The values of the weights λ_1 and λ_2 can also be determined based on their physical meaning in correlations between the preferred changes of the control actions and the errors between the desired and measured outputs. In this study λ_1=1000 (mm/100A)^2 and λ_2=4000 (mm/1mm/s)^2 is chosen, which implies that an error of 1mm in the weld pool width, 1mm in the length, and 0.1mm in the convexity has the same contribution to the cost function as current change of 0.033*100A = 3A, and speed change of 0.006mm/s.

The control law is calculated such that:

$$\frac{\partial J_k(\Delta \mathbf{u})}{\partial \Delta \mathbf{u}} = 0 \tag{4.10}$$

Equation (12) can be further expressed as:

$$\begin{aligned}
\frac{\partial J_k(\Delta u_k)}{\partial \Delta u_k} &= \frac{\partial \left(\left[\mathbf{X} - \mathbf{X}^* \right]^T \mathbf{P} \left[\mathbf{X} - \mathbf{X}^* \right] + \Delta u_k{}^T \mathbf{\Lambda} \Delta u_k \right)}{\partial \Delta u_k} \\
&= \frac{\partial \left(\left[\mathbf{X}_k + \mathbf{F} \Delta x_k - \mathbf{X}^* + \mathbf{G} \Delta u_k \right]^T \mathbf{P} \left[\mathbf{X}_k + \mathbf{F} \Delta x_k - \mathbf{X}^* + \mathbf{G} \Delta u_k \right] \right)}{\partial \Delta u_k} \\
&+ \frac{\partial \left(\Delta u_k{}^T \mathbf{\Lambda} \Delta u_k \right)}{\partial \Delta u_k} = 2\mathbf{G}^T \mathbf{P} \left(\mathbf{X}_k + \mathbf{F} \Delta x_k - \mathbf{X}^* \right) + 2 \left(\mathbf{\Lambda} + \mathbf{G}^T \mathbf{P} \mathbf{G} \right) \Delta u_k \\
&= 0
\end{aligned} \tag{4.11}$$

where $\Delta x_k = x_k - x_{k-1}$.

The predictive control law is finally expressed as:

$$\Delta u_k = -\left(\mathbf{\Lambda} + \mathbf{G}^T \mathbf{P} \mathbf{G} \right)^{-1} \mathbf{G}^T \mathbf{P} \left(\mathbf{X}_k + \mathbf{F} \Delta x_k - \mathbf{X}^* \right) \tag{4.12}$$

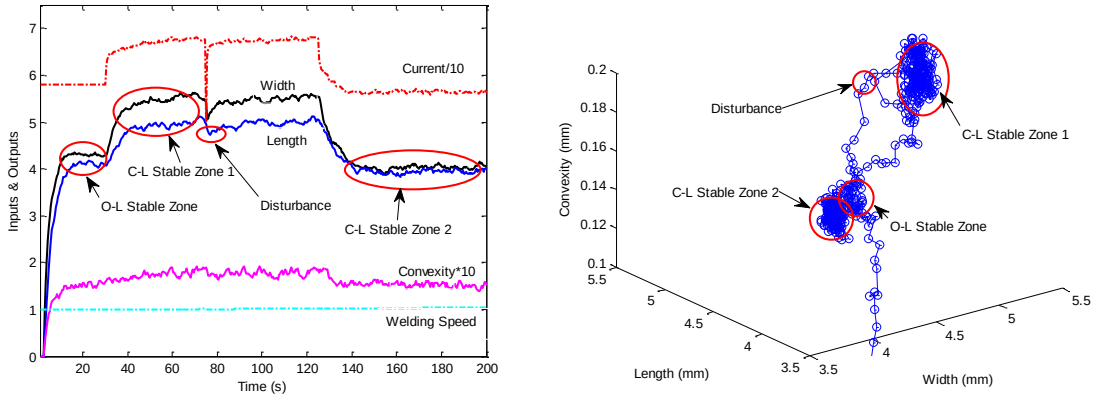

(a) (b)

Figure 4.6 Simulation experiment 1 for tracking various set-points and performance under current disturbance. (a) System inputs (welding current and speed) and outputs (weld pool width, length, and convexity) (b) System output parameter space.

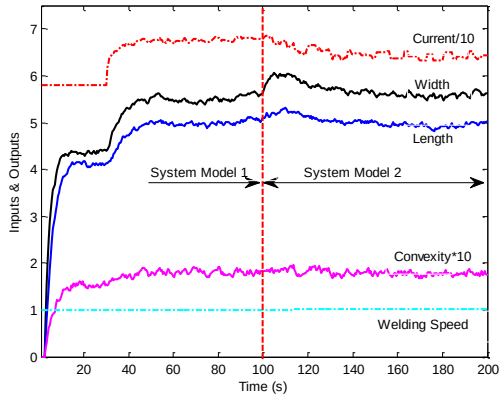

Figure 4.7 Simulation experiment 2 for performance under model variation.

4.4 Computer Simulation

The dynamic linear model identified in Section 3 is used as the system model. The initial welding condition is set at current 58A and welding speed 1mm/s, and the resulting weld pool width, length, and convexity is about 4.2mm, 4mm, and 0.15mm, respectively. The open-loop period is 30 seconds for both simulation experiments.

In the first simulation experiment the performance of the controller for tracking different set-point is evaluated, and the controller's robustness under current disturbance is also examined. The controller is set to track the reference point of [5.5mm, 5mm, 0.18mm] from 30 seconds to 120 seconds, and [4mm, 4mm, 0.15mm] from 120 seconds to 200 seconds. The system inputs and outputs are plotted in Figure 4.6(a) and the 3D output parameter space is visualized in Figure 4.6(b). It can be observed that the controller can track the different reference point with no overshoot and acceptable speed. At 70 seconds the current disturbance is applied, at which the current is artificially set to be 50A. As a result the width and length immediately decreases, and the convexity slightly decreases.

The controller is able to adjust the current according to the weld pool characteristic parameter feedback and the weld pool width, length, and convexity are controlled at the desired set-point despite the current disturbance. At 120 seconds, the set-point is set to [4mm, 4mm, 0.15mm]. As can be observed from Figure 9(a) the controller can adjust the welding inputs accordingly to control the process to the new set-point in a relatively quick response time. System output in 3D parameter space is visualized in Figure 9(b). The weld pool first reaches Open-Loop (O-L) stable zone during the open-loop period. After the controller is applied the weld pool state approaches Closed-Loop (C-L) stable zone 1. The disturbance makes the states deviates from C-L stable zone 1 but the controller is able to bring the state back to the stable zone. When the set-point is changed the weld pool state reaches another stable zone (C-L stable zone 2) in the output parameter space.

It is noticed that the speed adjustment is small in both simulations. The reason is that the diagonal control weighting matrix $\mathbf{\Lambda}$ is selected as $\mathbf{\Lambda}=diag(1000,4000)$ for our specific application. Typically in the weld pool control, the large speed adjustments cause severe variations in the welding process and the resulting welds may have significantly inconsistent weld penetration. However, for other applications different diagonal control weighting matrix $\mathbf{\Lambda}$ can be appropriately selected.

In simulation experiment 2 the controller's performance under varying system model is evaluated. In 100s the system model is changed, with the static gain of the speed artificially enlarged by 10%, simulating the possible variation of the system model under different welding conditions. It is observed from Figure 4.7 that the system output is

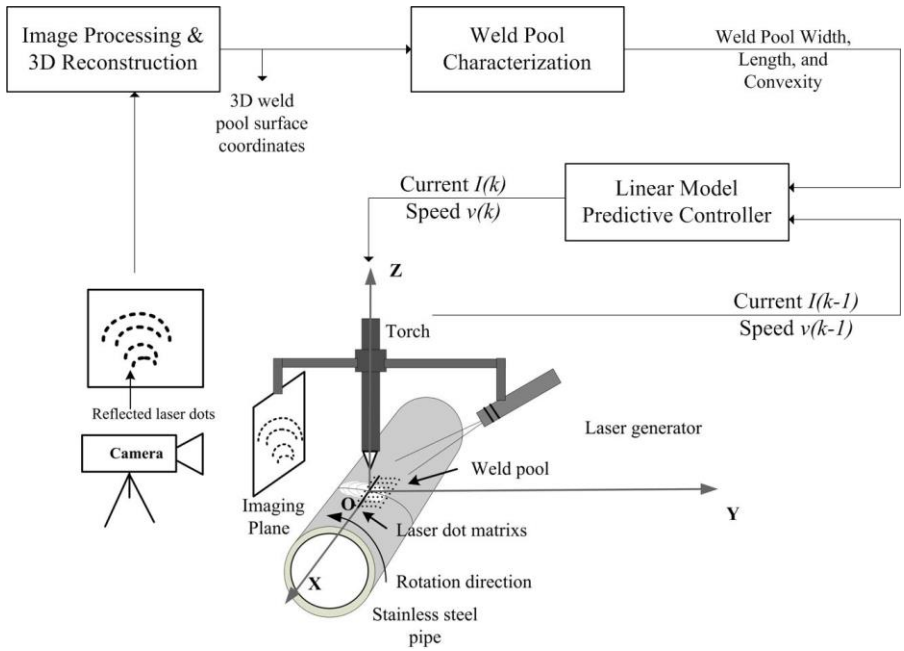

Figure 4.8 Proposed control system schematic. The sensing system is identical to Figure 3.1.

changed because of the variation in the system model. However, the proposed controller can control the weld pool characteristic parameters to the set point despite the variation of the system model robustly. In the next section, welding experiments are conducted to further verify the effectiveness and robustness of the proposed predictive controller.

4.5 Welding Experiments

The developed closed-loop control system can be illustrated using the diagram in Figure 4.8. In this diagram, the sensing system is identical to Figure 3.1. The measured weld pool width, length, convexity and the previous inputs are utilized by the proposed linear model predictive controller, and the calculated welding current / welding speed are applied to the welding process to generate a desired 3D weld pool state. The arc length is maintained at 5mm for all three experiments.

In order to demonstrate the robustness of the developed control system, various dynamic welding experiments have been designed and conducted in this section under different welding conditions and disturbances. In subsection 4.5.1 and the subsection 4.5.2 the welding current and welding speed disturbances are applied, accordingly and the robustness of the controller with input disturbances is tested. In subsection 4.5.3 the controller's performance for tracking different set-points is evaluated.

4.5.1 Experiment 1: Current Disturbance

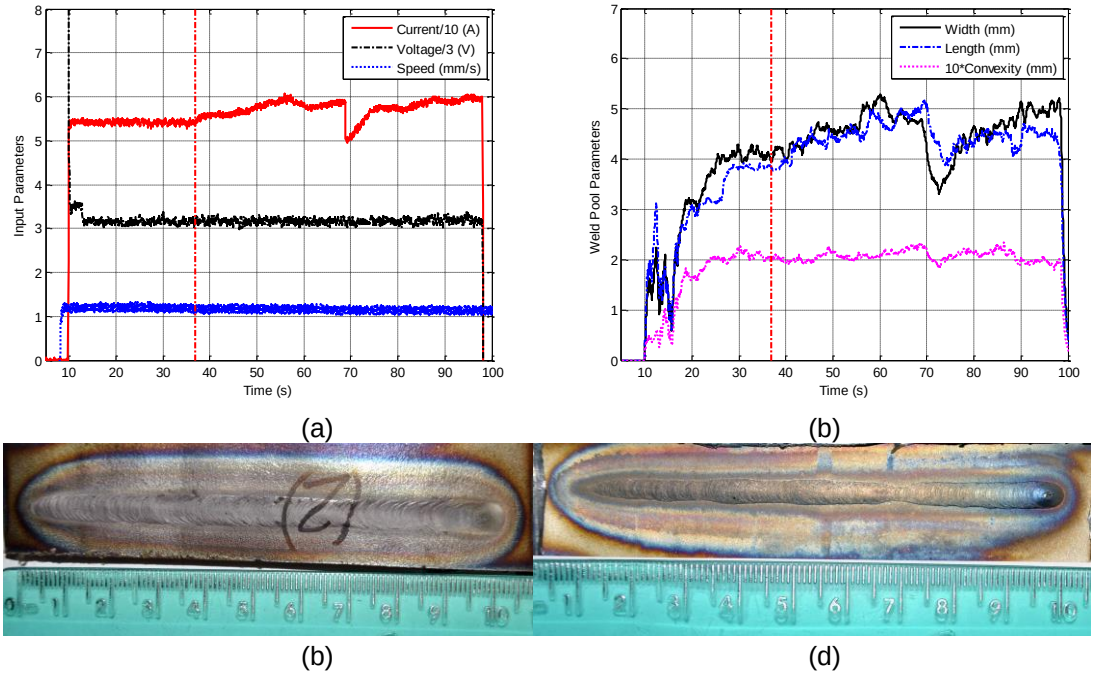

Figure 4.9 Welding experiment results under current disturbance. (a) Control input (b) weld pool characteristic parameters. The vertical dash line in (a) and (b) indicates the start time of the closed-loop control (c) Front-side weld bead (d) Back-side weld bead.

In this experiment the robustness of the control algorithm against current disturbances is evaluated. The set-points in this experiment are 5mm, 5mm, and 0.2mm for the weld pool width, length, and convexity, respectively. An artificial error between the calculated and applied values of the welding current is applied. The process begins with an open-loop period of about 27 seconds (with initial current 54A and initial welding speed 1.1mm/s), which brings the weld pool characteristic parameter (width, length, and convexity) to 4mm, 3.8mm, and 0.2mm, respectively. In the first 30 seconds after the open-loop period, no error exists between the calculated current and applied current. The controller is able to bring the weld pool width to 5mm, the length to 5mm and the convexity to 0.2mm, by increasing the welding current to about 60A (see Figure 4.9(a)).

At 68 seconds, the current is set at 50A, which is about 10A smaller than the calculated value at that time. As a result, the weld pool width, length and convexity decrease to 3.5mm, 4mm and 0.19mm, respectively (see Figure 4.9(b)). This current disturbance is also outside the input range we selected for the model (56A-68A shown in Table 4.1). However, the controller is able to adjust the welding current and the welding speed to compensate this large artificial error (see Figure 4.9(a)), and the 3D weld pool characteristic parameters can be maintained around the desired values again with a relatively quick response time. Figure 4.9(c)(d) depict the front and back-side weld bead, respectively.

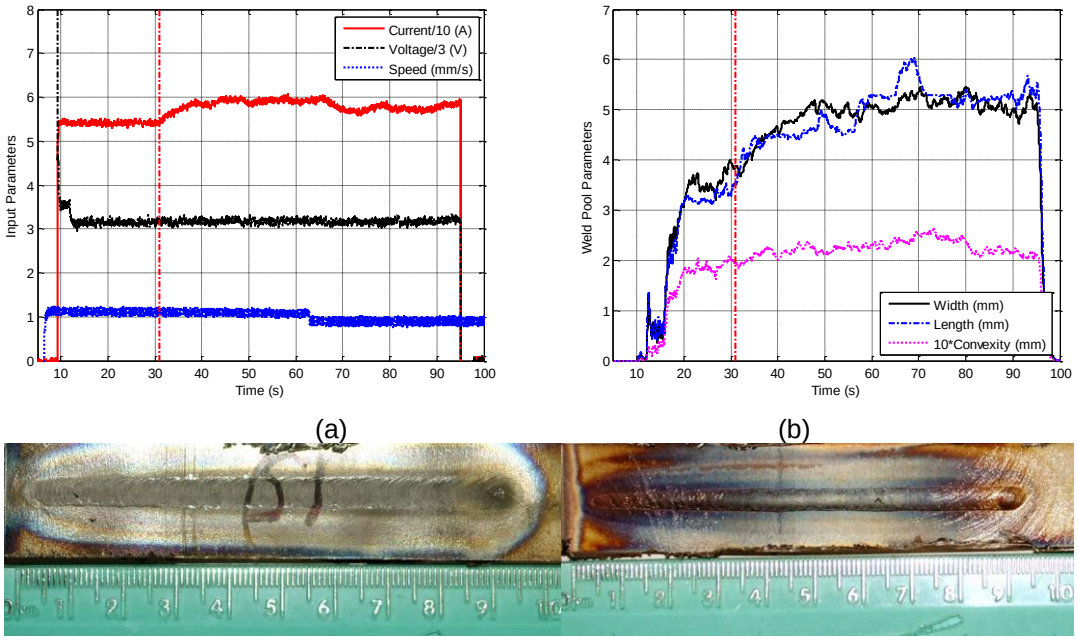

Figure 4.10 Welding experiment results under speed disturbance. (a) Control input (b) weld pool characteristic parameters. The vertical dash line in (a) and (b) indicates the start time of the closed-loop control (c) Front-side weld bead (d) Back-side weld bead.

4.5.2 Experiment 2: Speed Disturbance

In experiment 2, an artificial error between the actual and calculated values of the welding speed is applied to evaluate the robustness of the proposed control algorithm against welding speed disturbances. The process begins with an open-loop period of about 21 seconds (with initial current 54A and initial welding speed 1.1mm/s), which brings the weld pool characteristic parameter (width, length, and convexity) to 4mm, 3.5mm, and 0.2mm, respectively. During the first 31 seconds after the open-loop period, no error exists between the actual welding speed applied to the process and the welding speed calculated by the control algorithm. However, at 63 seconds the welding speed is set to 0.9 mm/s, which is about 0.2mm/s smaller than the calculated welding speed required for the weld pool characteristic parameter set-point. As can be seen from Figure 4.10 (b) the weld pool width, length, and convexity are increased to 5.2mm, 6mm, and 0.25mm, respectively. If no closed-loop controller is applied, the weld pool characteristic parameters will deviate from the set-points. However, by applying the controller the weld pool state may be maintained. From Figure 4.10(a) we observe that the controller is able to overcome the disturbance by decreasing the welding current to about 57A. Figure 4.10(c)(d) show the front and back-side weld bead obtained from the experiment. This experiment shows that the developed close-loop control system is robust to the variation in the welding speed.

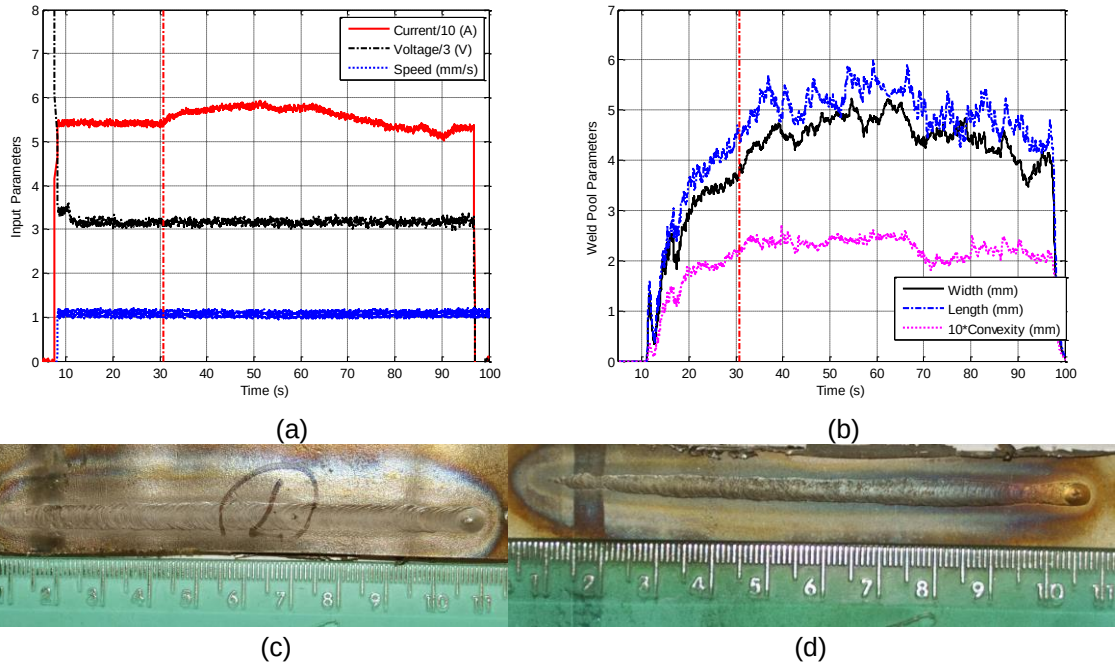

Figure 4.11 Welding experiment results for tracking varying set points. (a) Control input (b) weld pool characteristic parameters. The vertical dash line in (a) and (b) indicates the start time of the closed-loop control (c) Front-side weld bead (d) Back-side weld bead.

4.5.3 Experiment 3: Tracking Varying Set Points

In this experiment the controller's performance in tracking varying set-points is examined. After the open loop period of about 22 seconds, the weld pool width, length, and convexity are 3.8mm, 4.5mm, and 0.22mm, respectively (see Figure 14 (b)). The controller is able to bring the weld pool states to the set-point (5mm for the width, 5mm for the length, and 0.2mm for the convexity) by increasing the current to about 58A (see Figure 4.11(a)). At 62 seconds, the set-point is changed to [4mm, 4mm, 0.2mm]. The controller is able to decrease the current to about 52A for tracking the new set-point (see Figure 4.11(a)). Figure 4.11(c) shows the front-side weld bead and (d) shows the back-side weld bead.

In general, the dynamic properties of the nonlinear process vary with different operating points. For our specific application, however, the inputs are constrained to [50A, 60A] for the welding current and [0.9mm/s, 1.2mm/s] for the welding speed. In this specific input range, the nonlinear is not severe (see Figure 4.3) and the system can be modeled by a linear model with acceptable accuracy. For other applications where large range of inputs are required, nonlinear modeling and control methods are preferred over the linear predictive controller.

4.6 Summary

A linear model based predictive controller is developed to control the 3D weld pool geometry characterized by its width, length, and convexity in GTAW process. Dynamic experiments are conducted to establish the correlation between the weld pool characteristic parameters and the process inputs including the welding current and speed. A state space dynamic linear model is constructed, and the results are analyzed in detail. A linear predictive controller is formulated and an analytical solution is derived. Computer simulation is conducted to verify the effectiveness of the controller in tracking various set-points, and its robustness against disturbances and model variation. The closed-loop control experiments further demonstrate the controller's robustness against various disturbances.

Chapter 5 Skilled Human Welder Response Modeling and Intelligent Control

Because GTAW is primarily used in applications where appropriate degree of full penetration is required, the process should be automated if allowed. In manual welding, welders observe the weld pool and assure the desired full penetration is produced. However, in mechanized welding, welders are not required or allowed to observe the welding process with the similar level of concentration as in manual operation. Mechanized/automated systems rely on precision control of joint fit-up and welding conditions and tedious programming of welding parameters to produce repeatable results. Yet precision control of joints and welding conditions is very costly and not always guaranteed [54].

The system modeling and predictive control of the weld penetration and 3D front-side weld pool surface (detailed in chapter 3 and 4) has proven to be effective in accurately controlling the welding process to some extent. To ensure such an ideal performance, however, the control algorithm (structure) needs to be carefully designed per the process dynamics. The ability to develop an appropriate control algorithm requires extensive control system design experience and solid understanding of welding process dynamics. In addition, the needed online identification accuracy, especially for closed-loop identification, and convergence may add additional changes for relatively complex process dynamics like welding process. On the other hand, in manual GTAW process human welders can appraise the state of weld joint penetration through their directly observation of the weld pool and intelligently adjust the welding parameters accordingly to control the welding process to achieve the desired penetration state. The human welder's response model can be considered a verified controller for the controlled dynamic process. Thus, the mechanism of human welder's experience-based behavior should be fully explored. In addition, the resultant welder behavior models may help resolve the skilled welder shortage issue. It is thus of great interest to develop the intelligent welding machines that can sense the welding process like the human welder yet do not suffer from the limitations of the human welder [75-77]. In the following subsection the human welder's adjustment on the welding current is analyzed and implemented as an intelligent controller in an automated welding machine.

5.1 Human Welder's Behavior

The diagram of the human welder's behavior is shown in Figure 5.1 [76]. Given a certain welding task, a human welder starts with some initial estimation input I which may include the current, arc length, welding speed, etc. After the input of the initial control, the welder perceives necessary direct information Ω' from the weld pool. Ω is the

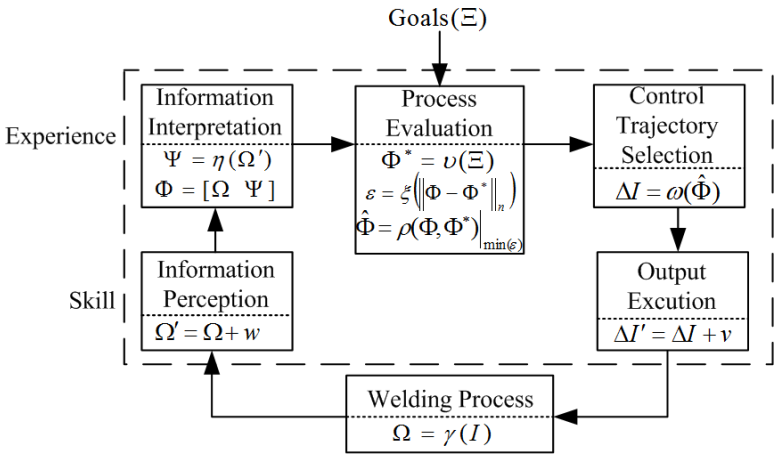

Figure 5.1 Illustration of an interpretation of human welder's behavior.

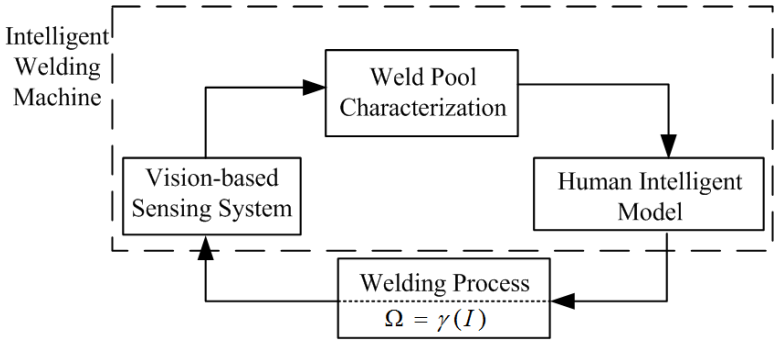

Figure 5.2 Illustration of intelligent welding machine that mimics human welder's behavior.

information that should be sensed from the welding process which is controlled by the welding parameters [54]:

$$\Omega = \gamma(I) \tag{5.1}$$

The welder may derive indirect information Ψ from the direct information:

$$\Psi = \eta(\Omega') \tag{5.2}$$

The instant state of welding process Φ may contain both the direct and indirect information of welding process.

The process evaluation involves the decision-making process. Given the inconsistent nature of human welder action, there may be certain inconsistency of welding performance even for a well-trained welder. The welder first maps the goals of the welding process Ξ into the desired state of welding process Φ^*:

$$\Phi^* = \upsilon(\Xi) \tag{5.3}$$

Then the welder evaluates the desired and the instant state similarly like with some norm-based cost function:

$$\varepsilon = \xi\left(\left\|\Phi - \Phi^*\right\|_n\right) \tag{5.4}$$

And the optimal state for the next instant $\hat{\Phi}$ can be considered to minimize the cost function:

$$\hat{\Phi} = \rho(\Phi, \Phi^*)\Big|_{\min(\varepsilon)} \tag{5.5}$$

Eventually, the welder performs a mathematic equivalence to mapping from the optimal state to the control:

$$\Delta I = \omega(\hat{\Phi}) \tag{5.6}$$

The output execution may be considered to be perturbed by a white Gaussian noise v, which reflects the maneuver skill of the human welder. There exists a common pattern from the direct information Ω to the welder's output I which is defined as the following equation:

$$\Delta I = F(\Omega) \tag{5.7}$$

The model of human welder's behavior (5.7) can be considered as the combination of the five elements from "Information perception" to "Output execution" in Figure 5.2. It is possibly nonlinear and time-varying.

As has been discussed above, human welder has limitations such as inconsistent concentration, fatigue and stress. For the intelligent welding machine that mimics the human welder's intelligence, these limitations can be overcome. The illustration of intelligent welding machine can be observed in Figure 5.2. In this figure, the information perception block in Figure 5.1 is substituted with a vision-based sensing system. The output of the sensing system is the 3D coordinates of the weld pool surface. Like the human welder's ability to interpret the complex weld pool shape, intelligent welding machine will characterize the weld pool, and output certain characteristic parameters to the human intelligent model. The outputs of the human intelligent model are the welding inputs, and will be inputted into the welding process.

5.2 Experimental Effort

5.2.1 Experimental System

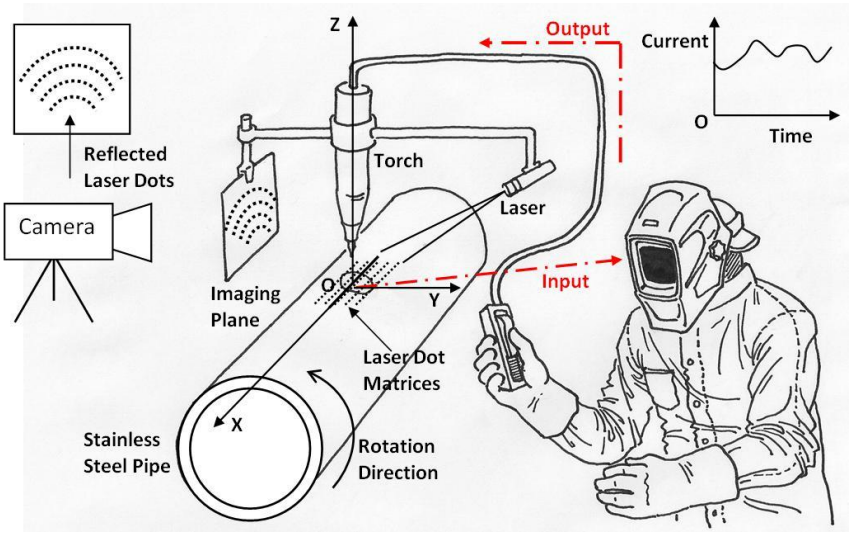

Figure 5.3 Manual control system of GTAW process.

A sensing and control platform was developed that records a human welder's current adjustments to varying penetration conditions while simultaneously recording topside pool characteristics. In this system skilled human welder holds the current regulator while observing the geometry of weld pool and adjusts the welding current accordingly in an effect to control the weld joint to full penetration. The pipe weld application is made using the DCEN GTAW. The material of the pipe is stainless steel 304. The outer diameter (OD) and wall thickness of the pipe are 113.5 mm and 2.03 mm, respectively. The pipe rotates during experiment while the positions of the torch, the imaging plane, the laser structure light generator and the camera are stationary. The rotation speed and motion of torch are controlled by a computer to achieve required welding speed and arc length.

5.2.2 Experimental Data

Nine dynamic experiments are conducted. In experiments 1 to 6 the welding speed is designed to vary within reasonable ranges [1mm/s, 2mm/s] in order to change the weld pool geometry. Then the skilled welder adjusts the current to try to maintain the same penetration state after the change of the welding speed. The arc length for these six experiments is set to 4 mm to 5.5 mm. During each individual experiment, the arc length is constant. In experiments 7 to 9 the arc length is varying from 4mm to 5.5 mm, and the human welder adjusts the current in response to the fluctuations of the weld pool. The welding speeds in these three experiments are between 1mm/s and 1.5 mm/s, which remain unchanged during each individual experiment. The other experimental parameters are shown in Table 5.1. The dynamic variation of weld pool geometry and the adjustment of current by the human welder are recorded respectively. It is noticed that in these experiments skilled human welder is able to control the welding process to desired

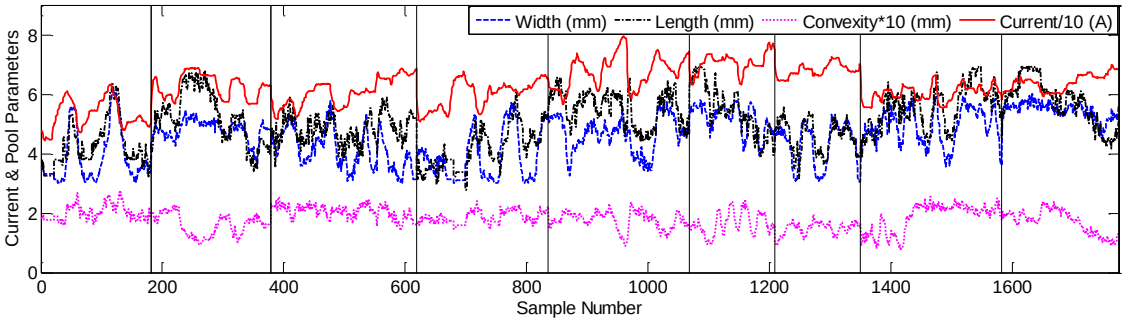

Figure 5.4 Weld pool characteristic parameters (width, length, convexity) and welding current adjusted by skilled human welder in nine dynamic experiments.

TABLE 5.1 EXPERIMENT PARAMETERS

Welding Parameters			
Current/A	Welding speed/mm/s	Arc length/mm	Argon flow rate/L/min
57~81	1~2	4-5.5	11.8
Monitoring Parameters			
Laser Project angle/ °	Laser to weld pool distance/mm		Imaging plane to weld pool distance/mm
35.5	24.7		101
Camera Parameters			
Shutter speed/ms	Frame rate/ fps		Camera to imaging plane distance/mm
4	30		57.8

penetration states. The obtained back-side bead width in these experiments are within certain ranges (4 mm to 6mm), which is considered acceptable in our applications.

During the welding process, the human welder always scans the weld pool with a certain frequency regardless of the welder's eye blink. The system's sampling frequency is 2 Hz in this study. There is also a finite time-delay existing in the linear model of the human welder's behavior as a result of the neuromuscular and central nervous latencies [54]. Based on the step response experiments it is observed that the average time delay of the welder's response is approximately 1.5 s, or 3 sampling periods.

Figure 5.4 plots the measured input parameters (the weld pool width, length, and convexity) and welding current adjusted by the skilled human welder. It can be seen that the tendency of current adjustment is roughly opposite to the length and width fluctuation. The trend of convexity basically coincides with the current variation. The variation of the geometry and the current indicates the human welder reduces the current as the weld pool length or width increases, and increases the current as the weld pool convexity increases. However, nonlinearity does occur in human welder adjustments corresponding to the weld pool characteristic parameters. Specifically, in sample number 1230 to 1280, the human welder increases the current as the weld pool width and length decreases, and the weld pool convexity increases. In sample number 1700 to 1800, on the other hand, the

human welder increases the current while the width, length, and convexity all decrease. This indicates that the skilled welder response to the weld pool characteristic parameters is indeed nonlinearly correlated and may be better modeled by a nonlinear model rather than simple linear model. In the next section, human response dynamics is analyzed.

5.3 Human Response Dynamics

It is apparent that a human welder makes adjustments based on multiple weld pools he/she observes, rather than a single pool at the current instant. However, the increase in the number of input parameters will complicate the nonlinear neuro-fuzzy model, and is thus not preferred. In this paper, filtered weld pool characteristic parameters are utilized as the inputs of the neuro-fuzzy model, which combine the information from multiple weld pools.

The designed filter can be expressed as:

$$\mathbf{CP}_f(k) = \alpha_f \mathbf{CP}_f(k-1) + (1-\alpha_f)\mathbf{CP}(k) \tag{5.8}$$

where $\mathbf{CP}_f(k) = \left[W_f(k), L_f(k), C_f(k)\right]^T$ and $\mathbf{CP}_f(k-1)$ are the filtered weld pool characteristic parameters at instant k and k-1, with W, L, C representing the width, length, and convexity, respectively. $\mathbf{CP}(k)$ is the measured weld pool characteristic parameters at instant k. α_f is the coefficient of the filter, which should be a tradeoff between the filtering effect and response speed. It is shown in the following figure that $\alpha_f = 0.6$ gives smaller modeling error and is thus chosen in our study.

It is also noticed that the current adjustment (dCurrent: $\Delta I(k) = I(k) - I(k-1)$) instead of

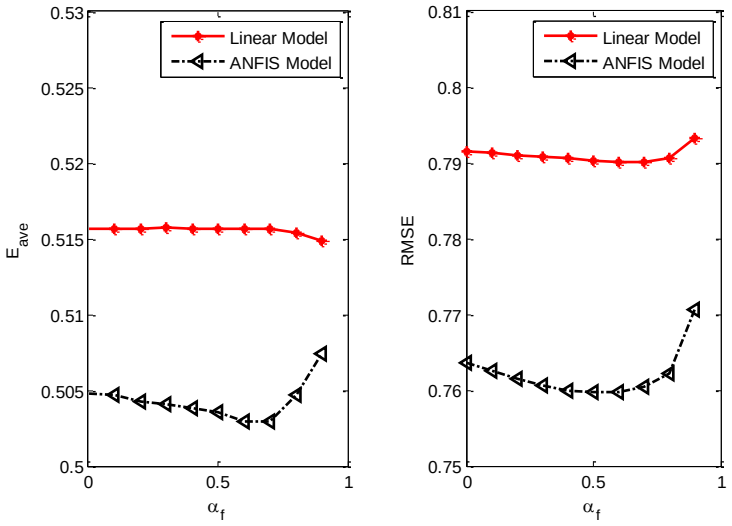

Figure 5.5 Modeling errors for both linear model and ANFIS model verses filtering coefficient.

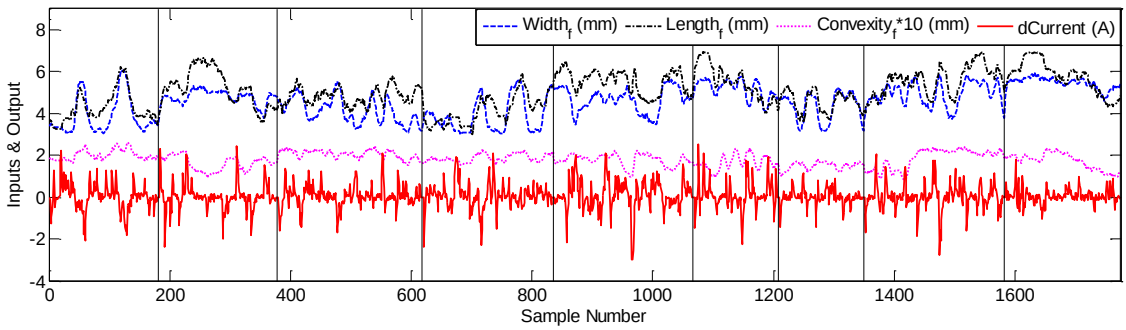

Figure 5.6 Filtered weld pool parameters (width, length, convexity) and current adjustments made by skilled welder.

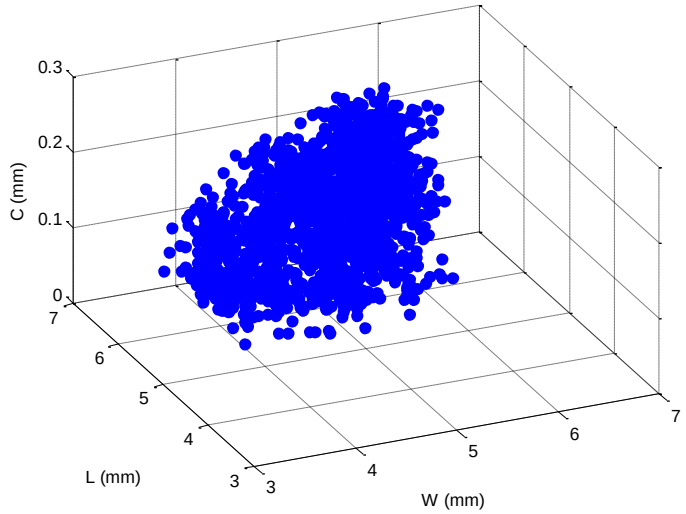

Figure 5.7 Distribution of the inputs for skilled welder modeling.

absolute current $I(k)$ is used to model the human behavior. This is because when the human welder makes adjustments on the current by using the current regulator, he/she doesn't know the absolute current value but the increase/decrease amount.

Figure 5.6 plots the inputs (filtered weld pool width, length, and convexity) and output (current adjustment dCurrent) of the human intelligence model. Figure 5.7 shows the distribution of the input parameters in these experiments. It can be observed that the weld pool parameters have filled the certain range of the input space and are nearly uniformly distributed. This distribution implies that the resultant model can be used during prediction of the human welder's response if the weld pool parameters are in this range.

In general, the human intelligent model can be written as:

$$\Delta I(k)=f(W_f(k-3), L_f(k-3), C_f(k-3), \Delta I(k-1)) \tag{5.9}$$

where the used human response delay 1.5 second (3 sampling periods) has been discussed in Experimental Data subsection.

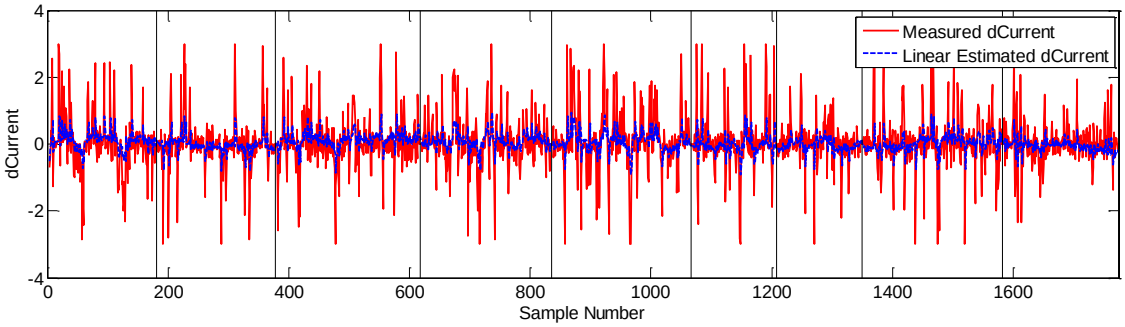

Figure 5.8 Linear modeling result.

TABLE 5.2 PARTITION OF FUZZY INPUT VARIABLES

Fuzzy Variables	Number of Fuzzy Sets	Partition
Width	2	wide, narrow
Length	2	long, short
Convexity	2	large, small
$dCurrent_p$	2	large, small

TABLE 5.3 FUZZY INPUT PARAMETERS FOR SKILLED WELDER

		MF1 Parameters	MF2 Parameters
Skilled Welder	Width	[2.565 1.993 1.103]	[2.558 1.996 6.189]
	Length	[2.673 2 1.598]	[2.677 1.996 6.937]
	Convexity	[0.0382 2.004 0.0561]	[0.0249 2.004 0.2277]
	$dCurrent_p$	[4.008 1.995 -3.996]	[4.004 1.993 4]

TABLE 5.4 MODEL COMPARISON BETWEEN NEURO-FUZZY MODEL AND LINEAR MODEL

	Average Model Error /A	RMSE /A	Maximum Model Error /A
Linear Model	0.52	0.79	3.15
ANFIS Model	0.50	0.76	3.03

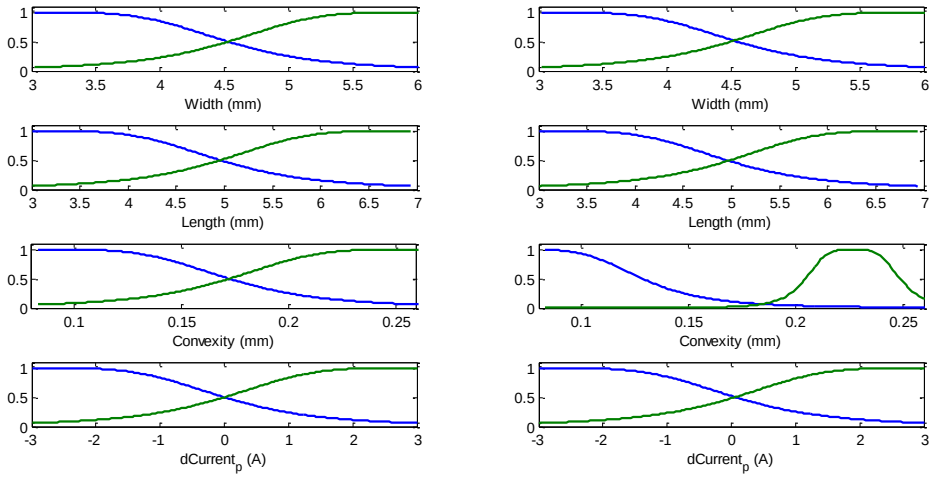

Figure 5.9 Fuzzy input membership functions before training (left) and after training (right).

The simplest form of (5.9) can be expressed by the following linear model:

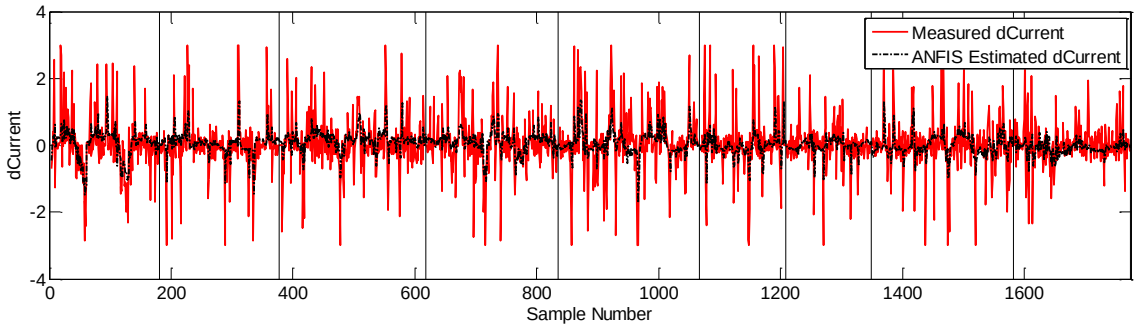

Figure 5.10 ANFIS modeling result.

$$\Delta I(k)=\alpha_1 W_f(k-3)+\alpha_2 L_f(k-3)+\alpha_3 C_f(k-3)+\alpha_4 \Delta I(k-1) \tag{5.10}$$

Using the standard least squares method the linear model can be fitted from the raw data. The identified linear models for skilled welder are shown in equation (5.10A):

$$\Delta I(k)=-0.16 W_f(k-3)-0.082 L_f(k-3)+1.81 C_f(k-3)+0.26 \Delta I(k-1) \tag{5.10A}$$

The linear modeling result is depicted in Figure 5.8. The average model error, maximum model error and RMSE for the identified linear model can be seen in Table 5.4 where all comparative models will be listed. In the next section, nonlinear neuro-fuzzy modeling is constructed to improve the model performance and the modeling results are analyzed.

5.4 ANFIS Modeling Result and Analysis

As a human inference mechanism, the human welder's response to the 3D weld pool surface is inevitably fuzzy and nonlinear. However, the abstract thoughts or concepts in human reasoning are difficult to extract from the domain knowledge [76-77]. In this subsection, ANFIS algorithm developed by Jang [117] will be used to model skilled human welder response.

5.3.1 Modeling Results

In order to further improve the modeling accuracy and better model the inherent fuzzy inference mechanism of the human welder, human intelligence model (5.9) is realized using the proposed ANFIS nonlinear model. The fuzzy input variables are partitioned by 2. The input fuzzy membership functions before and after training are depicted in Figure 5.9. Table 5.3 lists the trained parameters for these input membership functions. The estimation result is plotted in Figure 5.10. The resultant model RMSE and maximum model error are listed in Table 5.4. All criteria including the average model error, RMSE and maximum model error are improved by the proposed ANFIS model. Table IV lists the output membership parameters for the proposed ANFIS model.

TABLE 5.4 IDENTIFIED 16 NEURO-FUZZY MODEL RULES WITH FOUR INPUTS

Rule	IF	THEN (Skilled Welder)

(1,1,1,1)	P1 is “narrow”, P2 is “short”, P3 is “small”, and P4 is “small”	$y(1,1,1,1) = 5.87p_1 + 1.575p_2 - 79.03p_3 - 2.424p_4 - 7.464$
(1,1,1,2)	P1 is “narrow”, P2 is “short”, P3 is “small”, and P4 is “large”	$y(1,1,1,2) = -8.68p_1 - 2.08p_2 + 156.2p_3 - 1.5p_4 + 8.31$
(1,1,2,1)	P1 is “narrow”, P2 is “short”, P3 is “large”, and P4 is “small”	$y(1,1,2,1) = 0.338p_1 - 0.782p_2 + 47.85p_3 + 1.56p_4 - 5.91$
(1,1,2,2)	P1 is “narrow”, P2 is “short”, P3 is “large”, and P4 is “large”	$y(1,1,2,2) = -2.429p_1 + 1.33p_2 - 59.76p_3 - 1.63p_4 + 8.49$
(1,2,1,1)	P1 is “narrow”, P2 is “long”, P3 is “small”, and P4 is “small”	$y(1,2,1,1) = -3.05p_1 + 7.547p_2 + 443.8p_3 + 14.46p_4 - 65.44$
(1,2,1,2)	P1 is “narrow”, P2 is “long”, P3 is “small”, and P4 is “large”	$y(1,2,1,2) = 1.563p_1 - 0.592p_2 - 395.2p_3 + 8.146p_4 + 32.86$
(1,2,2,1)	P1 is “narrow”, P2 is “long”, P3 is “large”, and P4 is “small”	$y(1,2,2,1) = 1.934p_1 + 2.46p_2 + 189.8p_3 - 2.985p_4 - 59.65$
(1,2,2,2)	P1 is “narrow”, P2 is “long”, P3 is “large”, and P4 is “large”	$y(1,2,2,2) = -7.64p_1 - 3.43p_2 - 80.49p_3 + 0.4699p_4 + 60.33$
(2,1,1,1)	P1 is “wide”, P2 is “short”, P3 is “small”, and P4 is “small”	$y(2,1,1,1) = 2.05p_1 + 2.8p_2 - 48.32p_3 + 3.61p_4 - 10.93$
(2,1,1,2)	P1 is “wide”, P2 is “short”, P3 is “small”, and P4 is “large”	$y(2,1,1,2) = -4.77p_1 + 4.22p_2 + 33.41p_3 + 4.573p_4 + 3.56$
(2,1,2,1)	P1 is “wide”, P2 is “short”, P3 is “large”, and P4 is “small”	$y(2,1,2,1) = -1.65p_1 + 0.92p_2 - 77.76p_3 + 0.1138p_4 + 20.2$
(2,1,2,2)	P1 is “wide”, P2 is “short”, P3 is “large”, and P4 is “large”	$y(2,1,2,2) = -2.46p_1 + 0.03p_2 + 51.38p_3 + 1.148p_4 + 1.568$
(2,2,1,1)	P1 is “wide”, P2 is “long”, P3 is “small”, and P4 is “small”	$y(2,2,1,1) = -2.01p_1 - 0.994p_2 - 37.44p_3 - 1.534p_4 + 17.09$
(2,2,1,2)	P1 is “wide”, P2 is “long”, P3 is “small”, and P4 is “large”	$y(2,2,1,2) = 3.36p_1 + 1.763p_2 + 22.88p_3 - 2.229p_4 - 30.32$
(2,2,2,1)	P1 is “wide”, P2 is “long”, P3 is “large”, and P4 is “small”	$y(2,2,2,1) = 0.34p_1 - 0.003p_2 - 7.404p_3 + 0.3415p_4 - 2.028$
(2,2,2,2)	P1 is “wide”, P2 is “long”, P3 is “large”, and P4 is “large”	$y(2,2,2,2) = -1.12p_1 - 0.141p_2 - 11.77p_3 - 0.1821p_4 + 12.62$

5.3.2 Discussion and Validation

The linear model in Equation (5.10A) accounts for the average of the nonlinear human welder's response in the operation range of the parameters used to conduct the dynamic experiments. Specifically, the coefficient for the width is -0.16, indicating the average negative effect of the width on the current adjustment. The coefficient for the length is 0.08. This implies that the skilled welder treats width more importantly than the length, given the magnitude of the width and length are similar. For the weld pool convexity, the coefficient is 1.81. This implies that in general the human welder increases the current if the convexity is increased. The coefficient for the previous adjustment (0.26) indicates that the human welder adjustment at current instant also correlates to the previous adjustment, and the correlation is positive. One may think that the model improvement from Table V (4% to 7% for three criteria proposed in this study) is not significant. However, ANFIS model is derived in analytical form and can be implemented in real-time. The resultant model improvement is achieved at no additional costs. In addition, the human welder response is better modeled and understood. In this sense, the proposed ANFIS model is considered a better way to represent the intrinsic nonlinear and fuzzy inference human welder possesses. In addition, Figure 5.11 shows detailed view of the modeling result comparison between the linear model and ANFIS model from sample number 0 to 180, 480 to 620, and 1350 to 1460, respectively. It is observed that noticeable improvements are made by the proposed ANFIS model.

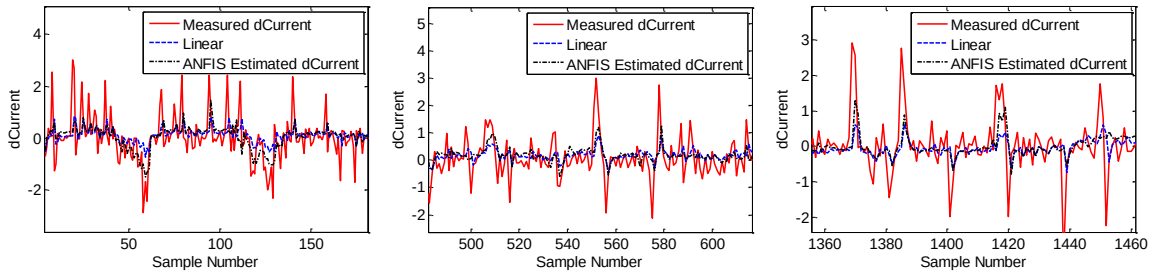

Figure 5.11 Model comparison between linear and ANFIS model.

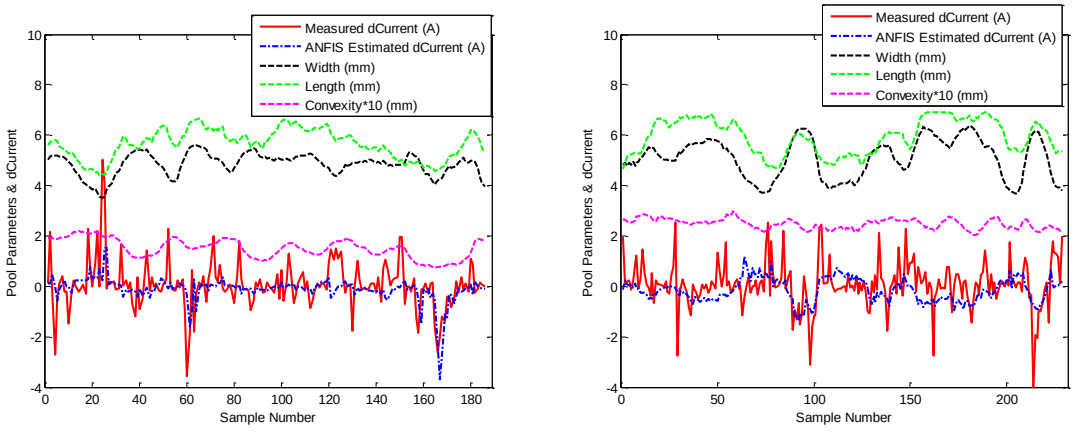

(a) (b)

Figure 5.12 Verification experiment results (a) experiment 1 (b) experiment 2.

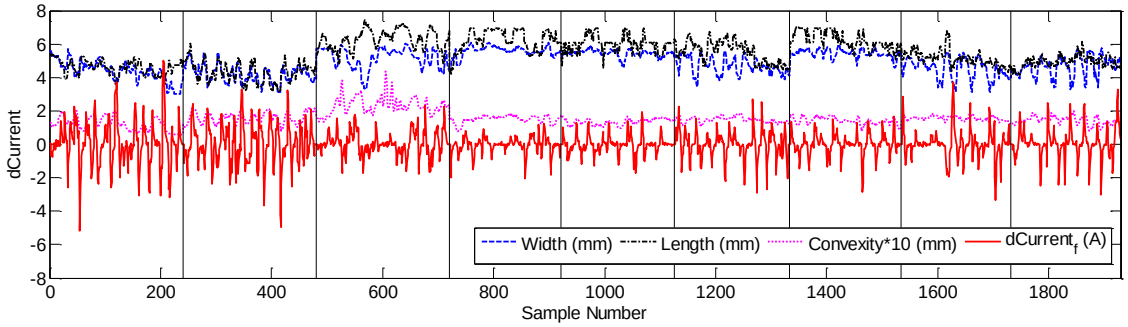

(a)

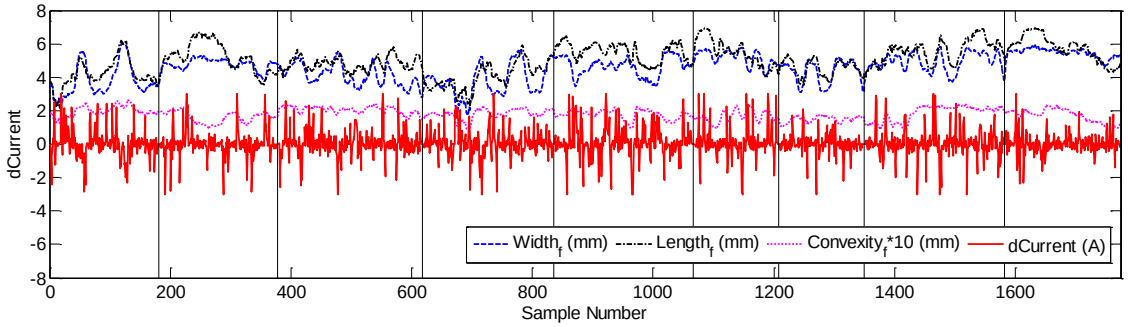

(b)

Figure 5.13 Inputs / output data for constructing welder response models: (a) novice welder model; (b) skilled welder model.

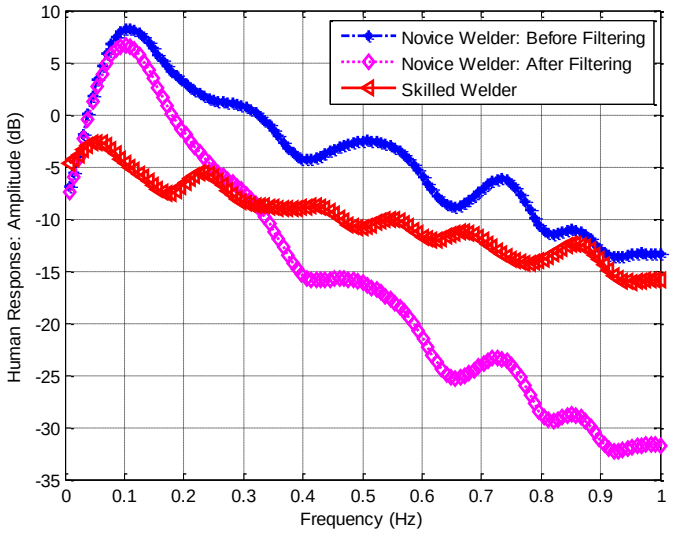

Figure 5.14 Frequency response for the novice welder and skilled welder.

Although the linear model analysis can reveal some information about skilled welder's adjustments, detailed information is lost because of the incapability of the linear modeling, which can only model the average effect of the input parameters over the output. The nonlinear ANFIS model, however, can discover detailed information about the human welder intelligence. Because of the relative complexity of the ANFIS model, its analysis will be more comprehensive. Hence, the ANFIS model will be analyzed and compared with that of the novice welder in the next section.

To further verify the skilled human welder model, verification experiments are conducted. The welding speed is designed to vary from 1mm/s to 2mm/s and the welders adjust the current in accordance to the varying weld pool geometry. The arc length is set at 4mm for both experiments. As can be observed in Figure 5.12, the proposed ANFIS model can estimate the welder's response in good accuracy.

In the next few sections the developed neuro-fuzzy human intelligence model will be analyzed and compared with that of novice welder and then be utilized as an intelligent controller to perform penetration control in automated GTAW process.

5.5 Data Analysis and Frequency Response

In this section the data used for constructing both novice and skilled human welder model are presented / analyzed, and the frequency responses of the skilled welder model and novice welder model are compared.

Figure 5.13 depicts the weld pool characteristic parameters and welder's adjustments made by both novice welder (Figure 5.13(a)) and skilled welder (Figure 5.13(b)). It has been shown [54, 76] that both novice welder and skilled welder can respond to the fluctuating weld pool surface and control the welding process in a certain degree. It is noticed that the current adjustments made by the novice welder has been filtered before modeling because of the frequently observed abrupt adjustments in the welding current. This is understandable because of the limited skill novice welder possess. For the skilled welder, on the other hand, the current adjustments are considered as correct responses to the changing welding process and are modeled directly. Instead, front-side weld pool characteristic parameters in multiple sampling times are combined and the filtered width, length, and convexity are then used as the model inputs [76].

Comparing the adjustments made by novice and skilled welder, it is observed that the novice welder adjustments are generally larger than those of the skilled welder. The maximum current adjustment of the novice welder is about 5 A, while the maximum adjustment of the skilled welder is about 3 A. To better illustrate the different behaviors of the novice and skilled welder, frequency analysis is performed and the result is shown in Figure 5.14.

It is observed from Figure 5.14 that the amplitude of the novice welder response (before filtering) is generally larger than that of the skilled welder. This coincides with the observation from the data plotted in Figure 5.13. The novice welder has larger and energetic response in all frequencies, indicating the frequently underestimation and overestimation of the process by the novice welder. The maximum response of the novice human welder is obtained at 0.1 Hz. However, for the skilled welder response, the maximum response is achieved at 0.05 Hz. This implies that the skilled human welder concentrates on the lower frequency than novice welder does. After the filter is applied,

the low frequency response of the novice welder is well preserved yet the high frequency response is largely attenuated. Comparing the filtered novice welder response and skilled human welder response, it is seen that the high frequency response of the novice welder is significantly lower. This makes sense because the adjustment made by the skilled welder is considered to be relatively accurate and correct, and its moderate response in different frequency ranges including relatively high frequencies is considered to be relevant to the change in the weld pool geometry in different frequencies. As will be seen in the closed-loop control experiments, the skilled human welder model based controller has faster convergence time.

5.6 Model Comparison

5.6.1 Linear Model Comparison

Linear model can sometimes be used as a reasonable approximation of the intrinsic nonlinear model of the welder's response. In this section, the comparison between the novice and skilled human welder linear models is performed and the results are analyzed. The simplicity of linear models will make the comparison be relatively straightforward and easier to follow.

The identified linear model for the novice and skilled human welder are expressed in Equation (5.11A) and (5.11B), respectively:

$$\Delta I(k) = -0.049W(k-3) - 0.0049L(k-3) + 1.73C(k-3) + 0.72\Delta I(k-1) \quad (5.11A)$$

$$\Delta I(k) = -0.16W_f(k-3) - 0.082L_f(k-3) + 1.81C_f(k-3) + 0.26\Delta I(k-1) \quad (5.11B)$$

where *W*, *L*, *C*are the weld pool width, length, convexity, respectively, and $\Delta I(k)$ is the current adjustment by the human welder at instant *k*. Filtered weld pool width, length, convexity can be calculated using the following equation [76]:

$$\mathbf{CP}_f(k) = \alpha_f \mathbf{CP}_f(k-1) + (1-\alpha_f)\mathbf{CP}(k) \quad (5.12)$$

where $\mathbf{CP}_f(k) = \left[W_f(k), L_f(k), C_f(k)\right]^T$ and $\mathbf{CP}_f(k-1)$ are the filtered weld pool characteristic parameters at instant *k* and *k* -1, respectively. $\alpha_f = 0.6$ gives smallest modeling error and is thus chosen in our study [1].

For the novice welder model described in Equation (1A), a low pass output execution filter is further added to improve the system performance [2], which can be expressed as:

$$I_f(k) = \alpha_{fo} I_f(k-1) + (1-\alpha_{fo})I(k) \quad (3)$$

where $I_f(k)$, $I_f(k\text{-}1)$ are the filtered currents at instant k and k-1, respectively, and $I(k)$ is the current at instant k. $0 < \alpha_{fo} < 1$ is the coefficient of the filter, which should be a tradeoff between the filtering effect and response speed. It is found that when α_{fo}=0.5, a good trade-off can be made between the smoothing effect of the filter and the response of the model.

In order to analyze the properties of the linear models, they are written in z-transfer functions [4], and are shown in Table 5.6. The poles and zeros of the z-transfer functions are listed in Table 5.7.

It is observed that all the poles of the model are inside the unit circle in Z-plane, which indicates that the model as the controller is asymptotically stable [77]. In fact, both novice and skilled human welder make the adjustment on the welding current as intelligent controllers. Even for a novice welder with limited training and possible overestimating and underestimating of the process, this controller can and should be able

TABLE 5.6 Z-TRANSFER FUNCTIONS OF THE LINEAR MODEL

Model	z-transfer function
Novice Human Model (Before Filtering) $H_n(z) = \frac{B_n^W(z)}{A_n(z)} + \frac{B_n^L(z)}{A_n(z)} + \frac{B_n^C(z)}{A_n(z)}$	$A_n(z) = z^3 - 0.72z^2$ $B_n^W(z) = -0.0492$ $B_n^L(z) = -0.0049$ $B_n^C(z) = -1.735$
Novice Human Model (After Filtering) $H_{nf}(z) = \frac{B_{nf}^W(z)}{A_{nf}(z)} + \frac{B_{nf}^L(z)}{A_{nf}(z)} + \frac{B_{nf}^C(z)}{A_{nf}(z)}$	$A_{nf}(z) = z^3 - 1.212z^2 + 0.3558z$ $B_{nf}^W(z) = -0.0246$ $B_{nf}^L(z) = -0.00245$ $B_{nf}^C(z) = -0.8674$
Skilled Human Model $H_s(z) = \frac{B_s^W(z)}{A_s(z)} + \frac{B_s^L(z)}{A_s(z)} + \frac{B_s^C(z)}{A_s(z)}$	$A_s(z) = z^3 - 0.8562z^2 + 0.1537z$ $B_s^W(z) = -0.06268$ $B_s^L(z) = 0.03284$ $B_s^C(z) = -0.7247$

TABLE 5.7 POLES OF THE LINEAR MODELS

Inputs	Poles
Novice Human Model (Before Filtering)	$[0.72, 0, 0]$
Novice Human Model (After Filtering)	$[0.72, 0.5, 0]$
Skilled Human Model	$[0.6, 0.26, 0]$

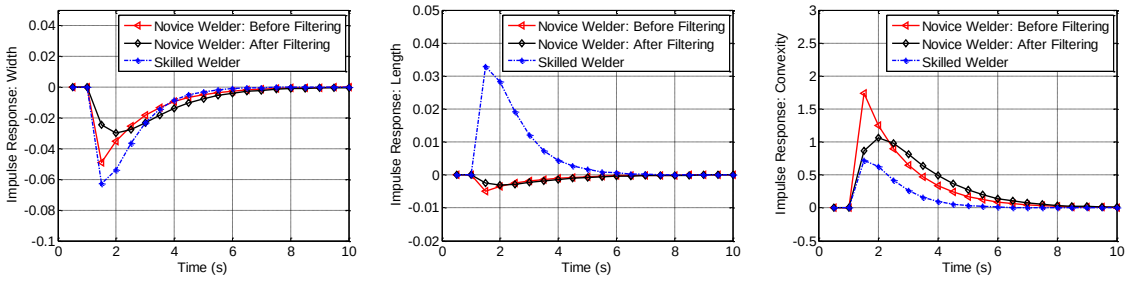

Figure 5.15 Impulse responses of the linear models for novice welder and skilled welder (a) width impulse response; (b) length impulse response; (c) convexity impulse response.

to deliver a stable welding process despite his/her limited experience training. Hence, the models for both novice and skilled welder's response should be stable. To further analyze the two linear models, impulse responses are calculated and shown in Figure 5.15.

Figure 5.15 depicts the impulse responses of the linear models for both novice welder and skilled welder for three inputs (weld pool characteristic parameters). For the width impulse response (Figure 5.15(a)), both the novice and skilled welder react negatively (decrease the welding current as the weld pool width increases). This is understandable because the increase of the width generally indicates the increase of the weld penetration, and the average effect of the welder response should be negative to compensate this positive increment of the weld pool width. However, the magnitude of the impulse response (i.e., the static gain of the linear model) is different. The skilled welder model reacts larger to the width increase (with static gain of 0.06 A/mm) than the novice welder (with static gain of 0.049 A/mm). After filtering the static gain of the novice welder is further reduced to 0.025 A/mm. On the other hand, the skilled welder model has slightly shorter settling time (about 5 seconds) compared to that of the novice welder model after filtering (about 6 seconds).For the weld pool length (Figure 5.15(b)), the skilled welder reacts differently than the novice welder. The novice welder is not sensitive to the length increase, and the adjustment is minimal (with maximum magnitude of 0.003A corresponding to 1 mm length increase). For the skilled welder, the response to the length is much more significant (with maximum magnitude of 0.033A corresponding to 1 mm length increase). The positive impulse response indicates that the average effect of the adjustment made by the skilled welder is positive (i.e., increase the current as the weld pool length increases). This makes sense because the increase of the length may indicate the increase of the welding speed, and decrease of the total heat input into the process, especially when the weld penetration is sufficient. In this case the welding current should be increased to compensate this increase of the weld pool length. Figure 5.15(c) shows the impulse response for the weld pool convexity input. Both novice and skilled welder react to the convexity with positive adjustments. This is understandable because the increase of the convexity generally indicates the decrease of the weld penetration. In this

sense, the welder should increase the current to compensate this effect. After the filter, the novice welder model reacts to the convexity less energetically and smoother. Comparing the convexity impulse response made by the skilled and novice welder, it is observed that skilled welder model has much shorter settling time (about 5 seconds) than that of the novice welder after filtering (about 7 seconds).

It is thus clear that the linear model derived from skilled human welder response has better performance than that derived from the novice human welder in terms of settling time. The difference between the impulse response relative to the weld pool width, length, and convexity also indicates the different adjustments made by the novice welder and skilled welder. In particular, the skilled welder responds to the weld pool length while the novice welder does not noticeably. The skilled welder thus not only responds faster and more accurately but also makes use of more information from the weld pool.

5.6.2 Nonlinear Model Comparison

Although linear models can give us some knowledge about the difference between novice welder and skilled welder, it is inevitable that the linear model can only model the average effect of the input parameters over the output. Detailed information is lost because of the incapability of the linear modeling. In the following, the proposed nonlinear ANFIS models for both novice welder and skilled welder are compared, and the results are analyzed in detail.

Figure 5.16 demonstrates the proposed neural fuzzy model surface for different weld pool geometry. It is observed that nonlinearity is substantial in modeling the human welder's response to 3D weld pool geometry. Careful observation in Figure 5.16 shows that when the weld pool convexity is small (i.e. the convexity=0.1mm in Figure 5.16(a)), the current adjustments are negative for both small and large weld pool area, while approaches zero for medium weld pool area (with the weld pool width at about 5mm, and length at about 5mm). This makes sense because such small convexity for small weld pool size generally indicates over penetration and the human welder should decrease the current to prevent burn-through. Compared the response of novice welder to that of skilled welder, it is observed that the difference appears when the width is small yet the length is relatively large (i.e., the length to width ratio is large). Novice welder is not sensitive to this scenario, and the adjustments are minimal. For the skilled welder, on the other hand, the current adjustment is positive, with largest adjustments of 3 A. It makes sense because when the length to width ratio is large, and the convexity is small, it indicates that the penetration is not sufficient because of the insufficient of the total heat input. The large length is probably caused by the large welding speed. In this case, the welder should increase the current to compensate this under-penetration. Moreover, this phenomenon indicates the nonlinear inference of the human welder's response rather than the linear approximation of the correlation provided by the linear models. As the convexity

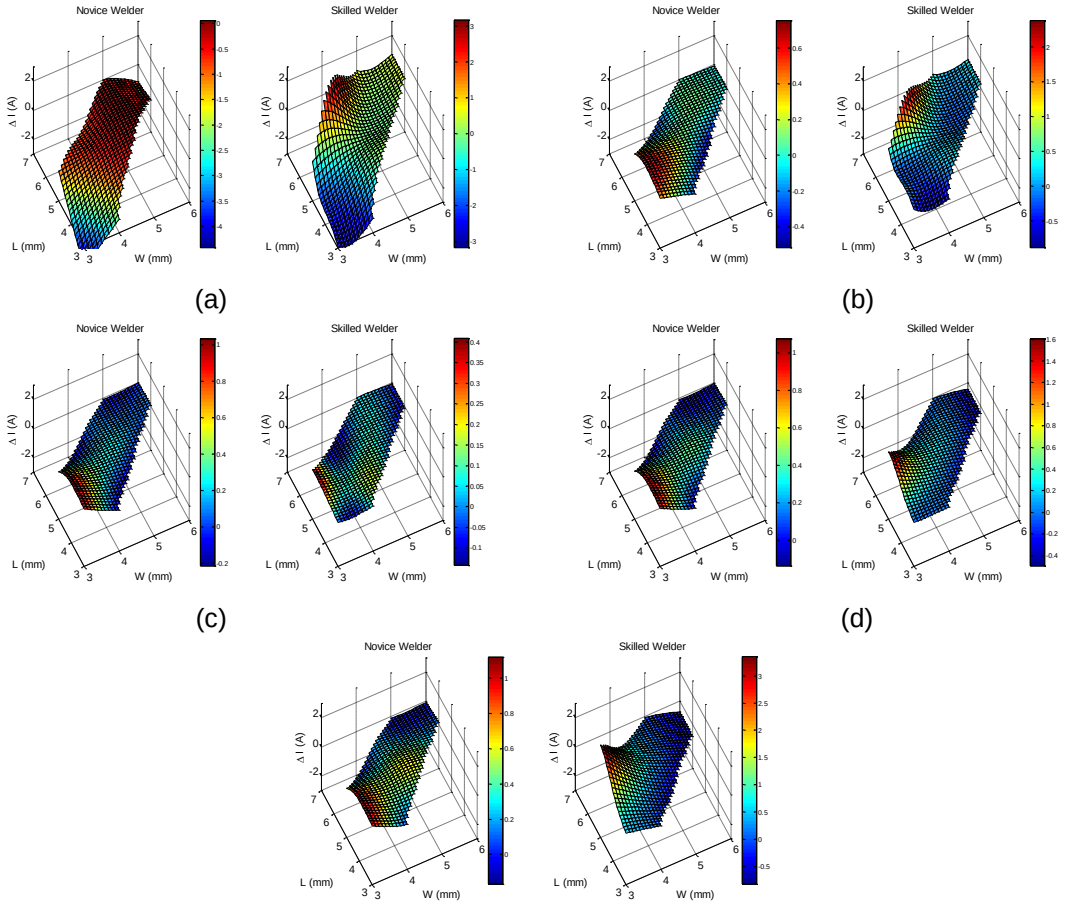

Figure 5.16 Nonlinear model surface of the ANFIS human welder model (left: novice welder, right: skilled welder) for convexity = (a) 0.10 mm (b) 0.14mm (c) 0.18mm (d) 0.22mm (e) 0.26mm. Previous response is zero for all cases.

becomes larger (Figure 4(c)), the adjustment made by the skilled welder is generally smaller than that of the novice welder. This indicates that the skilled welder tends not to adjust the current since the convexity is within the tolerance range. Figure 5.16(e) depicts the case when the weld pool convexity is relatively large. In this case, the skilled welder's current adjustment is larger than that of the novice welder. This implies that for this extreme case, the skilled welder is more sensitive and the large response represents the correct adjustment made by the human welder. It is observed that for all cases the nonlinearity is substantial and the nonlinear ANFIS model does provide detailed knowledge about the adjustments made by the skilled welder. This highly nonlinear adjustment made by the skilled welder is thus crucial to produce quality welds and mechanize the human welder's intelligence.

It is observed from Figure 5.16 that in normal cases the skilled welder's adjustments are minimal which can prevent the large oscillation and overshoot a novice welder model suffers. However, in other cases where the convexity is either considerably small or large, the adjustment made by the skilled welder is larger than that of the novice welder, which

can provide shorter settling time than a novice welder does. The skilled welder model does provide better adjustment than the novice welder. In the next section, closed-loop control experiments will be conducted to further verify the effectiveness of the skilled human welder model under various welding process disturbances and variations.

5.7 Control Experiments and Analysis

The developed closed-loop control system is illustrated in Figure 5.17. In this experimental system, the pipe weld application is made using the DCEN GTAW. The material of the pipe is stainless steel 304. The outer diameter (OD) and wall thickness of the pipe are 113.5 mm and 2.03 mm, respectively. The pipe rotates during the experiment while the positions of the torch, the imaging plane, the laser structure light generator and the camera are fixed in space. The rotation speed and motion of torch are controlled by a computer to achieve required welding speed and arc length. A computer connected to the camera processes the captured image, reconstructs the weld pool, and extracts three characteristic parameters of the weld pool (the width, length, and convexity) in real-time. The skilled human intelligence model then output the current. To imitate the welder's behavior as the human welder's response principle detailed in the first part of this study, in each experiment an initial welding input is first applied for the weld pool to grow and full penetration is achieved. Then the closed-loop control period of the human intelligence model starts. The experimental parameters (including welding parameters and imaging/monitoring parameters) used in the closed-loop control experiments are the same as those listed in the first part of this study.

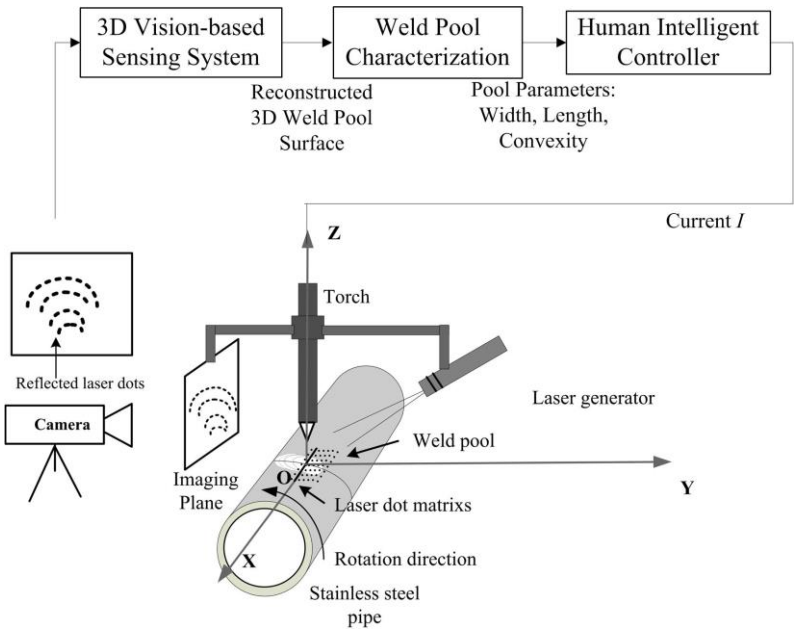

Figure 5.17 Illustration of the Closed-Loop Control System.

To confirm the effectiveness of the proposed skilled human welder model in controlling the GTAW process to achieve the desired weld penetration, various closed-loop control experiments have been designed and conducted in this section.

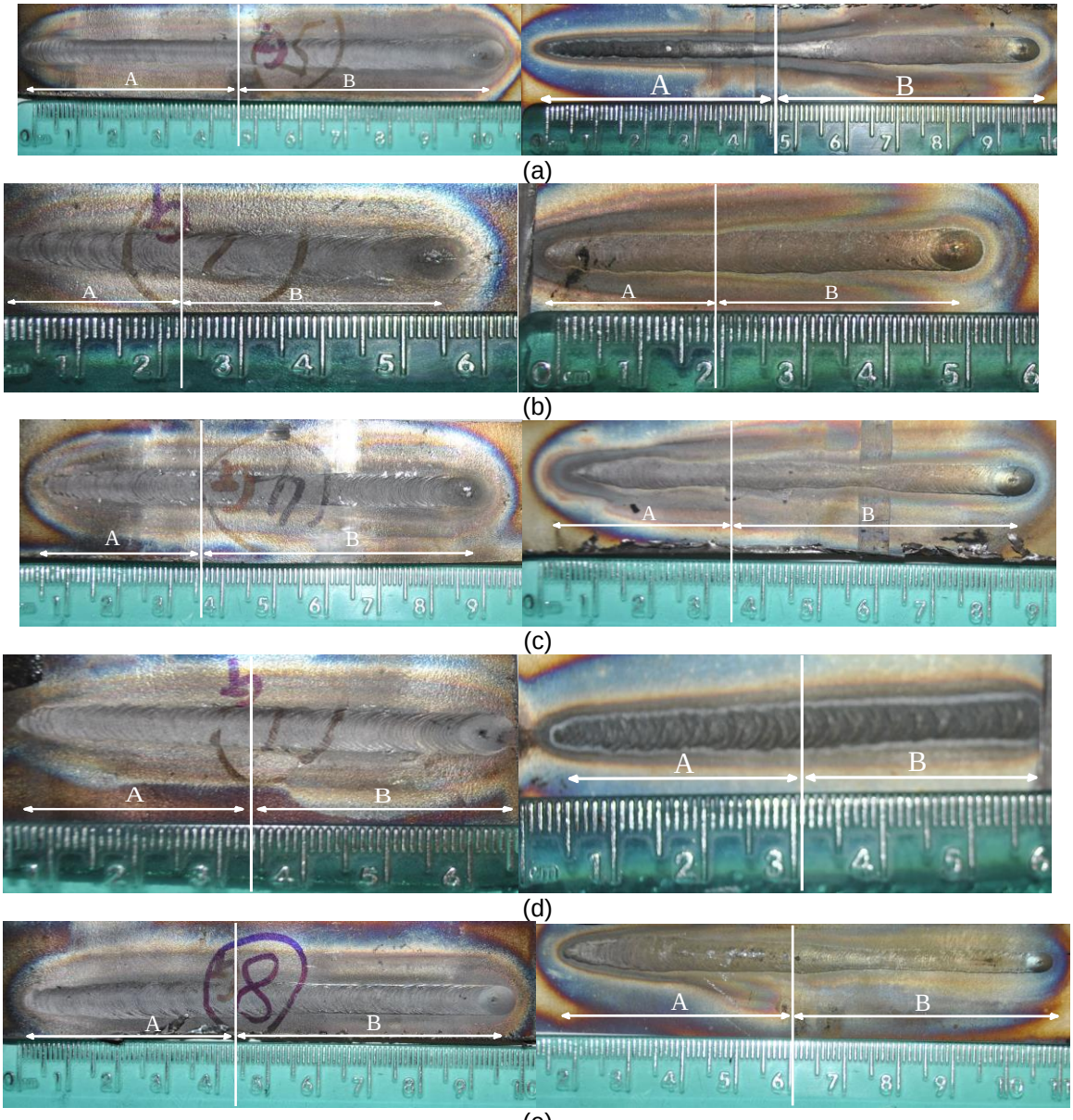

Figure 5.18 Front-side and backside weld bead from initial current experiments with initial current (a) 52A; (b) 54A; (c) 56A; (d) 58A; (e) 62A. Left: front-side weld bead, and right: back-side bead width. (The experiment in (c) is made without gas purging intentionally to examine the robustness of the response model against possible manufacturing conditions faults)

5.7.1 Robustness with initial current

Experiments with different initial welding currents are conducted in this subsection to test the robustness of the controller against different initial conditions. Five experiments are conducted, with initial current set to 52A, 54A, 56A, 58A and 62A. The arc length is set to 5mm and the welding speed is 1mm/s in all five experiments. The front-side and backside weld beads obtained are shown in Figure 5.18. The control inputs and real-time measured front-side weld pool characteristic parameters in these three experiments are

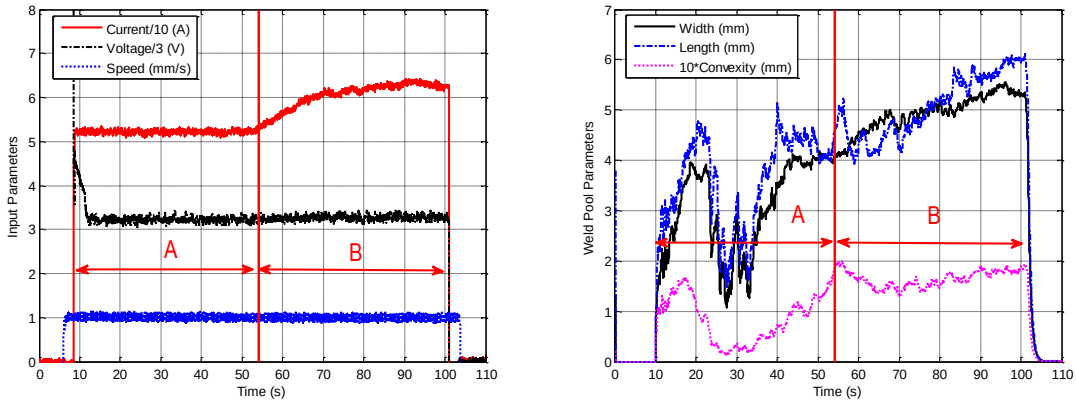

(a)

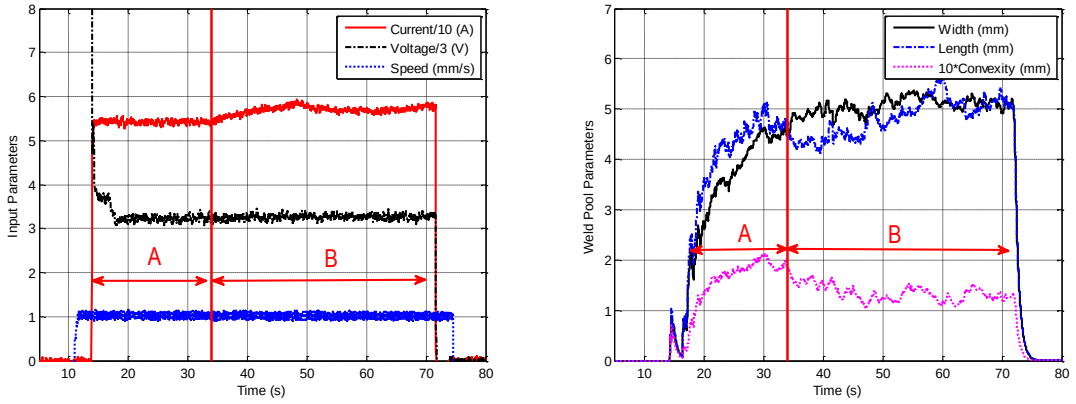

(b)

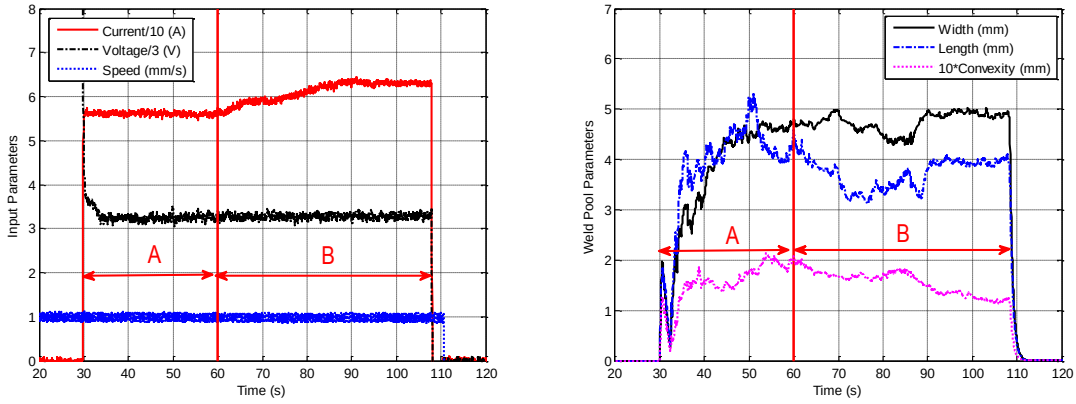

(c)

plotted in Figure 5.19. The off-line measured backside bead widths for five experiments are depicted in Figure 5.20. In these figures open-loop period and closed-loop period are identified as A and B. The vertical line indicates the start of the closed-loop control.

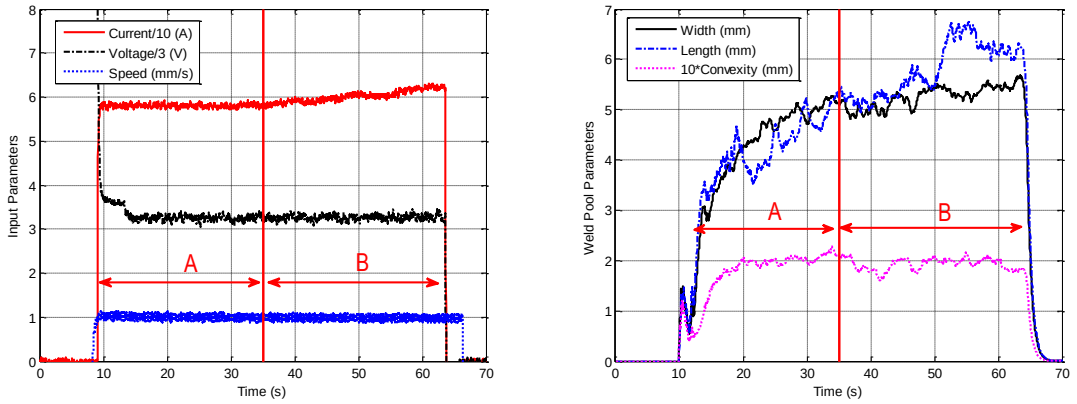

(d)

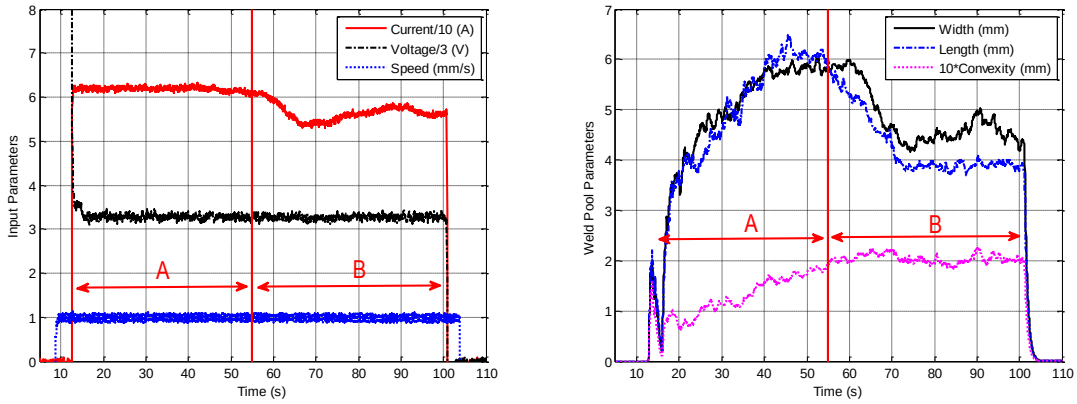

(e)

Figure 5.19 Control signals and weld pool characteristic parameters with different initial current (a) 52A; (b) 54A; (c) 56A; (d) 58A; (e) 62A. Left: control signals, and right: real-time measured front-side weld pool characteristic parameters.

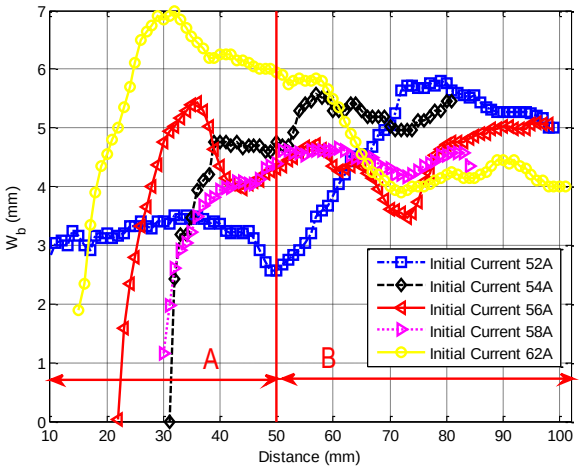

Figure 5.20 Offline measured back-side bead width for different initial current experiments.

As can be observed from Figure 5.20, the proposed intelligent human controller can drive the backside bead width to a desired value (i.e. about 5mm) despite the difference in initial current. The deviation of the backside bead width in these five experiments is about 1 mm, which is considered acceptable in our application. Compared to the novice human welder response model based controller in [75], the skilled human welder model can achieve shorter convergence/settling time.

Specifically, for the initial current 52A the back-side bead width at the end of the open-loop period is about 2.5 mm (see Figure 5.20), which is considered insufficient penetration in our application. The corresponding weld pool width, length, and convexity (see Figure 5.19(a)) are 4 mm, 4 mm, and 0.2 mm, respectively. Then the skilled human welder model is utilized to calculate the current adjustments applied to the system. The current reaches its steady-state (about 61 A) in 15 seconds. The front-side weld pool width, length, and convexity are about 5 mm, 5 mm, and 0.15 mm, respectively. The back-side bead width is controlled at about 5 mm. Similarly, for initial current 54A, 56A, 58A, and 62A, the proposed model is able to control the back-side bead width accordingly to achieve desired penetration. It is noticed that the steady-state current is slightly different in each experiments (61A for initial current 52A, 57A for initial current 54A, 60A for initial current 56A, 60A for initial current 58A, and 55A for initial current 62A). This is understandable because skilled human welder adjust the current based on his/her observation of the welding process. The back-side bead width controlled by the proposed model is about 5 mm with 1 mm deviation, which is considered acceptable in our application.

It is noticed in experiment 3 with initial current 56A, the controller is able to control the process to the desired penetration states with 59A after the closed-loop control starts (see Figure 5.19(c)). At 70 seconds, however, un-modeled welding process variation occurs. Accordingly, the back-side bead width is decreased from 4.6 mm to 3.6 mm. The corresponding front-side weld pool width, length, and convexity are decreased from 5 mm, 5 mm, and 0.2 mm to 4.5 mm, 3.5 mm, and 1.7 mm, respectively, indicating a smaller weld pool and insufficient penetration. The controller is able to increase the current to a new steady state (about 62A) in order to control the back-side bead width back to 5 mm. The controller's robustness against un-modeled process variations is demonstrated.

In experiment 4 with initial current 58A, the inner side of the pipe is not protected with the purging gas intentionally. It is observed from Figure 5.20 that the back-side bead width is controlled at about 4.5 mm, which is considered acceptable in our application. In other experiments the inner side of the pipe is well protected with purging gas. The robustness of the controller in achieving desired penetration with respect to different back-side protection conditions is thus verified.

5.7.2 Current Disturbance

In this subsection, the controller's robustness against current disturbance is investigated. The arc length and the welding speed are set at 5 mm and 1 mm/s, respectively. The experimental results are presented in Figure 5.21 to Figure 5.23. The process begins with an open-loop period of about 38 s (period A with initial current 52A), which brings the back-side bead width to about 3 mm. In the first 42 s after the open-loop period, no error exists between the calculated current and applied current. The skilled human welder model is able to control the back-side bead width to about 5 mm (see Figure 5.23) by increasing the current to about 62 A (see Figure 5.22). The corresponding front-side weld pool parameters are 4.8 mm, 4.8 mm, and 0.1 mm. In t = 103 s, the current disturbance is applied. The welding current is set at 50A, which is about 12A smaller than the calculated current. As the result, the weld pool width decreases to about 3.8 mm, the length first increases and then decreases to 4.2 mm, and the convexity increases from

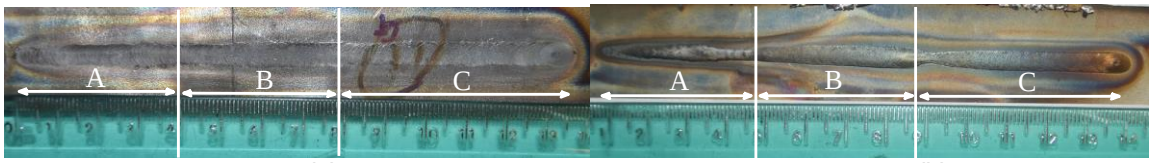

(a) (b)

Figure 5.21 Front-side and backside weld bead appearances for current disturbance experiment. (a) Front-side weld bead; (b) back-side weld bead.

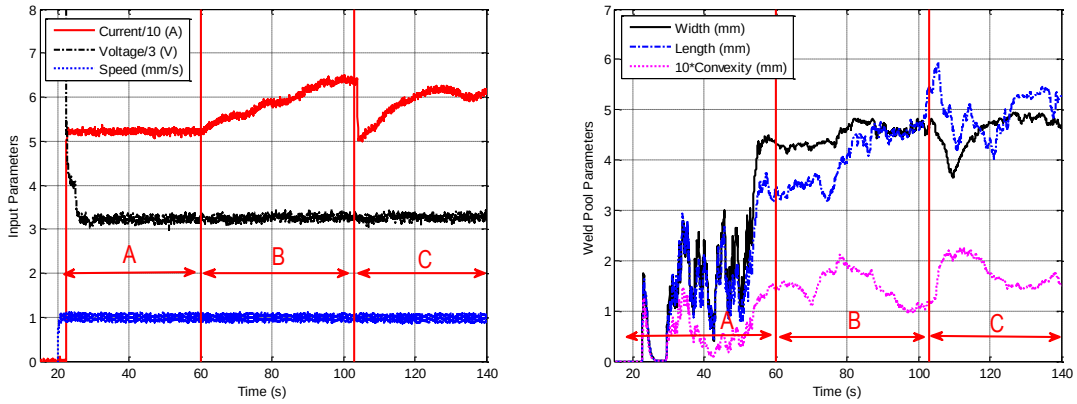

Figure 5.22 Control signals and weld pool characteristic parameters for current disturbance experiment. Left: control signals; Right: real-time measured front-side weld pool characteristic parameters.

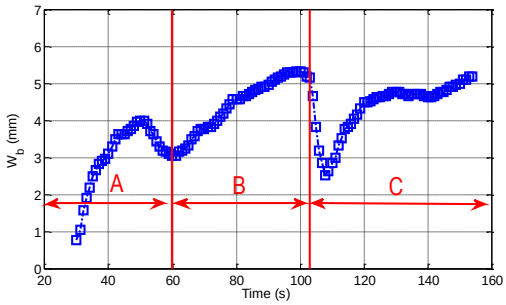

Figure 5.23 Offline measured back-side bead width for current disturbance experiment.

0.1 mm to 0.2 mm. The change in the front-side weld pool characteristic parameters indicates that the weld penetration becomes smaller. The skilled human welder model is able to adjust the welding current to about 61 A in an effect to compensate this artificial current disturbance (see Figure 5.22), and the back-side bead width can be maintained at around 5 mm. The controller's robustness against welding current disturbance is thus verified.

5.7.3 Arc Length Disturbance

Arc length is another welding process input which has impact on the weld pool geometrical appearance and penetration state. In this subsection the robustness of the proposed intelligent controller with arc length disturbance is examined.

In this experiment the initial arc length is 5mm and the initial welding current is 56 A.

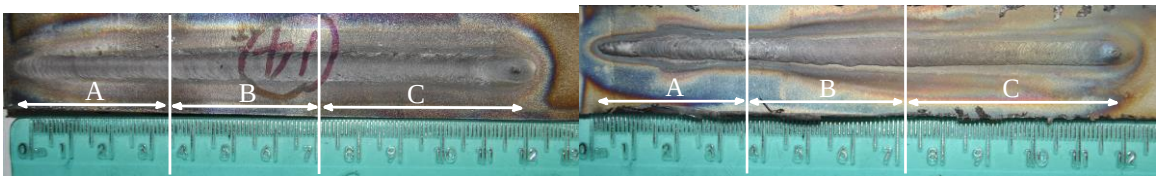

(a) (b)

Figure 5.24 Front-side and backside weld bead appearances for arc length disturbance experiment. (a) Front-side weld bead; (b) back-side weld bead.

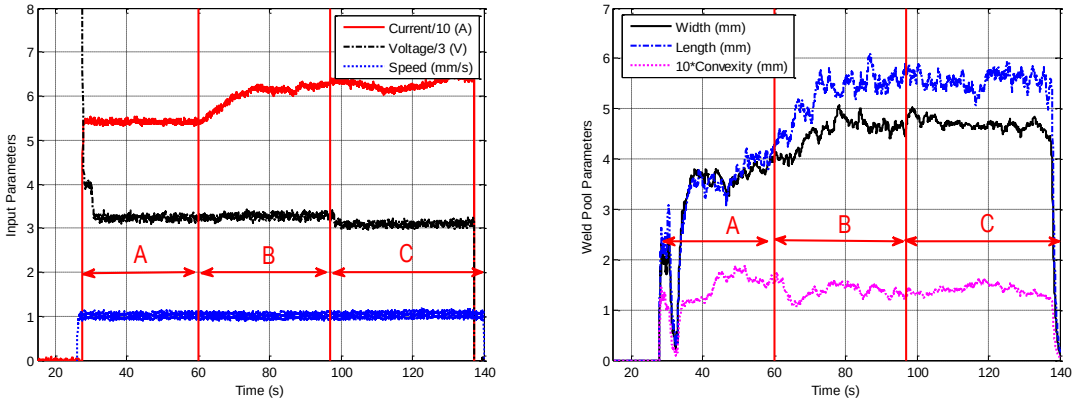

Figure 5.25 Control signals and weld pool characteristic parameters for arc length disturbance experiment. Left: control signals; Right: real-time measured front-side weld pool characteristic parameters.

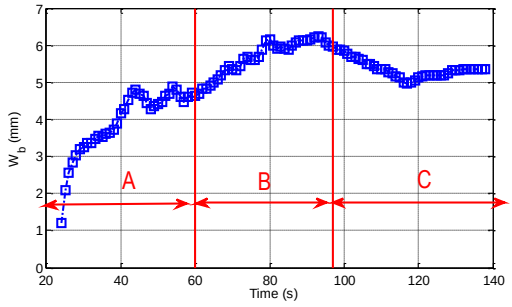

Figure 5.26 Offline measured back-side bead width for arc length disturbance experiment.

The open-loop period starts from 28 s to 60 s (marked by period A in Figure 5.25). At the end of the open-loop period, the front-side weld pool width, length, convexity are 4 mm, 4 mm, 0.15 mm, and the back-side bead width is 4.8 mm. Then the closed-loop control starts. The front-side weld pool width, length, convexity are controlled at 4.8 mm, 5.8 mm, 0.13 mm, and the back-side bead width is about 6 mm. At t= 96 s, the arc length changes to 3.5mm. As a result, the weld pool width immediately increases. If the current is unchanged (i.e., 62A in Figure 5.25), the penetration state will be increased and possible burn-through will occur. As can be observed in Figure 13, by decreasing the current, the closed-loop control system successfully eliminates the influence of the arc length variation and the resultant backside bead width is about 5 mm. The front-side weld pool width, length, and convexity are maintained at 4.8 mm, 5.5 mm, and 1.3 mm, respectively.

5.7.4 Welding Speed Disturbance

In arc welding, the welding speed is a major factor which influences the heat input into the process and has great impact on the weld penetration. In this experiment a step change of the welding speed is applied to examine the robustness of the controller over traveling speed variation. The experimental results are shown in Figure 5.27 to Figure 5.29. After an open-loop period (marked by A), controller is applied and the back-side bead width is increased from 3 mm (at the end of the open-loop period) to 5 mm. During the first 40 s of the closed-loop period (marked by B in these figures), the traveling speed is 1mm/s. Then the speed is changed to 1.1 mm/s in the second part of the closed-loop control (marked by C). As can be observed from Figure 5.28, the weld pool width and length immediately decreases, while the weld pool convexity increases due to the step change of the speed. This change in the weld pool characteristic parameters indicates a decrease in the weld penetration specified by the back-side bead width. The controller is able to increase the current according to this abrupt change in the weld pool and tries to maintain a constant full penetration. As can be seen in Figure 5.28, the current increases from 58 A (when the traveling speed is 1mm/s) to about 60A (when the traveling speed is 1.1 mm/s). As a result the backside bead width is adjusted back to about 4.5 mm.

It is noticed that despite various welding process disturbances, the skilled human welder response model is able to control the welding process within desired penetration state (5 mm with about 1 mm deviation). The robustness of the proposed intelligent controller is thus verified.

5.8 Summary

Analysis based on linear models for novice and skilled welders suggests that the skilled welder not only responds faster and more accurately but also makes use of more information from the weld pool. Further analysis based on nonlinear models reveals that

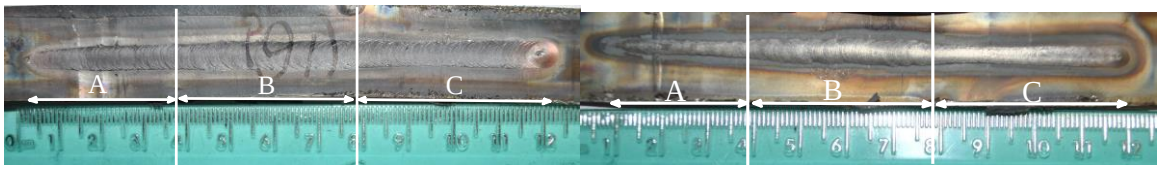

(a) (b)

Figure 5.27 Front-side and backside weld bead appearances for speed disturbance experiment. (a) Front-side weld bead; (b) back-side weld bead.

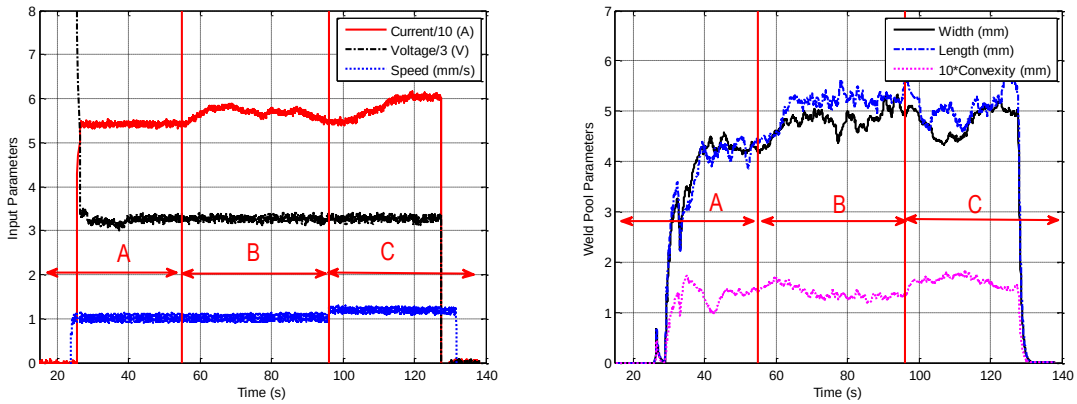

Figure 5.28 Control signals and weld pool characteristic parameters for welding speed disturbance experiment. Left: control signals; Right: real-time measured front-side weld pool characteristic parameters.

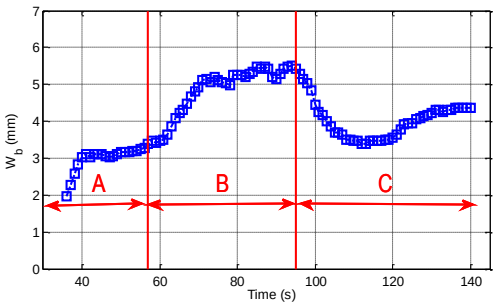

Figure 5.29 Offline measured back-side bead width for welding speed disturbance experiment.

in normal cases the skilled welder's adjustments are minimal to prevent large oscillation and overshoot novice welder model suffers, while in other cases where the convexity is either considerably small or large, the adjustment made by the skilled welder is larger than that of the novice welder, which can provide shorter settling time. The effectiveness and robustness of the proposed model based intelligent controller has been verified with different initial current and various welding process variations/disturbances, including the welding current, voltage, and welding speed disturbances. The skilled welder model obtained in this study performs better than that of the novice welder with faster convergence time, and no noticeable overshoot. A foundation is thus established to explore the mechanism and transformation of human welder's intelligence into robotic welding system.

Chapter 6 Virtualized Welding Platform and Teleoperation

From chapter 3 to chapter 5 both conventional welding process modeling and control as well as human intelligent learning based control are realized in an automated welding machine where the pipe rotates and the welding torch and the 3D weld pool sensing system remain stationary. A more common case in industrial pipe welding, however, is that the pipe stays stationary and the welding torch moves along the pipe. In this configuration, a welding robot is needed to move the welding torch along the pipe. For other more complex welding task, the welding robot also has greater potential and larger industrial impact than the conventional automated welding machines. From this chapter, we will focus on developing intelligent welding robots by learning human welder behaviors.

Robotic welding is often preferred for its outperformance over human welders who are subjected to physical limitations to maintain the needed consistence. Unfortunately, industrial welding robots are basically articulated arms with a pre-programmed set of movements, lacking the intelligence skilled human welders possess. They require precision prepared work pieces with little variation in geometry and material properties. Therefore their applications are mostly limited to assembly lines for mass-produced products, such as automobiles, where the work-piece preparation is controllable at reasonable costs. However, as outlined in the national robotic report [3], the trend of manufacturing is to produce customized products in small batches, where ideal automated production lines are not cost effective. As such, intelligent welding robots that possess intelligence comparable to skilled welders but with less physical restrictions and can work in harsh environment will be one of the keys to maintaining a competitive manufacturing industry despite relatively high labor costs/wages. The resultant intelligent welding robots may also help resolve the skilled welder shortage issue the manufacturing industry is currently facing [2].

This chapter aims to present a virtualized welding system that enables learning from human welder intelligence for transferring into a welding robot [123]. In particular, a 6-DOF UR-5 industrial robot arm equipped with sensors observes the welding process and performs actual welding. Human welder operates a virtualized welding torch to adjust the welding speed based on the visual feedback from the sensors and the motion of the virtualized torch is recorded and tracked by the robot arm. Nine such teleoperated welding experiments are conducted on pipe using GTAW under different welding currents to correlate the welding speed to the welding current. Robotic welding experiments, with the robot travel speed determined per the given welding current from the resultant correlation, verified that for top part of the pipe between 11 to 1 o'clock,

adjusting welding speed per the current used is adequate to generate acceptable welds. The obtained correlation between the welding speed and welding current could be used in human-machine cooperative control. It may also provide a constraint for automated welding process control. A foundation is thus established to utilizing the human intelligence and transferring it to welding robots.

6.1 Teleoperation System Overview

The proposed teleoperation system is illustrated in Figure 6.1. In this figure two stations referred to as virtual station and welding station are illustrated. In the virtual station a

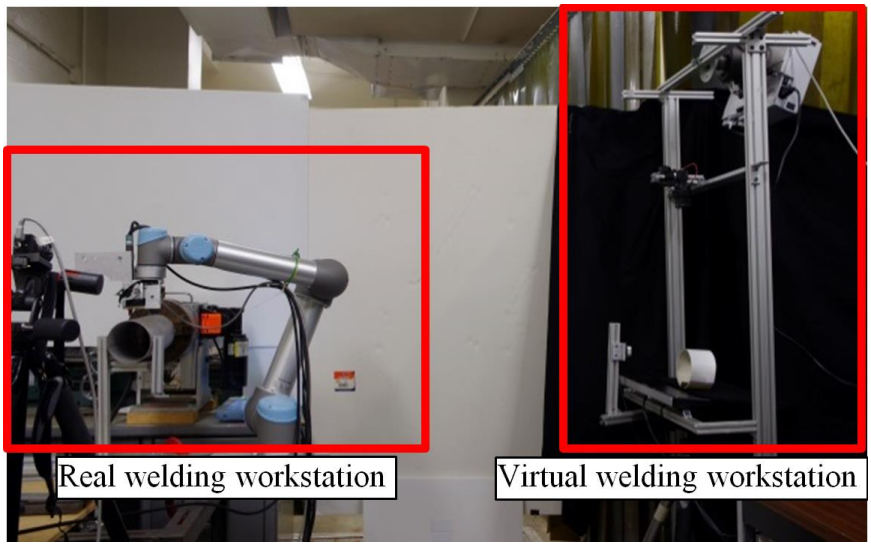

Figure 6.1 General view of the virtualized welding system. The system consists of real welding workstation and virtual welding workstation. Data communication between these two workstations is through Ethernet.

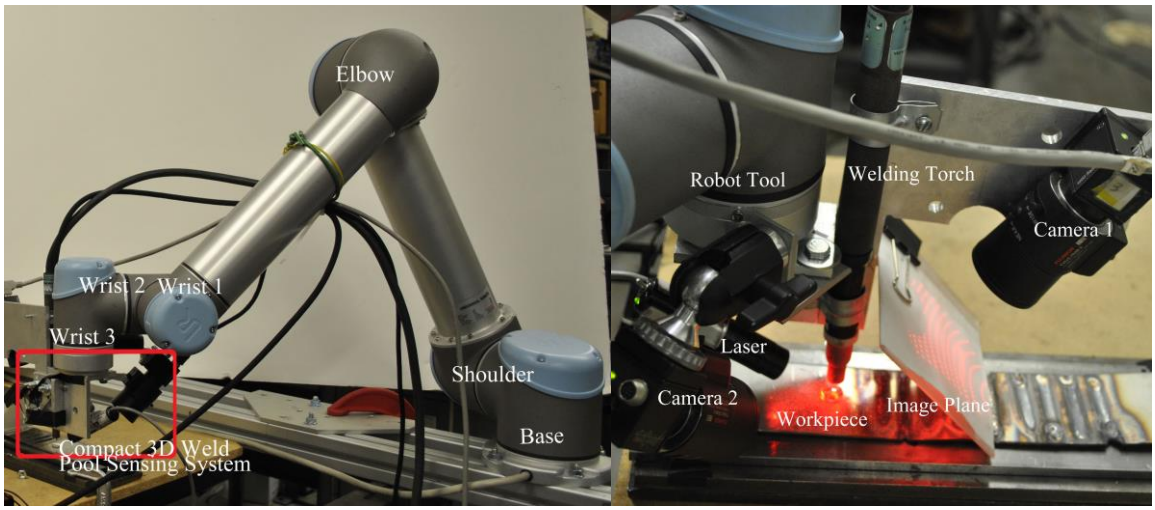

(a) (b)

Figure 6.2 UR-5 robot arm and sensing system (a) UR-5 robot arm with compact 3D weld pool surface sensing system attached to the robot tool (b) Detailed view of the compact sensing system.

TABLE 6.1 IMAGING PARAMETERS

Monitoring Parameters			
Laser projection angle / degree	Laser to weld pool distance / mm	Imaging plane to weld pool distance / mm	Imaging plane angle / degree
31.5	24.7	101	45

Camera Parameters			
Shutter speed/ms	Frame rate/fps	Camera to imaging plane distance/mm	Camera to imaging plane angle / degree
4	10	57.8	85

human welder can view the monitor where the work-piece geometry (from direct viewing or eyeview camera) and reconstructed 3D weld pool surface are displayed, and moves the virtual welding gun accordingly as if he/she is right in front of the work-piece. The human welder movement is accurately captured by a Leap sensor, and the obtained 3D coordinates will be sent to the PC. The PC also receives images captured by the eyeview camera and 3D weld pool surface sensing system and displays the image as well as the reconstructed weld pool onto the monitor. The robot arm equipped with the welding torch receives commands via Ethernet from the PC including the next pose (robot tool 3D position and orientation), and robot tool movement speed. It then executes the command and sends the current robot tool position back to the PC. In the following two subsections, the 6 DOF robot and compact 3D weld pool surface sensing system are introduced. A spherical convex mirror is reconstructed to illustrate the effectiveness of the proposed compact sensor.

6.1.1 Welding Station

The robot utilized in this study is Universal Robot UR-5 with six Degree of Freedom (DOF). UR-5 industrial robot is a six-jointed robot arm with a low weight of 18 kilos, lifting ability of 5 kilos, and working radius of 85 cm, respectively. The accuracy of the robot's repetitions is 0.1 mm.

Figure 6.2 (a) depicts the UR-5 robot with the weld pool surface sensing system. The joints of the robot shown in Figure 6.2 (a) are named as base, shoulder, elbow, wrist 1, wrist 2, and wrist 3. The joints can rotate between -360 ºto 360 º.The base of the robot is mounted on a fixed working station and the 3D weld pool surface sensing system (shown in Figure 6.2 (b)) is attached to the end of wrist 3 (robot tool).

The robot is connected to a controller which is used to control the motions of the robot. There is a touch pad user interface that allows the user to program, control and move the robot. The robot can also be programmed using URScript, a script language developed by the robot manufacturer. The robot (client) and PC (server) is communicated via Ethernet using TCP/IP protocol and socket programming. It is noticed that the system telecommunication delay caused by sending and receiving packages between the robot

and PC is smaller than 20ms most of the time. Thus, the system telecommunication delay can be safely neglected in our system.

Figure 6.2 (b) shows the developed compact 3D weld pool surface sensing system for our robotic welding system. In this system a low power laser (19 by 19 structure light pattern) is projected to the weld pool surface and its reflection from the specular weld pool surface is intercepted and imaged by a CCD camera (Camera 1 in Figure 2 (b)). It is

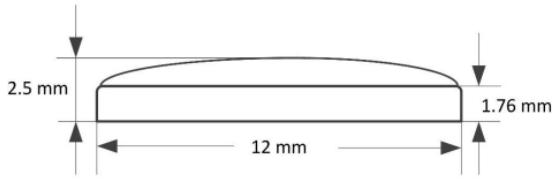

Figure 6.3 The convex spherical mirror. Its nominal radius is 12 mm, the nominal edge thickness is 1.76 mm, and nominal center thickness is 2.5 mm.

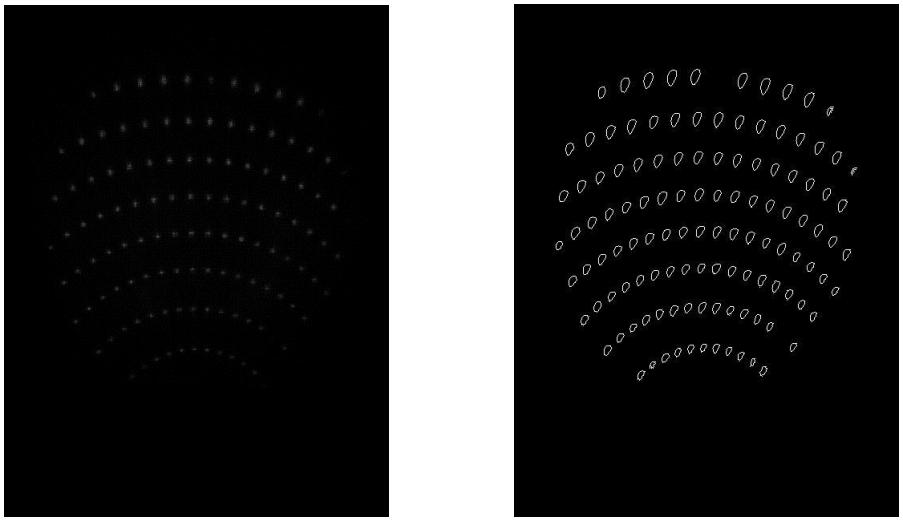

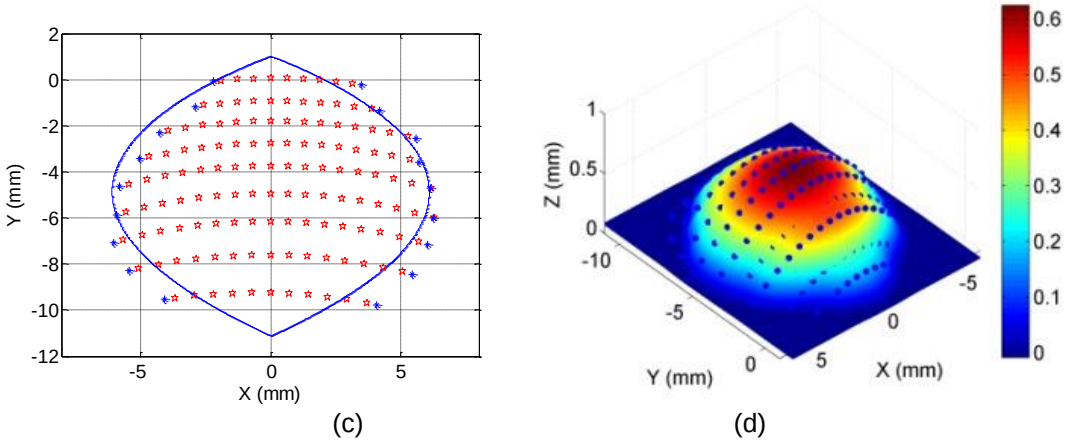

Figure 6.4 Results of spherical convex mirror reconstruction. (a) Original image (b) Processed image (c) Obtained boundary and reflection points (d) Reconstructed 3D surface.

known that arc light is an omni-directional light source. Its intensity decreases quadratically with the distance traveled, but the laser, due to its coherent nature, does not significantly lose its intensity. Hence, it is possible to intercept the reflection of the illumination laser from the weld pool surface with an imaging plane placed at an appropriate distance from the arc. From the distorted reflection pattern on the imaging plane and the assumption of a smooth weld pool surface, the 3D shape of the weld pool surface can be obtained. By using specific image processing and reconstruction algorithm [55], 3D specular weld pool can be reconstructed in real-time. The transmission and processing time of the image processing is about 60ms. The computer program captures the image at a frame rate of 10 Hz, processes the image, reconstructs the weld pool, and sends the calculated robot speed / coordinates to the robot. The whole system operates at a frame rate of 10 Hz, which is considered real-time in our application. In addition, camera 2 (in Figure 6.2 (b)) can provide an eyeview similar to what welders can see during the welding process.

To verify the effectiveness and accuracy of the compact 3D weld pool surface sensing system, a spherical convex mirror with known geometry (Edmund Optics NT64-057) is used as a benchmark. The geometry of the convex spherical mirror is shown in Figure 6.3. The diameter and the nominal height of the mirror are 5.6mm and 0.74mm, respectively. Note that the diameter (5.6mm) is actually smaller than its nominal diameter (6mm) because the chamfer angle on the edge of the mirror surface is not specular.

Imaging parameters used in this verification experiment are given in Table 6.1. Figure 6.4 illustrates the mirror surface reconstruction results. Figure 6.4 (a) is the original image obtained in camera 1 (after calibration), and Figure 6.4 (b) shows the image processed based on the image processing algorithm specified in [55]. Fitted boundary points and calculated reflection points are shown in Figure 6.4 (c), and the reconstructed 3D weld pool surface is depicted in Figure 6.4 (d). It is observed that most of the height errors are within 0.06mm, especially in the central range of the weld pool. Relatively large height errors do exist close to the boundary of the weld pool. Note that this error might be caused from image processing, welding machine, data acquisition process, and calibration errors of experimental set-up. However, the accuracy of the system is still considered sufficient for our application.

The reconstruction of the convex mirror illustrates the accuracy of the 3D weld pool surface sensing system, which will then be used to reconstruct the weld pool surface in real-time.

6.1.2 Virtual Station

The visualization system [123] employs a computer screen for displaying the rendered visual information from eye view camera over the flat work piece (Figure 6.5). If the

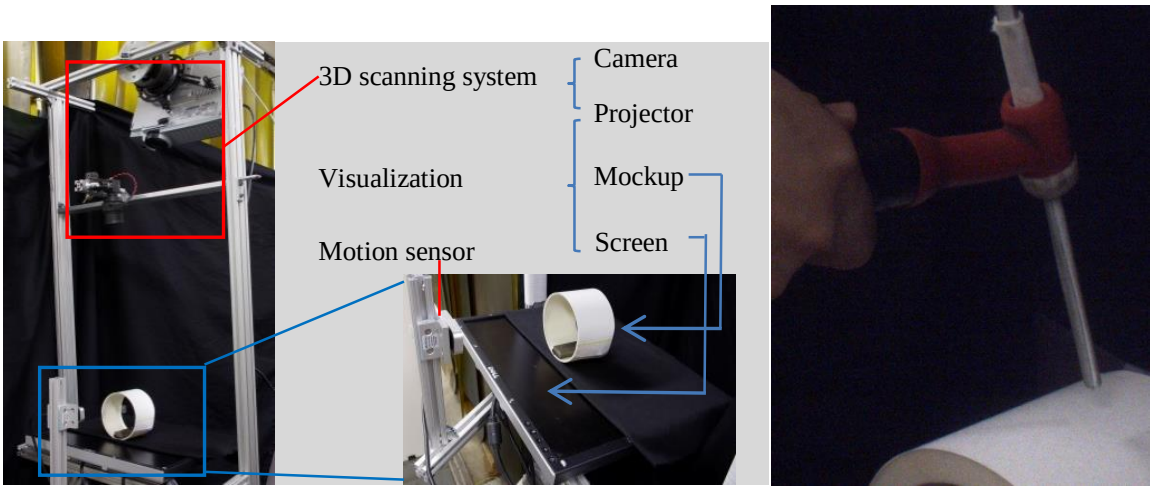

(a) (b)

Figure 6.5 (a) Detailed view of the virtual station. Major components in this station include a Leap motion tracking sensor, a mock up pipe, a computer screen, a high resolution camera and a projector. (b) Virtual welding torch.

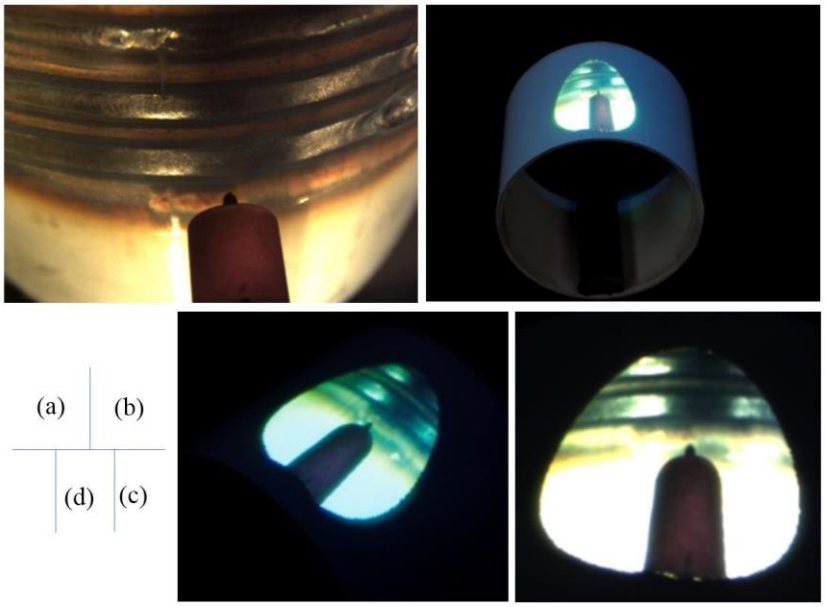

Figure 6.6 Visualization of the pipe. (a) eye view of the work piece. (b) virtual view of the mock-up. Image from eye view camera has been visualized on the mock-up. (c) close-up view. (d) view the mock-up at different point of view.

work piece is a 3D shaped object (e.g., pipe), the visualization system employs a mock up pipe with the same dimensions as actual pipe and projects rendered video on its surface. The 3D scanning system consists of a high resolution camera and a projector. By utilizing the structured light scan algorithm with subpixel refinement for reconstructing geometry of 3D object, this system can provide high accuracy point cloud and mesh of the mock up [123]. Figure 6.5(b) shows the virtual welding torch. Figure 6.6 shows the visualization of the pipe. Both eye view of the work piece (Figure 6.6(a)) and virtual view of the

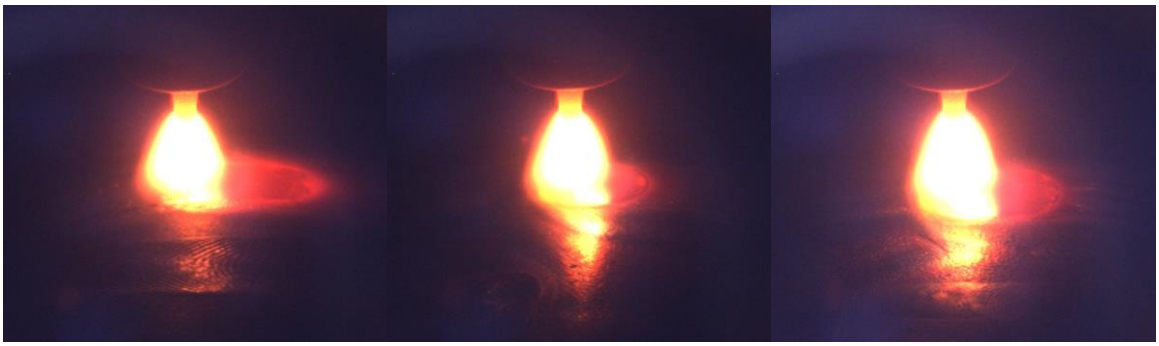

(a) (b) (c)

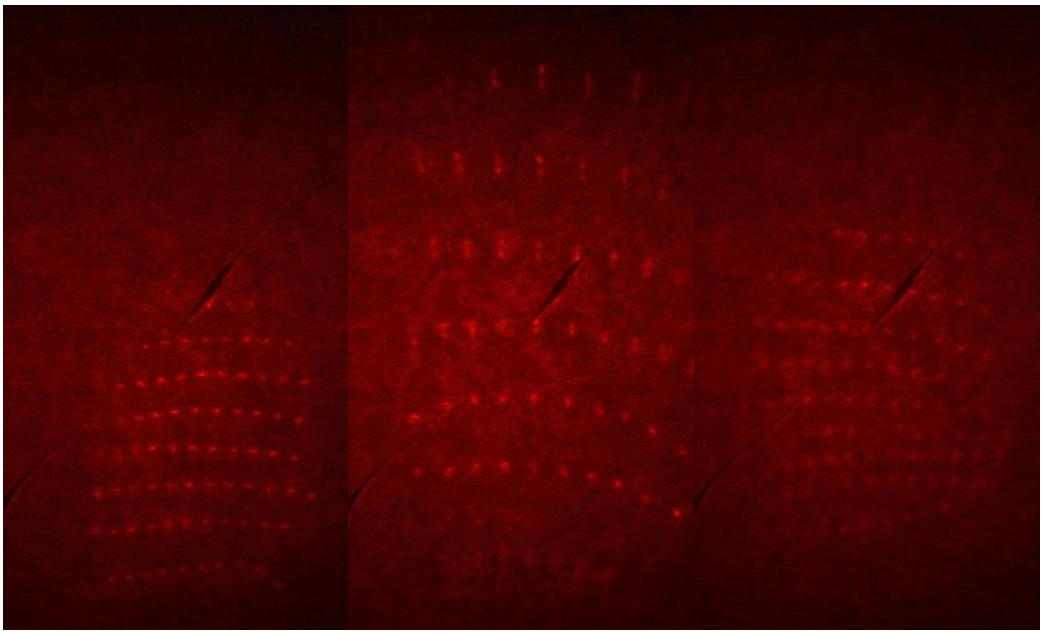

(d) (e) (f)

Figure 6.7 (a)-(c) Sample images from Camera 2 (eye view) with welding current 45 A, 50 A, and 55 A, respectively. (d)-(f) Corresponding images from Camera 1 (structured light laser dots which will then be used for 3D weld pool reconstruction) corresponding to (a)-(c).

mock-up (together with visualized eye view image) are presented. It will be shown that the proposed system is able to conduct virtual welding experiments whose data will then be recorded and utilized to form a welder response model.

6.2 Experimentation

Nine teleoperated experiments are conducted in this section and the experimental results are presented/ analyzed. Stainless steel pipe is welded using the direct current electrode negative GTAW process. The material of the pipe is stainless steel 304. The outer diameter and wall thickness of the pipe are 113.5 and 2.03 mm, respectively. The welding parameters are illustrated in Table 6.2. The welding current is selected as one of the three typical values representing small, medium, and large welding current (45 A, 50 A, and 55 A), and the arc length is maintained at 4 mm. The human welder observes the virtualized

TABLE 6.2 WELDING PARAMETERS

Current / A	Welding speed / (mm/s)	Arc length / mm	Argon flow rate / (L/min)
45, 50, 55	---	4	11.8

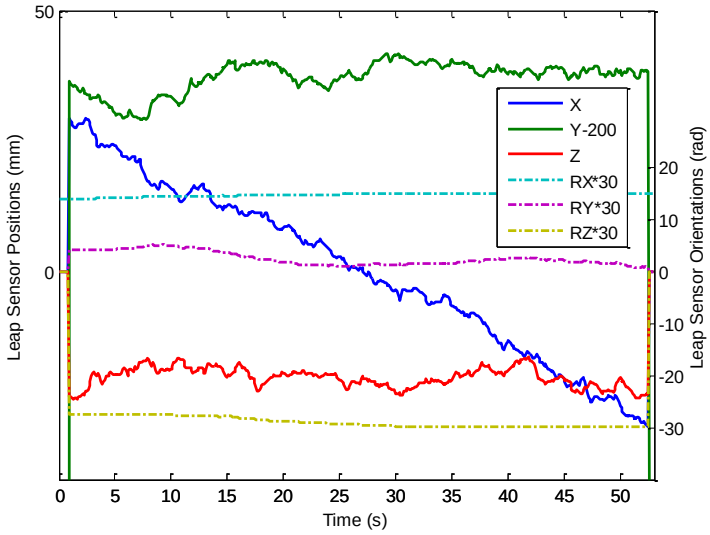

Figure 6.8 Human hand movement captured by Leap motion sensor in a sample experiment.

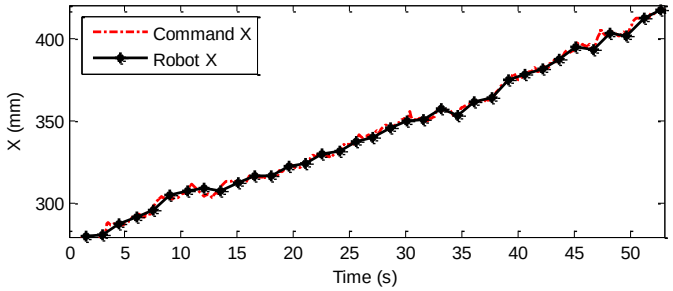

Figure 6.9 Tracking performance along welding direction (x axis) for human hand movement in Figure 6.7.

weld pool rendered on the mock-up pipe and control the virtual welding torch movement (i.e., welding speed) accordingly.

Figure 6.7 depicts sample images captured in these welding experiments, with the welding current being 45 A, 50 A, and 55 A, respectively. Figure 6.7(a)-(c) are the images captured by Camera 2 (i.e., eye view). As can be observed, different welding currents and welding speeds generate different weld pool shapes. The welder can thus observe the weld pool, and move the virtual welding torch accordingly based on this visual feedback. It is noted that images from the eye view camera are only for human welder to view and control the welding process. For automated welding task, however, eye view images can only be used to get 2D information from the weld pool (weld pool width and length). 3D weld pool geometry is relatively difficult to be extracted from these images. Instead, images from Camera 1 (in Figure 6.4 (b)) will be utilized to

reconstruct 3D weld pool shape using specific image processing and reconstruction algorithm [55]. Figure 6.7(d)-(f) are the images from Camera 1 (structured light laser reflection dots). It is observed that different weld pool shapes (shown in Figure 6.7(a)-(c)) generate different laser reflection patterns, and these patterns contain 3D shape information which can then be used for reconstruction.

Figure 6.8 illustrates welder's hand movement captured by the Leap motion sensor in a sample experiments. It is noticed that the welder moves the virtual welding torch along the welding direction (x axis). For y axis movement (perpendicular to the welding direction), the coordinates are near 240 mm most of the time. However, deviations are frequently observed. In our study which is pipe welding along a circular straight line around pipe circumference, the movement along y axis is not necessary and should be considered as noise. For other applications where y axis movement is necessary, y axis can also be tracked. In automated pipe welding with no filler metal, the welding torch should always be perpendicular to the workpiece. Once the x axis movement is accurately tracked, the movement along z axis and x, y, z orientations can thus be properly determined. It will be shown in section V that satisfactory welds can be obtained for welding top part of the pipe. For full position pipe welding, however, this is not the case. In positions other than top part of the pipe, certain angle between the welding torch and pipe surface may be required to provide additional control on the arc pressure acting on the weld pool against gravitational force [123]. Future study will focus on full position pipe welding where the torch orientation will also be tracked, learned and adjusted.

Figure 6.9 shows the tracking performance in x direction. It is observed that using the proposed predictive control algorithm in [124], the robot can track the human movement with sufficient accuracy.

6.3 Data Processing

Nine teleoperated experiments are conducted by a human welder. In experiments 1 to 3, the welding current is set at 45 A. In experiments 4 to 6, the welding current is set at 50 A. In experiments 7 to 9, the welding current is set at 55 A. Other welding parameters are the same as those specified in Table 6.1. Figure 6.10 presents the x position data in nine experiments. Generally, for relatively larger welding current (55 A), the human welder moves the torch with larger speeds (or finishes welding with less time, in about 45 s to 50 s). For medium welding current (50 A), the human welder uses medium movement speeds throughout the experiments and finishes the welding task in about 60 s. For small welding current (45 A), the welder uses small welding speed, and finishes the welding tasks in about 70 s to 90 s. It is noticed, however, that speed variations occur in these experiments for the same welding current. This is understandable because the human welder determines his/her movement based on his observation of the weld pool. However,

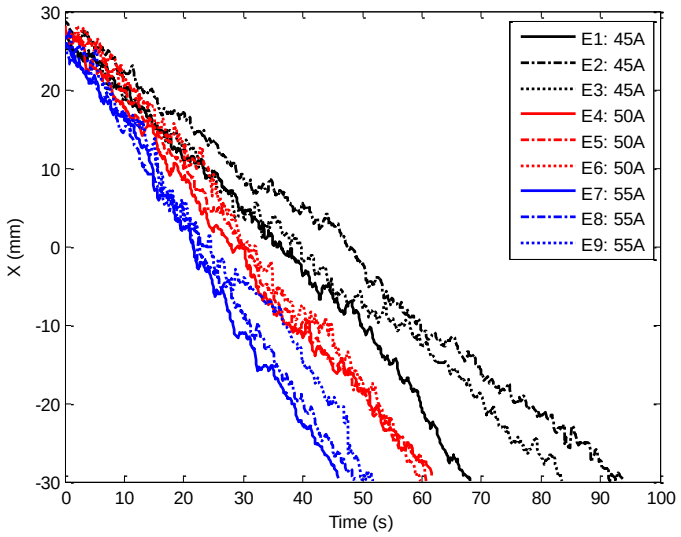

Figure 6.10 Nine welding experiments with different welding current.

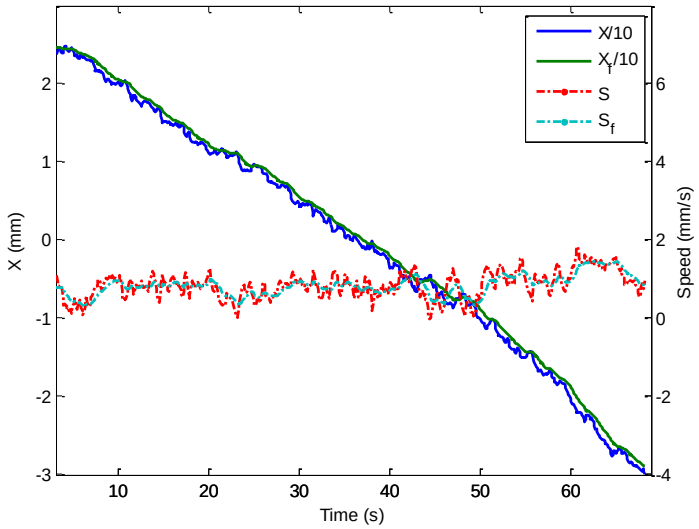

Figure 6.11 Comparison between before and after filtering (x position and welding speed) in experiment 4.

trends of the welding speed with respect to the welding current can be easily observed. In the next subsection, these data will be utilized to learn the human movement.

It is observed in Figure 6.10 that human hand movement contains high frequency movement and needs to be filtered before learning. A low pass filter is designed as follows

$$\begin{cases} D_{xf,k} = \alpha D_{xf,k-1} + (1-\alpha) D_{x,k} \\ S_{xf,k} = (D_{xf,k} - D_{xf,k}) / T_s \end{cases} \tag{6.1}$$

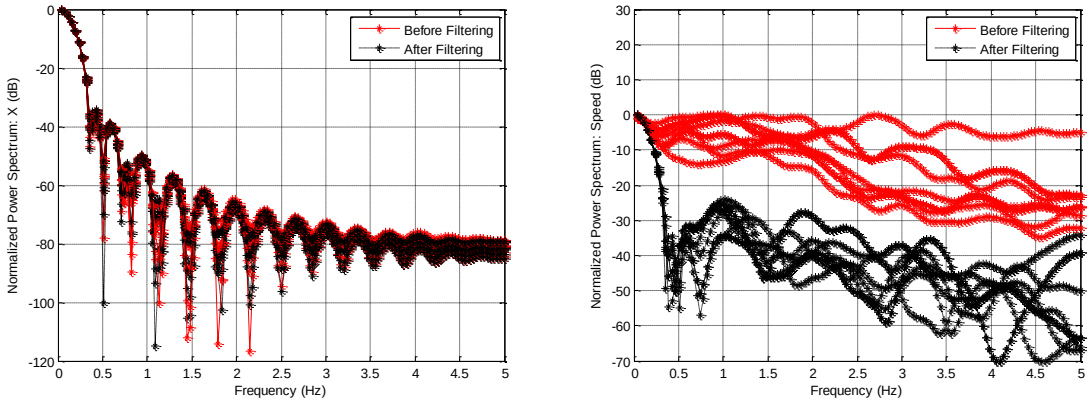

(a) (b)

Figure 6.12 Normalized power spectrum before and after filtering in nine welding experiments (a) x position (b) welding speed.

where $D_{x,k}$ is x position coordinate before filtering at instant k, $D_{xf,k}$ and $D_{xf,k-1}$ are filtered x position coordinates at instant k and k-1, respectively. $S_{xf,k}$ is the filtered speed along x axis, and T_s is sampling time (0.5 s). $\alpha \in (0,1)$ is the smoothing coefficient. As α becomes larger, the position deviates from the actual human movement but with better robustness and smoothness. It is observed that α=0.9 can achieve a good tradeoff between tracking human movement and smoothness. Figure 6.11 shows the filtered position and speed in experiment 4. It is observed that the filter is able to smooth the position and speed signal. Large oscillations in the speed are sufficiently depressed.

To further understand the filter effect, frequency domain analysis is presented. Figure 6.12 shows the normalized power spectrum for x position and movement speed in nine experiments. For position signal, the majority of the signal power is centered below 1 Hz (i.e., the majority of the energy for position response is below 1Hz). This makes sense because the human welder adjustment should be slow given the relative slow GTAW process. No noticeable differences are observed by applying the low-pass filter. For movement speed, on the other hand, the normalized signal power has been sufficiently suppressed for frequency larger than 0.5 Hz. This is expected because large high frequency movement corresponds to the tremor of the human hand and thus should be suppressed. It is observed that the proposed filter is able to suppress the high frequency movement that might degrade the welding performance.

Because the smoothness of the human hand movement varies from person to person, it is evident that different welders should have different smoothing coefficients. To obtain the smoothing coefficient for a specific operator, a training period can be conducted and process described in this section can be applied accordingly.

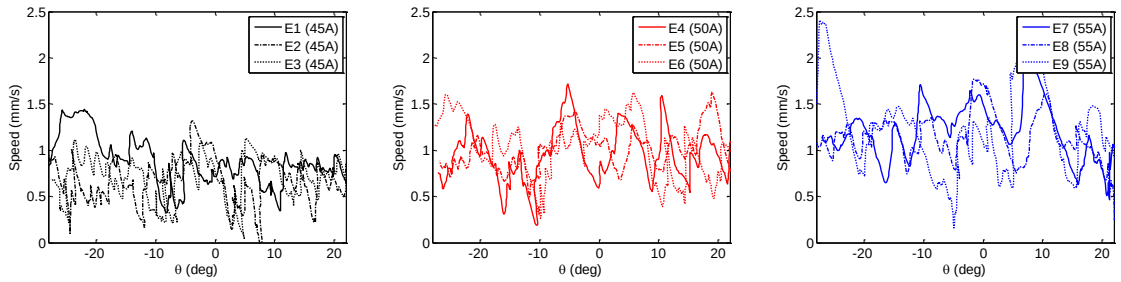

Figure 6.13 Calculated welding speed in nine experiments.

6.4 Learning Result and Analysis

Figure 6.13 depicts the welding speeds in nine experiments versus the torch orientation angle θ (0 degree corresponds to 12 o'clock) in relation to the gravitational direction. It is noticed that the average welding speed corresponding to different degree is fluctuating for all the three welding currents. However, no noticeable correlation is found between the fluctuations of the welding speed to the position of the torch. It will be further proved in the welding experiments that a constant welding speed is sufficient to produce satisfactory welds in the top part of the pipe, i.e., $-25° \leq \theta \leq 25°$ (approximately 11 o'clock to 1 o'clock). For full position pipe welding, however, different speeds should be applied for different positions and will be studied in the future using an advanced system whose projector and Leap sensor must move with the torch movement.

The data points to be used to correlate the welding current and welding speed are plotted in Figure 6.14. A linear model is fitted using least squares algorithm [123]:

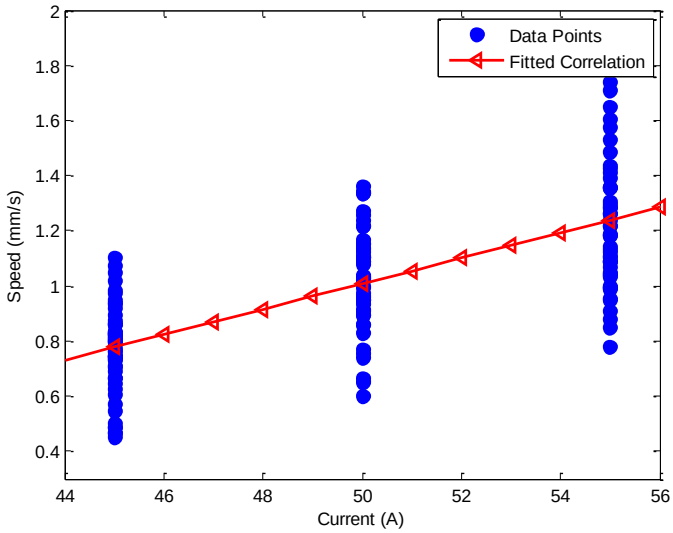

Figure 6.14 Data points and linear fitting result.

$$s = 0.0462I - 1.3 \tag{6.2}$$

or equivalently,

$$I = 10.13s + 39.77 \tag{6.3}$$

where s is the welding speed in mm/s and I is the welding current in A.

The above correlation between the welding current and welding speed can be used for human-machine cooperative teleoperated pipe welding applications where a unskilled human welder operates the torch (thus determining the actual welding speed) while the welding machine could compensate his/her inaccurate movement (inaccurate welding speed) by adjusting the welding current. It could also be used to provide a parameter interval for simultaneously controlling the front-side weld pool surface characteristic parameters and back-side joint penetration in automated welding. This learned correlation will then be applied in welding experiments to demonstrate the effectiveness of the learned welding speed from the human welder.

6.5 Automated Welding Experiment

Automated welding experiments using learned welding speeds are conducted and the experimental results are presented/ analyzed. The welding parameters are the same as those listed in Table I. Three welding experiments are conducted with the welding current set at 45 A, 50 A, 55 A, respectively, and the arc length maintained at 4 mm. It is observed from Figure 15 that by applying learned welding speed satisfactory welds are obtained. Consistent back-side weld bead widths are obtained in all three experiments. For welding current being 45 A, the back-side bead width is maintained at about 3.5 mm for all positions (from -25 degree to 25 degree). Similarly, for welding currents being 50 A and 55 A, back-side bead widths are properly maintained at about 3.7 mm and 3.6 mm.

To further demonstrate the proposed model in generating satisfactory welds under varying welding currents, welding experiment is conducted by varying welding current during an experiment, from 48 A to 53 A then to 45 A, and the welding speed calculated by Equation (2) is sent to the welding robot. The obtained weld is shown in Figure 6.16. It is observed that acceptable weld is obtained. Specifically, welding current 48 A is firstly applied for 20 s (seen in Figure 6.17). The calculated welding speed is 0.918 mm/s and the obtained back-side bead width is about 3.8 mm. Then the welding current increased to 55 A and last for 20 s. By increasing the welding speed to about 1.15 mm/s, nearly consistent back side bead width is achieved. Finally the welding current is set to 45 A for 20 s and the calculated welding speed is 0.78 mm/s. The back-side bead width is well maintained to about 3.9 mm.

It is thus concluded that by controlling the welding speed, satisfactory welds can be achieved, given the other welding parameters are maintained at their nominal values. If these welding parameters deviate from their nominal values, controlling the welding speed might not be sufficient to produce satisfactory welds. However, the learned welding speeds for different welding currents can provide an additional constraint in designing controller for the welding process. The 3D weld pool shape will be correlated to the welder's movement, and an adaptive control scheme will be developed to cope with complex variations in the process parameters in the next few chapters.

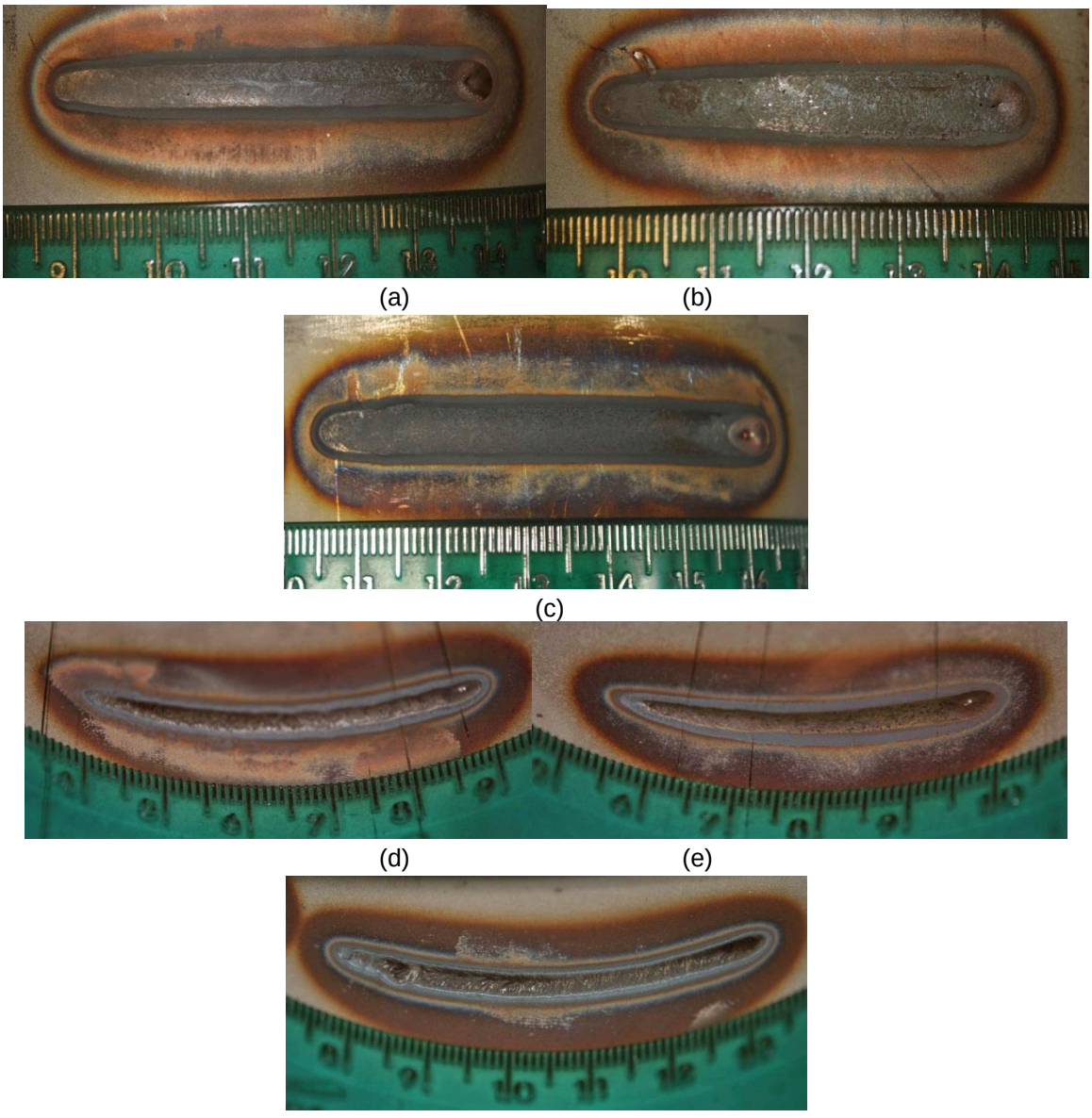

(a) (b) (c) (d) (e) (f)

Figure 6.15 Automated welding experiments result using different welding currents. (a)(d) front and back view of the welds for welding current 45 A (b)(e) front and back view of the welds for welding current 50 A (c)(f) front and back view of the welds for welding current 55 A.

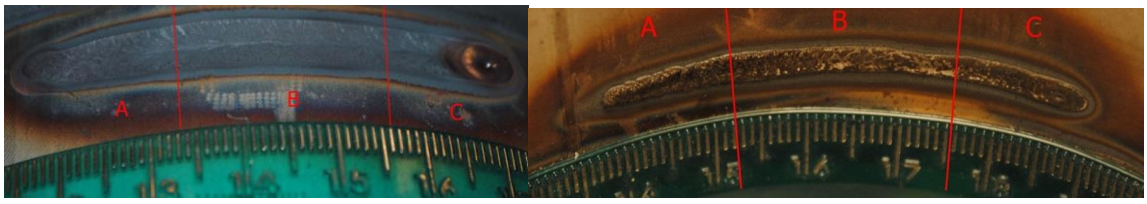

(a) (b)

Figure 6.16 Automated welding experiments result using varying welding currents from 48 A to 53 A to 45 A.

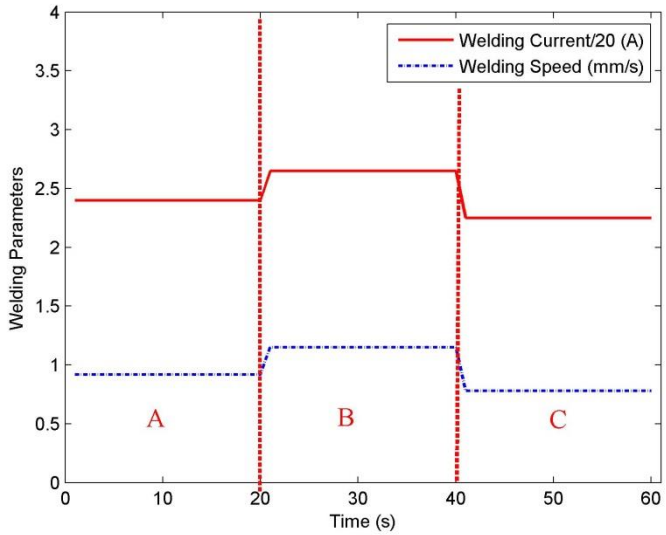

Figure 6.17 Welding current and speed in Figure 6.16.

6.6 Summary

This chapter utilizes a new human machine welding paradigm, virtualized welding, to learn human welder's speed adjustment under different welding currents. Learning experiments through teleoperation are conducted by a human welder to generate satisfactory welds under different welding currents. A correlation between the welding current and welding speed is proposed for GTAW pipe welding with specified welding conditions. Consistent penetration and satisfactory welds are generated in automated welding experiments. It is also observed that for top part of the pipe welding, instead of manipulating a full set of welding parameters (including torch orientation and arc length, etc.), adjusting welding speed is sufficient to generate satisfactory welds.

Chapter 7 Learning Human Welder Movement with Virtual Reality Enhancement

Combining human welder (with intelligence and versatility) and automated welding systems (with precision and consistency) can lead to intelligent welding systems. This chapter aims to present a data-driven approach to model human welder intelligence with Virtual Reality (VR) enhancement and use the resultant model to control automated GTAW process.

Section 7.2 aims at accurate control of human arm movement. In particular, an innovative teleoperated virtualized welding platform, in which the welder is visually instructed to adjust the welding speed and his movement is followed by a robot arm, is utilized to conduct dynamic experiments in order to correlate the human welder arm movement to the visual signal input. Static responses reveal that the human welder's response to the input signal is nonlinear and time-varying. Linear model is firstly identified and an ANFIS model is then proposed to improve the model accuracy. To account for the welder's time-varying responses, an adaptive ANFIS model is finally used to model the intrinsic nonlinear and time-varying characteristic of the human welder response. An adaptive nonlinear ANFIS model-based predictive control algorithm is then proposed to control the human arm movement. Assuming the controller inputs are not significantly changed, the optimization becomes linear and an analytical solution is derived. To further demonstrate the controller's performance, human control experiments are conducted. Results verified that the proposed controller is able to track varying set-point under measurement and input disturbances.

To learn human welder response with the virtual reality enhancement, an innovative machine-human cooperative virtualized welding platform is teleoperated to conduct training experiments: the welding current is randomly changed to generate fluctuating weld pool surface and the human welder tries to adjust his arm movement (welding speed) based on his observation on the real-time weld pool feedback/image superimposed with an auxiliary visual signal which instructs the welder to increase/reduce the speed. Linear model is first identified from the experimental data to correlate welder's adjustment on the welding speed to the 3D weld pool surface and a global ANFIS model is then proposed to improve the model accuracy. To better distill the detailed behavior of the human welder, K-means clustering is performed on the input space such that a local ANFIS model is identified. To further improve the accuracy, an iterative procedure has been performed. Compared to the linear, global and local ANFIS model, the iterative local ANFIS model provides better modeling performance and reveals more detailed intelligence human welders possess.

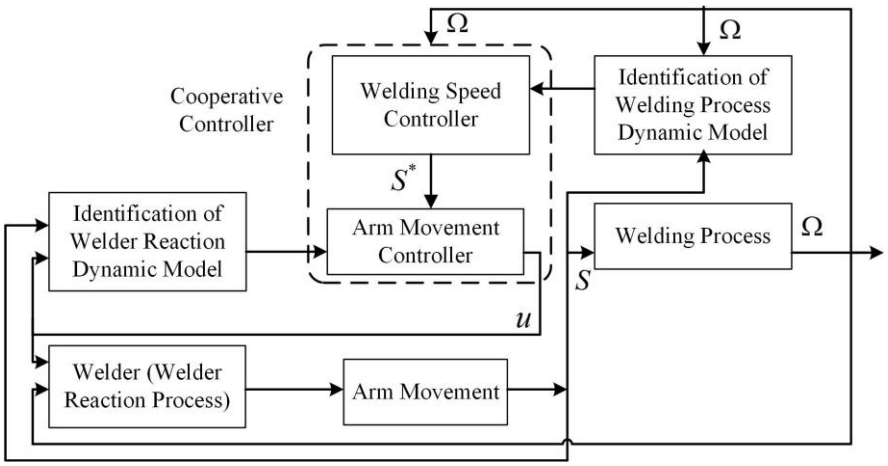

Figure 7.1 Schematic of machine-human cooperative control.

To demonstrate the effectiveness of the proposed model as an effective intelligent controller, automated control experiments have been conducted. Experimental results verified that the controller is robust under different welding currents and welding speed disturbance.

7.1 Principle of Machine-Human Cooperative Control

In this section the principle of the machine-human cooperative control is briefly introduced. Figure 7.1 illustrates the schematic of the proposed control system where two identification blocks are used to on-line identify models for the welding process and welder reaction process respectively. In this scheme human welder controls the welding speed S determined by his/her arm movement. The welding speed controller determines the optimal welding speed S^* for the human welder to follow. Arm movement controller calculates the visual signal u for human welder to view. The human welder sees the visual signal and weld pool images and moves his/her arm accordingly. The welding process outputs the 3D weld pool characteristic parameters Ω (i.e., the weld pool length, width, and convexity [55]) which will be inputted into the cooperative controller.

7.2 Control of Human Arm Movement

7.2.1 Human Hand Movement Tracking System and Experimentation

Figure 7.2 illustrates a detailed view of the human hand movement tracking system. A projector is used to project the visual signal (a sequence of arrows with both directions and amplitudes) for the welder to see. The welder then moves the virtual welding torch accordingly. Leap sensor is an advanced motion sensor which is utilized in this study to accurately capture the human welder arm movement. Using two cameras and three infrared LEDs, the sensor observes a roughly hemispherical area to a distance of about 1

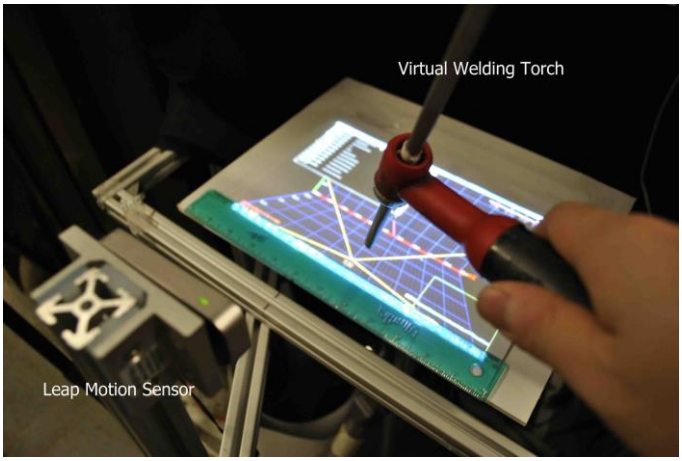

Figure 7.2 Human hand movement tracking system.

m. It can track fingers or similar items to a spatial precision of 0.01 mm [125]. The Leap sensor measures at 60 Hz, much faster than the sample rate of the system (10 Hz) and human response speed. The dynamic response of the Leap sensor and its negative effect on the proposed teleoperation system can thus be safely neglected.

It is noted that in this section the visual signal is displayed separately as the single source of information for the human welder. When the teleoperation welding experiment is conducted, this visual signal will be incorporated with the weld pool images. Human welders make adjustment based on this observation of the weld pool images and the visual signal to guide his/her movement.

7.2.1.1 Improvement on Response Consistency

The randomness/inconsistency of welder's movement may make the human response model to vary in both the structure and parameters. In order to minimize the

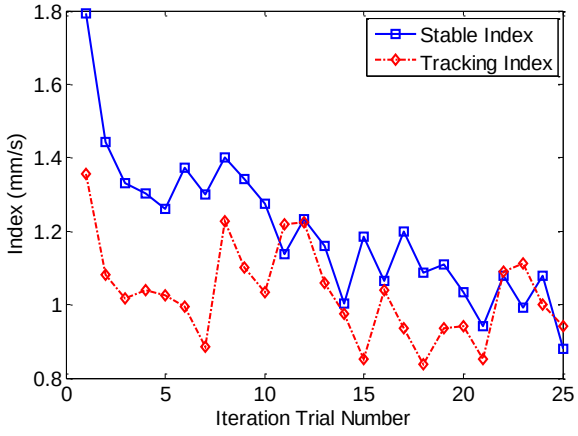

Figure 7.3 Illustration of the adaptation process.

inconsistency, an adaptation process is performed where the human welder goes through 25 iterative trials to adapt to the low speed movement in manual GTAW process. In these experiments the command speed is randomly varied from 1 mm/s to 3 mm/s in 5 s interval (or 10 sampling period). The input signal is calculated as the difference between the actual speed and the command signal. The human welder tries to track the varying command signal based on the visual input he/she perceives.

Two criteria are proposed to evaluate the consistency of performance for the human welder in this adaptation process: stable index (SI) and tracking index (TI):

$$SI = \frac{1}{n}\sum_{k=1}^{n}\left|s(k) - s(k-1)\right| \tag{7.1}$$

$$TI = \frac{1}{n}\sum_{k=1}^{n}\left|s(k) - s_c(k)\right|, (k = 1, ..., n) \tag{7.2}$$

where $s(k)$ and $s(k-1)$ are the human welder movement speeds at instant k and k-1, respectively. $s_c(k)$ is the speed command signal at instant k , and n is the number of samples in each iterative trial.

A reduced SI indicates a more stable movement and a reduced TI indicates a more accurate tracking performance. In the adaptation process, five command speeds are used: 1.0, 1.5, 2.0, 2.5, and 3.0 mm/s. In each experiment the command speeds are randomly varied among the five values each a 5s time interval. Both SI and TI are expected to be reduced after the adaptation process such that the randomness and inconsistency of the human movement can be minimized in the proposed model for the human welder movement. Figure 7.3 shows the improvement achieved by the adaptation process. As can be observed, both SI and TI graduate are reduced as the adaptation process is

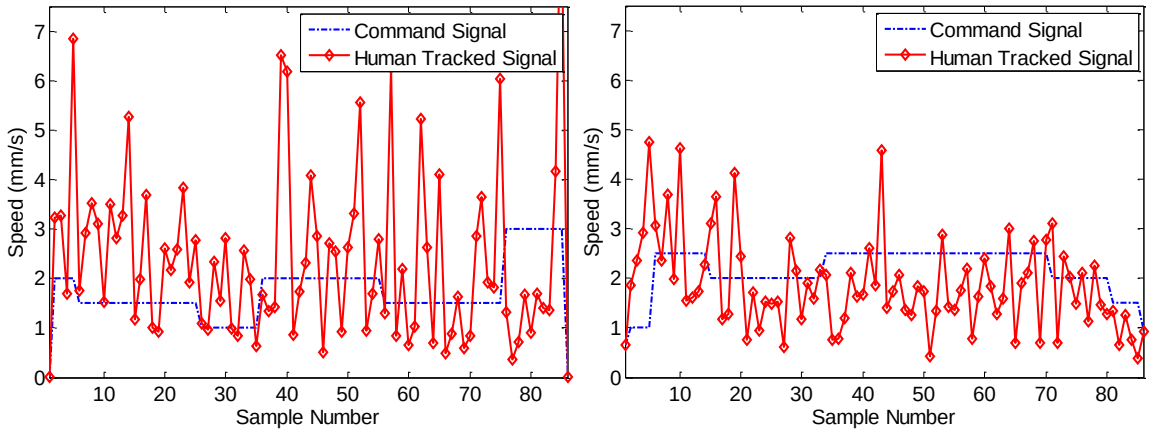

Figure 7.4 Two sample experiments before and after adaptation process. (a) Before adaptation; (b) After adaptation.

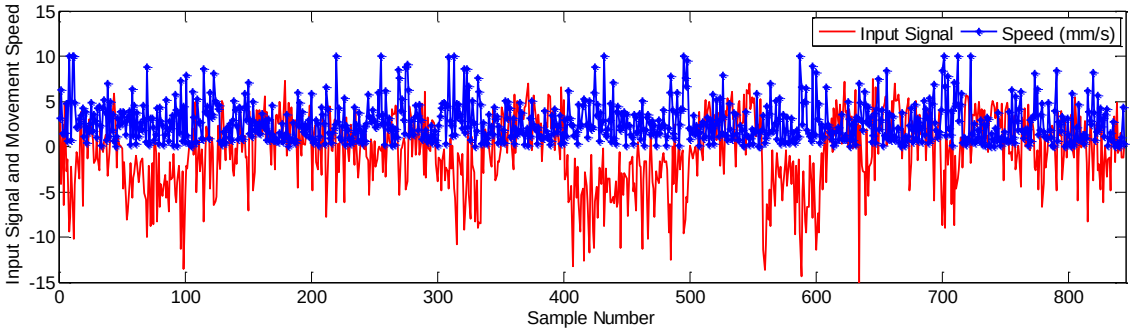

Figure 7.5 Measured input signal and human arm movement speed in twelve dynamic experiments.

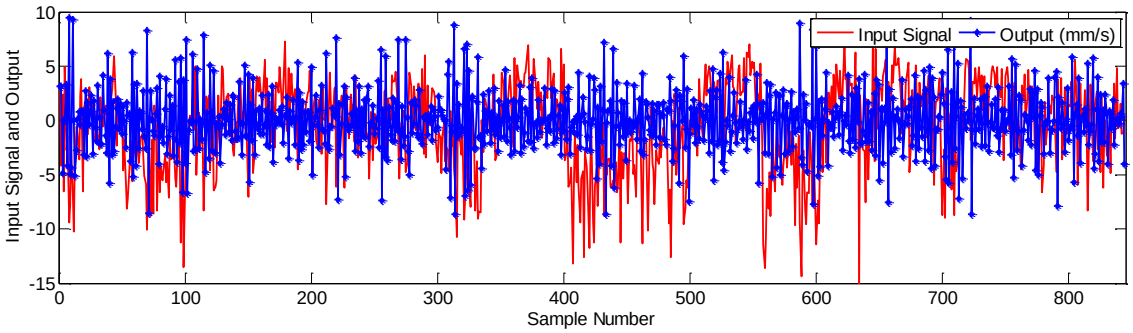

Figure 7.6 Measured input and output data in twelve dynamic experiments.

performed. Specifically, SI is decreased from 1.8 mm to about 0.9 mm, indicating a significant improvement in human hand stability. TI, on the other hand, is reduced from 1.35 mm to about 1 mm. This implies that the tracking accuracy of the human movement is also improved by the adaptation process. Figure 7.4 shows two sample experiments before and after the adaptation process. Before the adaptation process (Figure 7.4(a)), large adjustments of the movement speed are constantly observed, and large tracking errors occur throughout the entire experiment. After the adaptation process (shown in Figure 6(b)), however, the movement is more stable and accurate. The progress of the welder's gradual improvement during the adaptation is clearly shown.

7.2.1.2 Experiment Data

Twelve dynamic experiments have been conducted to model the correlation between the human arm movements to the input signal. Figure 7.5 plots the input and welder's arm movement speed. As can be observed, the human welder changes the movement speed accordingly based on the input visual signal he/she perceives. However, the correlation between the input and output is not clearly observed. For example, the input signals are relatively small from sample number 10 to 20, yet the human welder arm movement speed is increased to 10 mm/s. From sample number 90 to 100, the input signal is randomly changed, yet the arm movement speed is randomly changed as well. This is understandable because the human perceptions and responses are inevitably nonlinear and time-varying.

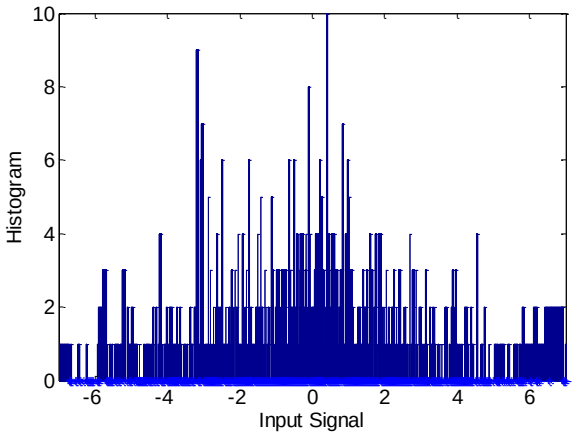

Figure 7.7 Histogram of the inputs in twelve dynamic experiments.

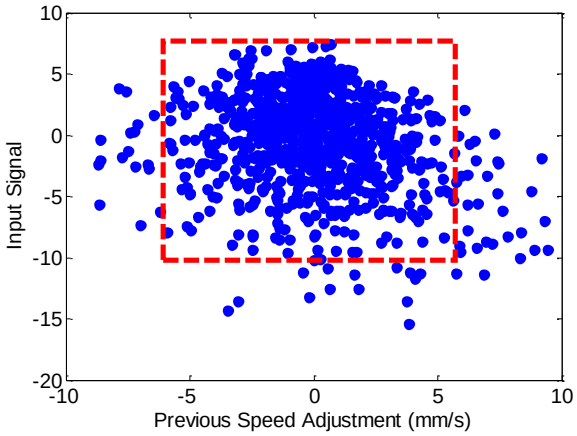

Figure 7.8 Distribution of inputs in twelve dynamic experiments.

It is noticed that human response to the speed difference rather than the speed. This is because welder does not know the exact speed he/she is moving. Instead, the speed adjustment should be modeled. Figure 7.6 plots the input and output (speed adjustment) in all the experiments. The sampling period in this study is 0.5 s because the welder controls his/her arm movement by observing the visual input signal and is a relatively slow process. A roughly positive correlation can be observed from the input to the output. When the input is increased, the speed adjustment is also increased. However, this correlation is nonlinear and time-varying. In the next section, an adaptive nonlinear ANFIS model will be utilized to model this complex nonlinear and time-varying human response model.

Figure 7.7 shows the histogram of the experimental data specified in Figure 7.6. It is shown that the majority of the inputs are centered from -4 to 2. This makes sense because a large negative input indicates a very steep decrease in the arm movement speed, which is not preferable in our application. Similarly, a large input indicates a rapid increase which instructs the human welder to increase his/her arm movement rapidly. This will

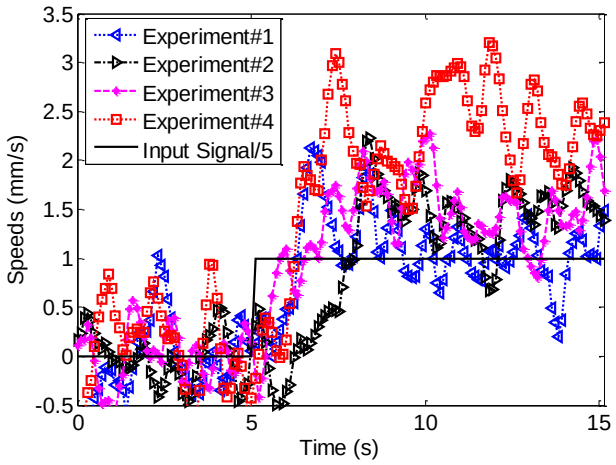

Figure 7.9 Step responses in four step input experiments.

cause possible unstable of the speed control system.

Figure 7.8 plots the distribution of the controller input variables (selected as the visual signal input and previous speed adjustment) in twelve dynamic experiments. The selection of the controller input variables are justified by performing F-test detailed in Section III. It is observed that the inputs have filled a certain range of control variables (marked by red block in Figure 7.8) in which acceptable tracking performance is achieved. This distribution implies that the resultant model can be used during closed-loop control if the control variables are in the range specified by this distribution.

7.2.2 System Modeling

In this section the system modeling is performed using the acquired inputs and output data. The following two criteria are proposed to evaluate the performance of the developed linear model, ANFIS and adaptive ANFIS model.

7.2.2.1 Step Response Analysis

Human response to the given visual signal is intrinsically nonlinear and time-varying. In this subsection step input experiments are conducted. Figure 7.9 depicts the step input and resulting human arm movement in four experiments. As can be observed, when the step input is applied at t=5 s, human welder starts to move his/her arm. The settling time in each experiment ranges from 2 s to 5 s. The static gains in these experiments range from about 1mm/s to 2.5 mm/s, indicating a nonlinear and time-varying response by the human welder.

7.2.2.2 Linear Modeling

The linear model can be expressed as the following Auto Regression Moving Average (ARMA) model:

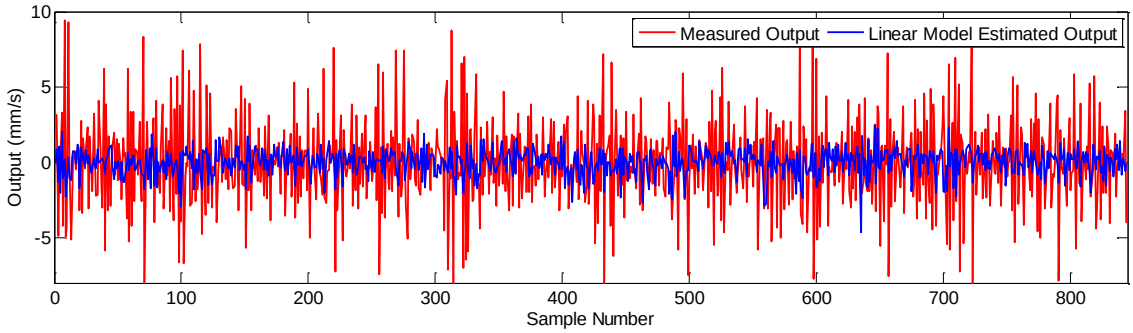

Figure 7.10 Linear modeling results.

$$\hat{y}(k)=\sum_{j=1}^{N_1} a(j)y(k-j)+\sum_{j=1}^{N_2} b(j)u(k-j)+c \tag{7.3}$$

where $y(k-j), j=1,...,N_1$ and $u(k-j), j=1,...,N_2$ are previous speed adjustments and visual signal inputs, $a(j), b(j), c$ are the model parameters, and N_1, N_2 are the ARMA model orders associated with $y(k-j)$ and $u(k-j)$, respectively.

The linear model parameters are identified by standard least squares method, and the linear model orders N_1, N_2 are selected based on F-test. F-value is given by:

$$F=\left(\frac{RSS_1-RSS_2}{p_2-p_1}\right)\Bigg/\left(\frac{RSS_2}{n-p_2}\right) \tag{7.4}$$

where RSS_i and p_i are the sum of squared residuals and number of regression factors/parameters of model (i=1, 2); model 2 with p_2 as its number of parameters is the higher order model with more parameters and n is the number of the samples that is 844 in this study.

Firstly 3-parameter model 1 ($N_1=2, N_2=1$) is compared with the 2-parameter model ($N_1=1, N_2=1$). Their number of parameters in the regression model is 3 and 2 respectively. For n=844 and a confidence level of $\alpha = 5\%$, the critical value of F distribution is 3.84. The calculated F value from the 2-parameter model to the 3-parameter model is 2.49. Hence, the reduction in the modeling error due to the increase in the model parameters is not significant such that the 2-parameter model is selected by the F-test over the 3-parameter model.

Then 3-parameter model 2 ($N_1=1, N_2=2$) is again compared with the 2-parameter model ($N_1=1, N_2=1$). The calculated F value is 2.54. It is thus concluded that the best N_1 and N_2 statistically are 1 and 1, respectively.

In this sense, the model structured is thus selected:

$$\hat{y}(k)=f\left(y(k-1),u(k-1)\right) \tag{7.5}$$

The linear modeling results are plotted in Figure 7.10. The identified linear model parameters are:

$$\hat{y}(k)=0.47y(k-1)+0.098u(k-1) \tag{7.6}$$

The static gain for the previous speed adjustment is 0.47, and the static gain for the visual signal input is 0.098. The average model error and RMSE are 1.868 mm/s and 2.459 mm/s, respectively. It is found that the human hand movement can be estimated by the

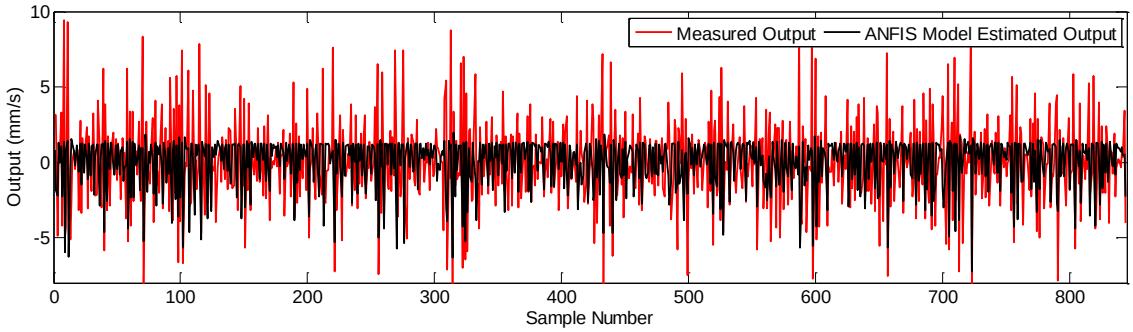

Figure 7.11 Nonlinear ANFIS modeling results.

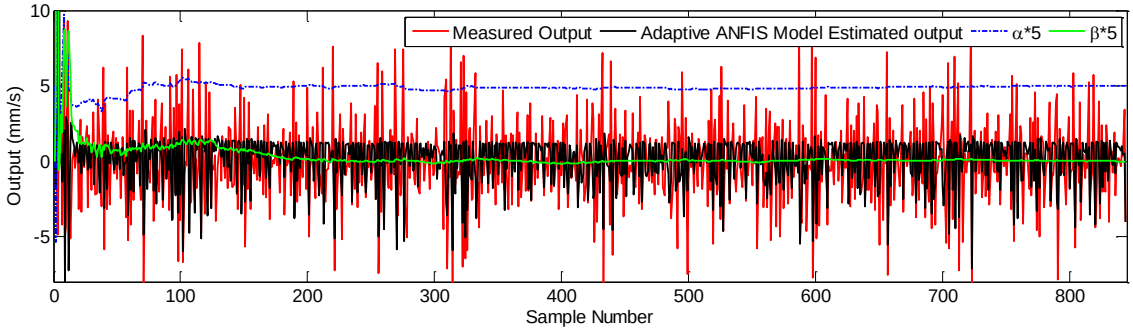

Figure 7.12 Adaptive nonlinear ANFIS modeling results.

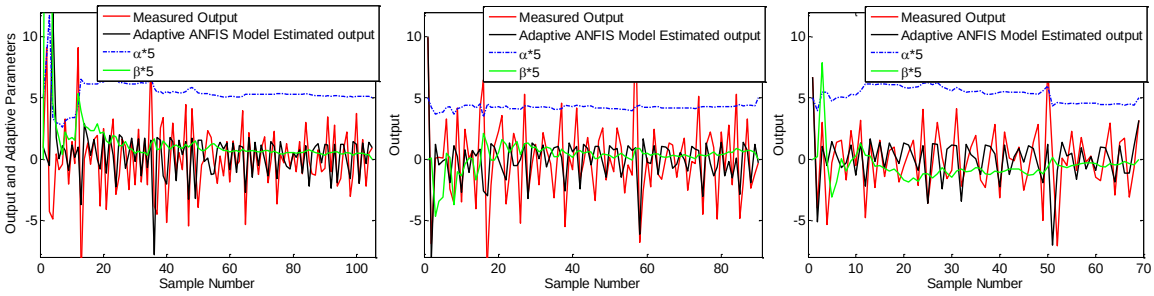

Figure 7.13 Model validation experiments.

inputs with acceptable accuracy. However, substantial static fitting errors are observed frequently.

7.2.2.3 ANFIS Modeling

The linear model described in the first subsection accounts for the average effect of the inputs on the human hand movement in the large input range. In order to further improve the model accuracy, nonlinear ANFIS modeling method is utilized in this section. The modeling result is shown in Figure 7.11 and the resulting models errors are listed in Table 7.1. It is seen that the model errors are improved by incorporating the nonlinear correlation between the inputs and model output.

7.2.2.4 Adaptive ANFIS Modeling

As an inherently time-varying system, human response is expected to be better modeled by an adaptive model. In this subsection, adaptive ANFIS model is proposed and the modeling results are presented.

The following adaptive model structure is proposed:

$$\hat{y}(k)=\alpha(k)y_{anfis}(k)+\beta(k) \tag{7.7}$$

where $y_{anfis}(k)$ is the calculated output by the proposed ANFIS, and $\alpha(k),\beta(k)$ are adaptive gain and constant at instant *k*, respectively.

Denote $\varphi_k=\left[y_{anfis}(k),1\right]$ being the regression vector, and $\theta_k=\left[\alpha(k),\beta(k)\right]$. Then the dynamic system parameters can be identified using the Recursive Least Squares (RLS) algorithm expressed as follows:

$$\begin{cases} P_k=\dfrac{1}{\lambda}\left[P_{k-1}-P_{k-1}\varphi_k\varphi_k^T P_{k-1}\Big/\left(\lambda+\varphi_k^T P_{k-1}\varphi_k\right)\right] \\ K_k=P_k\varphi_k \\ \theta_k=\theta_{k-1}+K_k\left(y_k-\varphi_k^T\theta_{k-1}\right) \end{cases} \tag{7.8}$$

where y_k is the measured output at instant *k*. λ is the forgetting factor.

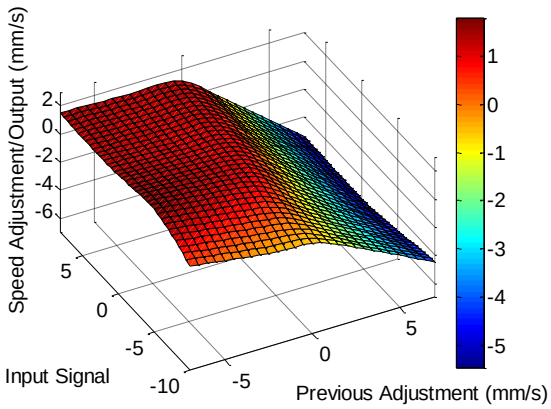

Figure 7.14 Nonlinear ANFIS model surface.

TABLE 7.1 MODEL COMPARISON BETWEEN NONLINEAR MODEL AND LINEAR MODEL

	RMSE /mm/s	Average Model Error /mm/s
Linear Model	2.459	1.868
ANFIS Model	2.365	1.804
Adaptive ANFIS Model	2.33	1.789

The fitting result using the proposed nonlinear model can be seen in Figure 7.12. It is observed that the modeling accuracy is improved. The resultant average model error and RMSE are 1.789 mm/s and 2.33 mm/s, respectively. For both criteria, the nonlinear adaptive ANFIS modeling results are superior to those from the ANFIS model and linear model. It is noted that although the proposed ANFIS model can better correlate the welding inputs and weld penetration, large errors cannot be fully eliminated. This is primarily due to the un-modeled factors which can also affect the human arm movement adjustments.

In order to validate the proposed nonlinear model, a validation experiment is carried out. The input and measured speed adjustments are plotted in Figure 7.13. The adaptive model parameters are also plotted. As can be observed the adaptive nonlinear ANFIS model can estimate the speed adjustment with sufficient accuracy.

Figure 7.14 depicts the nonlinear model surface with respect to input from -10 to 5, and previous speed adjustment from -6 mm/s to 6 mm/s. As can be observed, when the previous adjustment is large (i.e., about 5mm/s), as the input is increasing, the speed adjustment is gradually decreasing from -4 mm/s to -5.5 mm/s. Since the previous adjustment is relatively large, the human welder tends to decrease the speed at a relatively large rate. As the previous adjustment approaches zero, the increase in the input tends to increase the speed adjustment. However, as the input becomes larger, the speed adjustment saturates to about 2 mm/s. This makes sense because for the GTAW process, the human welder arm movement (i.e., welding speed) should not be larger than 2.5 mm/s. In this case, the speed adjustment should not be larger than 2 mm/s as the input increases.

7.2.3 Model Predictive Control Algorithm

In this section an analytical solution to the proposed adaptive nonlinear ANFIS model predictive control algorithm is derived. At instant k, the controller needs to determine the control action $u(k)$ based on the feedback/current movement speed $s(k)$ to drive the human hand to a desired movement speed. In a predictive control, prediction equations should be first developed to predict the output based on the inputs.

According to (7.7), the system incremental model can be expressed as:

$$\Delta s(k) = \alpha(k)\left[\sum_{i=1}^{2}\sum_{j=1}^{2} w_{ij}(k)\left(a_{ij}\Delta s(k-1) + b_{ij}u(k-1) + c_{ij}\right)\right] + \beta(k) \tag{7.9}$$

Suppose the future control action is constant, i.e. $\Delta u(k+j) = 0,\ j = 1,...,N$, where N is the prediction range, 1-step-ahead prediction of the speed increment yields:

$$\begin{aligned}
\Delta s(k+1) &= \alpha(k)\left[\sum_{i=1}^{2}\sum_{j=1}^{2} w_{ij}(k)\left(a_{ij}\Delta s(k) + b_{ij}u(k) + c_{ij}\right)\right] + \beta(k) \\
&= \underbrace{\left[\alpha(k)\sum_{i=1}^{2}\sum_{j=1}^{2} w_{ij}(k)\left(a_{ij}\Delta s(k) + c_{ij}\right)\right] + \beta(k)}_{Y(k+1)} \\
&+ \underbrace{\left[\alpha(k)\sum_{i=1}^{2}\sum_{j=1}^{2} w_{ij}(k)b_{ij}\right]}_{A(k+1)} u(k) = A(k+1)u(k) + Y(k+1)
\end{aligned} \tag{7.10}$$

2-step-ahead prediction of speed increment is shown in Equation (7.11).

$$\begin{aligned}
\Delta s(k+2) &= \alpha(k)\left[\sum_{i=1}^{2}\sum_{j=1}^{2} w_{ij}(k+2)\left(a_{ij}\Delta s(k+1) + b_{ij}u(k) + c_{ij}\right)\right] + \beta(k) \\
&= \alpha(k)\left[\sum_{i=1}^{2}\sum_{j=1}^{2} w_{ij}(k+2)\left(\begin{array}{l} a_{ij}\left\{\alpha(k)\left[\sum_{i=1}^{2}\sum_{j=1}^{2} w_{ij}(k+1)\left(a_{ij}\Delta s(k) + b_{ij}u(k) + c_{ij}\right)\right] + \beta(k)\right\} \\ + b_{ij}u(k) + c_{ij} \end{array}\right)\right] + \beta(k) \\
&= \underbrace{\left[\alpha(k)\sum_{i=1}^{2}\sum_{j=1}^{2} w_{ij}(k+2)a_{ij}A(k+1) + \alpha(k)A(k+1)\right]}_{A(k+2)} u(k) \\
&+ \underbrace{\alpha(k)\sum_{i=1}^{2}\sum_{j=1}^{2} w_{ij}(k+2)a_{ij}Y(k+1) + \alpha(k)Y(k+1)}_{Y(k+2)} = A(k+2)u(k) + Y(k+2)
\end{aligned} \tag{7.11}$$

Similarly, *l*-step prediction of speed increment can be expressed as

$$\Delta s(k+l) = A(k+l)u(k) + Y(k+l) \tag{7.12}$$

where $A(k+l) = \left[\alpha(k) \sum_{i=1}^{2} \sum_{j=1}^{2} w_{ij}(k) \right] A(k+l-1) + A(k+1)$ and

$Y(k+l) = \left[\alpha(k) \sum_{i=1}^{2} \sum_{j=1}^{2} w_{ij}(k) \right] Y(k+l-1) + Y(k+1)$ are iterative equations to compute $A(k+l)$ and $Y(k+l), l = 1, ..., N$, respectively.

The prediction equation can thus be expressed in the following matrix form

$$\mathbf{S} = \mathbf{S_k} + \mathbf{A_k} u + \mathbf{Y} \tag{7.13}$$

where

$$\mathbf{S} = \begin{bmatrix} \hat{s}(k+1) \\ \vdots \\ \hat{s}(k+N) \end{bmatrix}_{N\times 1}, \quad \mathbf{S_k} = \begin{bmatrix} s(k) \\ \vdots \\ s(k) \end{bmatrix}_{N\times 1}, \quad \mathbf{A_k} = \begin{bmatrix} A(k+1) \\ \vdots \\ A(k+N) \end{bmatrix}_{N\times 1}, \quad \mathbf{Y_k} = \begin{bmatrix} Y(k+1) \\ \vdots \\ Y(k+N) \end{bmatrix}_{N\times 1}$$

In order to achieve a desirable control, it is required the following cost function is minimized:

$$J(k,u) = \sum_{j=1}^{N} \left(\hat{s}(k+j) - s^*(k+j) \right)^2 \tag{7.14}$$

In a long-range predictive control, the prediction range *N* should be large enough to achieve a desirable control. However, the regulation speed decreases as *N* increases. It is found that *N*=5 can achieve a satisfactory regulation speed and robustness.

The desired trajectory should be designed depending on the application being addressed. In this study the desired trajectory $s^*(k+j)$ is defined as:

$$\begin{cases} s^*(k+j) = \gamma s^*(k+j-1) + (1-\gamma) s_c(k), \; j = 1, ..., N \\ s^*(k) = \hat{s}(k) \end{cases} \tag{7.15}$$

where $s_c(k)$ is the command speed that the welder tries to maintain, and $\gamma \in (0,1)$ is the smoothing coefficient. As γ becomes larger, the system will track the set point with slower speed but better robustness and smoothness. In this study γ=0.9 achieves an appropriate tradeoff between response speed and robustness.

The fluctuations in the input will generate non-smooth human adjustment and degrade human tracking performance, which is not desirable in our application. Thus, energetic control actions must be avoided. The modified following cost function is used to penalize changes in control:

$$\begin{aligned} J(k,u) &= \sum_{j=1}^{N}\left(\hat{s}(k+j)-s^*(k+j)\right)^2+\eta\left(u-u(k-1)\right)^2 \\ &= \left[\mathbf{S}^*-\mathbf{S}\right]^T\left[\mathbf{S}^*-\mathbf{S}\right]+\eta\left(u-u(k-1)\right)^2 \\ &= \left[\mathbf{S}^*-\mathbf{S_k}-\mathbf{Y}-\mathbf{A_k}u\right]^T\left[\mathbf{S}^*-\mathbf{S_k}-\mathbf{Y}-\mathbf{A_k}u\right]+\eta\left(u-u(k-1)\right)^2 \end{aligned} \tag{7.16}$$

where η is the penalty weight on the control change. The values of the weight η can be determined based on the scale of the static gain to the output. In this study η=0.1^2 $(\text{mm}/100\text{A})^2$ is chosen. This implies that an error of 1mm in the prediction has the same contribution to the cost function as current change of 0.1*100A = 10A, and speed change of 0.05mm/s.

It can be seen from (7.16) that $\mathbf{A_k}$ depends on the system input u being determined (since $w_{ij}(k)$ is dependent on u). Hence, minimization of the cost function is a nonlinear optimization problem. An iterative calculation is normally needed for this type of nonlinear optimization, which is not preferred for real-time control applications. When the amplitudes of $u-u(k-1)$ are not large, $w_{ij}(k+j),\ j=1,...,N$ can be approximated by $w_{ij}(k)$ so that $\mathbf{A_k}$ can be calculated before the optimization. Hence, the optimization becomes linear.

The control law is calculated such that:

$$\frac{\partial J(k,u)}{\partial u}=0 \tag{7.17}$$

The control signal is finally expressed as:

$$u=\left(\eta+\mathbf{A_k}^T\mathbf{A_k}\right)^{-1}\left[\mathbf{A_k}^T\left(\mathbf{S}^*-\mathbf{S_k}-\mathbf{Y}\right)+\lambda u(k-1)\right] \tag{7.18}$$

It is apparent that (7.18) provides a closed form solution and no online optimization is required. Thus, the obtained control algorithm can be easily incorporated into the real-time human movement tracking and machine-human cooperative control applications.

7.2.4 Human Control Experiments

In order to demonstrate the robustness of the developed control system, dynamic human

control experiments have been designed and conducted in this section under different disturbances. In subsection A, different set-points are applied. In subsection B and C the input and speed measurement disturbances are applied respectively, and the robustness of the controller with disturbances is tested.

7.2.4.1 Experiment 1: Tracking Varying Set-Point

In this experiment control experiment is conducted for tracking the varying set-point. From 0 s to 40 s the set-point is set at 1 mm/s, and from 40 s to 60 s the set-point is changed to 2 mm/s (Figure 7.15). It is observed that the controller is able to control the human arm movement accurately.

It is noticed, however, that small variations do occur during the experiment. This is expected because all human welders, despite the skilled level, all lack the consistency like most physical processes.

7.2.4.2 Input Disturbance

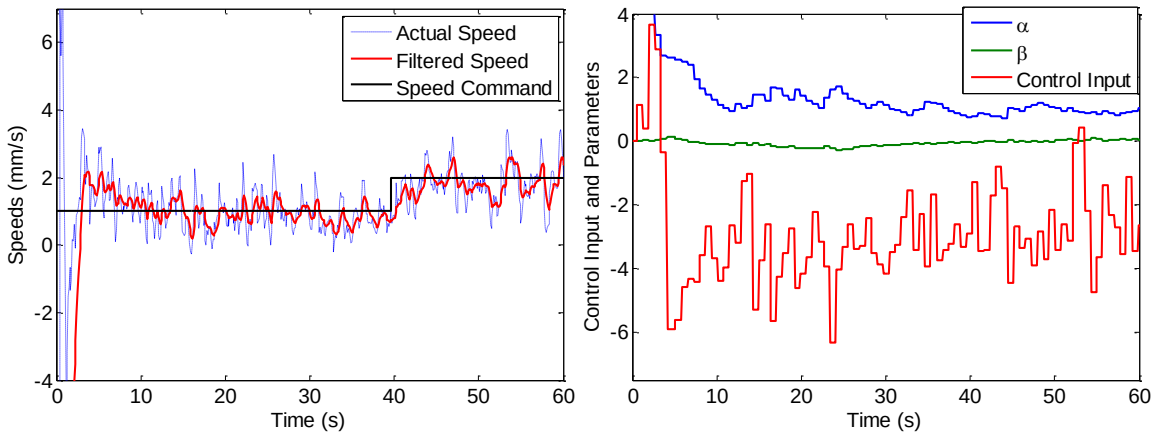

Figure 7.15 Experiment 1 results.

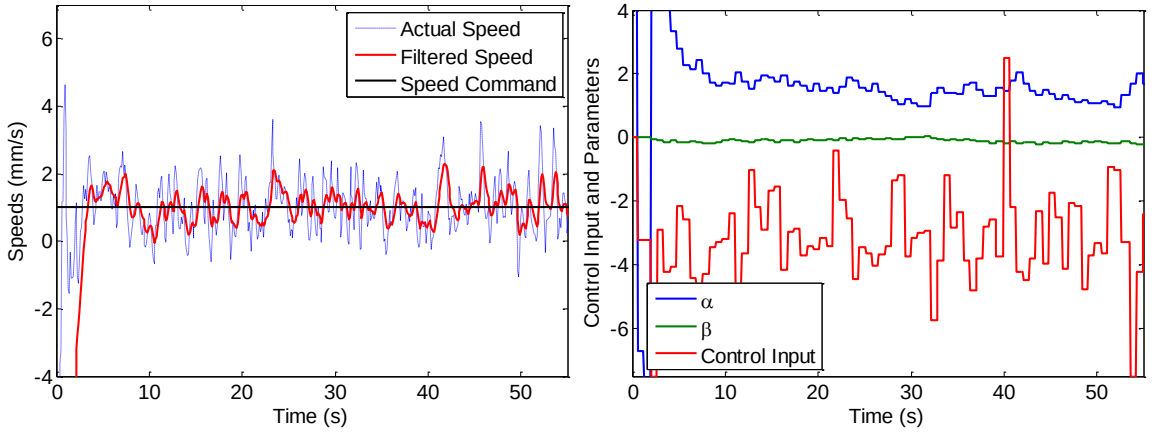

Figure 7.16 Experiment 2 results.

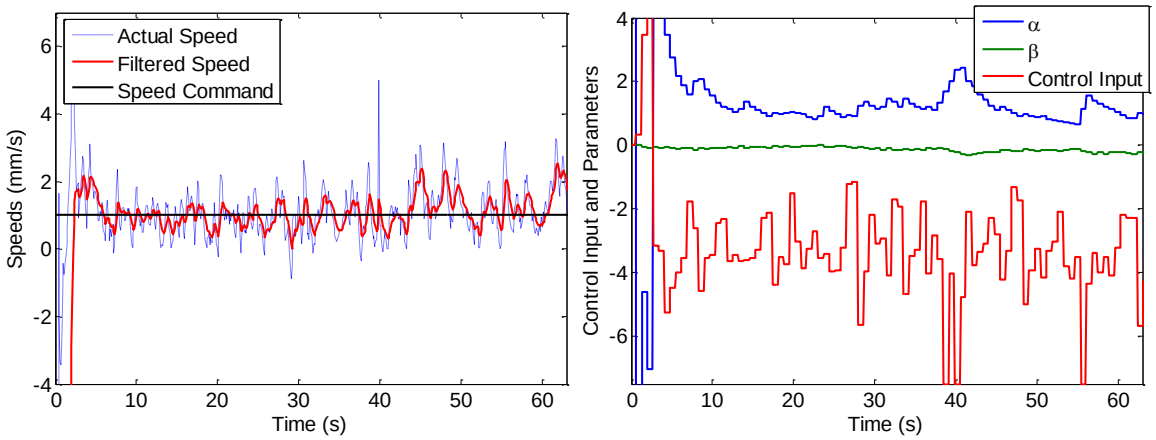

Figure 7.17 Experiment 3 results.

In this experiment the robustness of the control algorithm against input disturbances is evaluated. An artificial error between the calculated and applied values of the visual input signal is applied. In the first 40 s, no error exists between the calculated current and applied current. The controller is able to bring the human welder arm movement to about 1 mm/s. In t=42 s, the input signal is set at 5. As the result, human welder increases the arm movement speeds to about 3 mm/s (see Figure 7.16 (a)). However, the controller is able to adjust the visual signal input to compensate this artificial error (see Figure 7.16 (b)), and the arm movement speed can be maintained around the desired value (i.e., 1 mm/s) again (see Figure 7.16 (a)) with a relatively quick response time.

7.2.4.3 Experiment 3: Speed Disturbance

In experiment 3, an artificial error between the actual and measured values of the arm movement speed is applied to evaluate the robustness of the proposed control algorithm against measurement disturbances. During the first 40 s after the open-loop period, no error exists between the measured speed and actual speed. However, at t=40 s, the measured arm movement speed is set to 5 mm/s, which is about 4 mm/s larger than the actual human welder arm movement speed. As can be seen from Figure 7.17(b) the control signal is decreased to -7.5, and the human welder decreases his/her movement speed to about 0.5 mm/s. If no closed-loop controller is applied, this incorrect arm movement speed will be maintained. However, by applying the controller the desired arm movement speed is maintained. This experiment shows that the developed close-loop control system is robust to the variation in the welding speed.

7.3 Iterative Local ANFIS Based Human Welder Intelligence Modeling and Control

7.3.1 Experiment Data

Stainless steel pipe is welded using the DCEN GTAW process. The welding position is 5G (i.e., the pipe stays stationary during welding, and the welding torch moves along the weld joint). The material of the pipe is stainless steel 304. The outer diameter and wall thickness of the pipe are 113.5 and 2.03 mm, respectively. Sixteen dynamic experiments have been conducted to model the correlation between the human arm movements and weld pool characteristic parameters (weld pool width, length, and convexity). In these experiments the welding current is randomly changed from 40 A to 48 A resulting in a fluctuating weld pool surface. The welder sees the weld pool image overlaid with an assistant visual signal, and move the virtual welding torch accordingly. The robot follows the welder's movement and completes the welding task.. Three weld pool characteristic parameters are selected as the system inputs, which are considered as the major sources a human welder perceives to complete the welding experiments. Welder's fluctuating arm movement speed (i.e., welding speed) is filtered [126] to suppress the unwanted shaking during the experiments and the filtered speed is finally used as the system output. Figure 7.18 plots histograms for system inputs and output. It is observed that the weld pool width, length and convexity covers the range [4 mm, 7 mm], [3.5 mm, 8 mm], and [0.05 mm, 0.18 mm], respectively. Consequently, the arm movement speed ranges from 0.6 mm/s to 1.3 mm/s. The sampling period in this study is 0.5 s because the welder controls arm movement by observing the weld pool and is a relatively slow process. Figure 7.19 plots the inputs and welder's arm movement speed. As can be observed, the human welder changes the movement speed accordingly based on the weld pool geometry he/she perceives. A roughly positive correlation can be observed from the inputs to the output.

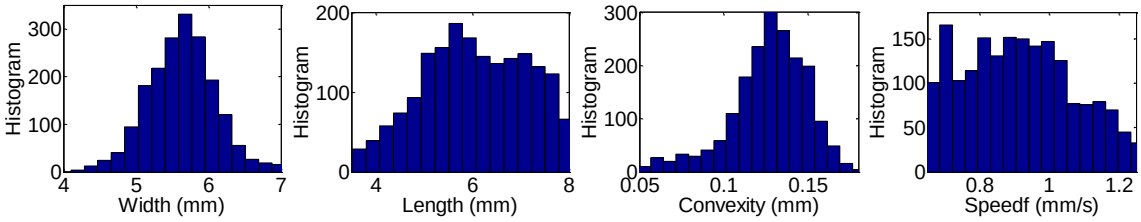

Figure 7.18 Histograms of the system inputs (weld pool width, length, convexity) and output (filtered welder's arm movement speed, i.e., welding speed).

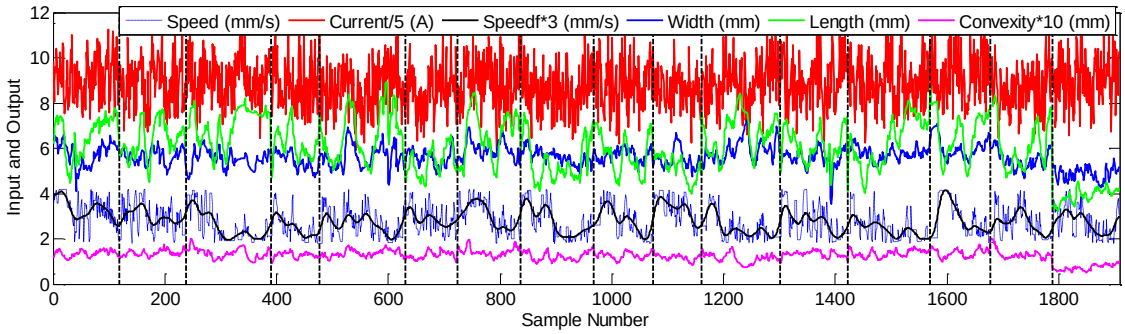

Figure 7.19 Measured system inputs (weld pool width, length, convexity) and output (filtered welder's arm movement speed) in sixteen dynamic training experiments.

When the welding current is increased, the heat input into the process is increased with an enlarged weld pool (increased width and length), the movement speed is also increased. However, this correlation is nonlinear and fuzzy because of the intrinsic fuzzy inference mechanism of the human welder. In the next two sections, linear model and various nonlinear ANFIS models will be utilized to model this complex nonlinear human response.

7.3.2 Linear and Global ANFIS Modeling

Based on the definition of system inputs and output detailed in previous section, a general model structured is described as:

$$\hat{y}(k)=f(W(k-1),L(k-1),C(k-1)) \tag{7.19}$$

where $\hat{y}(k)$ is the model estimated speed at instant k, $W(k-1),L(k-1),C(k-1)$ are the width, length, and convexity at instant $k-1$, respectively.

7.3.2.1 Linear Modeling

The following linear model is first constructed and identified using standard least squares algorithm:

$$\hat{y}(k)=\alpha_W W(k-1)+\alpha_L L(k-1)+\alpha_C C(k-1) \tag{7.20}$$

The linear modeling results are plotted in Figure 7. The identified linear model parameters are:

$$\hat{y}(k)=0.188W(k-1)-0.071L(k-1)+0.232C(k-1) \tag{7.21}$$

The static gains for the width, length, and convexity are 0.188, -0.071, and 0.232, respectively. The welder increases the speed when the weld pool and convexity increases. This makes sense because an increasing in the width or convexity generally indicating an increase in the weld penetration, thus the speed should be increased to maintain a consistent penetration. For the length, the negative coefficient is understandable because a long weld pool normally indicates an insufficient penetration caused by large welding speed. In this case, the welder should decrease the welding speed. The average model error and RMSE are 0.1359 mm/s and 0.1676 mm/s, respectively. It is found that the welding speed can be estimated by the linear model with acceptable accuracy. However, substantial static fitting errors are frequently observed.

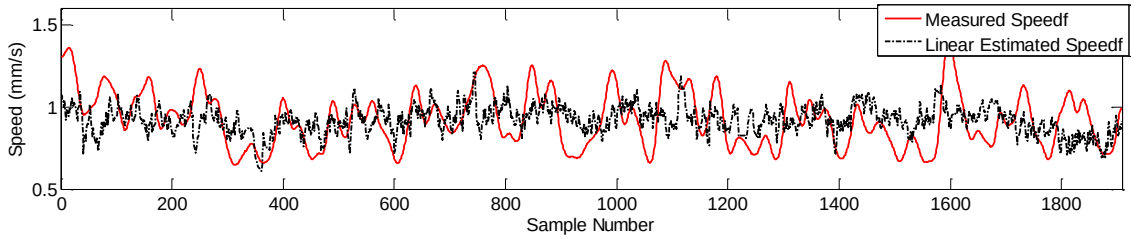

Figure 7.20 Linear modeling results.

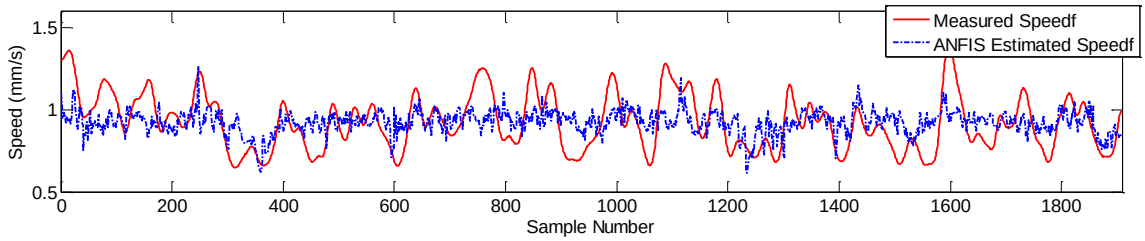

Figure 7.21 Global ANFIS modeling results.

TABLE 7.2 MODEL ERROR COMPARISONS

	RMSE /mm/s	Average Model Error /mm/s
Linear Model	0.1676	0.1359
Global ANFIS Model	0.1517	0.1218
Local ANFIS Model	0.1446	0.1147
Iterative Local ANFIS Model	0.1416	0.1100

7.3.2.2 Global ANFIS Modeling

The linear model described in the first subsection accounts for the average effect of the weld pool parameters on the speed in the large input range. In order to further improve the model accuracy, nonlinear ANFIS modeling method is utilized. Modeling trails suggest that when input parameters are partitioned by 2, a good trade-off is obtained between model performance and number of model parameters. The modeling result is shown in Figure 7.21 and the resulting models errors are listed in Table 7.2. It is seen that the model errors are improved by incorporating the nonlinear correlation between the inputs and model output.

7.3.3 Iterative Local ANFIS modeling

7.3.3.1 Local ANFIS Modeling Based on K-means Clustering

The global ANFIS model described in previous section could capture the nonlinear behavior of the human welder speed adjustment. To further improve the model accuracy, local ANFIS models based on clustering of the input space are constructed in this section.

K-means clustering [126] is one of the most commonly used unsupervised clustering

algorithms and has found numerous applications. The clustering algorithm minimizes the following objective function:

$$J = \sum_{j=1}^{K} \sum_{i=1}^{n} \left\| x_i^{(j)} - c_j \right\|^2 \tag{7.22}$$

where $\left\| x_i^{(j)} - c_j \right\|^2$ is a chosen distance measure between a data point $x_i^{(j)}$ and the cluster center c_j.

Because *K*-means clustering treats each input equally, normalization on the input space is first performed using:

$$pr_i = p_i / \max(p_i), i = 1,2,3 \tag{7.23}$$

where $p_i, i = 1,2,3$ represent the width, length, and convexity, and pr_i is the normalized value relative to the maximum.

In this subsection *K*-means clustering is utilized to cluster the normalized input space, and the local ANFIS models are consequently constructed. Figure 7.22 shows the measurement distance with respect to K. It is shown that when the number of clusters is

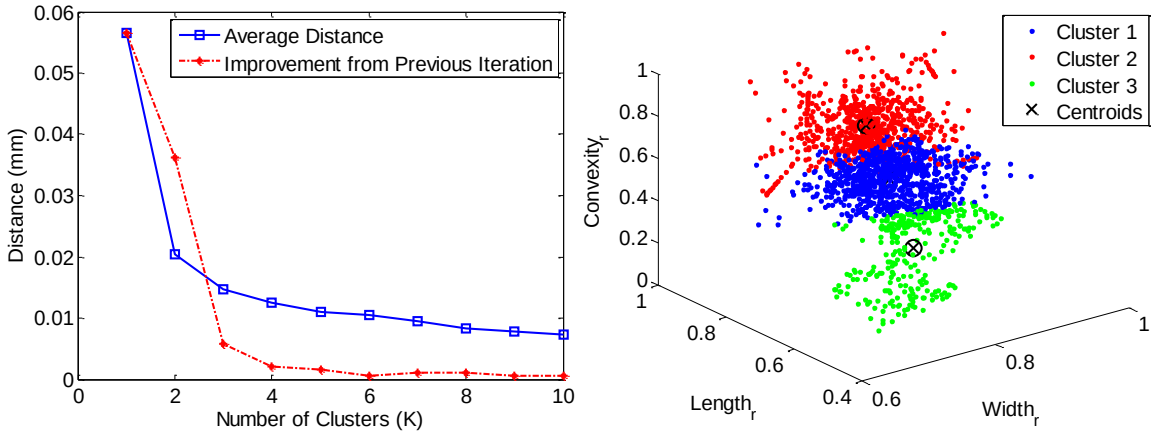

Figure 7.22 (a) Distance measure with respect to number of clusters *K*. (b) clustering result.

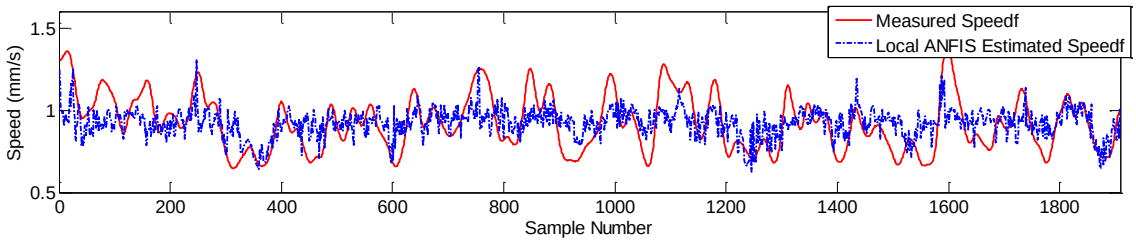

Figure 7.23 Local ANFIS modeling results.

increased from 1 to 2, the error is improved by 0.035 mm. Similarly, when *K* is increased from 2 to 3, the error is improved by 0.005 mm. When *K* is further increased to 4, the resultant improvement becomes insignificant (less than 0.001 mm). Thus, *K* is selected as 3, and the clustering result is shown in Figure 10.

Based on the clustering result, local ANFIS is constructed and the overall fitting result is shown in Figure 7.23. As can be seen from Figure 7.23, model performance is further enhanced by clustering the input space and constructing local ANFIS model. The model errors are listed in Table II. Both errors are further reduced compared to the linear and global ANFIS model.

7.3.3.2 Improved Model Using an Iterative Procedure

In local ANFIS modeling described in previous subsection, the clustering has outliers that may deteriorate the clustering and modeling performance. In this section an iterative procedure is performed to further improve the model performance. During each iteration

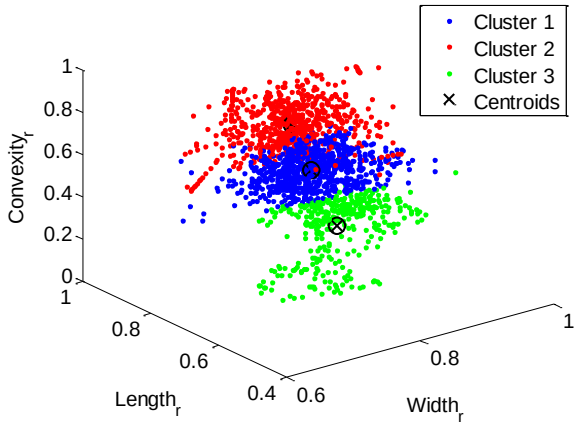

Figure 7.24 *K*-means clustering result after iteration procedure.

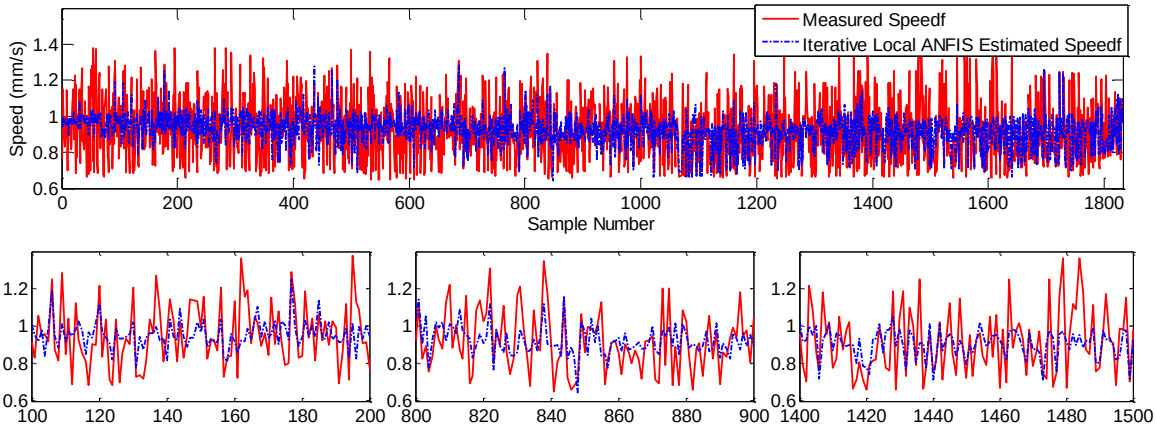

Figure 7.25 Iterative local ANFIS modeling results. Above: modeling results, below: enlarged figures for samples from 100-200, 800-900, and 1400-1500.

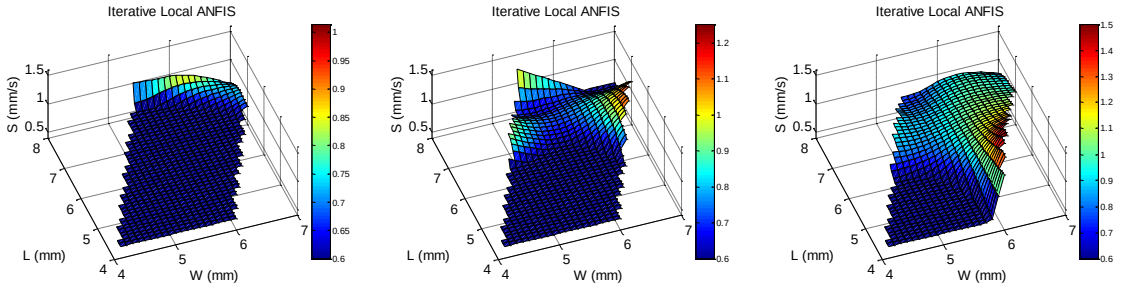

(a) (b) (c)

Figure 7.26 Nonlinear modeling surface for iterative local ANFIS with the weld pool convexity is (a) 0.06 mm, (b) 0.11 mm, (c) 0.16 mm.

step 1% of the data points that have the largest distance to the cluster centers (i.e., outliers) are discarded, and the iteration procedure stops when the maximum iteration number is reached (10 in this study).

The clustering result after iteration procedure is shown in Figure 7.24 and the model fitting result is depicted in Figure 7.25. As can be observed in Figure 7.24, clustering result is improved with less outlier data, and model errors (shown in Table II) is further reduced.

Figure 7.26 plots the nonlinear modeling surfaces for iterative local ANFIS model, under different weld pool convexity. As can be observed, nonlinearity is substantial in modeling the human welder's response to 3D weld pool geometry. Specifically, when the weld pool convexity is small (0.06 mm in Figure 7.26(a)), the speed adjustment is relatively small when the width and length are relatively small (about 0.6 mm/s). As the width and length become larger, the speed adjustment gradually increases to about 0.9 mm/s. This makes sense because a small convexity generally indicates an insufficient penetration when the width and length are also small, and the corresponding welding speed should be small. Similarly for the convexity being 0.11 mm (Figure 7.26(b)), iterative local ANFIS model outputs small welding speed for small width and length. As the width and length both increase, the human welder reacts nonlinearly. When the convexity is relatively large (0.16 mm as is depicted in Figure 7.26(c)), the iterative local ANFIS model outputs small speed for small weld pool width and length yet increases the speed as the width and length increases.

It is apparent that the above observations provide us detailed knowledge about the correlation between the welder's responses and weld pool geometry. If a linear model is used, the correlation acquired between the welder's response and the weld pool geometrical parameters will only be an average over the entire range of the weld pool geometrical parameters. Hence, the developed ANFIS modeling plays an important role in deriving the detailed correlation between the welder's response and the weld pool geometry.

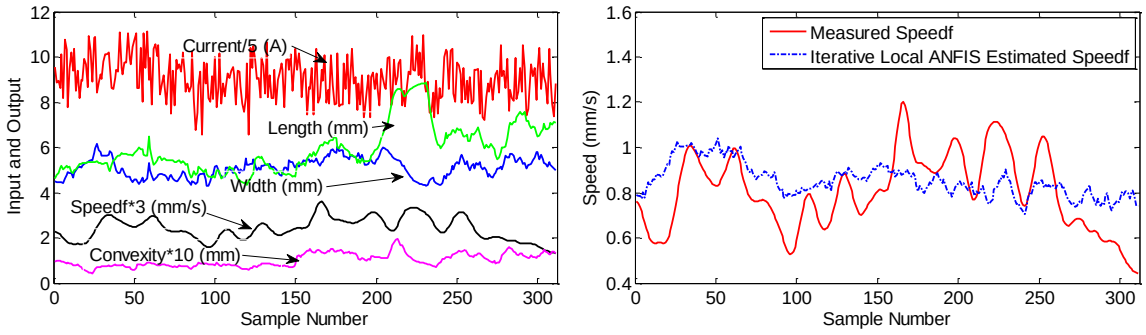

(a) (b)

Figure 7.27 Verification experiment results. (a) Input and welding parameters (b) measured and estimated speed.

7.3.3.3 Model Verification

To verify the proposed iterative local ANFIS model, verification experiment is conducted and the results are shown in Figure 7.27. It is shown in Figure 7.27 (b) that the model can estimate the welder's movement with acceptable accuracy. It is noticed, however, that from sample number 160 to 170, 210 to 240, and 250 to 255, the measured speed is relatively large (fluctuating from 1 mm/s to 1.2 mm/s), yet the model estimated speed is maintained at 0.85 mm/s. Actually the relatively large welding speed measurement is due to the welder's incorrect hand movement. However, using the proposed data-driven model, correct speed adjustment is distilled and effectively modeled. In this sense, the proposed model is able to output correct speed adjustment and sometimes outperform the human welder.

7.3.4 Automated Welding Experiments

In order to demonstrate the robustness of the developed control system, automated welding experiments have been designed and conducted in this section under different disturbances.

7.3.4.1 Experiment 1: Different Welding Current

In this subsection the control experiment is conducted under different welding current. From 40 s to 58 s is the open loop period where no controller is applied. The welding speed and the welding current are set at 0.8 mm/s and 42 A, and the pool parameters reach the steady states at the end of the open loop period (4.2 mm for the width, 5 mm for the length, and 0.15 for the convexity). From 58 s the proposed controller is applied, and the welding speed is adjusted based on the inputs (weld pool characteristic parameters). At 80 s, the welding current is changed to 46 A (Figure 7.28(a)). As a result, the weld pool width, length and convexity gradually increase to about 6 mm, 8 mm, and 0.19 mm, respectively. From Figure 7.28(d) it is also observed that the back-side bead width is increased because of this current increase. If no closed loop control is applied, this current increase cannot be compensated. From Figure 7.28(b) it is shown that the

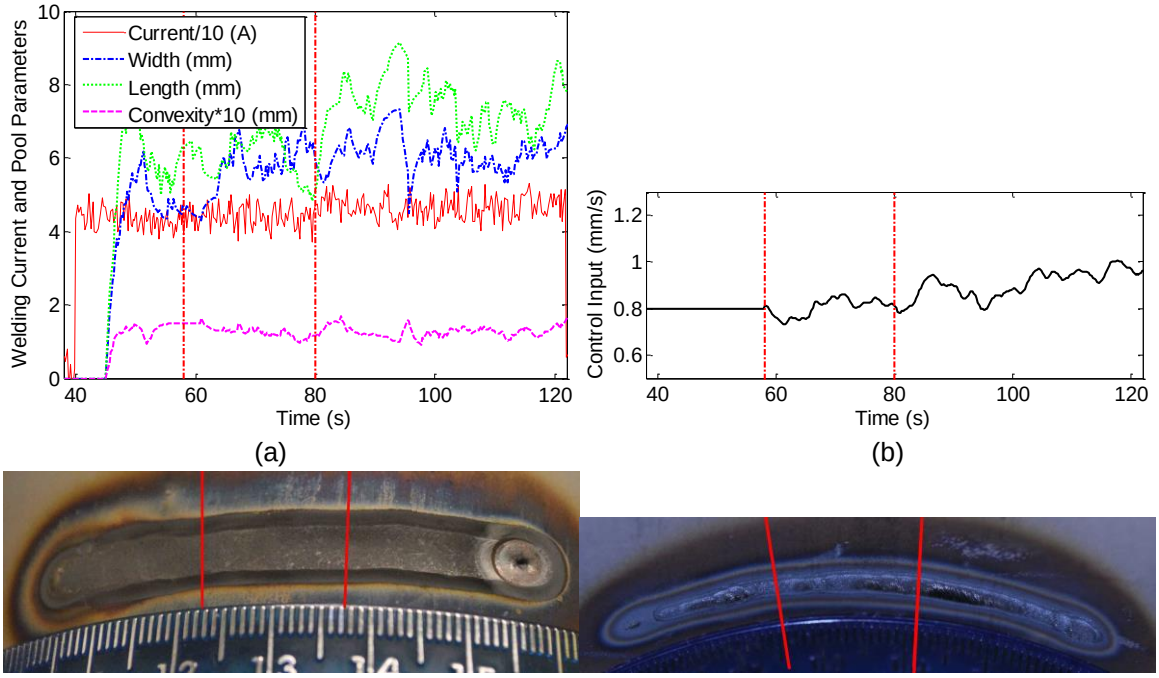

Figure 7.28 Experiment 1 results (a) Welding current and weld pool parameters (b) Control input (c) Front-side bead (d) Back-side bead.

controller is able to increase the welding speed to compensate this increase in the welding current. The back-side bead width is also well maintained at about 3.5 mm.

7.3.4.2 Experiment 2: Welding Speed Disturbance

In this experiment the robustness of the control algorithm against welding speed disturbance is evaluated. The welding current is 43 A throughout the experiment. An artificial error between the calculated and applied values of the welding speed is applied. In the first 33 s of the closed loop control (52 s to 85 s), no error exists between the calculated speed and applied speed. The controller is able to bring the back-side bead width to about 3.3 mm. From 85 s to 87 s, the control input is set at 0.5 mm/s. As the result, the back-side bead width increases to about 4 mm (see Figure 7.29 (d)). However, the controller is able to adjust the welding speed to compensate this artificial error (see Figure 7.29(c)), and the back-side bead width can be maintained around the desired value (i.e., 3.5 mm) again (see Figure 7.29(d)) with a relatively quick response time.

7.4 Summary

In this paper an innovative iterative local ANFIS model based data-driven approach to control the welding process is proposed. A machine-human cooperative control scheme in virtualized welding platform is utilized. Teleoprated training experiments are conducted by a human welder, whose adjustments on the welding speed and the corresponding 3D weld pool characteristic parameters are recorded. Linear model is

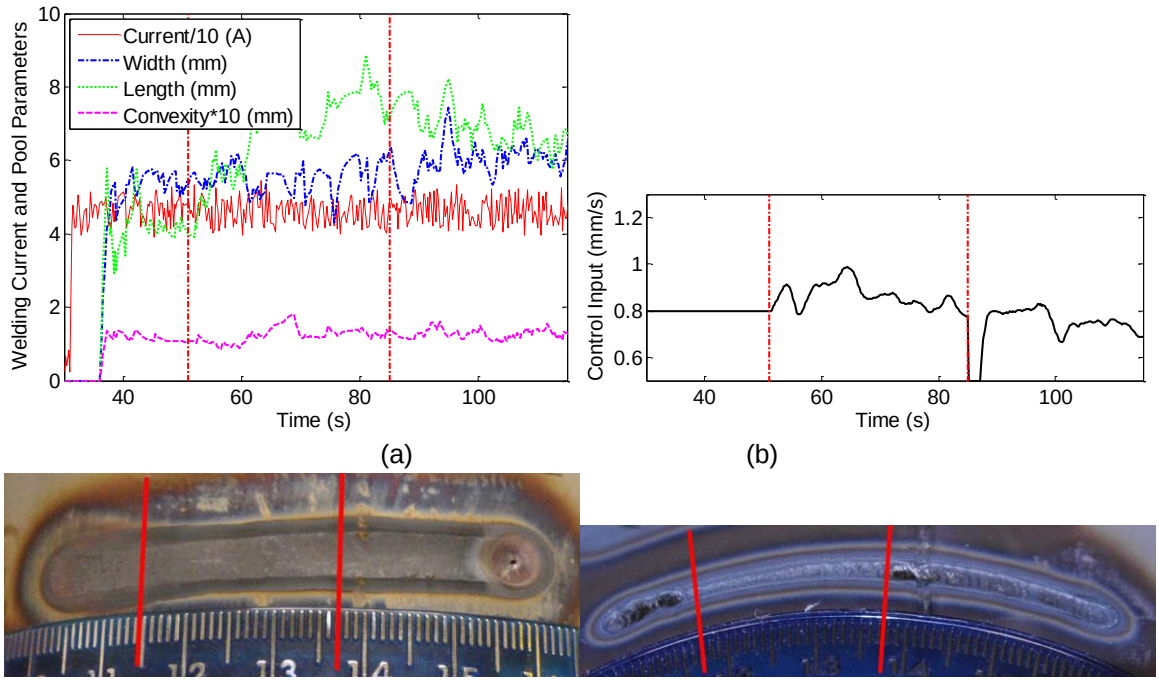

Figure 7.29 Experiment 2 results (a) Welding current and weld pool parameters (b) Control input (c) Front-side bead (d) Back-side bead.

firstly identified and a global ANFIS model is proposed to improve the model accuracy. K-means clustering is performed on the input space and a local ANFIS model is proposed. To further improve the model performance, an iterative procedure is performed to filter the outliers. Compared to the linear, global and local ANFIS models, the proposed iterative local ANFIS model provides better modeling performance and distills detailed intelligence human welder possess. Automated control experiments are conducted and results verified the effectiveness of the proposed controller under different welding current and welding speed disturbance.

Chapter 8 Learning Human Welder Movement without Virtual Reality Enhancement

Previous chapter illustrates how the human welder's intelligence is enhanced by virtual reality system and transferred to welding robots. Alternatively, human welder's intelligence can still be distilled without virtual reality enhancement. In these cases, the performance might degrade. In this chapter human welder's response against 3D weld pool surface is learned and transferred to the welding robots to perform automated welding tasks. To this end, teleoperated virtualized welding platform described in chapter 6 is utilized to conduct dynamic training experiments by a human welder whose arm movements together with the 3D weld pool characteristic parameters are recorded. The data is off-line rated by the welder and a fuzzy classifier is trained, using an ANFIS, to automate the rating. Data from the training experiments are then automatically classified such that top rated data pairs are selected to model and extract "good response" minimizing the effect from "bad operation" made during the training. A supervised ANFIS model is then proposed to correlate the 3D weld pool characteristic parameters and welder's adjustment on the welding speed. The obtained model is then transferred to the welding robot to perform automated welding task as an intelligent controller. Experiment results verified that the proposed model is able to control the process under different welding current as well as under disturbances in speed and measurement. A foundation is thus established to selectively learn "good response" to rapidly extract human intelligence to transfer into welding robots.

8.1 Training Experiment Data

Thirteen dynamic training experiments have been conducted to model the correlation between the human arm movements to the fluctuating 3D weld pool surface. Stainless steel pipe is welded using the direct current electrode negative GTAW process. The material of the pipe is stainless steel 304. The outer diameter and wall thickness of the pipe are 113.5 and 2.03 mm, respectively. In these experiments the welding current is randomly changed from 40 A to 48 A resulting in a fluctuating weld pool surface. The welder sees the projected weld pool image and moves the virtual welding torch accordingly. The robot follows the welder's movement and completes the welding task. Three weld pool characteristic parameters [55] are selected as the system inputs, which are considered as the major sources human welder perceives to complete the welding experiments. Welder's fluctuating arm movement speed (i.e., welding speed) is filtered [127] to suppress the unintentional shaking during the experiments and the filtered speed is finally used as the system output.

Figure 8.3 plots the histogram of the inputs and welder's arm movement speed in these dynamic training experiments and Figure 8.1 depicts the measured data. It is observed

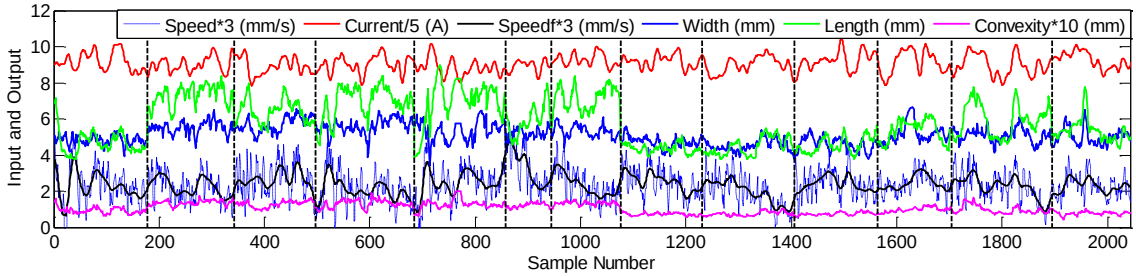

Figure 8.1 Measured welding current, weld pool characteristic parameters and human arm movement speed in thirteen dynamic training experiments.

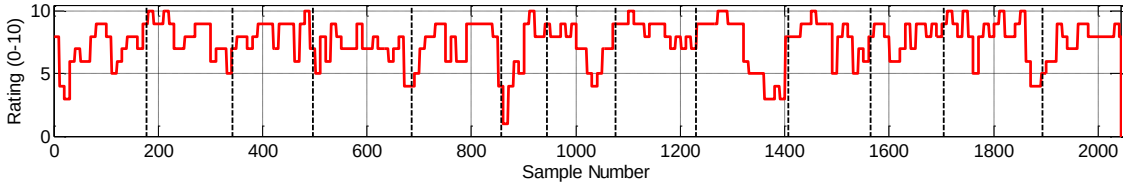

Figure 8.2 Rating assigned by human welder in thirteen dynamic experiments.

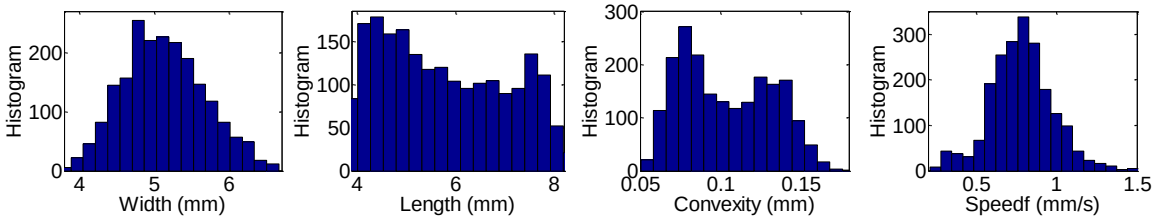

Figure 8.3 Histograms of the system inputs and output.

that the weld pool width, length and convexity covers the range [3.8 mm, 7 mm], [3.9 mm, 8 mm], and [0.05 mm, 0.18 mm], respectively. Consequently, the arm movement speed ranges from 0.3 mm/s to 1.5 mm/s. The sampling period in this study is 0.5 s because the welder controls arm movement by observing the weld pool and is a relatively slow process. It is noted that because of the limited skill of the welder and the intrinsic stochastic nature of the human controlled process, the speed adjustment might not always be ideal. For example, from sample number 850 to 900 the welder's movement is

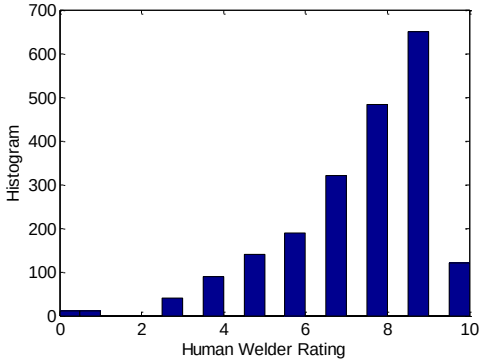

Figure 8.4 Histogram of rating assigned by the human welder.

considered relatively fast for a medium welding current (45 A) and consequently a normal sized weld pool.

To better distill the correct response of the human welder, the human welder evaluates the measured data (including the welding current, weld pool characteristic parameters) and corresponding back-side weld penetration, then assigns a rating (from 0 to 10) in each 5 s interval. (Assigning a rating is an off-line process requiring no real-time operation/control and is thus much less skill demanding for the welder.) Figure 8.2 shows the assigned rating and Figure 8.4 plots its histogram. It is seen that over 60% of the data points are rated above 8, however about 10% of the data points have been rated below 4. If all the data points are used to model the human welder response, the model might not reflect the correct behavior. In the next section, an ANFIS based fuzzy classifier is trained and analyzed.

8.2 Fuzzy Classification Result

The classifier (i.e., welder rating system) is defined as

$$R(k) = f\left(W(k), L(k), C(k), S(k)\right) \tag{8.1}$$

where $W(k), L(k), C(k)$ represents the measured weld pool parameters at instant k, and $S(k)$ is the filtered welder's movement speed.

Linear model can be fitted using standard least squares method:

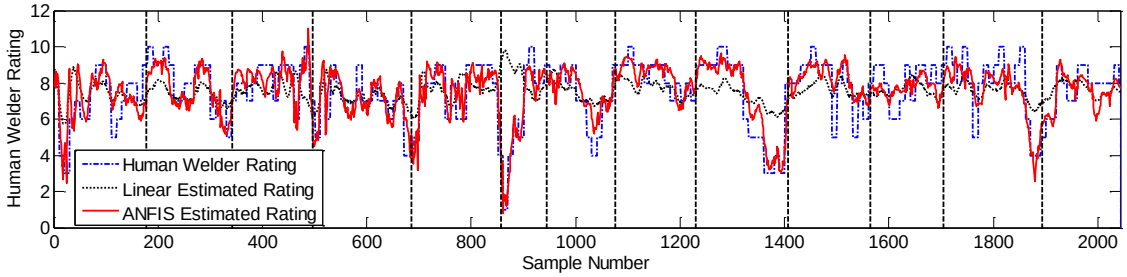

Figure 8.5 Linear and ANFIS modeling of the rating.

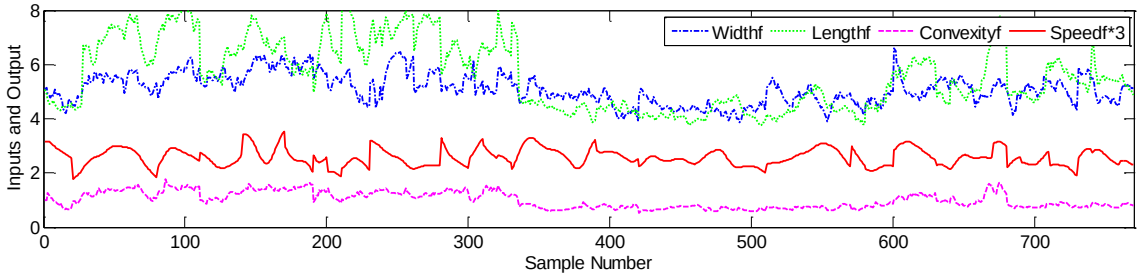

Figure 8.6 Selected training experiment data after fuzzy classification.

$$R_l(k) = -0.06W(k) + 0.19L(k) - 9.42C(k) + 2.87S(k) + 5.5 \quad (8.2)$$

The linear fitting result is depicted in Figure 8.5. Substantial fitting errors are frequently observed. ANFIS modeling technique described in previous subsection is utilized to improve the classifier performance. Modeling trials suggest that when the four inputs are partitioned by 3, a good trade-off between fitting errors and model parameter numbers is obtained. ANFIS fitting result is also plotted in Figure 8.5. Compared to linear model result, the proposed ANFIS model provides much better fitting result with the RMSE for the rating is reduced from 1.6607 to 1.0626.

The trained classifier will be used to classify the training experiment data (shown in Figure 8.5). Measurements (with associated ratings larger than 8) are selected and depicted in Figure 8.6. In the next section, modeling of human welder response is conducted and correct human welder response is distilled and analyzed. The proposed classifier can also be used as welder rating system which may be helpful in training unskilled welder faster.

8.3 Modeling of Human Welder Response

8.3.1 Linear Modeling

The human welder response model structure is expressed as:

$$S(k) = g\left(W(k), L(k), C(k)\right) \quad (8.3)$$

The linear modeling results are plotted in Figure 10, and the identified linear model is:

$$S_l(k) = 0.0016W(k) - 0.0087L(k) + 0.91C(k) + 0.81 \quad (8.4)$$

The static gain for the width, length, and convexity is 0.0016, -0.0087 and 0.91, respectively. It indicates the welder increases the speed when the weld pool width and convexity is increased and the length is decreased. This makes sense because an increase in the width and convexity generally indicates an increase in the heat input and penetration, and the welder should increase the welding speed to compensate this heat input increase to maintain a consistent penetration. The negative coefficient for the length is also understandable because the increase in the length may be caused by the large welding speed. The average model error and RMSE are 0.0861 mm/s and 0.1048 mm/s, respectively. It is found that the welding speed can be estimated by the inputs with acceptable accuracy. However, substantial static fitting errors are frequently observed.

8.3.2 Supervised ANFIS Modeling

ANFIS modeling is employed to model the nonlinear correlation between the weld pool

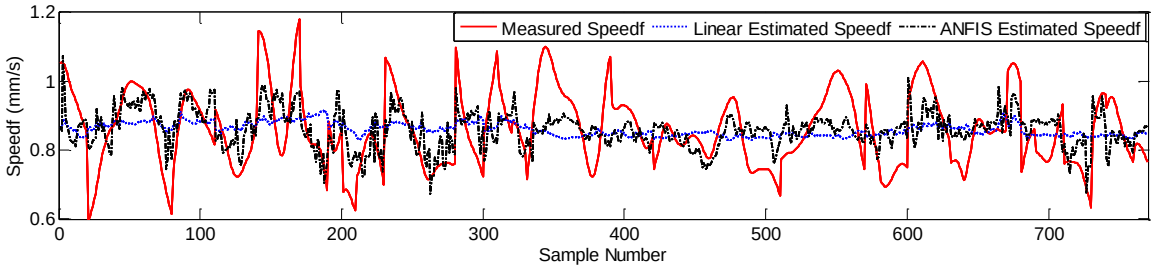

Figure 8.7 Linear and supervised ANFIS modeling of the welder response.

characteristic parameters and the welder's movement speed. The model is developed based on the classified data (depicted in Figure 8.6) and is thus referred to as supervised ANFIS model. The modeling result is also shown in Figure 8.7 and the resulting models errors are listed in Table I. The average model error and RMSE are 0.0730 mm/s and 0.0916 mm/s, respectively. From Table I, it appears that the ANFIS did not significantly reduce the modeling error. However, careful observation of Figure 8.7 suggests that the adjustment/fluctuation in the speed is much more accurately fitted by the ANFIS model. The large variations in the human welder speed caused by operation inconsistence /randomness are not be model-able and bound the lower limit of the modeling error. (The inconsistence should not be learned and modeled to transfer into welding robots. Modeling thus provides a method to further better retrieve the "good response" from the human welder.) Hence, the actual reduction in the modeling error due to the use of the ANFIS model may be much more significant than that is reflected by the reduction in the quantified model errors.

8.3.3 Model Analysis

The identified supervised ANFIS model can provide more accurate prediction on the welder's adjustment on the welding speed than the linear model. However, it is much more complicated. For its intended use in welder response modeling and control, this complexity is not a concern because of the strong computation power of today's industrial computers and embedded systems. However, the understanding of its implication is less straightforward than that of the linear model. Moreover, the model's reasonableness needs to be examined against our observations and knowledge on weld pool and welding process since it was identified statistically from experimental data. As a comparison, a global ANFIS model trained from the original (non-discriminated by the rating) measurement data (depicted in Figure 8.6) is also constructed to illustrate the effectiveness of the proposed fuzzy classifier.

Figure 8.8 illustrates the nonlinear model surface for both global ANFIS model and supervised ANFIS model. When the weld pool convexity is small (i.e., 0.06 mm shown in Figure 11(a)(d)), global ANFIS model outputs a relatively large speed (about 0.85 mm/s) when both the weld pool width and length are small; the welding speed remains

smaller than 0.6 mm/s otherwise. For supervised ANFIS model, on the other hand, the speed gradually increases as the pool width and length increases. When the pool is extremely large (for a width of 6.5 mm and length of 8 mm, the welding speed reaches 1.5 mm/s). Actually for small convexity the weld penetration is mainly determined by the weld pool size. A small pool size indicates small amount of metals being melted and thus an insufficient penetration. In this case, the welding speed should be kept small. As the pool size increases, more metals are melted and the welding speed should be increased accordingly. The response generated by supervised ANFIS model coincides with our understanding about the welding process. For medium weld pool convexity (about 0.11 mm shown in Figure 8.8 (b)(e)), supervised ANFIS model remains at 0.75 mm/s to 0.85 mm/s for most of the weld pool size. This is understandable because for medium convexity the weld penetration is larger than that of the small convexity. The welder response should kept minimal rather than a steep curve depicted by global ANFIS model surface in Figure 8.8(b). For large convexity case (Figure 8.8(c) and (f)), global ANFIS model outputs a large peak at a medium pool size, which does not make sense. For supervised ANFIS model, on the other hand, no such unexplainable behavior is observed. When the pool size is small, a large weld pool convexity indicates that no penetration occurs because of the large surface tension force being applied. In this case, the speed is expected to be extremely small to produce enough heat input for full penetration. Supervised ANFIS model is able to generate a welding speed of 0.3 mm/s to compensate the insufficient penetration. As the pool size increases, the supervised ANFIS model outputs an increased welding speed. The speed reaches its maximum (about 0.95 mm/s) for a weld pool width at 5.5 mm and length at about 8 mm. In this case, large weld pool

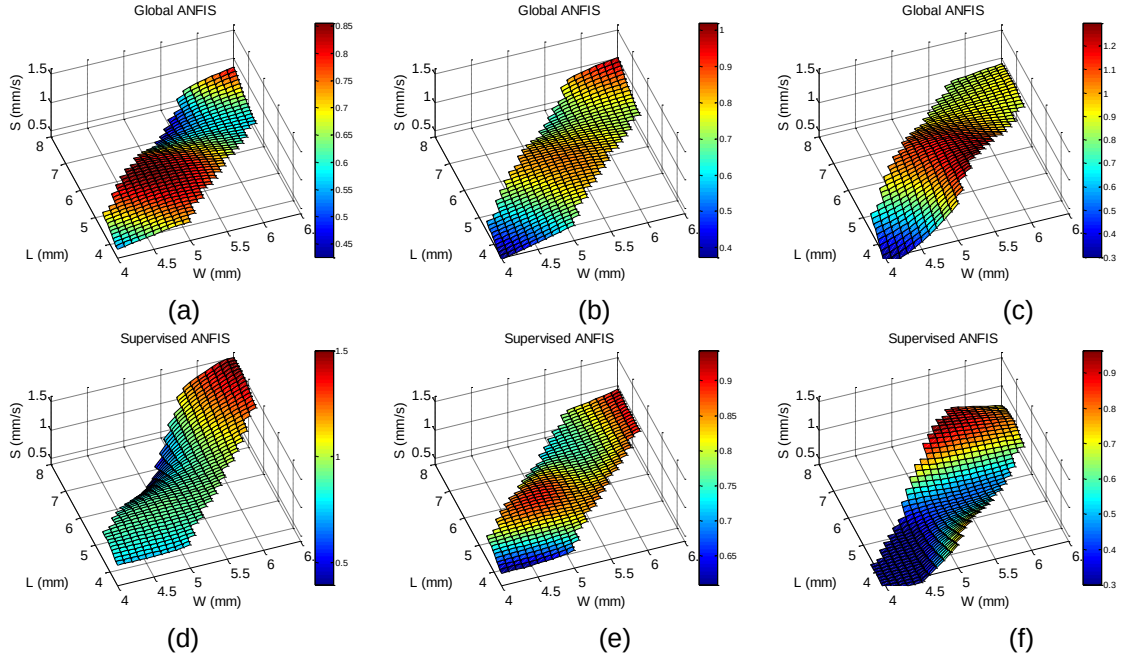

Figure 8.8 Nonlinear model surface for global ANFIS (a-c) and supervised ANFIS (d-f) model with the weld pool convexity is (a)(d) 0.06 mm, (b)(e) 0.11 mm, (c)(f) 0.16 mm.

size and relatively large convexity indicates a sufficient penetration, and the welding speed should be relatively large to maintain a consistent penetration status. It is thus concluded that the supervised ANFIS model generates correct welding speed adjustment for varying weld pool geometry and is better than global ANFIS model which could not discriminate between correct and incorrect adjustment made by the human welder during the training experiments.

It is apparent that the identified supervised ANFIS model does help understand the correlation between the weld pool and welder's adjustment. The linear model, although also uses the data reflecting the correct adjustment, averages the effects and thus may not be adequate to gain detailed in-depth knowledge. For applications where computation power is not much concerned, the supervised ANFIS model is apparently much more superior than the linear model.

8.3.4 Model Verification

To verify the proposed supervised ANFIS model, an additional experiment is conducted and the results are shown in Figure 8.9. It can be seen from Figure 8.9 (b) that the model can estimate the welder's movement with acceptable accuracy. It is noticed, however, that from sample number 0 to 50, the measured speed is relatively large (fluctuating from 1 mm/s to 1.5 mm/s), yet the model estimated speed is maintained from 0.8 mm/s to 1 mm/s. From Figure 8.9(a) it is observed at during this period the weld pool width is maintained between 5.5 mm and 6 mm and the convexity is about 0.13 mm to 0.15 mm. Instead of fluctuating the welding speed like the human welder, the proposed supervised ANFIS model is able to make appropriate adjustments on the welding speed based on the weld pool surface characteristic parameters because the modeling has served as a

TABLE 8.1 Model Comparison between Nonlinear Model and linear model

	RMSE /mm/s	Average Model Error /mm/s
Linear Model	0.1048	0.0861
Supervised ANFIS Model	0.0916	0.0730

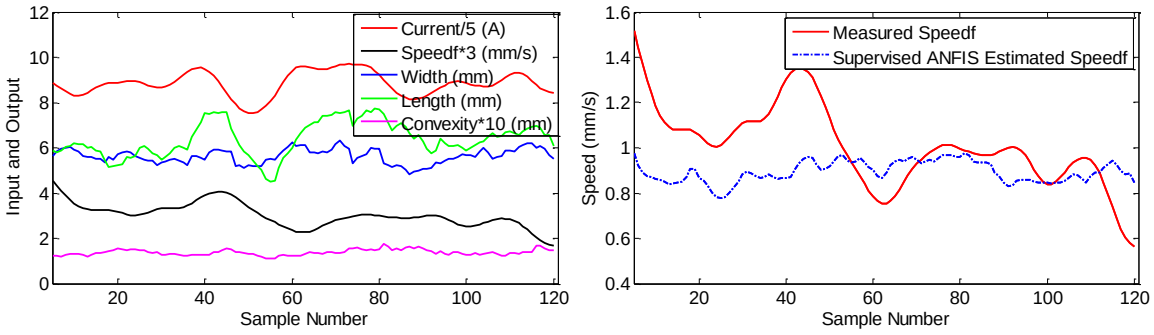

(a) (b)

Figure 8.9 Verification experiment result. (a) Measured welding process input and pool parameters (b) Measured and supervised ANFIS model estimated speed.

benifical process to filter out the inconsistence/randomness in human operation. In this case, the relatively large welding speed measurement may have been due to the welder's incorrect hand movement and possible underestimation/overestimation of the welding process because of the limited skill of the human welder. Fortunately, using the proposed supervised ANFIS model, correct speed adjustment is distilled and effectively modeled. In this sense, the proposed model is able to output correct speed adjustment and sometimes outperform the human welder.

8.4 Automated Control Experiments

In order to demonstrate the robustness of the developed control system, automated control experiments have been designed and conducted in this section.

8.4.1 Experiment 1: Different Welding Current

Control experiment is firstly conducted under different welding currents. Before 58 s is the open loop period with no closed loop control. From 58 s to 80 s the welding current is set at 43 A, and from 80 s to 115 s the welding current is changed to 48 A (Figure 8.10(a)). It is observed that the controller is able to increase the welding speed accordingly to maintain a consistent penetration (about 4.5 mm shown in Figure 8.10(d)).

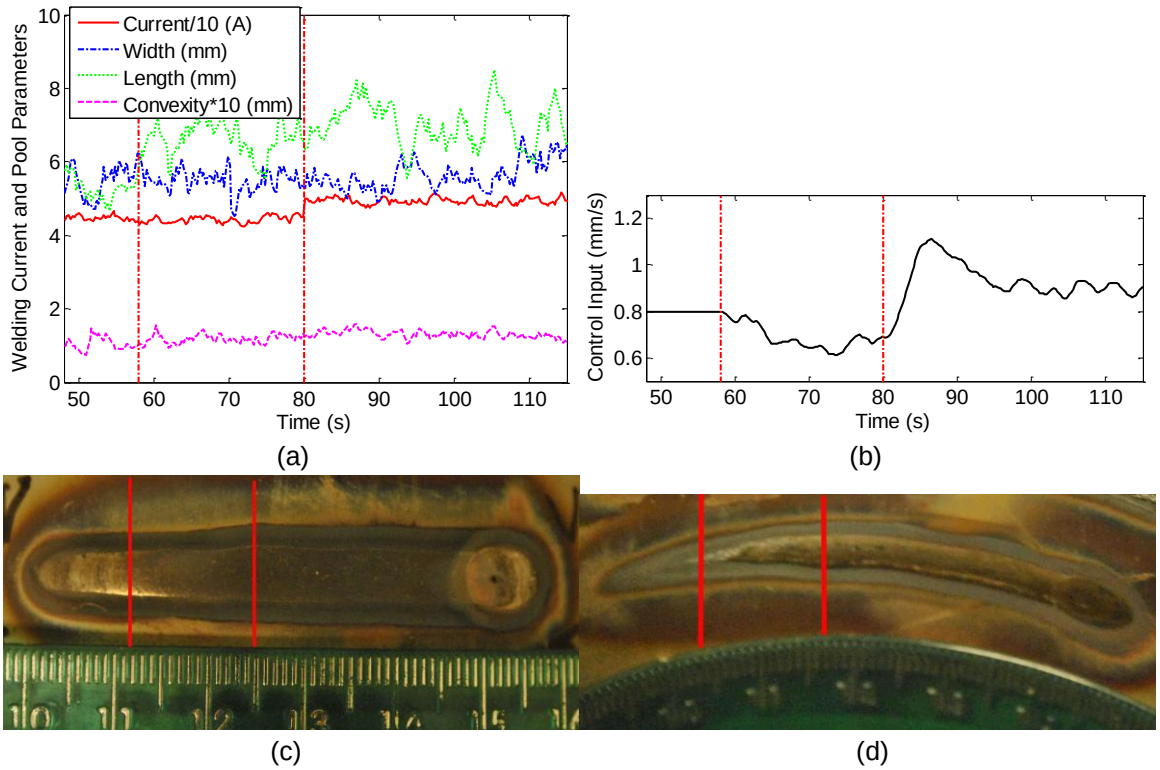

Figure 8.10 Experiment 1 results (a) Welding current and weld pool parameters (b) Control input (c) Front-side bead (d) Back-side bead.

8.4.2 Experiment 2: Speed Disturbance

In experiment 2, an artificial error between the calculated and applied welding speed is applied to evaluate the robustness of the proposed control algorithm against input disturbances. During the first 23 s after the start of the closed-loop period, no error exists between the calculated speed and applied speed. However, at 85 s, the applied welding speed is set to 0.5 mm/s, which is about 0.3 mm/s smaller than the calculated welding speed. As can be seen from Figure 8.11 (d) the back-side bead width is increased from 3.5 mm to about 4 mm. However, by applying the controller the desired welding speed is maintained. This experiment shows that the developed close-loop control system is robust against speed disturbance.

8.4.3 Experiment 3: Measurement Disturbance

An artificial error between the actual and measured values of the weld pool surface is applied. At 83 s, the measured weld pool width, length, and convexity are set to 3 mm, 3.5 mm, and 0.1 mm, respectively. As can be seen from Figure 15 (b) the control input (i.e., welding speed) is decreased from 0.85 mm/s to about 0.78 mm/s, and the back-side bead width is slightly increased (Figure 8.12(d)). By applying the controller the desired back-side bead width is well maintained.

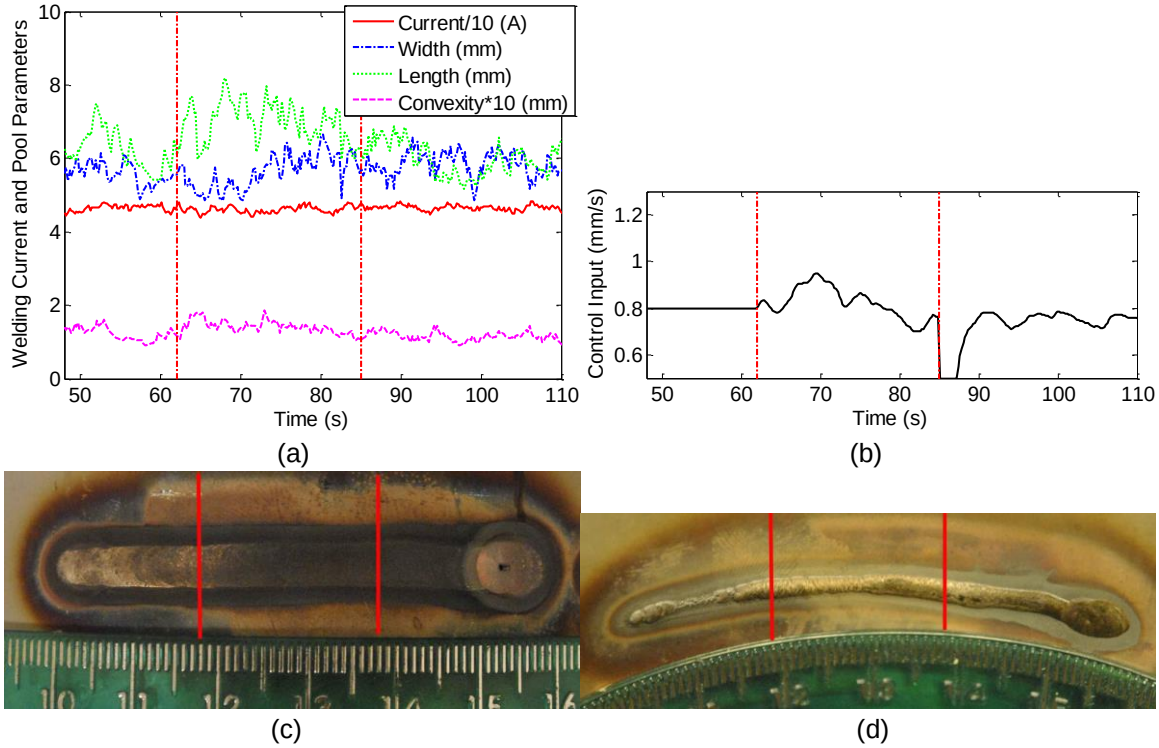

Figure 8.11 Experiment 2 results (a) Welding current and weld pool parameters (b) Control input (c) Front-side bead (d) Back-side bead.

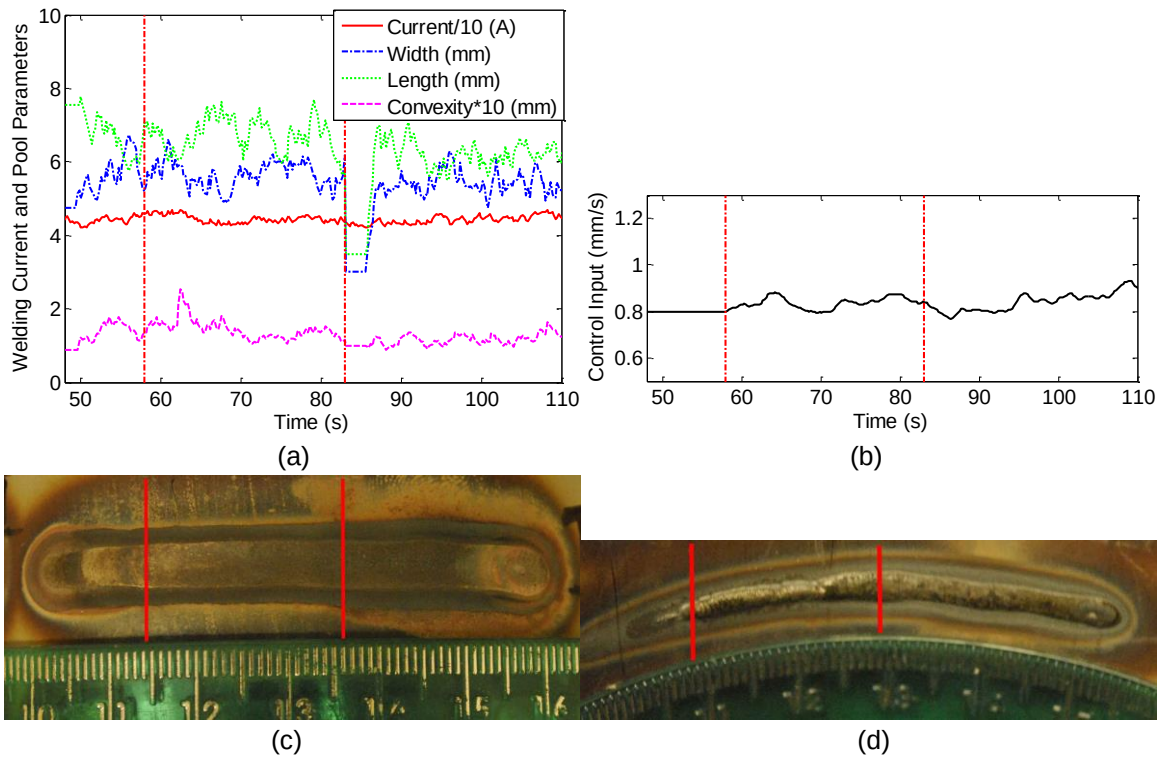

Figure 8.12 Experiment 3 results (a) Welding current and weld pool parameters (b) Control input (c) Front-side bead (d) Back-side bead.

8.5 Summary

In this chapter human welder's response against 3D weld pool surface is learned and transferred to the welding robots to perform automated welding tasks. A fuzzy classifier is trained using the label provided by the welder and the top ranked data pairs are selected. A supervised ANFIS model is then proposed to correlate the 3D weld pool characteristic parameters and welder's adjustment on the welding speed. Automated welding experiments are conducted using the proposed model and it is shown that the controller is able to control the process with different welding currents and under speed/measurement disturbances.

Chapter 9 Fuzzy Weighting Based Data Fusion: Combining Machine and Human Intelligence

In this chapter a fuzzy weighting based data fusion approach is proposed for intelligent welding robot to perform automated pipe GTA welding. The welder rating system detailed in Section 8.2 is utilized to rate calculated welding speed from three control algorithms: super welder model based on process modeling and predictive control [128], welder intelligent model without VR (detailed in chapter 8), and welder intelligent model with VR (detailed in chapter 7). Model with highest rating are firstly selected and the obtained data fusion result thus can achieve highest rating. However, constant switching from different models results in energetic speed adjustments, which is not preferred in welding applications. Generalized bell fuzzy membership function is then proposed to weight welding speeds calculated from three models [129]. Simulation results confirm that the data fusion algorithm can obtain a smooth speed adjustment yet maintain a high rating, and is superior to any of the three algorithms. Automated welding experiments are conducted and results show that the proposed data fusion based welding speed controller is robust under varying welding currents and input disturbance.

9.1 Machine Algorithm Based Control

9.1.1 Experiment Data

Stainless steel pipe is welded using the DCEN GTAW process [128]. The material of the pipe is stainless steel 304. The outer diameter and wall thickness of the pipe are 113.5 and 2.03 mm, respectively. Six dynamic experiments have been conducted to model the correlation between the welding speed and 3D weld pool characteristic parameters. The welding speed is randomly changed from 0.5 mm/s to 1.5 mm/s. The welding current is from 40 A to 50 A to ensure full penetration occurs, yet keep unchanged during each experiment. The sampling period in this study is 0.5 s. Figure 9.1 plots the system input (welding speed) and outputs (weld pool width, length, and convexity). As can be observed, the weld pool parameters are fluctuating because of the changing welding

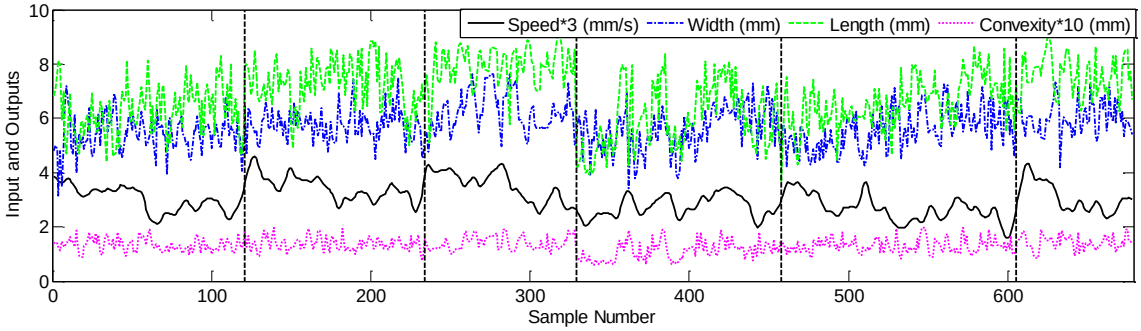

Figure 9.1 Measured system input (welding speed) and outputs (weld pool width, length, convexity) in six dynamic experiments.

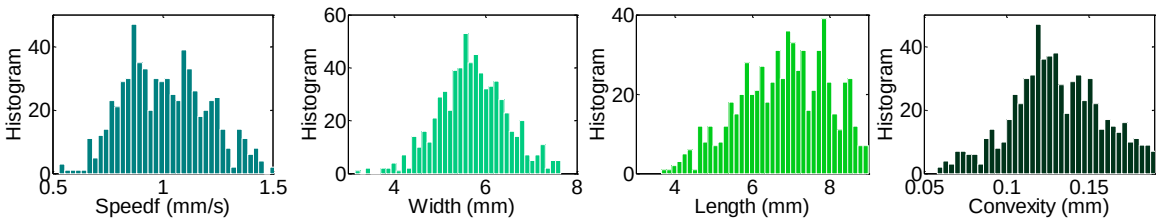

Figure 9.2 Histogram of the input and outputs in six dynamic experiments.

speed.

Figure 9.2 shows the histogram of the experimental data specified in Figure 9.1. It is observed that the welding speed ranges from 0.5 mm/s to 1.5 mm/s. Consequently, the weld pool width, length and convexity covers the range [4 mm, 7 mm], [3.5 mm, 8 mm], and [0.05 mm, 0.18 mm], respectively. The histogram and ranges that the inputs reside implies that the resultant model can be used to estimate the weld pool parameters if the welding speed falls within the range defined by this distribution.

9.1.2 System Modeling

In this section the system modeling is performed using the acquired welding speed and outputs (weld pool width, length, and convexity) data.

The heat input of the arc in a unit interval along the travel direction can be written as a nonlinear function of I^2 and $1/S$:

$$\Delta H \propto f\ (I^2, 1/S) \tag{9.1}$$

Roughly speaking, one can assume that the area of the weld pool is approximately proportional to the heat input. A linear model structure thus should be expressed as follows:

$$[W, L, C] \propto g\ (I, 1/\sqrt{S}) \tag{9.2}$$

where g's are linear functions of the current and square root of the reciprocal of welding speed. Given a constant welding current, the input of the system is defined as $u = 1/\sqrt{S}$. In the following subsections, MA and ARMA models are proposed and the model orders are carefully selected to form a linear model of the system output (i.e., weld pool parameters).

9.1.2.1 Moving Average (MA) Modeling

MA model is commonly used in linear system modeling and control applications. In this subsection, MA models are first considered with the following model structure [128]:

$$y(k) = \sum_{j=1}^{N} \beta_i u(k-j) + r \tag{9.3}$$

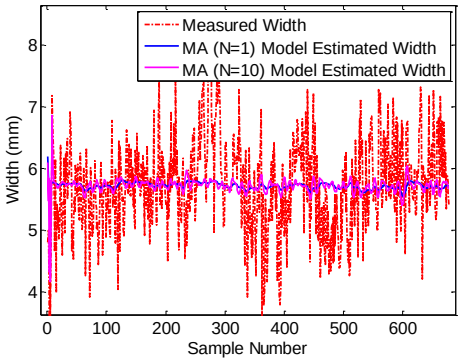

Figure 9.3 MA model fitting result for the weld pool width.

where $y(k)$ represents the weld pool parameters $[W, L, C]$ at instant k, β_i and r are MA model parameters, $u(k-j)$ are the system inputs, and N is the MA model order.

Modeling trails suggest that for our system, MA model (with only the input information) is not sufficient to capture the dynamic response of the weld pool parameters, even with large model orders. As an example, Figure 9.3 shows the MA model fitting result of the weld pool width with model order $N = 10$. As can be observed, constant fitting errors are observed. To better model the weld pool parameters, ARMA models with previous weld pool measurements are considered in the next subsection.

9.1.2.2 Auto-Regressive Moving Average (ARMA) Modeling

The linear models for the width, length, and convexity can be expressed as the following Auto Regression Moving Average (ARMA) models:

$$W(k)=\sum_{j=1}^{NP_W} a_W(j)W(k-j)+\sum_{j=1}^{NI_W} b_W(j)u(k-j) \tag{9.4}$$

$$L(k)=\sum_{j=1}^{NP_L} a_L(j)L(k-j)+\sum_{j=1}^{NI_L} b_L(j)u(k-j) \tag{9.5}$$

$$C(k)=\sum_{j=1}^{NP_C} a_C(j)C(k-j)+\sum_{j=1}^{NI_C} b_C(j)u(k-j) \tag{9.6}$$

where $W(k-j), L(k-j), C(k-j)$ are the weld pool width, length, and convexity at instant $k-j$, NP_W, NP_L, NP_C are the orders for the previous measurements, and NI_W, NI_L, NI_C are the orders for the input. $a_W(j), a_L(j), a_C(j)$ and $b_W(j), b_L(j), b_C(j)$ are the parameters for the ARMA models to be identified.

The model orders are selected based on evaluating the model errors and are visualized in Figure 9.4. RMSEs and average errors with respect to *NI* and *NP* for order from 1 to 20

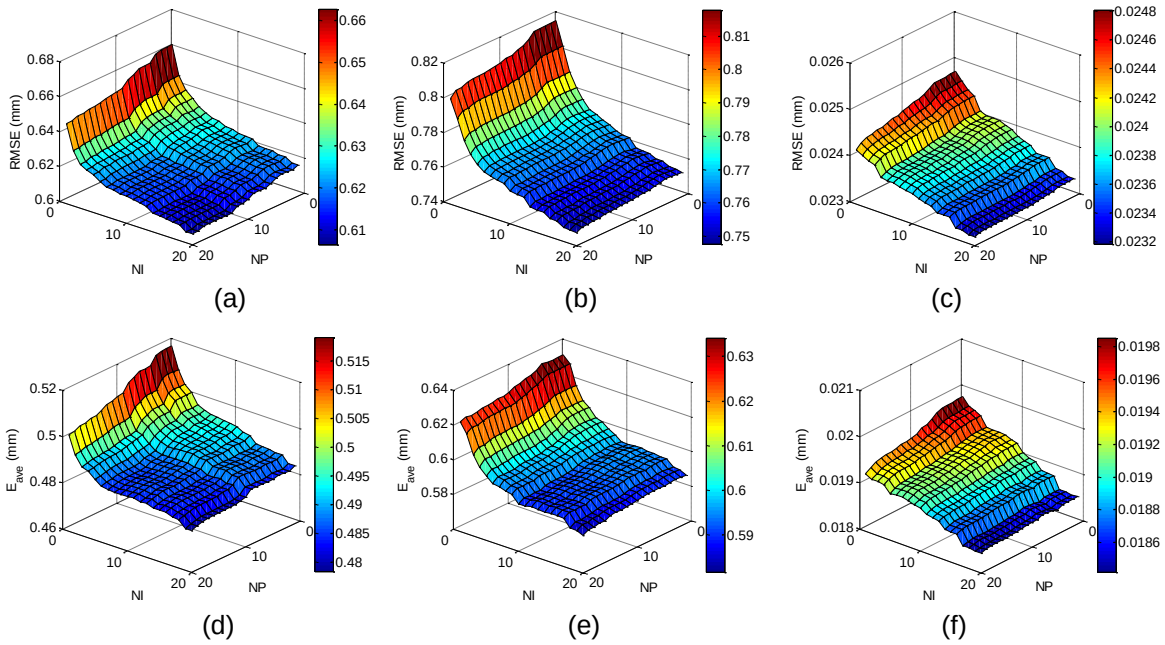

Figure 9.4 ARMA model errors with respect to order of previous input and order of input.

are plotted. For the width, it is observed that when NP_W is larger than 1, the differences in RMSE becomes negligible. In this sense, $NP_W = 1$ is selected. Similarly, the order of the input can be determined. For the weld pool length and convexity, identical procedure can be employed and the full set of model orders is listed in Table 9.1. It is noticed that statistical based method may also be employed to determine the model order, such as F-test. However, by visualizing the model errors for the width, length, and convexity, on the other hand, the trends of the errors with respect to the model orders are directly observed.

TABLE 9.1 MODEL ORDER SELECTION

	Previous measurements order	Input order
Width	1	3
Length	1	5
Convexity	1	5

TABLE 9.2 MODEL PARAMETERS

	Previous measurements	Input
Width	0.7273	[1.7093, -0.5674, 0.3929]
Length	0.8341	[1.0687, 0.5568, -0.1396, -1.0487, 0.6717]
Convexity	0.6589	[0.0480, -0.001609, -0.01991, -0.01368, 0.03125]

TABLE 9.3 MODEL ERRORS

	E_{ave} (mm)	$RMSE$ (mm)
Width	0.5172	0.6594
Length	0.6318	0.8118
Convexity (Linear)	0.0200	0.0250

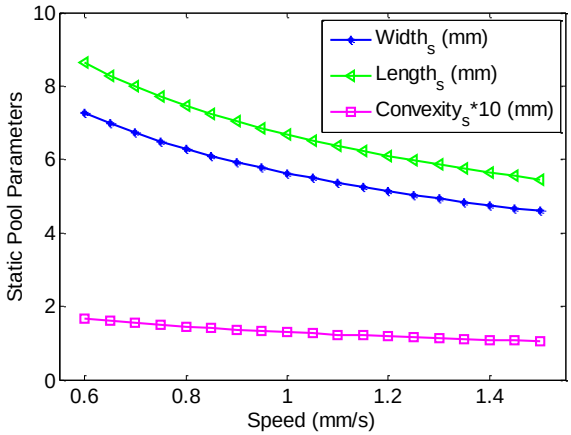

Figure 9.5 Steady state pool parameters.

9.1.2.3 Modeling Result and Analysis

Least squares algorithm is utilized to identify the model parameters in Equation (9.4-9.6). The identified model parameters are listed in Table 9.2. The fitting result is plotted in Fig. 8 and the model errors are shown in Table 9.3. It is observed that the identified model can correlate the weld pool parameters to the system input with acceptable accuracy. From Figure 9.5 it is shown that the proposed ARMA model is able to model the fluctuating weld pool parameters.

Steady state models for the width, length, and convexity are expressed as:

$$W_s = 5.6274/\sqrt{S} \tag{9.7}$$

$$L_s = 6.6846/\sqrt{S} \tag{9.8}$$

$$C_s = 0.1292/\sqrt{S} \tag{9.9}$$

Figure 9.5 plots the steady state width, length, and convexity for welding speeds from 0.6 mm/s to 1.5 mm/s. It is observed that as the welding speed increases, the width, length, and convexity all decrease. This is understandable because the increase in welding speed significantly decrease the heat input, which is a major source to influence the weld pool shape. A decreased heat input causes the decrease in the pool width and length. Because the amount of metals melted is also decreased, the convexity tends to decrease as well.

9.1.3 Model Predictive Control Algorithm

In this section an analytical solution to the proposed ARMA model predictive control algorithm is derived.

9.1.3.1 MPC Algorithm

At instant k, the controller needs to determine the control action $u(k)$ based on the feedback/current movement speed $s(k)$ to drive the human hand to a desired movement speed. In a predictive control, prediction equations should be first developed to predict the output based on the inputs.

According to Equation (9.4-9.6), the system incremental model can be expressed as:

$$W(k)=a_W W(k-1)+\sum_{j=1}^{3} b_W(j)u(k-j) \tag{9.10}$$

1-step-ahead prediction of the weld pool width yields:

$$\begin{aligned} W(k+1) &= a_W W(k)+\sum_{j=1}^{3} b_W(j)u(k+1-j) \\ &= a_W W(k)+\sum_{j=2}^{3} b_W(j)u(k+1-j)+b_W(1)u(k) \end{aligned} \tag{9.11}$$

Similarly, 1-step-ahead predictions of the length and convexity are expressed as:

$$L(k+1)=a_L L(k)+\sum_{j=2}^{5} b_L(j)u(k+1-j)+b_L(1)u(k) \tag{9.12}$$

$$C(k+1)=a_C C(k)+\sum_{j=2}^{5} b_C(j)u(k+1-j)+b_C(1)u(k) \tag{9.13}$$

In order to achieve a desirable control, it is required the following cost function is minimized:

$$\begin{aligned} J(k,u) &= \left(W(k+1)-W^*(k+1)\right)^2+\eta_1\left(L(k+1)-L^*(k+1)\right)^2 \\ &+\eta_2\left(C(k+1)-C^*(k+1)\right)^2 \end{aligned} \tag{9.14}$$

where $y^*(k+1)\in\left[W^*(k+1) \quad L^*(k+1) \quad C^*(k+1)\right]$ represents the desired set-point for 1-step prediction, η_1 and η_2 are the relative coefficients for the length and convexity, respectively. In this study it is chosen based on pool parameters' importance relative to the weld penetration specified in [55]:

$$w_b = 1.79W-0.57L-10.8C-0.99 \tag{9.15}$$

η_1=0.57/1.79=0.32 and η_2 =10.8/1.79=6.03 are thus chosen.

The desired set-point for 1-step prediction should be designed depending on the application being addressed. In this study the desired 1-step set-point $y^*(k+1)$ is defined as:

$$y^*(k+1)=\gamma y(k)+(1-\gamma)y_c(k+1) \tag{9.16}$$

where $y_c(k)$ represents the desired weld pool parameters (width, length, and convexity), and $\gamma \in (0,1)$ is the smoothing coefficient. As γ becomes larger, the system will track the set point with slower speed but better robustness and smoothness. In this study γ=0.5 achieves an appropriate tradeoff between response speed and robustness.

The fluctuations in the input will generate non-smooth human adjustment and degrade human tracking performance, which is not desirable in our application. Thus, energetic control actions must be avoided. The modified following cost function is used to penalize changes in control:

$$\begin{aligned} J(k,u) &= \left(W(k+1)-W^*(k+1)\right)^2+\eta_1\left(L(k+1)-L^*(k+1)\right)^2 \\ &+\eta_2\left(C(k+1)-C^*(k+1)\right)^2+\lambda_1\left(u(k)-u(k-1)\right)^2 \\ &+\lambda_2\left(u(k)-u^*(k)\right)^2 \end{aligned} \tag{9.17}$$

where λ_1 is the penalty weight on the control change, which can be determined based on the scale of the static gain to the output. In this study $\lambda_1=5^2\left(mm^2/mm/s\right)$ is chosen. This implies that an error of 1 mm in the width has the same contribution to the cost function as the input change of $5/\sqrt{mm/s}$. λ_2 is the penalty weight on the control signal deviation from the expected welding speed value, which represents another constraint on the speed control based on authors' previous study on human welder's intelligence learning and control [123]. In this study $\lambda_2=1^2\left(mm^2/mm/s\right)$ is chosen.

The control law is calculated such that:

$$\partial J(k,u)/\partial u=0 \tag{9.18}$$

The control signal is finally expressed as:

$$u(k)=-N/D \tag{9.19}$$

where

$$D = b_W^2(1) + \eta_1 b_L^2(1) + \eta_2 b_C^2(1) + \lambda_1 + \lambda_2 \tag{9.20}$$

$$\begin{aligned} N = {} & b_W(1)\left[a_W W(k) + \sum_{j=2}^{3} b_W(j) u(k+1-j) - W^*(k+1) \right] \\ & + \eta_1 b_L(1)\left[a_L L(k) + \sum_{j=2}^{5} b_L(j) u(k+1-j) - L^*(k+1) \right] \\ & + \eta_2 b_C(1)\left[a_C L(k) + \sum_{j=2}^{5} b_C(j) u(k+1-j) - C^*(k+1) \right] \\ & - \lambda_1 u(k-1) - \lambda_2 u^*(k) \end{aligned} \tag{9.21}$$

It is apparent that (9.21) provides a closed form solution and no online optimization is required. Thus, the obtained control algorithm can be easily incorporated into the real-time welder training applications.

9.1.3.2 Controller Simulation

In this section the controller is simulated and the results are analyzed. Open-loop control is first simulated and the result is plotted in Fig. 10. From 0 s to 20 s, the welding speed is set at 1.4 mm/s, and the weld pool width, length, and convexity is 4.8 mm, 5.8 mm/s, and 0.1 mm, respectively. From 20 s to 40 s, the welding speed is changed to 1.2 mm/s. The weld pool parameters are thus gradually reach different steady state values. The settling time is about 4 s for the width, 5 s for the length, and 3 s for the convexity. For 40 s to 60 s, 60 s to 80 s, and 80 s to 100 s, the welding speed is set to 1.0 mm/s, 0.8 mm/s, and 0.6 mm/s, respectively. With no closed-loop control, the weld pool parameters cannot be maintained at a desired value.

Fig. 11 shows the simulation result with proposed closed-loop control algorithm. From 0 s to 15 s is open-loop control period, with the welding speed set at 1.4 mm/s. From 15 s to 60 s, the desired pool parameters are set at [7 mm, 8 mm, 0.16 mm]. The controller is

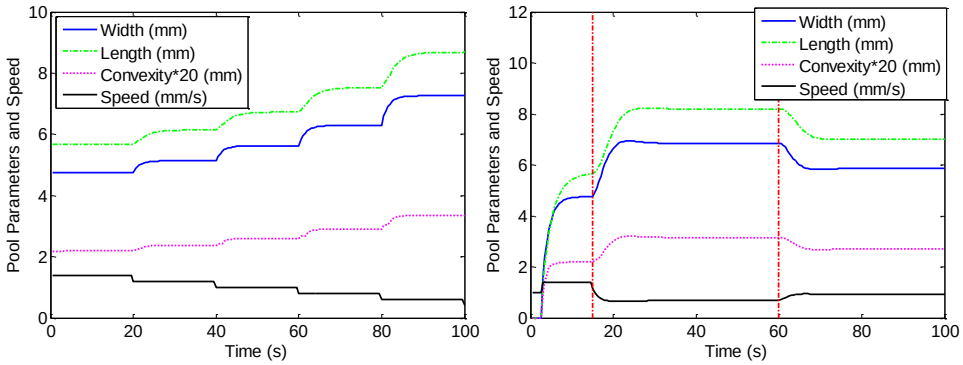

Figure 9.6 (a) Open loop simulation result. (b) Closed loop simulation result.

able to adjust the welding speed to 0.7 mm/s. It is noticed that the weld pool cannot reach the exact set-point as specified. It is expected because the formation of the weld pool is a physical process, and thus cannot be specified arbitrarily. From 60 s to 100 s, the desired pool parameters are set at [6 mm, 6.5 mm, 0.13 mm]. The welding speed is controlled at 0.9 mm/s. The weld pool parameters are controlled at [5.9 mm, 6.8 mm, 0.14 mm]. To further demonstrate the controller's performance, in the next section automated welding experiments are conducted and the results are analyzed.

9.1.4 Automated Welding Experiments

Automated control experiments have been designed and conducted in this section. In subsection 9.1.4.1, different set-points are applied. In subsection 9.1.4.2 and 9.1.4.3 different welding current and speed disturbance are applied respectively, and the robustness of the controller is tested.

9.1.4.1 Experiment 1: Tracking Varying Set-Point

In this subsection control experiment is conducted for tracking the varying set-point. An open-loop period is firstly applied to establish the weld pool. From 57 s to 85 s the set-point is set at [4.5 mm, 6.5 mm, 0.11 mm], and from 40 s to 60 s the set-point is changed to [5 mm, 6 mm, 0.1 mm]. It is observed that the controller is able to control the weld pool characteristic parameters by increasing the welding speed from 0.7 mm/s to 0.75

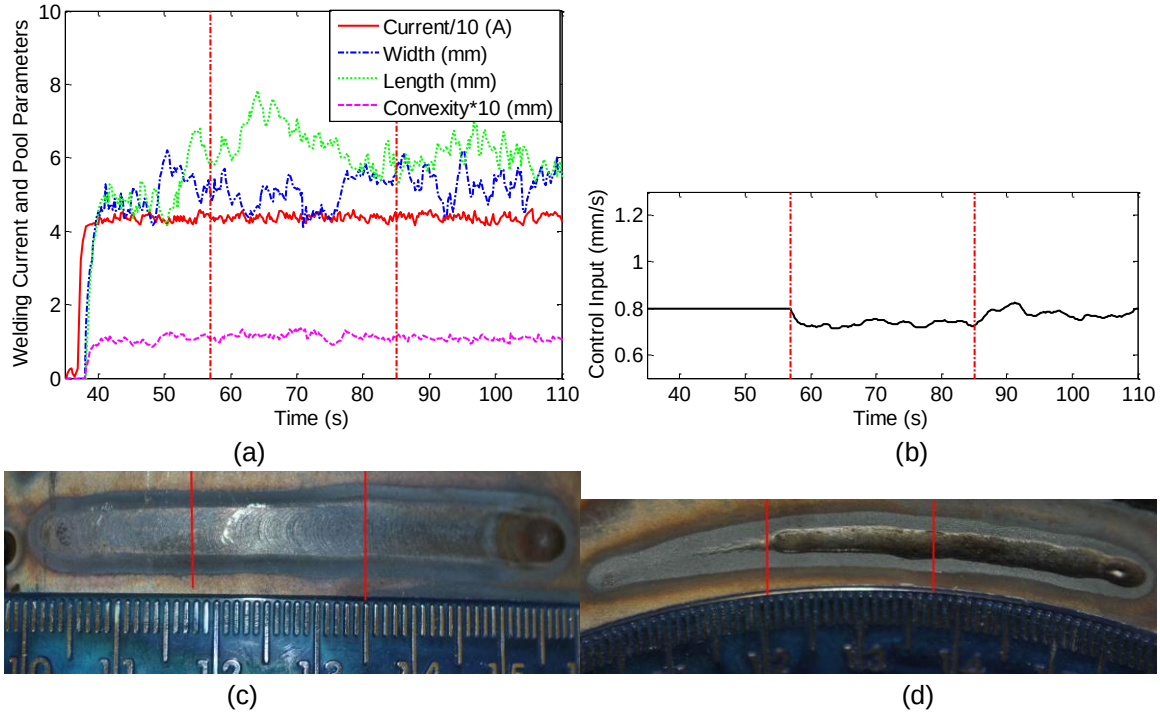

Figure 9.7 Experiment 1 results (a) Welding current and weld pool parameters (b) Control input (c) Front-side bead (d) Back-side bead.

mm/s. The back-side bead width is maintained at about 3 mm (Figure 9.7(d)).

It is noticed, however, that small variations do occur and the weld pool characteristic parameters are not accurately controlled at their set-points. This is expected because the pool parameters are governed by physical law and controlling welding speed is not sufficient to control three pool parameters.

9.1.4.2 Experiment 2: Current Disturbance

In this experiment the robustness of the control algorithm against different welding current is tested. From 60 s to 80 s, the welding current is 43 A. The controller is able to bring the pool parameters to about the set-point [5 mm, 6 mm, 0.1 mm] by adjusting the welding speed to 0.72 mm/s. After 80 s, the welding current is set at 46 A. As the result, the weld pool width, length and convexity increase. However, the controller is able to increase the welding speed to about 0.9 mm/s to compensate this heat input increase (see Figure 9.8 (b)). The back-side bead width is maintained at about 3 mm (Figure 9.8(d)).

9.1.4.3 Experiment 3: Speed Disturbance

In experiment 3, an artificial error between the actual and measured values of the welding speed is applied to evaluate the robustness of the proposed control algorithm against speed disturbances. During the first 28 s after the open-loop period, no error exists between the measured speed and actual speed, and the controller is able to control the

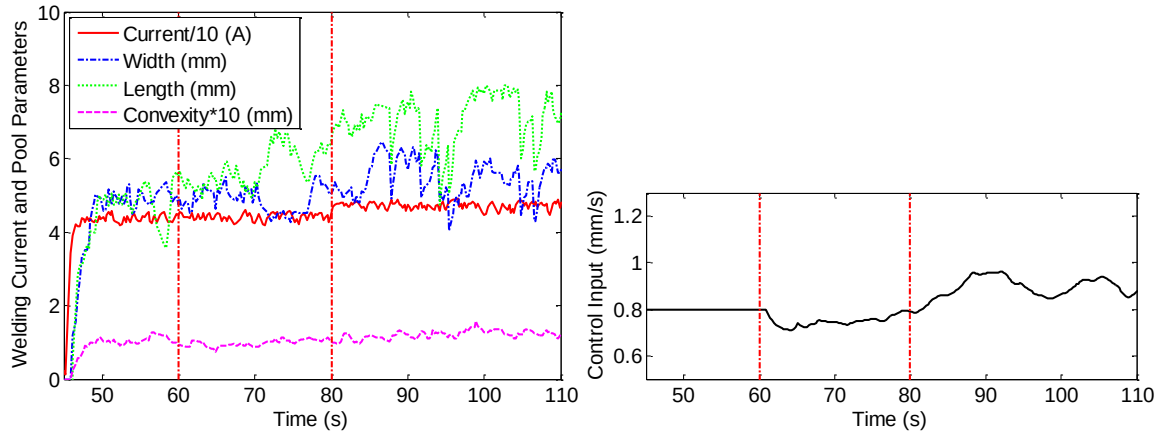

(a) (b)

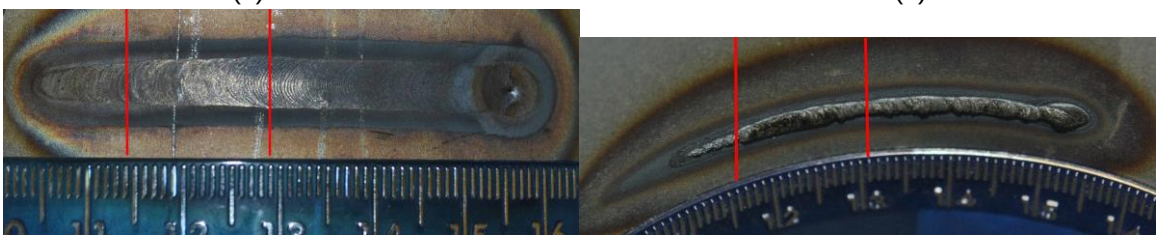

(c) (d)

Figure 9.8 Experiment 2 results (a) Welding current and weld pool parameters (b) Control input (c) Front-side bead (d) Back-side bead.

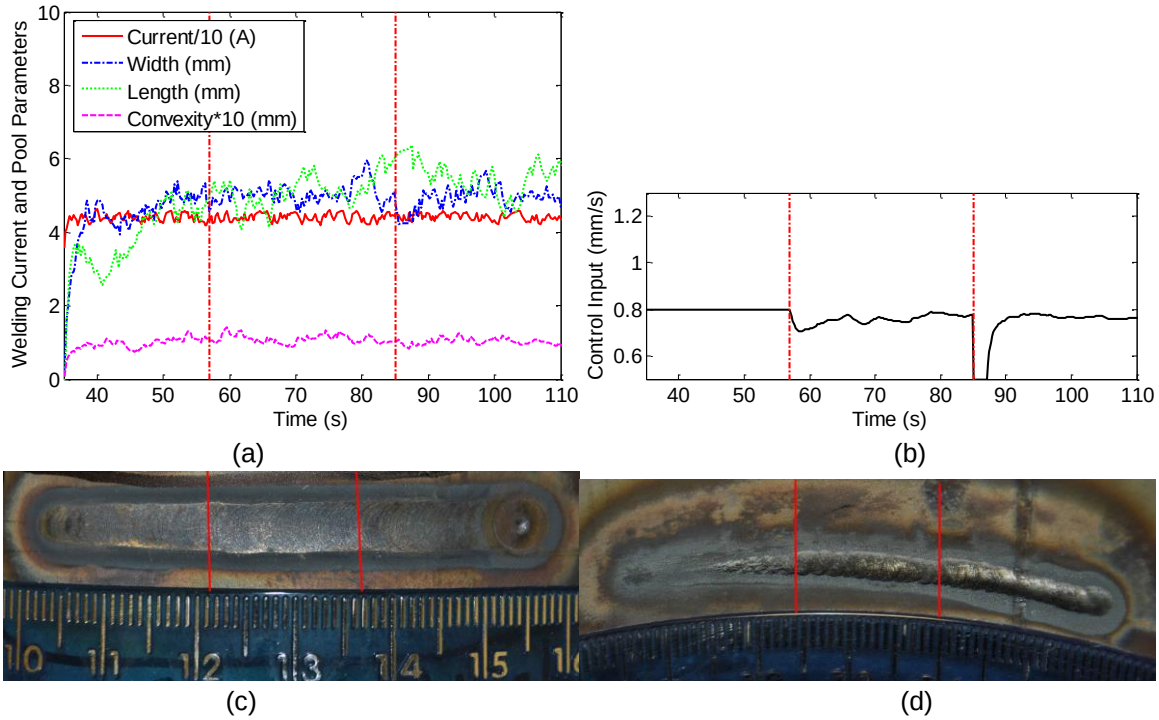

Figure 9.9 Experiment 3 results (a) Welding current and weld pool parameters (b) Control input (c) Front-side bead (d) Back-side bead.

pool parameters to the set-point [4.5 mm, 4.5 mm, 0.11 mm]. However, from 85 s to 87 s, the welding speed is set to 0.5 mm/s, which is about 0.23 mm/s larger than the calculated welding speed. As can be seen from Figure 9.9 (a) the weld pool width decreases, and the length increases. However, by applying the controller the desired pool parameters and consequent back-side penetration is maintained at about 3 mm (Figure 9.9(d)). This experiment shows that the developed close-loop control system is robust to the disturbance in the welding speed.

9.2 Data Fusion Algorithm

Three criteria are proposed to evaluate the performance of the data fusion models: Mean, Variance of the rating, and root mean square of input change (RMSIC)

$$RMSIC = \sqrt{\sum_{k=2}^{n}(u(k)-u(k-1))^2 \Big/ (n-1)} \tag{9.22}$$

where n is the number of data points, $u(k)$ is the calculated speed adjustment at instant k.

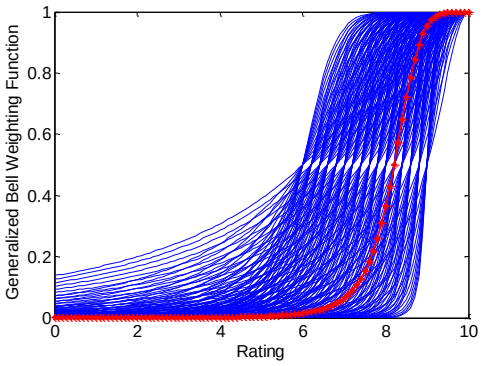

Figure 9.10 Fuzzy weighting function sets and selected fuzzy weighting function.

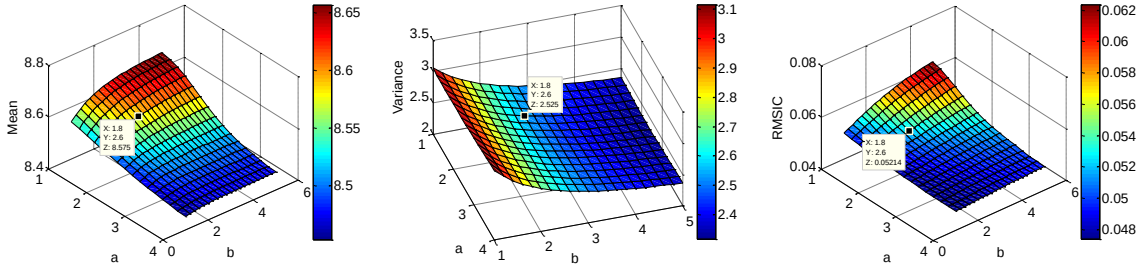

Figure 9.11 Mean, variance, and RMSIC versus generalized bell fuzzy MF parameters.

9.2.1 Fuzzy Labeling Based Data Fusion Algorithm

With the proposed welder rating system described in section 8.2, given a 3D weld pool characteristic and welding speed adjustment, a fuzzy label can thus be calculated as a rating or confidence level for a particular speed adjustment [129].

An intuitive approach to fuse the speed adjustments calculated by three algorithms detailed in Section III would be simply selecting the calculated speed that achieves highest rating. The rating would thus always be optimal. This data fusion algorithm is referred to as "data fusion 1":

$$S_{df1}(k) = \underset{\max R_i(k)}{\arg} S_i(k) \tag{9.23}$$

where $S_i(k), i = 1,2,3$ is the welding speed calculated by i^{th} algorithm at instant k, R_i is the corresponding rating, and $S_{df1}(k)$ is the fused welding speed by data fusion 1.

However, from simulation results (depicted in Figure 9.12) it is observed that the aggressively searching for highest rating results in constantly switching from one algorithm to another. The welding speed output calculated by the data fusion algorithm has energetic adjustment. This welding speed, if applied to the welding process, could generate non smooth welds, which is not acceptable in our application. In the next subsection, an improved data fusion algorithm by fuzzy weighting is proposed.

9.2.2 Improved Date Fusion by Fuzzy Weighting

Generalized bell fuzzy MF is utilized in this study to provide smooth weighting of three algorithm outputs:

$$A_i(R_i;a,b,c)=\frac{1}{1+\left|\left(R_i-c\right)/a\right|^{2b}} \tag{9.24}$$

where a,b,c are the input fuzzy MF parameters.

The modified data fusion algorithm based on fuzzy weighting, referred to as "data fusion 2", is finally expressed as:

$$S_{df\,2}(k)=\sum_{i=1}^{N}A_i(k)S_i(k)\Big/\sum_{i=1}^{N}A_i(k) \tag{9.25}$$

where $S_{df\,2}$ is the optimal welding speed calculated by "data fusion 2".

The input fuzzy MF parameters a,b,c in equation (9.24) need to be carefully selected. Among these input parameters, c stands for the center of the fuzzy MF, thus c =10. Figure 9.10 plots the MFs with ranges $a=[1,4],b=[1,5]$. It is observed that with the specified input parameter ranges, different ratings can be assigned to different fuzzy weightings. Specifically, a steep MF indicates a more aggressive weighting where relatively small ratings have nearly zero weightings. While a shallow MF indicates a more average weighting effect, where speeds from a large range of ratings are all considered. Figure 9.11 visualizes the effect of parameters a,b on the data fusion performance. The objective is to select a,b such that the mean of the rating is large, variance of the rating is small, and RMSIC of the speed input is small. It is observed that when $a=1.8$ and $b=2.6$, a good trade-off is made among these three contradictory performance measures.

It is apparent that (9.25) provides a convenient way to fuse the welding speed from different machine algorithms. Since the proposed welder rating system represented by an ANFIS model and fuzzy weighting does not require online optimization, the obtained data fusion method can be easily incorporated into the real-time automated welding process control and welder training applications.

9.3 Simulation

In this section three algorithms introduced in chapter 7-9 and two data fusion algorithms are simulated on data set depicted in Figure 8.1, and the results are analyzed in detail.

Figure 9.12 plots the calculated welding speeds and their corresponding ratings. Comparing noVR welder, VR welder, and super welder models, neither one algorithm is always superior to the other two algorithms. Specifically, from sample 200 to 220, super welder model achieves highest ratings, and noVR welder outputs a relatively low ratings. Data fusion 1 thus select welding speed calculated by super welder model. From sample 230 to 240, noVR welder and VR welder model output nearly identical welding speeds, and data fusion 1 algorithm selects this welding speed. However, from sample 250 to 280, welding speeds calculated by data fusion 1 is constantly switching between different models. Data fusion 2, on the other hand, outputs a relatively smooth welding speeds, yet preserves a relatively high rating. From sample 1060 to 1070, super welder model and VR welder model perform worse than noVR welder model and the corresponding ratings are lower than 8. Both data fusion 1 and data fusion 2 models can output a welding speed of about 0.78 mm/s, and the corresponding ratings are much higher than super welder

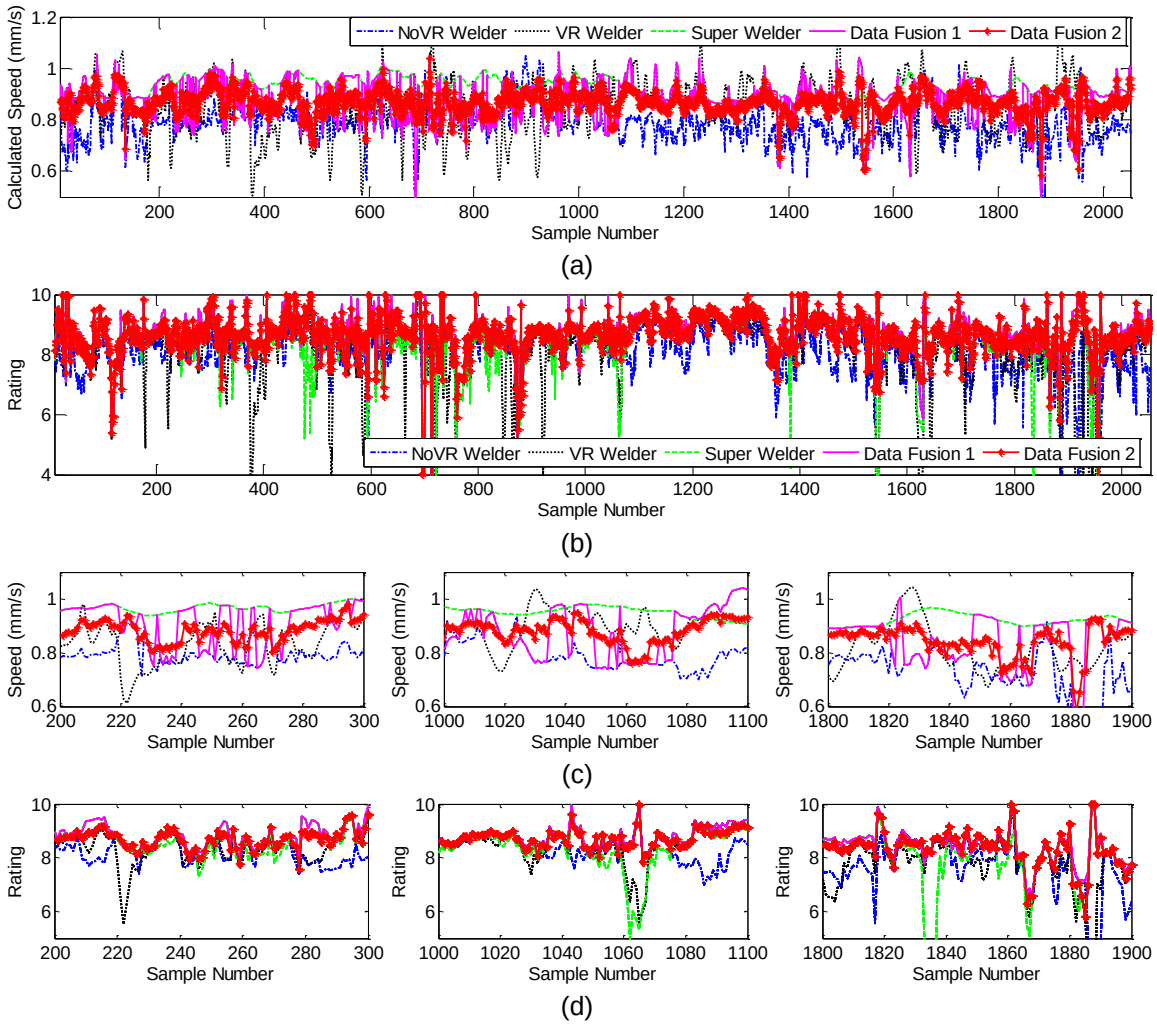

Figure 9.12 Simulation results. (a) Calculated welding speeds by noVR welder, VR welder, super welder, data fusion 1 and 2 algorithms; (b) corresponding ratings (c) (d) detailed welding speed and rating from sample 200-300, 1000-1100, and 1800-1900.

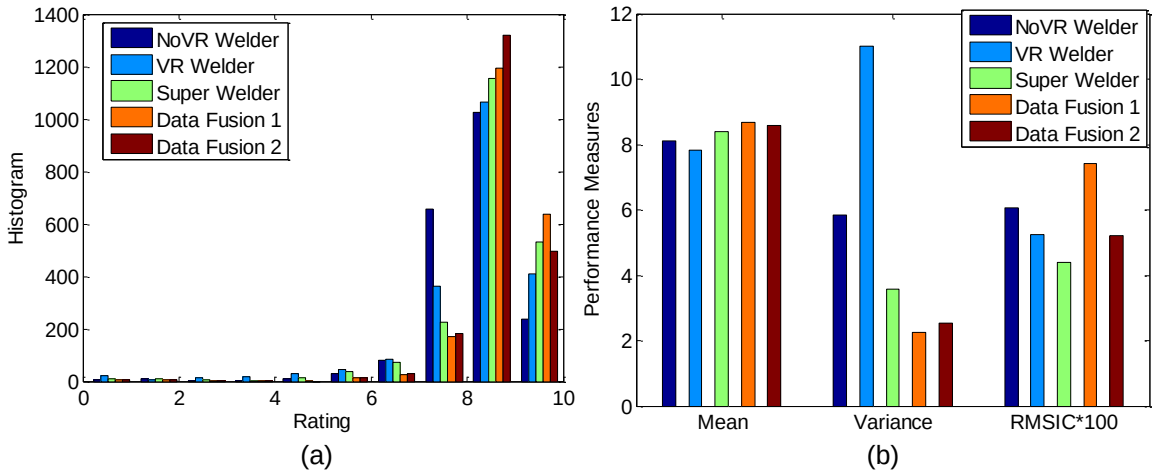

Figure 9.13 (a) Histogram of the ratings for data set depicted in Figure 8.1 (b) Performance measures for data set depicted in Figure 8.1.

model and VR welder model. Comparing data fusion 1 and data fusion 2 algorithms from sample 1820 to 1880, it is observed that data fusion 2 algorithm is able to output a nearly identical rating, yet prevent large energetic change in the welding speed outputted from data fusion 1 algorithm.

Figure 9.13(a) depicts the histogram of the ratings obtained by different algorithms. Comparing NoVR welder, VR welder, and super welder model, all three algorithms has few calculated speeds that have ratings smaller than 8. This indicates that all algorithms are acceptable in controlling the welding process, and can be applied individually. VR welder model has more ratings equals 8 and less ratings 9 and 10 than other two models, which indicates that VR welder model does not perform as good as other two models. This is understandable because NoVR model employs a data selection procedure which selects only good data points for modeling, while super welder model is based on model predictive control to optimize welding speeds. Comparing data fusion 1 and data fusion 2, it is observed that data fusion 1 has slightly more 10 ratings than those obtained from data fusion 2; although majority of these two data fusion algorithms are rated either 9 or 10. However, if we compare performance measures (detailed in Figure 9.13(b)), it is clearly shown that although data fusion 1 and 2 achieves similar mean and variance of the rating, data fusion 2 has a much smaller RMSIC, indicating a much smoother welding speed adjustments.

9.4 Automated Control Experiments

In order to demonstrate the robustness of the developed data fusion algorithm, automated welding experiments have been designed and conducted in this section under varying welding current and speed disturbance.

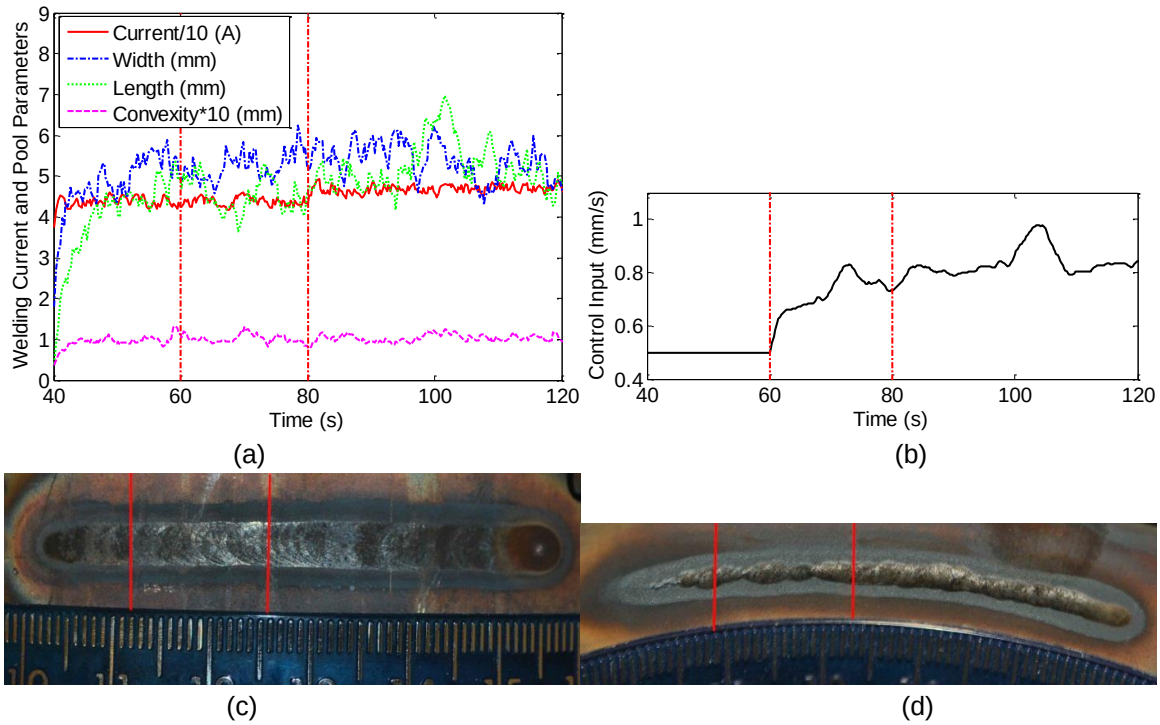

Figure 9.14 Experiment 1 results (a) Welding current and weld pool parameters (b) Control input (c) Front-side bead (d) Back-side bead.

9.4.1 Experiment 1: Varying Welding Current

In this experiment control experiment is conducted under varying welding currents. An open-loop period (from 40 s to 60 s) is first applied to establish the weld pool and weld penetration. From 60 s to 80 s the welding current is 43 A, and from 80 s to 120 s the welding current is 46 A (Figure 9.14(a)). It is observed that the controller is able to control the welding speed accordingly (about 0.7 mm/s for 43 A welding current and 0.8 mm/s for 46 A welding current in Figure 9.14(b)), and maintain a consistent back-side bead width (about 3 mm in Figure 9.14(d)).

It is noticed, however, that small speed variations do occur during the experiment (e.g., the speed is increased from 0.8 mm/s to 1 mm/s from 100 s to 110 s). This is because the weld pool width, length and convexity are increased due to un-modeled welding parameters. However, the data fusion controller is able to adjust the welding speed to maintain a consistent weld penetration.

9.4.2 Experiment 2: Input Disturbance

In this experiment the robustness of the control algorithm against input disturbances is evaluated. An artificial error between the calculated and applied values of the welding speed is applied. In the first 25 s after open-loop period, no error exists between the calculated speed and applied speed. The controller is able to bring the back-side bead width to about 3 mm (Figure 9.15(d)). During 85 s to 87 s, the welding speed is set at 0.5

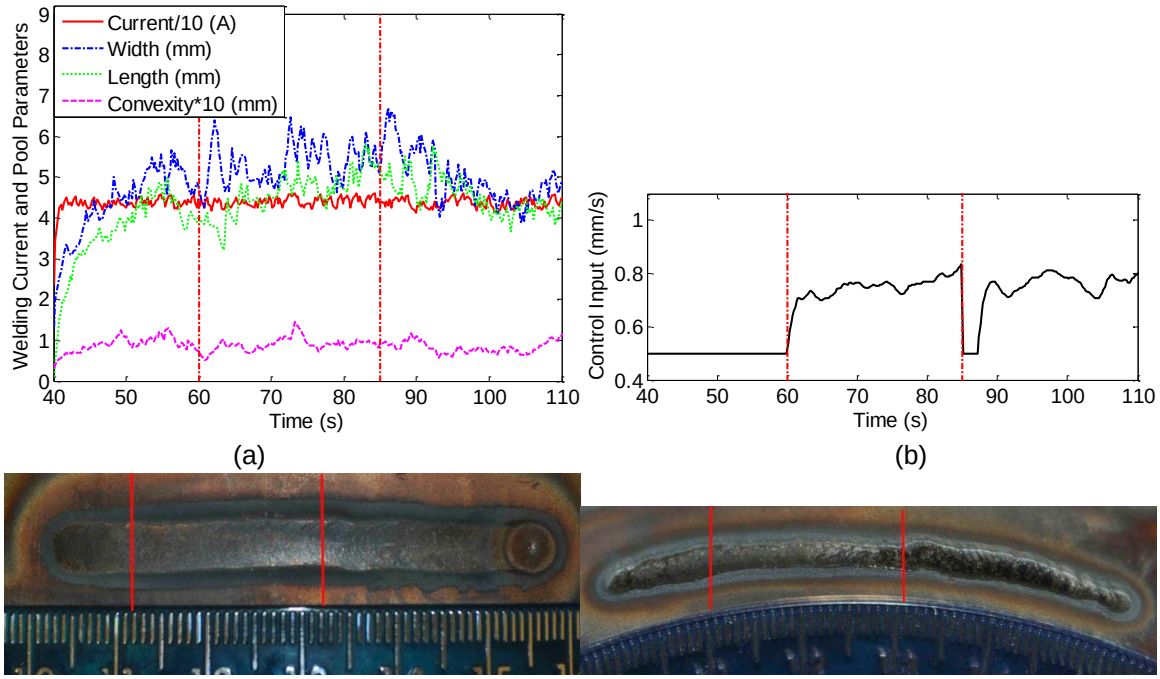

Figure 9.15 Experiment 2 results (a) Welding current and weld pool parameters (b) Control input (c) Front-side bead (d) Back-side bead.

mm/s. As the result, the weld pool width is increased to 6.5 mm, length is decreased to 4.5 mm, and convexity is also decreased to 0.09 mm (see Figure 9.15 (a)). The back-side bead width is also increased (Figure 9.15(d)). However, the controller is able to adjust welding speed back to about 0.8 mm/s (see Figure 9.15 (b)), and the back-side bead width is maintained around the desired value (3 mm) again with a relatively quick response time.

9.5 Summary

In this chapter a fuzzy weighting based data fusion approach to combine different machine and human intelligent model is proposed for developing intelligent welding robot in pipe GTA Welding. Simulation results confirm that the proposed fuzzy weighting based data fusion algorithm can obtain a good trade-off between high rating and smooth speed adjustment. Automated welding experiments are conducted and results show that the proposed data fusion based welding speed controller is robust under different welding current and input disturbance.

Chapter 10 Full 3D Position and Orientation Learning and Control

In previous chapters, welding speed adjustment made by the human welder are learned and transferred to the welding robot to perform automated welding. Actually the welding parameters in GTAW include welding current and speed, arc length, and torch orientations, etc. Both welding current and speed can significantly affect the heat input into the welding process and thus influencing the weld pool surface geometry and weld penetration considerably. Arc length also has certain impact on welding arc's penetration capabilities. Because the welding current in GTAW is controlled by the constant current power supply, an increase in the arc length results in an increase in the arc voltage and arc power. However, the distribution of the arc energy is decentralized such that the efficiency of the arc and the penetration capability might decrease consequently. Torch orientations are also considered to be correlated to the weld quality and appearance. Inappropriate torch manipulations may cause weld defects including undercut, porosity, and cracks. In this chapter a virtualized welding platform detailed in Chapter 6 is utilized to perform teleoperated training experiments, an ANFIS based data-driven approach to model the human welder's adjustments in 3D is proposes, and this model is transferred to the welding robot to perform automated welding [130].

10.1 Human Motion Analysis

Human hand motion consists of both deterministic and stochastic movement. By utilizing the leap motion sensor, fine human hand movement can be accurately detected and recorded. However, it is not clear when the teleoperation training experiments are conducted, what types of human hand motion should be followed by the robot. If the stochastic and high frequency human hand tremor or large movement is transferred to the robot, the robot tracking performance cannot be guaranteed.

To analyze the human hand motion, ten experiments are conducted where human welder moves the virtual welding torch along the mock-up pipe, and his/her movement is recorded by the leap sensor. Figure 10.1 depicts human hand motion in a sample experiment. It is seen that human moves the virtual welding torch along x axis (i.e., welding direction), from -20 mm to 20 mm (corresponding to about -20 degree to 20

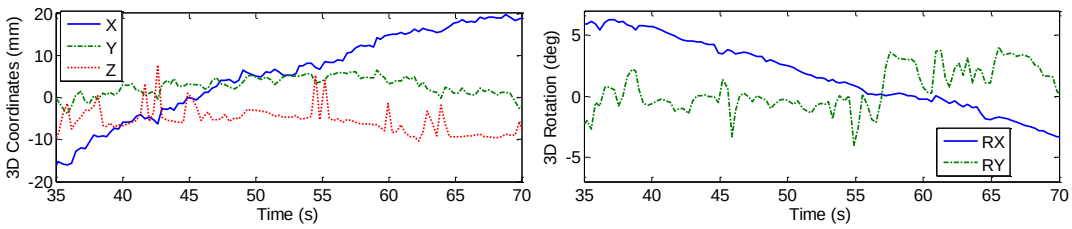

Figure 10.1 Sample human hand motion captured by leap sensor for movement along the pipe.

degree relative to the vertical direction). Sudden movements along z axis (i.e., arc length) are also observed. For example, from 42 s to 43 s, movement along z axis fluctuates between -8 mm and 8 mm. This type of movement is considered as noise and should not be followed by the robot. Movement along y axis (perpendicular to the welding direction) should be following the shape of the weld seam. For our application which is pipe welding along a straight line, y coordinate should kept constant (0 mm in this study). However, from Figure 10.1 it is observed that y coordinates vary from -2 mm to 3 mm. This is expected because the human welder movement includes the stochastic part, thus can't be accurately controlled like the welding robot. RX movement, i.e., rotation along the welding direction ranges from -4 degree to 6 degree in this sample experiment. For automated welding machines, RX is normally kept perpendicular to the pipe surface. For manual welding process, however, this rotation along the welding direction is controlled

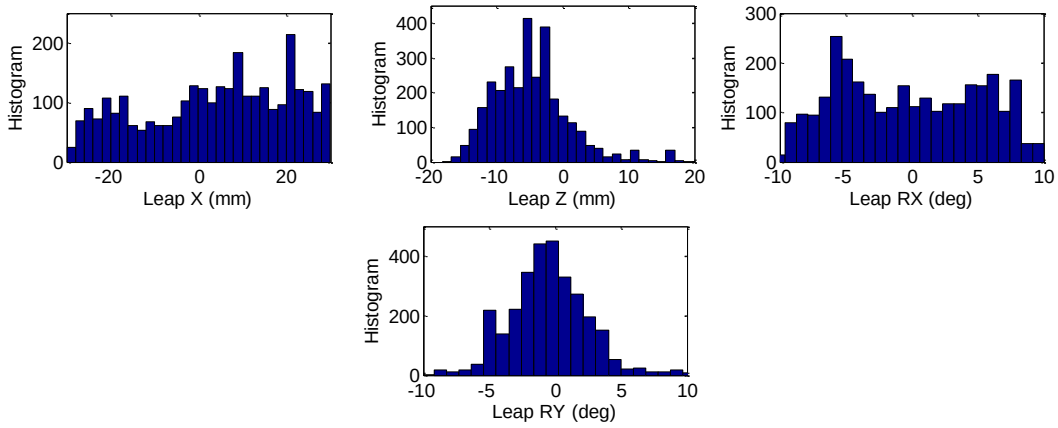

Figure 10.2 Histograms for human adjustments in ten experiments.

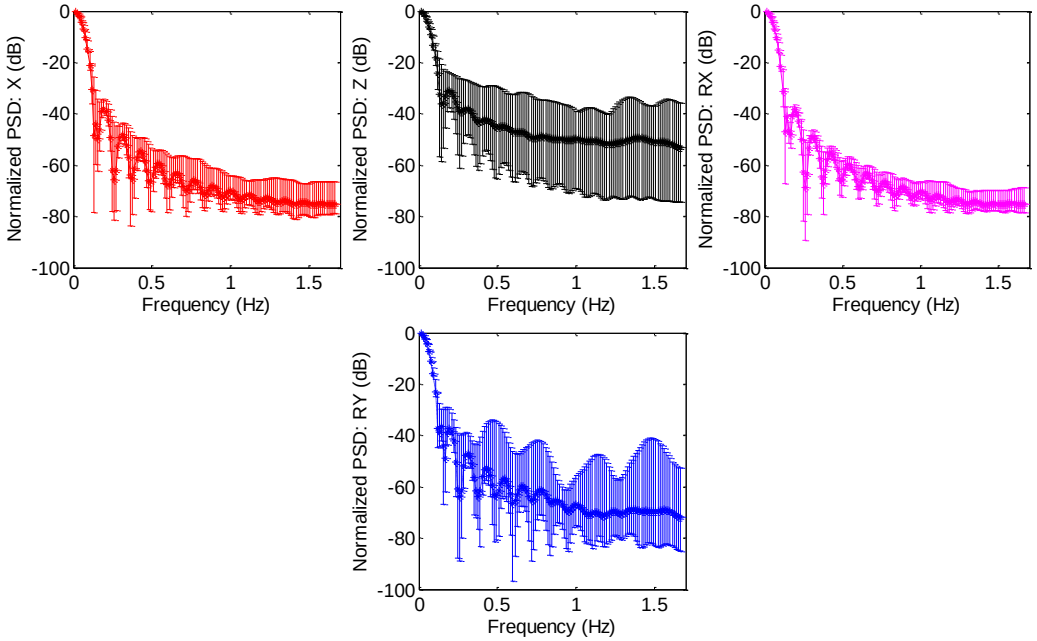

Figure 10.3 Normalized PSDs for human adjustments in ten experiments.

by the human welder. RY, i.e., rotation perpendicular to the welding direction, ranges from -4 degree to 4 degree with certain fluctuations. RZ, or rotation along the welding torch, does not affect the welding performance and is thus not considered in this study. To summarize, four human movements are considered: X, Z, RX, RY, which correspond to the welding speed, arc length, orientation along and perpendicular to welding direction, respectively.

Figure 10.2 plots the histograms for these four movements in ten experiments. Figure 10.3 depicts the Power Spectral Density (PSD) in these experiments. It is observed that coordinate and orientation along welding direction (X and RX) have smaller variation in PSD than Z and RY movements. The following low-pass filter is proposed to filter the human hand motion:

$$m_{i,f}(k)=\alpha_{i,f} m_{i,f}(k)+(1-\alpha_{i,f})m_i(k) \tag{10.1}$$

where $m_{i,f}(k), i=1,...,4$ is the filtered movement for X, Z, RX and RY at instant *k*, $\alpha_{i,f}$ is the corresponding filtering coefficient, and $m_i(k)$ is the measured movement at instant *k*.

From Figure 10.3 it is observed that different filtering coefficients should be applied for different movements. In this study $\alpha_{i,f}=[0.1,0.7,0.15,0.5]$, selected based on each movement's PSD variances ($\text{var}(\text{PSD}_i)=[19.2,98.6,11.9,67.5]$). In the next section, teleoperated training experiments are conducted where the filtered human motion are tracked by the welding robot, and the experimental data are presented / analyzed.

10.2 Training Experiment and Data Analysis

10.2.1 Training Experiments

In the training experiments pipe welding is performed using the direct current electrode negative GTAW process. The welding position is 5G (i.e., the pipe stays stationary during welding, and the welding torch moves along the weld joint). The material of the pipe is stainless steel 304. The outer diameter and wall thickness of the pipe are 113.5 and 2.03 mm, respectively. Seven training experiments are performed by a human welder to model the correlation between the weld pool characteristic parameters (weld pool width, length, and convexity) and human hand movements. In these experiments the welding current is randomly changed from 40 A to 48 A resulting in a fluctuating weld pool surface. The welder adjusts the movement based on the weld pool image feedback; the adjustments (X, Z, RX, and RY) are measured by leap sensor, filtered using Equation (1), and sent to the robot. The robot follows the welder's movement and completes the welding task. Three weld pool characteristic parameters are selected as the system inputs, which are considered as the major sources a human welder perceives to complete the welding tasks. Four human welder movements are the system outputs. The sampling

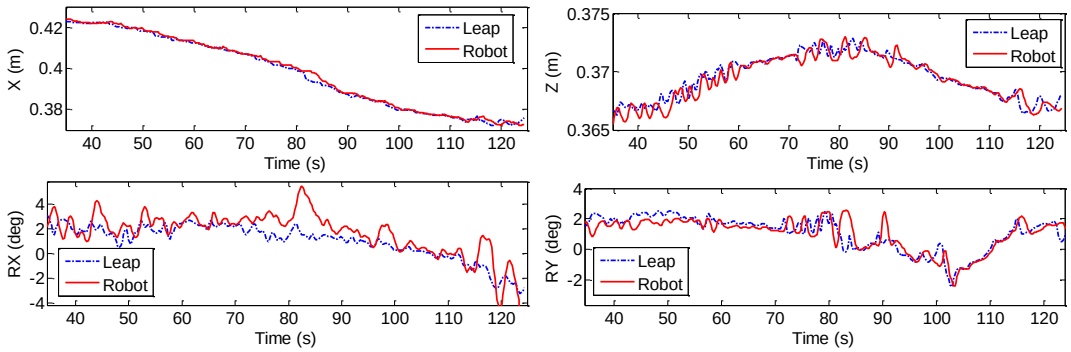

Figure 10.4 Robot tracking performance in a sample teleoperation learning experiment.

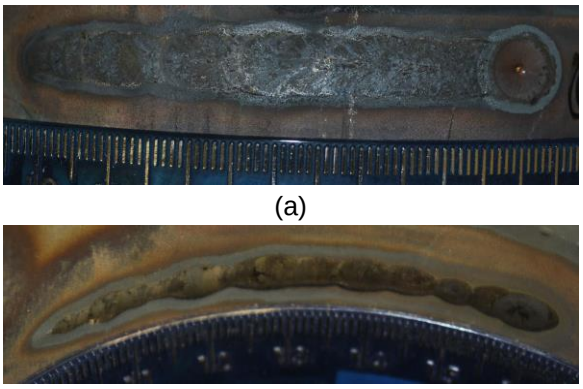

(a)

(b)

Figure 10.5 Front-side (a) and back-side (b) weld bead in the sample teleoperation learning experiment in Figure 10.4.

frequency in this study is 3 Hz because the welder controls the torch movement by observing the weld pool and is thus a relatively slow process.

Figure 10.4 shows the robot tracking performance in a sample training experiment, and Figure 10.5 depicts the front-side and back-side weld bead in this experiment. Acceptable tracking performance is achieved in all four movements. It is noted, however, that certain human hand movements are not perfectly tracked, especially in RX and RY. Accurate tracking performance is challenging when the human makes large movement, which will be authors' future research.

Figure 10.6 plots the welder's movement adjustments, and weld pool characteristic parameters (weld pool width, length, and convexity) in seven training experiments. As can be observed, the human welder manipulates the virtual welding torch accordingly based on the weld pool geometry he/she perceives.

10.2.2 Data Analysis

To evaluate each human hand movement's impact on the weld pool characteristic parameters and consequent weld penetration (characterized by its back-side bead width),

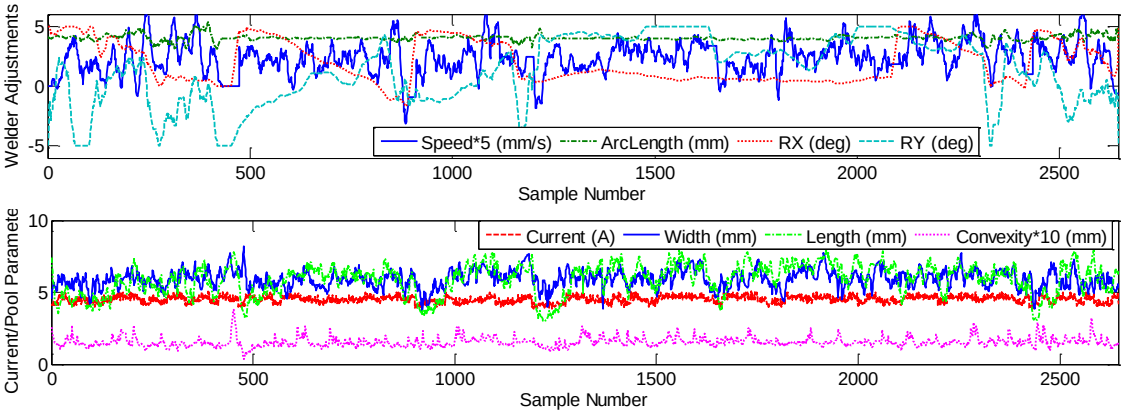

Figure 10.6 Measured welder adjustments and pool parameters in seven teleoperated training experiments.

linear modeling is conducted. The following first order Auto Regression Moving Average (ARMA) model is proposed:

$$\begin{cases} W_k = a_W W_{k-1} + \sum_{j=1}^{4} b_{W,j} u_{j,k-1} + c_W \\ L_k = a_L L_{k-1} + \sum_{j=1}^{4} b_{L,j} u_{j,k-1} + c_L \\ C_k = a_C C_{k-1} + \sum_{j=1}^{4} b_{C,j} u_{j,k-1} + c_C \end{cases} \tag{10.2}$$

where W_k, L_k, C_k are the weld pool width, length, and convexity at instant k. $u_{j,k-1}, j = 1,...,4$ are the welding speed S, arc length A (relative to 4 mm), rotation adjustment along welding direction RX (relative to the normal of the pipe surface), and rotation perpendicular to the welding direction RY, respectively. a, b, c are the model parameters associated with each model. These parameters can be identified using standard least squares method. The identified models are:

$$\begin{cases} W_k = 0.3W_{k-1} + 0.04S_{k-1} + 0.05A_{k-1} - 0.04RX_{k-1} + 0.01RY_{k-1} + 4.2 \\ L_k = 0.6L_{k-1} + 0.2S_{k-1} + 0.08A_{k-1} - 0.08RX_{k-1} + 0.03RY_{k-1} + 2.6 \\ C_k = 0.01C_{k-1} - 0.06S_{k-1} + 0.04A_{k-1} + 0.004(RX_{k-1} + RY_{k-1}) + 0.4 \end{cases} \tag{10.3}$$

The corresponding steady state models are:

$$\begin{cases} W_s = 0.059S_s + 0.066A_s - 0.053RX_s + 0.008RY_s + 5.99 \\ L_s = 0.56S_s + 0.18A_s - 0.18RX_s + 0.06RY_s + 5.93 \\ C_s = -0.059S_s + 0.042A_s + 0.004(RX_s + RY_s) + 0.42 \end{cases} \tag{10.4}$$

Based on authors' previous study [112], the following steady state model between the back-side bead width and pool parameters can be expressed as:

$$Wb_s = 0.9W_s - 0.45L_s + 1.27C_s + 1.7 \quad (10.5)$$

where Wb_s is the back-side bead width in steady-state.

Substituting Equation (10.4) in Equation (10.5), we have:

$$Wb_s = -0.27S_s + 0.03A_s + 0.04RX_s - 0.01RY_s + 4.96 \quad (10.6)$$

This steady-state correlation indicates that when the welding speed increases, the back-side bead width decreases. This makes sense because an increase in the welding speed decreases the heat input into the process and the penetration is thus reduced. Comparing the impact between four welder movements, it is observed that the welding speed, arc length, rotations along and perpendicular to the welding direction contribute to the back-side bead width with percentages of [76.4%, 8.6%, 11%, 4%], respectively. It is thus concluded that the welding speed adjustment has dominant contribution to the weld penetration, but welder adjustment in arc length and torch orientations also contribute to the weld penetration to some extent. In the next section, the normalized coefficients (i.e., [0.764, 0.086, 0.11, 0.04]) will be utilized to form the welder rating system.

10.3 Welder Rating System

Because the limit of the welder's skill, the real-time adjustments depicted in Fig. 9 might contain certain amount of "bad operation". However, only "good response" should be utilized to form the human response model. In this section, a welder rating system is constructed, and "good response" is selected as the data pairs for the human response modeling process detailed in Section 10.4.

To better distill the correct response of the human welder, the human welder evaluates the measured data (including the welding current, weld pool characteristic parameters) and corresponding back-side weld penetration, then assigns a rating (from 0 to 10) in each 5 s interval. (Assigning a rating is an off-line process requiring no real-time operation/control and is thus much less skill demanding for the welder.) Figure 10.7 shows the assigned rating and Figure 10.8 plots its histogram. It is seen that over 60% of the data points are rated above 8, however about 10% of the data points have been rated below 4. If all the data points are used to model the human welder response, the model might not reflect the correct behavior. In this section, an ANFIS based automated welder rating system (i.e., classifier) is synthesized.

From steady state models derived in Section 10.2.2 it is observed that each welder adjustment has certain impact on the weld penetration and thus should be accordingly weighted. The individual welder rating systems corresponding to each input are defined as:

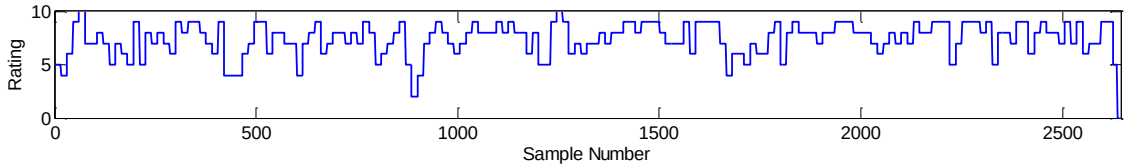

Figure 10.7 Human welder rating in seven dynamic training experiments.

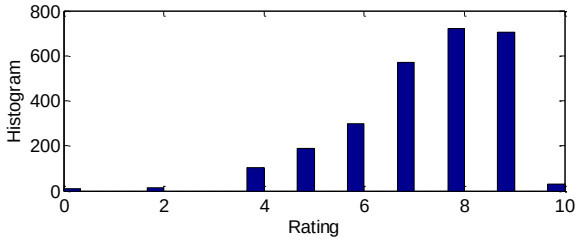

Figure 10.8 Histogram of the human welder rating specified in Figure 10.7.

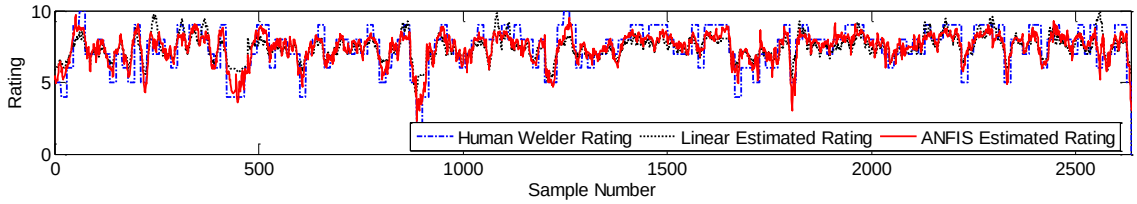

Figure 10.9 Human welder rating, linear and ANFIS estimated rating in seven dynamic training experiments.

$$\begin{cases} R_{S,k} = f_1\left(W_k, L_k, C_k, S_k\right) \\ R_{A,k} = f_2\left(W_k, L_k, C_k, A_k\right) \\ R_{RX,k} = f_3\left(W_k, L_k, C_k, RX_k\right) \\ R_{RY,k} = f_4\left(W_k, L_k, C_k, RY_k\right) \end{cases} \tag{10.7}$$

where W_k, L_k, C_k represent the measured weld pool parameters at instant *k*.

Then both the linear and ANFIS welder rating system can be synthesized by weighting the individual welder rating system for four inputs using the normalized coefficients:

$$R_k = 0.764R_{S,k} + 0.086R_{A,k} + 0.11R_{RX,k} + 0.04R_{RY,k} \tag{10.8}$$

Linear model can be fitted using standard least squares method:

$$\begin{cases} R_{S,k} = 0.018W_k - 0.107L_k - 0.111C_k + 3.831S_k + 6.17 \\ R_{A,k} = -0.016W_k + 0.098L_k - 1.152C_k - 0.279A_k + 7.29 \\ R_{RX,k} = -0.012W_k + 0.163L_k - 1.678C_k + 0.102RX_k + 6.83 \\ R_{RY,k} = -0.006W_k + 0.009L_k - 1.149C_k + 0.124RY_k + 7.59 \end{cases} \tag{10.9}$$

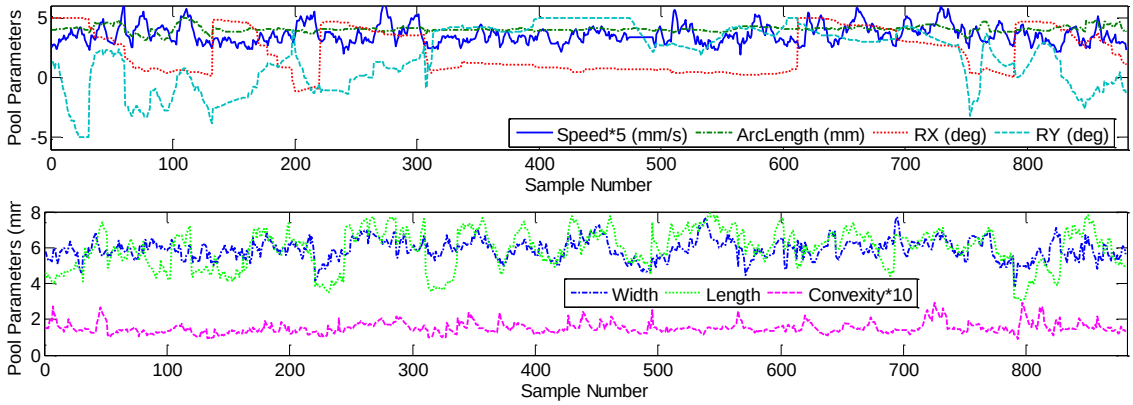

Figure 10.10 Selected data pairs (measurements with ratings larger than 8) from Figure 10.6.

The linear fitting result is depicted in Figure 10.9. Substantial fitting errors are frequently observed. The model average error and RMSE are 0.876 and 1.112, respectively.

ANFIS modeling technique described in previous subsection is then utilized to improve the classifier performance. Modeling trials suggest that when the four inputs are partitioned by 2, a good trade-off between fitting errors and model parameter numbers is obtained. ANFIS fitting result is also plotted in Figure 10.9. Compared to the linear model result, the proposed ANFIS model provides much better fitting result with the model average error and RMSE being reduced to 0.692 and 0.878, respectively.

The trained classifier will be used to classify the training experiment data (shown in Figure 10.6). Measurements (with associated ratings larger than 8) are then selected and depicted in Figure 10.10. These measurements are considered to be the "correct response" generated by the human welder. In the next section, modeling of human welder response is conducted and correct human welder response is distilled and analyzed. The proposed classifier can also be used in the welder training systems to rate welder adjustments, which may be helpful in training unskilled welder faster, and resolve the skilled welder shortage issue in the manufacturing industry.

10.4 Data-driven ANFIS modeling of human hand movement

Based on the definition of system inputs and output detailed in previous section, a general model structured is described as:

$$\begin{cases} S_k = g_1(W_{k-1}, L_{k-1}, C_{k-1}) \\ A_k = g_2(W_{k-1}, L_{k-1}, C_{k-1}) \\ RX_k = g_3(W_{k-1}, L_{k-1}, C_{k-1}) \\ RY_k = g_4(W_{k-1}, L_{k-1}, C_{k-1}) \end{cases} \tag{10.10}$$

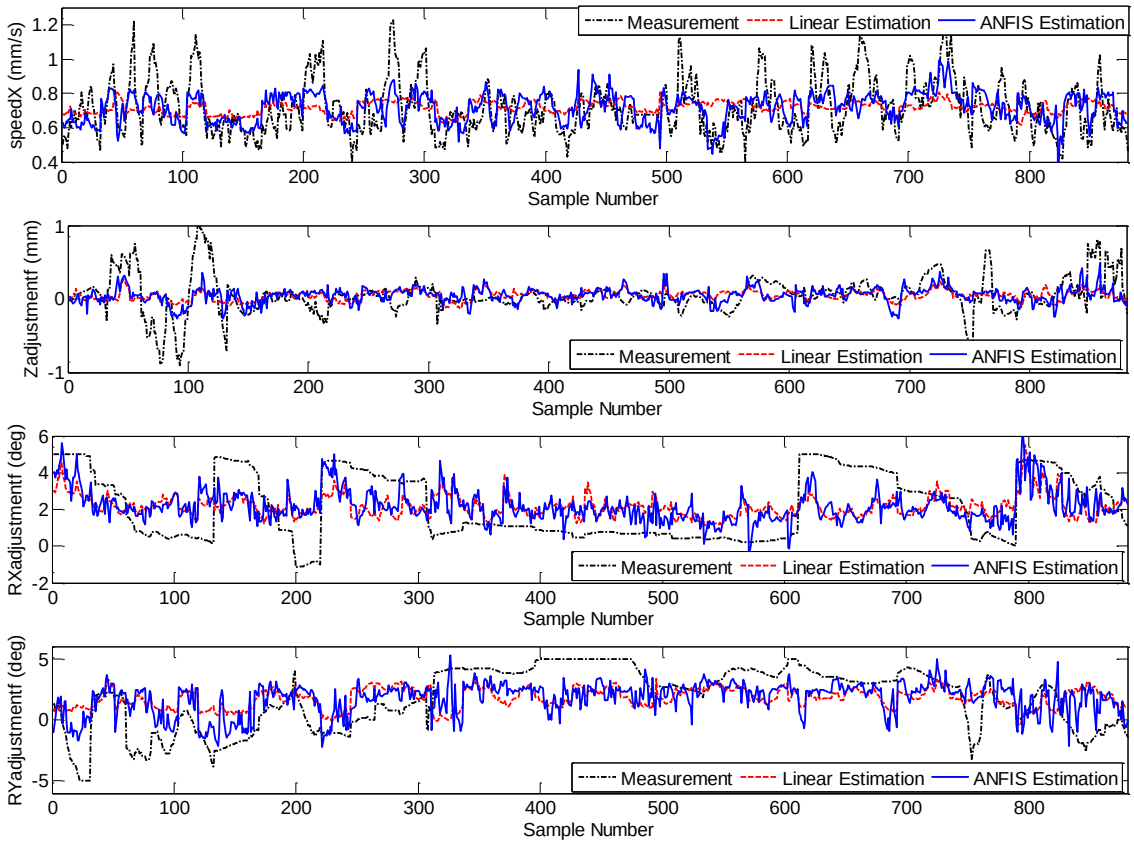

Figure 10.11 Modeling results of human welder adjustments.

TABLE II MODEL ERROR COMPARISONS

		Average Model Error	RMSE
S (mm/s)	Linear	0.121	0.152
	ANFIS	0.102	0.129
A (mm)	Linear	0.167	0.245
	ANFIS	0.158	0.232
RX (deg)	Linear	1.524	1.685
	ANFIS	1.356	1.571
RY (deg)	Linear	1.981	2.352
	ANFIS	1.717	2.122

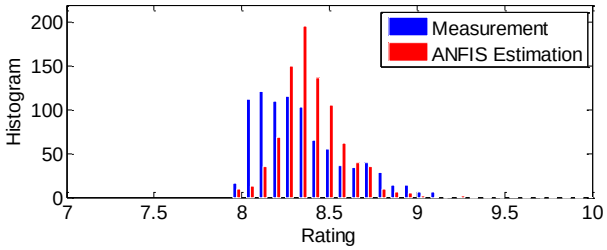

Figure 10.12 Histogram of the human welder ratings calculated from data pairs specified in Figure 10.10.

In the next two subsections, linear and ANFIS modeling are performed to correlate the weld pool characteristic parameters to the welder adjustments.

10.4.1 Linear Modeling

The following linear models are first proposed and identified using standard least squares algorithm:

$$\begin{cases} S_{k,l} = 0.0014W_{k-1} + 0.0278L_{k-1} + 0.2322C_{k-1} + 0.4551 \\ A_{k,l} = -0.0352W_{k-1} + 0.028L_{k-1} + 0.683C_{k-1} - 0.123 \\ RX_{k,l} = -0.0445W_{k-1} - 0.597L_{k-1} + 6.558C_{k-1} + 3.961 \\ RY_{k,l} = 0.0631W_{k-1} + 0.646L_{k-1} + 3.595C_{k-1} - 3.592 \end{cases} \tag{10.11}$$

The linear modeling results are plotted in Figure 10.11. The average model errors and RMSEs are listed in Table 10.1. It is found that the human movements can be estimated by the linear model with acceptable accuracy. However, substantial static fitting errors are frequently observed.

10.4.2 ANFIS modeling

The linear model described in the first subsection accounts for the average effect of the weld pool parameters on the welder adjustments in the large input ranges. In order to further improve the modeling accuracy, nonlinear ANFIS modeling method is utilized. Modeling trails suggest that when input parameters are partitioned by 2, a good trade-off is obtained between model performance and number of model parameters. The modeling result is shown in Figure 10.11 and the resulting ANFIS model errors are listed in Table 10.1. It is seen that the model errors are improved by incorporating the nonlinear correlation between the model inputs and outputs. Hence, the developed ANFIS modeling plays an important role in deriving the detailed correlation between the welder's response and the weld pool geometry.

Figure 10.12 plots the histogram of the rating for data specified in Figure 10.10. It is observed that after ANFIS modeling, the overall rating is increased, with more ratings above 8.4, and less ratings from 8 to 8.4. This indicates that the proposed ANFIS modeling is able to distill the correct response made by the human welder.

10.4.3 Model Verification

To verify the proposed ANFIS model, verification experiment is conducted and the results are shown in Figure 10.13. It is shown in Figure 10.13 (b) that the model can estimate the welder adjustments with acceptable accuracy. It is noticed, however, that certain human adjustments are not learned by the models. Careful analysis indicates that these adjustments are caused by human welder's underestimation and overestimation of the weld penetration, and thus should not be learned.

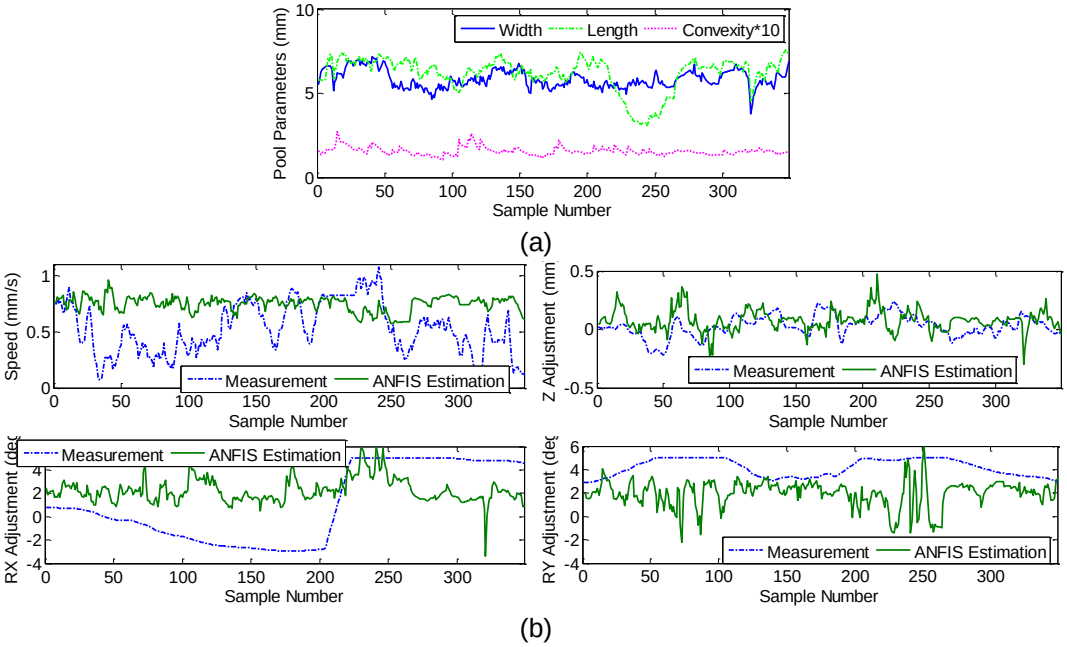

Figure 10.13 Verification experiment results. (a) Weld pool characteristic parameters (b) Measured and estimated welder adjustments.

10.5 Automated Welding Experiments

In order to demonstrate the robustness of the developed control system, automated welding experiments have been designed and conducted in this section under different disturbances. In subsection 10.5.1, different welding currents are applied. In subsection 10.5.2 and 10.5.3 the welding speed and weld pool measurement disturbances are applied and the robustness of the controller with speed disturbance is tested.

10.5.1 Experiment 1: Different Welding Current

In this subsection the control experiment is conducted under different welding currents. From 40 s to 50 s is the open loop period where no controller is applied. The welding speed and the welding current are set at 0.5 mm/s and 43 A, and other adjustments are set at zeros. The pool parameters reach their steady states at the end of the open loop period (6 mm for the width, 6 mm for the length, and 0.13 mm for the convexity). From 50 s the proposed controller is applied, and the welding speed is adjusted to about 0.7 mm/s based on the inputs (weld pool characteristic parameters). Other welding parameters including the arc length and torch orientations are adjusted accordingly. It is noticed that for the same welding current (i.e., 43 A), the weld pool parameters are fluctuating because of other un-modeled factors that might influence the welding process. For example, from 75 s to 80 s, an increase in the weld pool convexity is observed. Consequently, the welding speed is increased, the arc length is slightly decreased, and the orientations are also adjusted accordingly to compensate this change in the weld pool parameters, similar to the adjustments that would be made by the human welders.

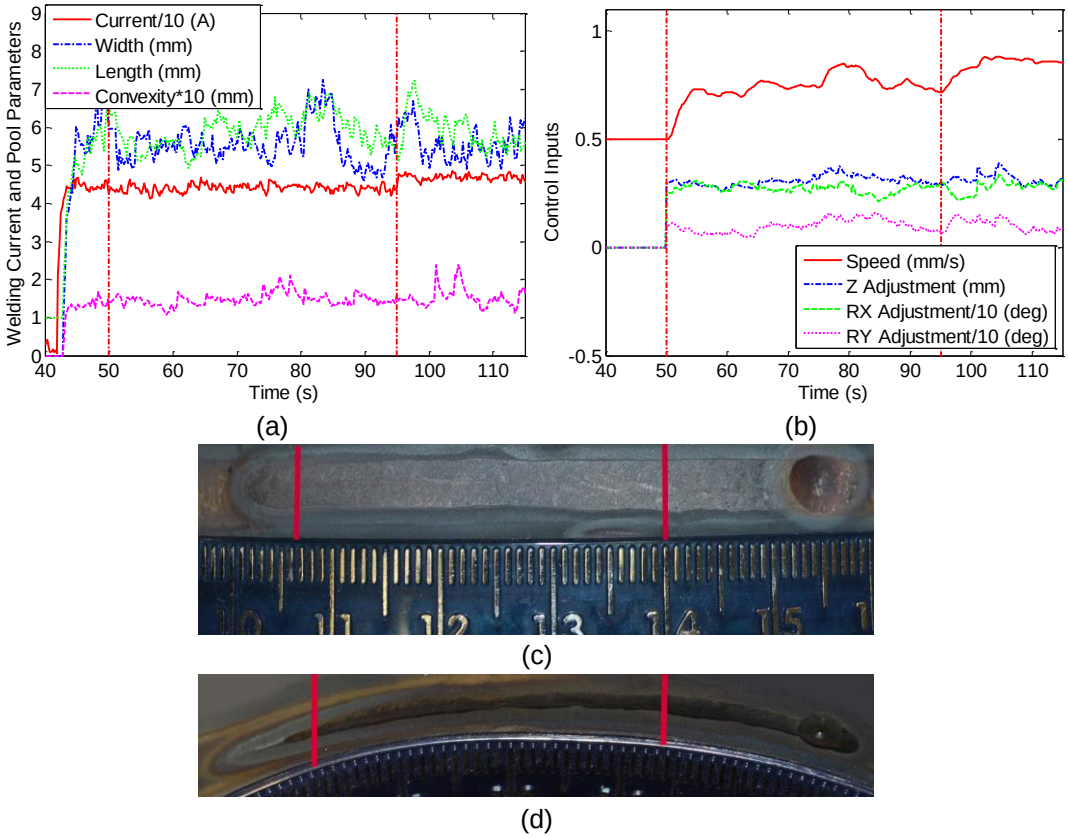

Figure 10.14 Experiment 1 results (a) Welding current and weld pool parameters (b) Control inputs (c) Front-side bead (d) Back-side bead.

At 95 s, the welding current is changed to 46 A (Figure 10.14 (a)). As a result, the weld pool width, length and convexity gradually increase to about 6.5 mm, 7 mm, and 0.14 mm, respectively. From Figure 10.14 (d) it is also observed that the back-side bead width is increased because of this current increase. If no closed loop control is applied, this current increase cannot be compensated. From Figure 10.14 (b) it is shown that the controller is able to increase the welding speed to about 0.8 mm/s to compensate this increase in the welding current. The back-side bead width is also well maintained at about 2 mm.

10.5.2 Experiment 2: Welding Speed Disturbance

In this experiment the robustness of the control algorithm against welding speed disturbance is evaluated. The welding current is set at 43 A throughout the experiment. An artificial error between the calculated and applied values of the welding speed is applied. In the first 35 s of the closed loop control (60 s to 95 s), no error exists between the calculated speed and applied speed. The controller is able to bring the back-side bead width to about 2.1 mm. From 95 s to 97 s, the welding speed is set at 0.5 mm/s. As the result, the back-side bead width increases to about 2.5 mm (see Figure 10.15 (d)). However, the controller is able to adjust the welding speed to compensate this artificial

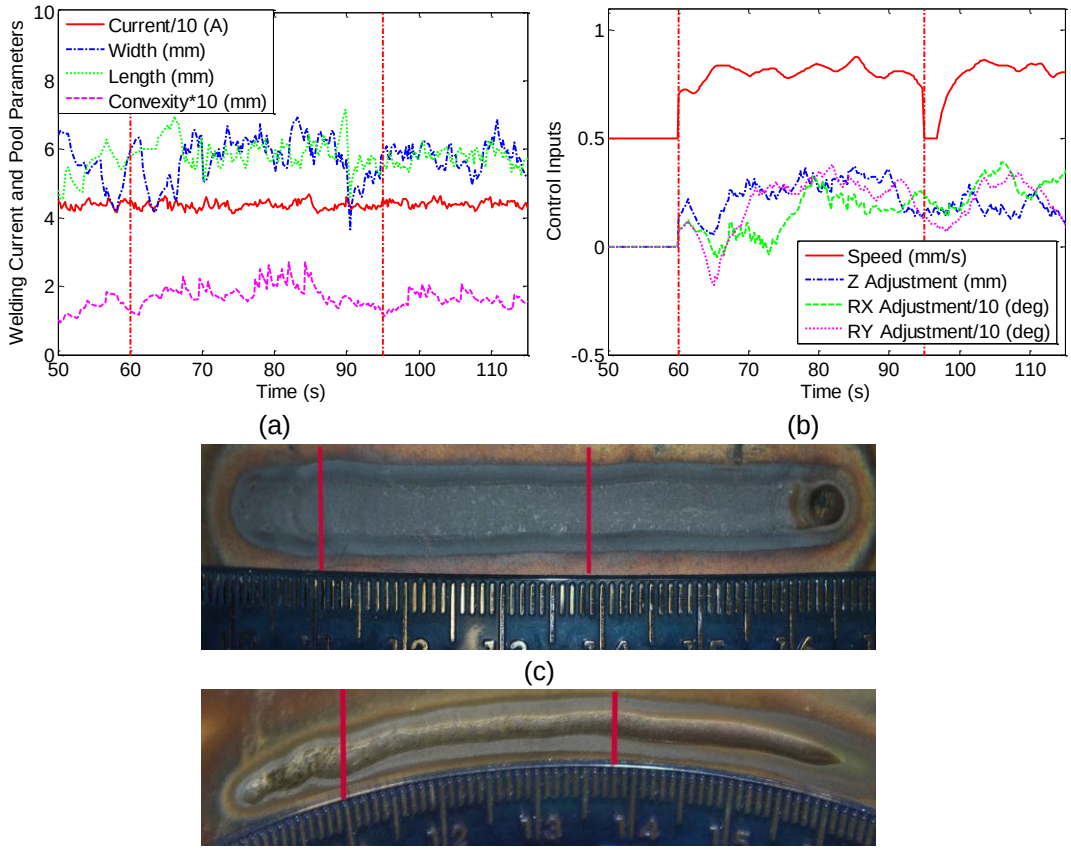

Figure 10.15 Experiment 2 results (a) Welding current and weld pool parameters (b) Control inputs (c) Front-side bead (d) Back-side bead.

error (see Figure 10.15 (c)), and the back-side bead width can be maintained around 2.1 mm again (see Figure 10.15 (d)) with a relatively quick response time.

10.5.3 Experiment 3: Measurement Disturbance

An artificial error between the actual and measured values of the weld pool surface is applied in this experiment. At 113 s, the measured weld pool width, length, and convexity are set to 3 mm, 3.5 mm, and 0.05 mm, respectively. As can be seen from Figure 10.16 (b) the welding speed is slightly decreased from 0.8 mm/s to about 0.76 mm/s, and the back-side bead width is slightly increased (Figure 10.16 (d)). Other welding parameters are also adjusted by the controller accordingly. By applying the controller the desired back-side bead width is well maintained at about 2.1 mm. The robustness of the proposed intelligent controller is thus demonstrated.

10.6 Summary

In this chapter a data-driven approach to model human welder intelligence in 3D is proposed. A virtualized welding platform is utilized to conduct teleoperated training experiments. Human welder's arm gestures (including movement speed, arc length, and

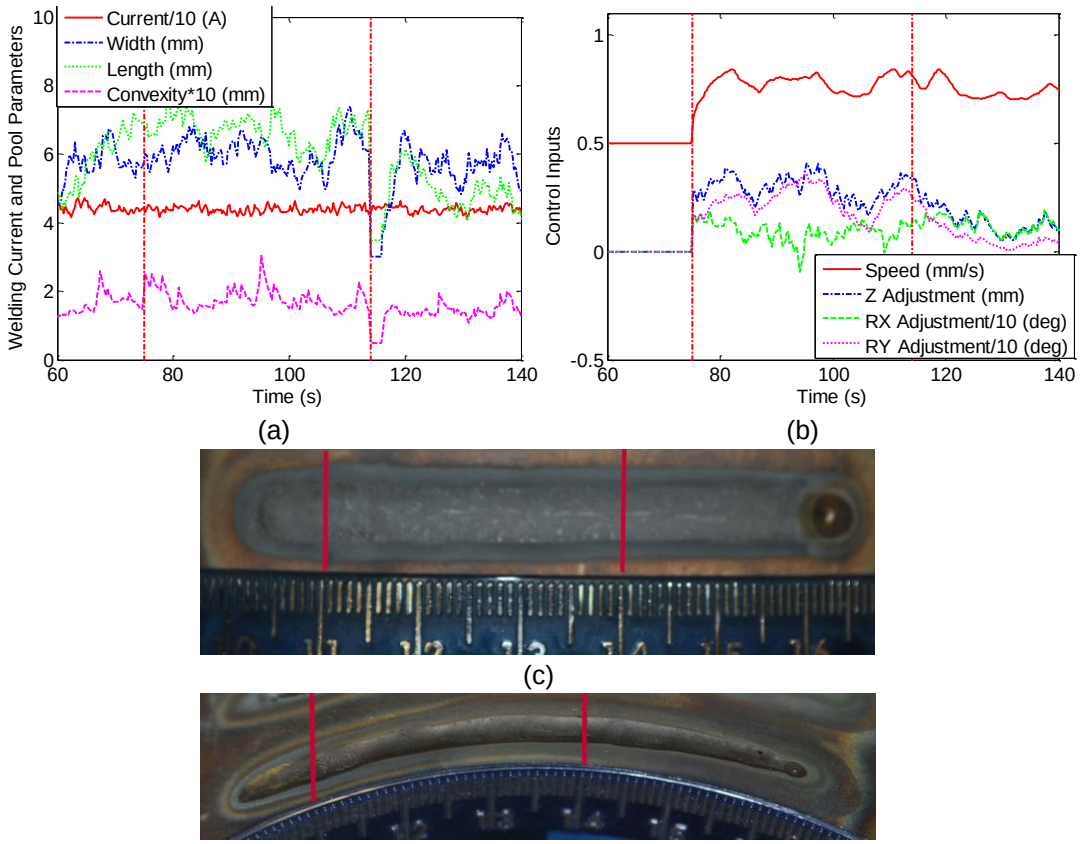

Figure 10.16 Experiment 3 results (a) Welding current and weld pool parameters (b) Control inputs (c) Front-side bead (d) Back-side bead.

torch orientations) together with the 3D weld pool characteristic parameters are recorded and analyzed. The data is off-line rated by the welder and an automated welder rating system is obtained by synthesizing individual rating system corresponding to each welder adjustment using weights from their steady state models. Data from the training experiments are then selected and ANFIS models are proposed to correlate the 3D weld pool characteristic parameters and welder's movement adjustments. To demonstrate the effectiveness of the proposed data-driven model, automated control experiments are conducted. Results show that the proposed model as an intelligent controller is able to control the welding process under different welding currents, and is robust against welding speed and measurement disturbances. A fundation is thus established to rapidly extract human intelligence and transfer such intelligence into welding robots.

Chapter 11 Conclusion and Future Work

11.1 Conclusion

Manual GTAW process is commonly used in industry especially for the applications where the weld quality is critical. Automated welding robots, on the other hand, outperform human welders whose performance may degrade because of their physical limitations (inconsistent concentration, fatigue, stress and long-term health issues, etc.). It would thus be beneficial to combine the adequate sensing, invaluable experience, and intelligence from human welders with accurate machine execution and physical capabilities. In this dissertation accurate welding process controller and intelligent welding robot are developed by conventional modeling / control method and learning the human welder behavior. The main work in the dissertation can be divided into three parts: automated GTAW modeling and control (Chapter 3 "Weld Penetration Control for Automated GTAW Process" and Chapter 4 "3D Weld Pool Surface Control"), learning of the skilled welder adjustment on the welding current (Chapter 5 "Skilled Human Welder Response Modeling and Intelligent Control"), and virtual welding platform as well as various methods for learning human welder movement (Chapter 6 "Virtualized Welding Platform and Teleoperation", Chapter 7 "Learning Human Welder Movement with Virtual Reality Enhancement", Chapter 8 "Learning Human Welder Movement without Virtual Reality Enhancement", Chapter 9 "Fuzzy Weighting Based Data Fusion: Combining Machine and Human Intelligence", and Chapter 10 "Full 3D Position and Orientation Learning and Control"). The main achievements and contributions in this dissertation can be summarized as follow:

- Weld penetration is accurately controlled in automated GTAW process. Dynamic experiments are conducted to establish the model that relates the back-side bead width to the welding current and speed. Weld penetration is accurately estimated by the 3D weld pool surface. Dynamic linear model is first constructed and the modeling result is analyzed. The linear model is then improved by incorporating a nonlinear operating point modeled by an ANFIS. Model predictive control algorithm is then derived. Welding experiments confirm that the developed control system is effective in achieving the desired weld joint penetration under various disturbances and initial conditions.
- 3D weld pool surface is accurately controlled in automated GTAW process. Dynamic response of 3D weld pool characteristic parameters to welding current and speed as control variables is modeled. A predictive control algorithm is developed to control these characteristic parameters. Welding experiments confirm that the developed control system is effective in achieving the desired 3D weld pool surface geometry despite various disturbances.

- The skilled welder response to 3D weld pool surface by adjusting the welding current is modeled using ANFIS, and compared to the novice welder. Control experiments confirm the effectiveness of the proposed human response model.
- A virtualized welding system is developed that enables learning from human welder intelligence for transferring into a welding robot. Teleoperation experiments are conducted under different welding currents and results are analyzed. A correlation between the welding current and welding speed is proposed for GTAW pipe welding with specified welding conditions. Consistent penetration and satisfactory welds are generated in automated welding experiments.
- The learning of human welder movement is realized with virtual reality enhancement. Machine-human cooperative control is firstly introduced, and the virtual reality enhancement system is provided. Learning experiments are conducted and modeled using iterative K-means based ANFIS model.
- The learning of human welder movement is performed without virtual reality enhancement. To better distill the correct movement of the human welder, a fuzzy classifier is proposed to rank the data and only preserve the high ranking "correct" response. The trained ANFIS model is transferred to the welding robot and the performance of the controller is examined.
- A fuzzy weighting based data fusion approach to combine multiple machine and human intelligent models is proposed for developing intelligent welding robot in pipe GTAW process. The data fusion model outperform individual machine algorithm (super welder) and welder intelligence models (both with and without VR).
- A data-driven approach to model human welder intelligence in 3D is proposed. Teleoperated training experiments are conducted in which a human welder tries to adjust the torch movements in 3D (including welding speed, arc length, and torch orientations) based on his observation on the real-time weld pool image feedback. The data is off-line rated by the welder and a welder rating system is trained. ANFIS model is then proposed to correlate the 3D weld pool characteristic parameters and welder's torch movements.

11.2 Future Work

More future work can be done to further distill the intelligence of the human welder, improve the performance of the intelligent welding robot and develop an advanced welder training system, which include:

- Improve the 3D weld pool sensing system under large orientations. Separate projector, imaging plane and robot movement such that good reflections can be obtained especially when the torch deviate from normal significantly.

- Learn human welder performance in 3D with large operation range. The welding speed, arc length, and torch orientations need to be decoupled to better derive the human intelligent controller in 3D. Teleoperation training experiments will be conducted by skilled human welder. The adjustments made by the skilled welder will be compared to those made by novice welder, and the obtained model can be analyzed to understand why unskilled welder does not perform as good as the skilled welder. This may also help resolve the skilled welder shortage issue the manufacturing industry is currently facing.
- Establish a welder training system that can accelerate the training process of the unskilled human welder. Augmented signals can be superimposed into the weld pool image feedback for the human welder to view, including information about how to adjust the welding speed, arc length, and torch orientations. The performance of the training system will be evaluated by training welders with different skill levels.
- Realize machine-human cooperative control, where human welder controls the torch manipulations and the machine algorithm determines the welding current needed to compensate possible incorrect behavior of the human welder. Welder performance can be further enhanced and better welds can be obtained by the human welder.
- Perform full circumference pipe welding and welding of complex or irregular shapes. The 3D weld pool sensing and visualization system will be modified accordingly and welder's complex 3D adjustments will be extensively studied / modeled and utilized as an intelligent controller.

References

[1] R. O'Brien, Ed., Welding Handbook, 8th Edition vol.2-Welding Processes, AWS, 1998.

[2] G. D. Uttrachi, Welder shortage requires new thinking. *Welding Journal*, vol. 86(1), pp.6, 2007.

[3] A Roadmap for US Robotics: From Internet to Robotics, http://www.us-robotics.us/reports/CCC%20Report.pdf, May 2009.

[4] W.J. Zhang, Y. K. Liu, Y.M. Zhang, "*Real-time Measurement of Three Dimensional Weld Pool Surface in GTAW*" in book "Welding Process" ISBN 979-953-307-1089-4. 2012.

[5] D. J. Kotecki, D. Cheever, and D. Howden, "Mechanism of ripple formation during weld solidification," *Welding Journal*, vol. 51(8), pp. 386s– 391s, 1972.

[6] R. Renwick and R. Richardson, "Experimental investigation of GTA weld pool oscillations," *Welding Journal*, vol. 62(2), pp. 29s–35s, 1983.

[7] M. Zacksenhouse and D. Hardt, "Weld pool impedance identification for size measurement and control," *ASME Journal of Dynamic Systems, Measurement, and Control*, vol. 105(3), pp. 179–184, 1984.

[8] Y.H. Xiao and G. den Ouden, "Weld pool oscillation during GTA welding of mild steel," *Welding Journal*, vol. 72(8), pp. 428s–434s, 1993.

[9] A.J.R. Anedenroomer and G. den Ouden, "Weld pool oscillation as a tool for penetration sensing during pulsed GTA welding," *Welding Journal*, vol. 77(5), pp. 181–187, 1998.

[10] K. Andersen, G.E. Cook, R.J. Bamett, A.M. Strauss, "Synchronous weld pool oscillation for monitoring and control," *IEEE Transactions on Industry Applications*, vol. 33(2), pp. 464–471, 1997.

[11] D.A. Hartman, D.R. DeLapp, G.E. Cook, and R.J. Barnett, "Intelligent fusion control throughout varying thermal regions," in *Proceedings of the IEEE Industry Applications Conference*, 1999.

[12] J. Ju, Y. Suga, K. Ogawa, "Penetration control by monitoring molten pool oscillation in tig arc welding," *International Journal of Offshore and Polar Engineering*, vol. 14(2), pp. 145–149, 2002.

[13] B. Yudodibroto, M. Hermans, Y. Hirata, and G. den Ouden G, "Influence of filler wire addition on weld pool oscillation during gas tungsten arc welding," *Science and Technology of Welding and Joining*, vol. 9(2), pp. 163–168, 2004.

[14] E. Siores. "Development of a Realtime Ultrasonic Sensing System for Automated and Robotic Welding". PhD Thesis, Brunel University. 1~341, 1988.

[15] D. E. Hardt. "Ultrasonic Measurement of Weld Penetration". *Welding Journal*. 63(9): 273s~285s, 1984.

[16] R. Fenn, "Ultrasonic Monitoring and Control during Arc Welding". *Welding Journal*. 64(9): 18~24, 1985.

[17] N. M. Carlson, J. A. Johnson. "Ultrasonic Sensing of Weld Pool Penetration". *Welding Journal*. 67(11): 239s~246s, 1988.

[18] G. M. Graham, I. C. Ume. "Automated System for Laser Ultrasonic Sensing of Weld Penetration," *Mechatronics*. 7(8): 711~721, 1997.

[19] B. Mi, C. Ume. “Real Time Weld Penetration Depth Monitoring with Laser Ultrasonic Sensing System”. *Transactions of ASME: Journal of Manufacturing Science and Engineering*. 128(2): 280~286, 2006.
[20] J. Aussel, B. Le, J. Baboux. “Generation Acoustic Wave by Laser: Theoretical and Experimental Study of the Emission Source”. *Ultrasonics*. 24: 246~255, 1988.
[21] A. Kita. “Measurement of Weld Penetration Depth using Non-contract Ultrasound Method”. Ph.D. Dissertation, Georgia Institute of Technology. 22~28, 2005.
[22] S. Dixon, C. Edwards, S. Palmer. “A Laser-EMAT System for Ultrasonic Weld Inspection”. *Ultrasonics*. 37(4): 273~281, 1999.
[23] W. Chen, B. A. Chin. “Monitoring Joint Penetration Using Infrared Sensing Techniques”. *Welding Journal*. 69(4): 181s~185s, 1990.
[24] S. Nagarajan, B. A. Chin, W. Chen. “Control of the Welding Process Using Infrared Sensors”. *IEEE Transactions on Robotics and Automation*. 8(1): 86~93, 1992.
[25] H. Wikle, S Kottilingam, R. Zee, B. Chin. “Infrared sensing techniques for penetration depth control of the submerged arc welding process,” *Journal of Material Processing Technology*, 113(13): 228~233, 2001.
[26] R. J. Barnett, G. E. Cook, D. Damrongsak, et al. “Through-the-Arc Sensing and Control in Pulsed Gas Metal Arc Welding,” *ASM Proceedings of the International Conference: Trends in Welding Research. Pine Mountain, GA, USA*, 1068~1072, 1998.
[27] W. G. Essers, M. R. M. Van Gompel. “Arc Control with Pulsed GMA Welding,” *Welding Journal*. 63(6): 26~32, 1984.
[28] B. J. Corlett, J. Lucas, J. S. Smith. “Sensors for Narrow-Gap Welding.” *IEE Proceedings A: Physical Science. Measurement and Instrumentation. Management and Education. Reviews*. 138(4): 213~222, 1991.
[29] H. Nomura, Y. Sugitani. “Sensing and Control of Arc Welding.” *Advances in Welding Science and Technology, TWR '86: Proceedings of an International Conference on Trends in Welding Research. Gatlinburg, TN, USA*. 427~434, 1986.
[30] A. Bicknell, J. S. Smith, J. Lucas. “Arc Voltage Sensor for Monitoring of Penetration in TIG Welds.” *IEE Proceedings: Science, Measurement and Technology*. 141(6): 513~520, 1994.
[31] J. Y. Wang, K. Kusumoto, K. Nezu. “Microweld Penetration Monitoring Techniques by Arc Sensing.” *Proceedings of the 2003 IEEE/ASME International Conference on Advanced Intelligent Mechatronics*. 1 & 2: 1027~103, 2003.
[32] S. I. Rokhlin and A. C. Guu, “A study of arc force, pool depression, and weld penetration during gas tungsten arc welding,” *Welding Journal*, 72(8): 381s-390s, 1993.
[33] S. I. Rokhlin and A. C. Guu, “Computerized radiographic sensing and control of an arc welding process,” *Welding Journal*, 69(3): 83s-97s, 1990.
[34] A. C. Guu and S. I. Rokhlin, “Computerized radiographic weld penetration control with feedback on weld pool depression,” *Material Evaluation*, 47: 1204-1210, 1989.
[35] C. Mnich, “Development of a Synchronized High-speed, Stereovision System for in situ Weld Pool Measurement.” MS Thesis, Engineering Division, Colorado School of Mines, 2004.

[36] C. Mnich, et al., "In situ weld pool measurement using stereovision," *Japan-USA Symposium on Flexible Automation, Denver, Colorado*, July, 19-21, 2004.
[37] Zhao, D. B., Yi, J. Q., et al. "Extraction of three-dimensional parameters for weld pool surface in pulsed GTAW with wire filler." *Journal of Manufacturing Science and Engineering*, 125: 493–503, 2003.
[38] R. Kovacevic, and Y. M. Zhang, "Sensing free surface of arc weld pool using specular reflection: principle and analysis," *Proceedings of the Institution of Mechanical Engineers, Part B, Journal of Engineering Manufacturing*, 210(6): 553-564, 1996.
[39] R. Kovacevic, Y. M. Zhang, "Real-time image processing for monitoring of free weld pool surface," *ASME Journal of Manufacturing Science and Engineering*, 119(2): 161-169, 1997.
[40] Y. M. Zhang, Liguo E, and R. Kovacevic, "Active metal transfer control by monitoring excited droplet oscillation," *Welding Journal*, 77(9): 388s-395s, 1998.
[41] G. Saeed and Y.M. Zhang, "Mathematical formulation and simulation of specular reflection based measurement system for gas tungsten arc weld pool surface," *Measurement Science and Technology*, 14(8): 1671-1682, 2003.
[42] G. Saeed, M.J. Lou, and Y.M. Zhang, "Computation of 3D weld pool surface from the slope field and point tracking of laser beams," *Measurement Science and Technology*, 15(2): 389-403, 2004.
[43] G. Saeed. "Three Dimensional Measurement of Specular Surfaces and Its Application in Welding Process." PhD Dissertation, University of Kentucky, 2005.
[44] G. Saeed, Y.M. Zhang, S. Cook, "A compact vision sensor for weld pool surface sensing," *Special Issue on Advanced Sensing, Modelling and Control of Welding Processes, International Journal of Modelling, Identification and Control*, 1(2): 94-100, 2006.
[45] G. Saeed and Y.M. Zhang, "Weld pool surface depth measurement using calibrated camera and structured-light," *Measurement Science & Technology*, 18: 2570-2578, 2007.
[46] Y.M. Zhang, H.S. Song, and G. Saeed, "Observation of a dynamic specular weld pool surface," *Measurement Science and Technology*, 17 (6): L9-L12, 2006.
[47] H.S. Song, Y.M. Zhang, "Three-dimensional reconstruction of specular surface for gas tungsten arc weld pool," *Measurement Science & Technology*, 18: 3751-3767, 2007.
[48] H.S. Song, Y.M. Zhang, "Image processing for measurement of three-dimensional GTA weld pool surface," *Welding Journal*, 86(10): 323s-330s, 2007.
[49] H.S. Song and Y.M. Zhang, "Measurement and analysis of three-dimensional specular gas tungsten arc weld pool surface," *Welding Journal*, 87(4): 85s-95s, 2008.
[50] H.S. Song and Y.M. Zhang, "Error analysis of a three-dimensional GTA weld pool surface measurement system," *Welding Journal*, 88(7): 141s-148s, 2009.
[51] H.S. Song, "Machine Vision Recognition of Three-Dimensional Specular Surface for Gas Tungsten Arc Weld Pool." PhD Dissertation, University of Kentucky, 2007.
[52] W. J. Zhang, Y. M. Zhang, "Analytical real-time measurement of three-dimensional specular weld pool surface", *Measurement Science and Technology*, 24(11), 2013.

[53] W. J. Zhang, X. Zhang, Y. M. Zhang, "Robust Pattern Recognition for Measurement of Three Dimensional Weld Pool Surface in GTAW", *Journal of Intelligent Manufacturing*, accepted for publication, 2014.
[54] Y. K. Liu, W.J. Zhang, Y.M. Zhang, "A Tutorial on Learning Human Welder's Behavior: Sensing, Modeling, and Control", *Journal of Manufacturing Processes* (Elsevier), vol. 16, pp. 123-136, 2014.
[55] W.J. Zhang, Y. K. Liu, X. Wang, Y.M. Zhang, "Characterization of Three-dimensional Weld Pool Surface in Gas Tungsten Arc Welding", *Welding Journal*, 91: 195s-203s, 2012.
[56] K. Andersen, Synchronous weld pool oscillation for monitoring and control, PhD Thesis, Vanderbilt University, 1993.
[57] D.A. Hartman, "Intelligent control in arc welding: intelligent engineering systems through artificial neuro networks," *ASME*, 1999.
[58] A.C. Guu, S.I. Rokhlin, "Arc weld process control using radiographic sensing," *Materials Evaluation*, 50(11):1344, 1992.
[59] J. B. Song, D.E. Hardt, "Closed-loop control of weld pool depth using a thermally based depth estimator," *Welding Journal*, 72(10): 471s-478s, 1993.
[60] K.S. Boo, H.S. Cho, "A self-organizing fuzzy control of weld pool size in GMA welding process," *Control Engineering Practice*, 2(6): 1007-1018, 1994.
[61] W. Chen and B. A. Chin, "Monitoring joint penetration using infrared sensing techniques," *Welding Journal*, 69(4): 181s–185s, 1990.
[62] P. Banerjee, S. Govardhan, H. C. Wikle, H. Y. Liu, and B. A. Chin, "Infrared sensing for on-line weld geometry monitoring and control," *Journal of Engineering for Industry-Transactions of ASME*, 117(3): 323–330, 1995.
[63] A. R. Vorman and H. Brandt, "Feedback control of GTA welding using puddle width measurement," *Welding Journal*, 55(9): 742–749, 1976.
[64] K. Ohshima, M. Yamamoto, T. Tanii, et.al, "Digital control of torch position and weld pool in MIG welding using image processing device," *IEEE Transactions on Industry Applications*, 28(3): 607-612, 1992.
[65] K.A. Pietrzak, S.M. Packer, "Vision-based weld pool width control," *Journal of Engineering for Industry-Transactions of ASME*, 116(1): 86-92, 1994.
[66] J.B. Song and D.E. Hardt, "Dynamic modeling and adaptive control of the gas metal arc welding process," *ASME J. Dynamic Syst., Meas., Contr.*, 116(3): 405–413, 1994.
[67] R. Kovacevic, Y.M. Zhang, S. Ruan, "Sensing and control of weld pool geometry for automated GTA welding," *Journal of Engineering for Industry-Transactions of ASME*, 117(2): 210-222, 1995.
[68] Y.M. Zhang, R. Kovacevic, L. Wu, "Dynamic analysis and identification of gas tungsten arc welding process for weld penetration contro," *Journal of Engineering for Industry-Transactions of ASME*, 118(1): 123-136, 1996.
[69] Y.M. Zhang, R. Kovacevic, "Neurofuzzy model-based predictive control of weld fusion zone geometry," *IEEE Transactions on Fuzzy Systems*, 6(3): 389-401, 1998.
[70] S.B. Chen, Y.J. Lou, L. Wu, et.al, "Intelligent methodology for sensing, modeling and control of pulsed GTAW: Part I-Bead-on-plate welding," *Welding Journal*, 79(6): 151s-163s, 2000.

[71] D.B. Zhao, S.B. Chen, L. Wu, "Intelligent control for the shape of the weld pool in pulsed GTAW with filler metal," *Welding Journal*, 80(11): 253s-260s, 2001.
[72] C.H. Tsai, K.H. Hou, H.T. Chuang, "Fuzzy control of pulsed GTA welds by using real-time root bead image feedback," *Journal of Materials Processing Technology*, 176(1): 158-167, 2006.
[73] M. Kong, S.B. Chen, "Al alloy weld pool control of welding robot with passive vision," *Sensor Review*, 29(1): 28-37, 2009.
[74] H. Chen, F. Lv, T. Lin, et.al., "Closed-loop control of robotic arc welding system with full-penetration monitoring,", *Journal of Intelligent and Robotic Systems*, 56(5): 565-578, 2009.
[75] Y.K. Liu, W. Zhang, Y.M. Zhang, "Dynamic Neuro-fuzzy Based Human Intelligence Modeling and Control in GTAW", *IEEE Transactions on Automation Science and Engineering*, in print, 2014.
[76] Y.K. Liu, Y.M. Zhang, L. Kvidahl, "Skilled Human Welder Intelligence Modeling and Control: Part I - Modeling," *Welding Journal*, 93: 46s-52s, 2014.
[77] Y.K. Liu, Y.M. Zhang, L. Kvidahl, "Skilled Human Welder Intelligence Modeling and Control: Part II - Analysis and Control Applications," *Welding Journal*, 93: 162s-170s, 2014.
[78] L.R. Yong, "On adaptive manual control," *IEEE Transaction on Man and Machine System*, 10: 292-331, 1969.
[79] C.R. Kelly, *Manual and automatic control, A theory of manual control and its application to manual and automatic systems*. New York: Wiley, 1968.
[80] D.T. McRuer, E.S. Krendel, "Dynamic response of human operators," WADC-TR-56-524. US Airforce, 1957.
[81] D.T. McRuer, H. R. Jex, "A review of quasi-linear pilot models," *IEEE Transaction on Human Factor Electronics*, 8: 231-249, 1967.
[82] D. McRuer, D. Graham, E. Krendel, W. Reisener, "Human Pilot Dynamics in Compensatory Systems.Technical report,"AFFDL-TR-65-15, Air Force Flight Dynamics Laboratory, Wright-Patterson AFB. Ohio, 1965.
[83] D. L. Kleiman, S. Baron, and W. H. Levison, "An optimal model of human response, part I. Theory and validation," *Automatica*, 6: 357-369, 1970.
[84] D. L. Kleiman, S. Baron, and W. H. Levison, "An optimal model of human response, part II.Prediction of human performance in a complex task," *Automatica*, 6: 371-383, 1970.
[85] M. Tomizuka, and D. E. Whitney, "Optimal discrete finite preview problems (why and how is future information important?)," *Journal of Dynamics and System Measurement Control*, 97:319-325, 1975.
[86] M. Tomizuka, and D. E. Whitney, "The human operator in manual preview tracking (an experiment and its modeling via optimal control)," *Journal of Dynamics and System Measurement Control*, 98: 407-413, 1976.
[87] J.B. Davidson, and D. K. Schmit, "Modified optimal control pilot model for computer-aid design and analysis," Technical Report TM-4384, NASA, 1992.
[88] L.R. Yong, "On adaptive manual control," *IEEE Transaction on Man and Machine System*, 10: 292-331, 1969.

[89] W.S. Kim, F. Tendick, S. R. Ellis, andL. W.Stark, "A comparison of position and rate control of tele-manipulation with consideration of manipulator system dynamics," *IEEE Journal of Robot Automation*, 3: 426-436, 1987.
[90] H. Inooka, T. Koitabashi, "Experimental studies of manual optimization in control tasks," *IEEE Control System Magazine*, 10: 20-23, 1990.
[91] D. B. Doman, and M. R.Anderson, "A fixed-order optimal control model of human operator response," *Automatica*, 36: 409-418, 2000.
[92] L. K.Chen, A. G. Ulsoy, "Identification of a nonlinear driver model via narmax modeling," *Proceedings of American Control Conference*.2533-2537, 2000.
[93] T. Tsuji, Y. Tanaka, "Tracking control properties of human-robotic systems based on impedance control," *IEEE Transactions on Systems, Man, and Cybernetics- Part A: Systems and Humans*. 35(4): 523-535, 2005.
[94] E. Itoh, and S.Suzuki, "Nonlinear approach for human internal models: Feedforward and feedback roles in pilot maneuver," *Systems. Man and Cybernetics. 2005 IEEE International Conference*. 3: 2455 – 2462, 2005.
[95] I. I. Delice, and S. Ertugrul, "Intelligent modeling of human driver: A survey," *2007 IEEE Intelligent Vehicles Symposium*. 648 – 651, 2007.
[96] S. Ertugrul, "Predictive modeling of human operators using parametric and neuro-fuzzy models by means of computer-based identification experiment," *Engineering Applications of Artificial Intelligence*. 21: 259-268, 2008.
[97] Y. Uno, M. Kawato and R. Suzuki, "Formation and control of optimal trajectory in human multi-joint arm movement-minimum torque change model," *Biological Cybernetics*, 61: 89-101, 1989.
[98] H. Imamizu, S. Miyauchi, T. Tamada, etc., "Human cerebellar activity reflection an acquired internal model of a new tool," *Nature*, 403: 192-195, 2000.
[99] M. Ito, "Internal model visualized," *Nature*, 403: 153-154, 2000.
[100] M. Arif, H. Inooka, "Iterative manual control model of human operator," *Biological Cybernetics*, 81: 445-455, 1999.
[101] R.W. Brockett, "Minimum attention control," in *Proceeding of 36th IEEE CDC San Diego, CA*: 2628-2632, 1999.
[102] K.J. Astrom, B. M. Bernhardsson, "Comparison of Riemann and lebesgue sampling for first order stochastic systems," in *Proceeding of 41st IEEE CDC Las Vegas, NV*: 2011-2016, 2002.
[103] EWI AdvancedTrainer™ http://www.ewi.org/ewi-advancetrainer %E2%84%A2-innovation -in-welder-training, 2011.
[104] EWI RealWelder Trainer™ http://www.realweldsystems.com/tag/ewi/, 2013.
[105] K. Fast, T. Gifford, R. Yancey, "Virtual training for welding," in *Proc. 3rd IEEE and ACM International Symposium on Mixed and Augmented Reality*: 298-299, 2004.
[106] Choquet, C. "Arc+: Today's virtual reality solution for welders," in *Proc. International Conference of Safety and Reliability of Welded Components in Energy and Processing Industry*, 2008.
[107] Fronius International, Fronius Virtual Welding, http://www.fronius.com/cps/rde/xchg/SID-A0A61DDC-33C5ACA6/ fronius_international/hs.xsl/79_15490_ENG_HTML.htm, 2011,

[108] The Lincoln Electric Company, VREX 360-Virtual Reality Arc Welding (VRAW™) training trainer, http://www. Lincolnelectric .com /en-us/equipment/training-equipment/Pages/ vrtex360.aspx, 2011,
[109] R. T. Azuma, "A Survey of Augmented Reality," *Teleoperators and Virtual Environments*, vol. 6(4), pp. 355-385, 1997.
[110] D.W.F. van Krevelen, R. Poelman, "A survey of Augmented Reality Technologies, Applications and Limitations," *The International Journal of Virtual Reality*, 9(2): 1-20, 2010.
[111] Y.K. Liu, Y.M. Zhang, "Model-based Predictive Control of Weld Penetration in Gas Tungsten Arc Welding," *IEEE Transactions on Control Systems Technology*, 22(3): 955-966, 2014.
[112] Y.K. Liu, W.J. Zhang, Y.M. Zhang, "Estimation of Weld Joint Penetration Under Varying GTA Pools," *Welding Journal*, 92(11): 313s-321s, 2013.
[113] Hayashi, K., et.al.,"Neuro fuzzy transmission control for automobile with variable loads," *IEEE Transactions on Control Systems Technology*, 3(1): 49-53, 1995.
[114] K. Tanaka, M.Sano, and H. Watanabe, "Modeling and Control of Carbon Monoxide Concentration Using a Neuro-Fuzzy Technique," *IEEE Transactions on Fuzzy Systems*, 3(3): 271-279, 1995.
[115] R. Kovacevic, and Y.M. Zhang, "Neurofuzzy model-based weld fusion state estimation," *IEEE Control System Magazine*,17(2): 30-42, 1997.
[116] Y.M. Zhang, and R. Kovacevic, "Neurofuzzy model based control of weld fusion zone geometry," *IEEE Transactions on Fuzzy Systems*, 6(3): 389-401, 1998.
[117] J.S.R Jang, and C.T. Sun, "Neuro-Fuzzy Modeling and Control", *Proceedings of the IEEE*, 83(3): 378-406, 1995.
[118] J.S.R Jang, "ANFIS: Adaptive-network-based Fuzzy Inference Systems", *IEEE Transactions on Systems, Man, and Cybernetics*, 23(3): 665-685, 1993.
[119] W. Lih, et.al., "Adaptive Neuro-Fuzzy Inference System Modeling of MRR and WIWNU in CMP Process with Sparse Experimental Data," *IEEE Transactions on Automation Science and Engineering*, 5(1): 71-83, 2008.
[120] J. Zhai, et.al.," The Dynamic Behavioral Model of RF Power Amplifiers with the Modified ANFIS," *IEEE Transactions on Microwave Theory and Techniques*, 57(1): 27-35, 2009.
[121] M. Imen, M. Mansouri, and M.A. Shoorehdeli, "Tracking Control of Mobile Robot Using ANFIS," *Proceedings of the 2011 IEEE International Conference on Mechatronics and Automation*, Aug. 7-10, Beijing, China, 2011.
[122] Y.K. Liu, and Y.M. Zhang, "Control of 3D Weld Pool Surface," *Control Engineering Practice (Elsevier)*, 21(11): 1469-1480, 2013.
[123] Y.K. Liu, Z. Shao, Y.M. Zhang, "Learning Human Welder Movement in Pipe GTAW: A Virtualized Welding Approach," *Welding Journal*, accepted for publication, 2014.
[124] Y.K. Liu, and Y.M. Zhang, "Toward Intelligent Welding Robot: A Remotely-Controlled Approach," *IEEE Transactions on Automation Science and Engineering*, under review, 2014.
[125] Y.K. Liu, and Y.M. Zhang, "Control of Human Arm Movement in Machine-Human Cooperative Welding Process," *Control Engineering Practice*, accepted for publication, 2014.

[126] Y.K. Liu, and Y.M. Zhang, "Iterative Local ANFIS Based Human Welder Intelligence Modeling and Control in Pipe GTAW Process: A Data-Driven Approach," *IEEE/ASME Transactions on Mechatronics*, under review, 2014.
[127] Y.K. Liu, and Y.M. Zhang, "Supervised Learning of Human Welder Behaviors for Intelligent Robotic Welding," *IEEE Transactions on Automation Science and Engineering*, under review, 2014.
[128] Y.K. Liu, and Y.M. Zhang, "Controlling 3D Weld Pool Surface by Adjusting Welding Speed," *Welding Journal*, under review, 2014.
[129] Y.K. Liu, and Y.M. Zhang, "Fuzzy Weighting Based Data Fusion in Intelligent Welding Robots: Combining Machine and Human Intelligence," *Control Engineering Practice*, under review, 2014.
[130] Y.K. Liu, and Y.M. Zhang, "Learning Welder's Intelligence in 3D: A Data-Driven Approach," *Automatica*, under review, 2014.

VITA

Yukang Liu was born in Taiyuan, Shanxi, China

Education

M.S. in Electrical Engineering, University of Kentucky, Lexington, KY, Dec. 2012

B.Eng. in Electrical Engineering Northwestern Polytechnical University, Xi'an, Shanxi, China, Jun. 2009

Industrial Experiences

Research Intern, *Corning Incorporated*, Corning, NY, May 2014-Aug 2014

Software Engineering Intern, *The MathWorks*, Natick, MA, Sep 2013-May 2014

C++ Algorithm Software Engineering Intern, *The MathWorks*, Natick, MA, May 2013-Aug 2013

Publications

Published/Accepted Journal Publications

1. **Liu, Y.K.**, Zhang, Y.M., "Model-based Predictive Control of Weld Penetration in Gas Tungsten Arc Welding," *IEEE Transactions on Control Systems Technology*, vol. 22(3), pp. 955-966, 2014.
2. **Liu, Y.K.**, Zhang, Y.M., "Toward Welding Robot with Human Knowledge: A Remotely-Controlled Approach," *IEEE Transactions on Automation Science and Engineering*, accepted for publication, 2014.
3. **Liu, Y.K.**, Zhang, W.J., Zhang, Y.M., "Dynamic Neuro-fuzzy Based Human Intelligence Modeling and Control in GTAW", *IEEE Transactions on Automation Science and Engineering*, accepted for publication, 2014.
4. **Liu, Y.K.**, Zhang, Y.M., "Control of Human Arm Movement in Machine-Human Cooperative Welding Process," *Control Engineering Practice*, vol. 32, pp. 161-171, 2014.
5. **Liu, Y.K.**, Zhang, Y.M., "Control of 3D Weld Pool Surface," *Control Engineering Practice*, vol. 21(11), pp. 1469-1480, 2013.
6. **Liu, Y.K.**, Zhang, W.J., Zhang, Y.M., "A Tutorial on Learning Human Welder's Behavior: Sensing, Modeling, and Control," *Journal of Manufacturing Processes (Elsevier)*, vol. 16, pp. 123-136, 2014.

7. **Liu, Y.K.**, Shao, Z., Zhang, Y.M., "Learning Human Welder Movement in Pipe GTAW: A Virtualized Welding Approach," *Welding Journal*, vol. 93, pp. 388s-398s, 2014.
8. **Liu, Y.K.**, Zhang, Y.M., Kvidahl, L., "Skilled Human Welder Intelligence Modeling and Control: Part I-Modeling," *Welding Journal*, vol. 93, pp. 46s-52s, 2014.
9. **Liu, Y.K.**, Zhang, Y.M., Kvidahl, L., "Skilled Human Welder Intelligence Modeling and Control: Part II-Analysis and Control Applications," *Welding Journal*, vol. 93, pp. 162s-170s, 2014.
10. **Liu, Y.K.**, Zhang, W.J., Zhang, Y.M., "Estimation of Weld Joint Penetration Under Varying GTA Pools," *Welding Journal*, vol. 92(11), pp. 313s-321s, 2013.
11. **Liu, Y.K.**, Zhang, W.J., Zhang, Y.M., "Adaptive Neuro-Fuzzy Inference System (ANFIS) Modeling of Human Welder's Response to 3D Weld Pool Surface in GTAW", *Journal of Manufacturing Science and Engineering-Transactions of the ASME*, vol. 135, pp. 0210101-02101011, 2013.
12. Zhang, W.J., **Liu, Y.K.**, Wang, X., Zhang, Y.M., "Characterization of Three-dimensional Weld Pool Surface in Gas Tungsten Arc Welding", *Welding Journal*, vol. 91, pp. 195s-203s, 2012.
13. Chen, S.J., Huang, N., **Liu, Y.K.**, Zhang, Y.M., "Machine Assisted Travel Speed Control in Manual Welding Torch Operation", *International Journal of Advanced Manufacturing Technology*, accepted for publication, 2014.
14. Wang, Y., Yang, Y., Ma, Y., He, Z., **Liu, Y.K.**, "Broadband pattern synthesis for circular sensor arrays", *Journal of the Acoustical Society of America Express Letters (JASA-EL)*, vol. 136(2), pp. 153-158, 2014.
15. Marksberry, P., Chang, C. H., **Liu, Y.K.**, "Managing the Quality Circle (QC) Process: A New Investigation of Toyota's Quality Circle Practices", *International Journal of Productivity and Quality Management (IJPQM)*, vol. 8, No. 2, pp.113-133, 2011.

Journal Publications under Review

16. **Liu, Y.K.**, Zhang, W.J., Zhang, Y.M., "Nonlinear Modeling of 3D Weld Pool Surface in Gas Tungsten Arc Welding," *Journal of Manufacturing Science and Engineering-Transactions of the ASME*, under review, 2014.
17. **Liu, Y.K.**, Zhang, Y.M., "Iterative Local ANFIS Based Human Welder Intelligence Modeling and Control in Pipe GTAW Process: A Data-Driven Approach," *IEEE/ASME Transactions on Mechatronics*, under review, 2014.
18. **Liu, Y.K.**, Zhang, Y.M., "Supervised Learning of Human Welder Behaviors for Intelligent Robotic Welding," *IEEE Transactions on Automation Science and Engineering*, under review, 2014.
19. **Liu, Y.K.**, Zhang, Y.M., "Controlling 3D Weld Pool Surface by Adjusting Welding Speed," *Welding Journal*, under review, 2014.

20. **Liu, Y.K.**, Zhang, Y.M., "Fuzzy Weighting Based Data Fusion in Intelligent Welding Robots: Combining Machine and Human Intelligence," *Control Engineering Practice*, under review, 2014.
21. **Liu, Y.K.**, Zhang, Y.M., "Learning Welder's Intelligence in 3D: A Data-Driven Approach," *Automatica*, under review, 2014.

Referred Conference Publications

1. **Liu, Y.K.**, Zhang, Y.M., "Dynamic Control of 3D Weld Pool Surface Based on Human Response Model," in *Proc. 19th IFAC World Congress, Cape Town, South Africa, Aug. 24-29, 2014*.
2. Fu, B., Seidelman, W., **Liu, Y.K.**, Kent. T., Carswell, M., Zhang, Y.M., Yang, R., "Towards Virtualized Welding: Visualization and Monitoring of Remote Welding," in *Proc. 2014 IEEE International Conference on Multimedia & Expo (ICME 2014), Chengdu, China, July 14-18, 2014*.
3. **Liu, Y.K.**, Shao, Z., Zhang, Y.M., Fu, B., Yang, R., "Virtualized Welding based Teleoperation with Pipe Gas Tungsten Arc Welding Applications," in *Proc. 2014 IEEE/ASME International Conference on Advanced Intelligent Mechatronics (AIM 2014), Besan ̧on, France, July 8-11, 2014*.
4. Huang, N., **Liu, Y.K.**, Chen, S.J., Zhang, Y.M., "Control of Human Welder's Arm Movement in Manual Gas Tungsten Arc Welding (GTAW) Process," in *Proc. 2014 IEEE/ASME International Conference on Advanced Intelligent Mechatronics (AIM 2014), Besan ̧on, France, July 8-11, 2014*.
5. **Liu, Y.K.**, Wang. Y., "Low-Frequency Sound Transmission through Water-Air Interface: A Comparison between Ray and Wave Theory," in *Proc. Oceans'14, MTS/IEEE Oceans Conference, Taipei, Taiwan, Apr 7-10, 2014*.
6. **Liu, Y.K.**, Zhang, Y.M., "Weld Penetration Control in Gas Tungsten Arc Welding Process," in *Proc. 39th Annual Conference of IEEE Industrial Electronics Society (IECON13), Vienna, Austria, Nov. 10-13, 2013*.
7. **Liu, Y.K.**, Zhang, Y.M., Fu, B., Yang, R.G., "Predictive Control for Robot Arm Teleoperation," in *Proc. 39th Annual Conference of IEEE Industrial Electronics Society (IECON13), Vienna, Austria, Nov. 10-13, 2013*.
8. **Liu, Y.K.**, Wang, Y., Du, J., Yang, Y., He, Z., "Robust Mode Space Supergain Beamforming for Circular Array Against Unknown Mismatch," in *Proc. Oceans'13, MTS/IEEE Oceans Conference, San Diego, CA, Sep 23-26, 2013*.
9. **Liu, Y.K.**, Zhang, W.J., Zhang, Y.M., "Data Driven Modeling of Human Welder Intelligence: A Neuro-fuzzy Approach, " in *Proc. 9th International Conference on Automation Science and Engineering (2013 CASE), Madison, Wisconsin, Aug 17-21, 2013*.
10. **Liu, Y.K.**, Zhang, W.J., Zhang, Y.M., "Neuro-fuzzy Based Human Intelligence Modeling and Robust Control in Gas Tungsten Arc Welding Process," in *Proc. 2013 American Control Conference (2013 ACC), Washington DC, Jun 17-19, 2013*.

11. **Liu, Y.K.**, Zhang, W.J., Zhang, Y.M., "Dynamic Neuro-fuzzy Estimation of the Weld Penetration in GTAW Process," in *Proc. 2013 IEEE International Instrumentation and Measurement Technology Conference (I2MTC 2013), Minneapolis, MN, May 6-9, 2013*.
12. Zhang, W.J., **Liu, Y.K.**, Zhang, Y.M., "Real-time Measurement of the Weld Pool Surface in GTAW Process," in *Proc. 2013 IEEE International Instrumentation and Measurement Technology Conference (I2MTC 2013), Minneapolis, MN, May 6-9, 2013*.
13. Zhang, W.J., Zhang, X., **Liu, Y.K.**, Zhang, Y.M., "Robust Pattern Recognition of Three Dimensional Weld Pool Surface in Gas Tungsten Arc Welding," in *Proc. 2013 IEEE International Instrumentation and Measurement Technology Conference (I2MTC 2013), Minneapolis, MN, May 6-9, 2013*.
14. **Liu, Y.K.**, Zhang, Y.M., "Adaptive Modeling of Weld Pool Geometry in Gas Tungsten Arc Welding", in *Proc. 2013 IEEE International Conference on Networking Sensing and Control (ICNSC 2013), Paris-Evry, France, Apr 10-12, 2013*.
15. **Liu, Y.K.**, Chen, S., Zhang, W., Zhang, Y.M., "Nonlinear Dynamic Modeling of Weld Penetration in Gas Tungsten Arc Welding Process," in *Proc. 2012 International Conference on Materials and Manufacturing Research (ICMMR2012), Hong Kong, Dec 19-20, 2012*.
16. **Liu, Y.K.**, "Phase Modes Circular Array Superdirective Beamforming," in *Proc. Oceans'12, MTS/IEEE Oceans Conference, Hampton Roads, VA, Oct 14-19, 2012*.
17. **Liu, Y.K.**, Zhang, W., Zhang, Y.M., "Neuro-fuzzy Modeling of Human Welder's Response to 3D Weld Pool Surface in GTAW", in *Proc. of 21th IEEE International Symposium on Industrial Electronics (IEEE-ISIE 2012), Hangzhou, China, May 28-31, 2012*.
18. Wang, X., **Liu, Y.K.**, Zhang, W., Zhang, Y.M., "Estimation of Weld Penetration Using Parameterized Three-Dimensional Weld Pool Surface in GTAW", in *Proc. of 21th IEEE International Symposium on Industrial Electronics (IEEE-ISIE 2012), Hangzhou, China, May 28-31, 2012*.
19. **Liu, Y.K.**, "Spherical Array Superdirective Beamforming based on Spherical Harmonic Decomposition of the Soundfield," in *Proc. Oceans'12, MTS/IEEE Oceans Conference, Yeosu, Korea, May 21-24, 2012*.

Book Chapter

1. Zhang, W.J., **Liu, Y.K.**, Zhang, Y.M., "Real-time Measurement of Three Dimensional Weld Pool Surface in GTAW", *Welding Process, ISBN 979-953-307-1089-4*.

Presentations & Talks

1. **Liu, Y.K.**, Huang, N., Zhang, Y.M., "Human Welder Intelligent Modeling and Control Using Virtualized Welding Platform," in *Technical Program for Annual FABTECH International & AWS Welding Show, Atlanta, GA, Nov 10-13, 2014*.
2. Huang, N., Chen, S.J., **Liu, Y.K.**, Zhang, Y.M., "Machine Assisted Travel Speed Control in GTAW," in *Technical Program for Annual FABTECH International & AWS Welding Show, Atlanta, GA, Nov 10-13, 2014*.
3. **Liu, Y.K.**, Zhang, Y.M., "Weld Penetration Control in GTAW based on 3D Weld Pool Measurements," in *Technical Program for Annual FABTECH International & AWS Welding Show, Chicago, IL, Nov 18-21, 2013*.
4. **Liu, Y.K.**, Zhang, W.J., Zhang, Y.M., "Control of Welding Process based on Modeling of Human Welder Response," in *Proc. 7th Asian Pacific IIW International Congress 2013, Singapore, Jul 8-10, 2013*.
5. **Liu, Y.K.**, Zhang, W., Zhang, Y.M., "Nonlinear Neuro-fuzzy Modeling of Welder's Response", in *Technical Program for Annual FABTECH International & AWS Welding Show, Las Vegas, Nevada, Nov 12-14, 2012*.
6. Ma, X.J., **Liu, Y.K.**, and Zhang, Y.M., "Vision-Based Weld Pool Surface Geometry Measurement System for Pulsed-GMAW Process," in *Proc. 9th International Conference on Trends in Welding Research, Chicago, IL, USA, June 4-8, 2012*.